EXPERIMENTAL INVESTIGATION OF MECHNICAL BEHAVIOR OF AN OXIDE/OXIDE CERAMIC COMPOSITE IN INTERLAMINAR SHEAR AND UNDER COMBINED TENSION-TORSION LOADING

THESIS

Skyler R. Hilburn, Captain, USAF

AFIT-ENY-14-M-26

DEPARTMENT OF THE AIR FORCE
AIR UNIVERSITY

AIR FORCE INSTITUTE OF TECHNOLOGY

Wright-Patterson Air Force Base, Ohio

DISTRIBUTION STATEMENT A.
APPROVED FOR PUBLIC RELEASE; DISTRIBUTION UNLIMITED.

The views expressed in this thesis are those of the author and do not reflect the official policy or position of the United States Air Force, Department of Defense, or the United States Government. This material is declared a work of the U.S. Government and is not subject to copyright protection in the United States.

AFIT-ENY-14-M-26

EXPERIMENTAL INVESTIGATION OF MECHNICAL BEHAVIOR OF AN OXIDE/OXIDE CERAMIC COMPOSITE IN INTERLAMINAR SHEAR AND UNDER COMBINED TENSION-TORSION LOADING

THESIS

Presented to the Faculty

Department of Aeronautics and Astronautics

Graduate School of Engineering and Management

Air Force Institute of Technology

Air University

Air Education and Training Command

In Partial Fulfillment of the Requirements for the

Degree of Master of Science in Material Science

Skyler R. Hilburn, BS

Captain, USAF

March 2014

DISTRIBUTION STATEMENT A.
APPROVED FOR PUBLIC RELEASE; DISTRIBUTION UNLIMITED.

AFIT-ENY-14-M-26

EXPERIMENTAL INVESTIGATION OF MECHNICAL BEHAVIOR OF AN OXIDE/OXIDE CERAMIC COMPOSITE IN INTERLAMINAR SHEAR AND UNDER COMBINED TENSION-TORSION LOADING

Skyler R. Hilburn, BS

Captain, USAF

Approved:

//signed//	
Marina B. Ruggles-Wrenn, PhD (Chairman)	12 March 2014 Date
//signed//	
Thomas G. Eason, PhD (Member)	10 March 2014 Date
//signed//	
Richard B. Hall, PhD (Member)	12 March 2014 Date

AFIT-ENY-14-M-26

Abstract

Creep behavior in interlaminar shear of an oxide-oxide ceramic composite was investigated at 1100°C in laboratory air and in steam. The Nextel™720/aluminosilicate (N720/AS) composite studied in this effort consists of a porous aluminosilicate matrix reinforced with laminated, woven mullite/alumina Nextel™720 fibers, has no fiber coating, and relies on the porous matrix for flaw tolerance. The interlaminar shear properties were measured. The interlaminar shear strength (ILSS) was determined as 7.65 MPa. The creep behavior was examined for interlaminar shear stresses in the 2-6 MPa range. Primary and secondary creep regimes were observed in all tests conducted in air and in steam. Tertiary creep was noted in the tests performed at 6 MPa. Creep run-out, defined as 100 h at creep stress, was not achieved in any of the tests. Larger creep strains and higher creep strain rates were produced in steam. Surprisingly, the presence of steam had a beneficial effect on creep lifetimes. Composite microstructure, as well as damage and failure mechanisms were investigated. It appears that matrix strengthening occurred in steam, which resulted in longer creep lifetimes in interlaminar shear.

Additionally, exploratory tension-torsion tests of thin-walled tubular specimens of the N720/AS composite were performed at room temperature in laboratory air. These tests were complemented with uniaxial compression tests designed to measure compressive strength of the composite. The failure stress levels determined in combined tension-torsion tests and in compression tests were used together with data from literature to construct a biaxial failure envelope. The efficacy of Tsai-Wu and Tsai-Hill multiaxial failure theories in predicting failure of the oxide-oxide N720/AS CMC was also explored.

Acknowledgments

Ultimately, this thesis would not have been possible without Dr. Marina Ruggles-Wrenn. She always made time to explain, correct, and guide me throughout the course of my master's program and I cannot thank her enough. I would like to recognize Mr. Larry Zawada (AFRL/RXCC) and Dr. Craig Przybyla (AFRL/RXCC) for sponsoring this research effort along with Dr. Thomas Eason (AFRL/RQHF) and Dr. Richard Hall (AFRL/RXCC) for serving on my thesis committee. Without Mr. Chris Zickefoose and Mr. Matt Thomas, I would still be fighting with equipment to run my tests and I appreciate their assistance. I would like to thank the AFIT machine shop for putting in countless hours in machining specimens for this effort. Additionally, I would like to thank Capt Michael Wilkinson for providing encouragement as we spent many hours working in the same laboratory. Finally, I want to thank my wife, for supporting and loving me while my research was the priority.

Skyler R. Hilburn

Table of Contents

Page

Abstract iv

Table of Contents vi

List of Figures ix

List of Tables xii

I. Introduction 1

- 1.1 Motivation 1
- 1.2 Problem Statement 2
- 1.3 Research Objective 3
- 1.4 Methodology 4

II. Background 6

- 2.1 Ceramics 6
- 2.2 Ceramic Matrix Composites 6
- 2.3 Previous Research 10

III. Material and Specimen Geometry 14

- 3.1 Nextel^{TM} 720/Aluminosilicate (N720/AS) Ceramic Matrix Composite 14
- 3.2 Specimen Geometry 17
  - *3.2.1 Double Notch Shear (DNS) Specimen* 17
  - *3.2.2 Uniaxial compression specimen* 20
  - *3.2.3 Thin-Walled Tubular Specimens* 20

IV. Experimental Set-Up and Test Procedures 23

- 4.1 Mechanical Test Equipment 23
  - *4.1.1 Environmental Test Equipment* 27
  - *4.1.2 Temperature Calibration* 28
- 4.2 Test Preparation 28
  - *4.2.1 Uniaxial Tests* 28
  - *4.2.2 Biaxial Tension-Torsion Tests* 30
- 4.3 Specimen Preparation 33
- 4.4 Test Procedures 35
- 4.5 Microstructural Characterization 36

V. Results and Discussion..40

5.1 Creep Behavior in Interlaminar Shear of N720/AS CMC at 1100^{o}C.................40
5.1.1 Interlaminar Shear Strength 40
5.1.2 Creep Behavior in Interlaminar Shear 41
5.1.3 Fractography 47
5.2 Compressive Stress-Strain Behavior and Compressive Properties of N720/AS CMC...56
5.3 Stress-Strain Behavior and Failure of N720/AS Composite under Combined Tension-Torsion Loading..57

VI. Conclusions and Recommendations..72

Appendix A: Procedures 74

Monotonic Compression to Failure of DNS Specimens 74
Monotonic Compression to Failure of Straightsided Specimens 74
Biaxial Loading of Tension-Torsion Thin Walled Tubes 75
DNS Specimens tested in Interlaminar Compressive Creep 75

Appendix B: Optical Micrographs of Specimen 1...76

Appendix C: Optical Micrographs of Specimen 2...78

Appendix D: Optical Micrographs of Specimen 3 80

Appendix E: Optical Micrographs of Specimen 4...84

Appendix F: Optical Micrographs of Specimen 5...88

Appendix G: Optical Micrographs of Specimen 6 89

Appendix H: Optical Micrographs of Specimen 7 92

Appendix I: Optical Micrographs of Specimen 8..94

Appendix J: Optical Micrographs of Specimen 9..96

Appendix L: Optical Micrographs of Specimen 11.......................................101

Appendix M: Optical Micrographs of Specimen 12.....................................103

Appendix N: Optical Micrographs of Specimen 13 104

Appendix O: Optical Micrographs of Specimen 14 105

Appendix P: Optical Micrographs of Specimen 15 105

Appendix Q: SEM Images of Specimen 1 – DNS Compression to Failure
in Air at 1100°C..106

Appendix R: SEM Images of Specimen 5 – DNS Creep at 6 MPa
in Air at 1100°C..116

Appendix S: SEM Images of Specimen 9 – DNS Creep at 2 MPa
in Air at 1100°C..128

Appendix T: SEM Images of Specimen 11 – DNS Creep at 6 MPa
in Steam at 1100°C..138

Appendix U: SEM Images of Specimen 13 – DNS Creep at 2 MPa
in Steam at 1100°C..151

References.. 165

List of Figures

Page

Figure 1. Schematic of the matrix surrounding the fibers in a composite. After Figure 1.1 in [2]. 7

Figure 2. Optical micrograph (side view) of the N720/AS panels comprised of 18 0/90 layers. 15

Figure 3. Simplified schematic of the novel involute ply layup used to fabricate thin-walled tubular specimens. 16

Figure 4. Schematic of the DNS specimen and the loading mode. 19

Figure 5. Optical micrograph of a typical DNS after failure in interlaminar shear. Note that failure occurs along the shear plane. 19

Figure 6. Schematic of the thin walled tubular specimen showing approximate dimensions. 21

Figure 7. MTS 810 load frame. 23

Figure 8. MTS 809 load frame. 25

Figure 9. Rack mounted Vishay 2310 strain gage SCAs. 26

Figure 10. High speed camera setup. 26

Figure 11. AMTECO hot rail furnace and steam generator. 27

Figure 12. Extensometer positioning on the DNS specimen. 29

Figure 13. Schematic of the end inserts for thin-walled tubular specimens. All dimensions are in inches. 31

Figure 14. Schematic showing placement of strain gages on a thin-walled tubular specimen. Gage 1 and 2 were 180^o apart, gage 3 was 90^o with respect to gage 1. 32

Figure 15. Diagram showing the strain directions on a rosette. 33

Figure 16. Zeiss Discovery.V12 stereoscopic optical microscope. 36

Figure 17. Quanta 450 scanning electron microscope. 37

Figure 18. Buehler IsoMet 5000 linear precision saw. 37

Figure 19. Interlaminar shear stress vs. compressive strain curve obtained for N720/AS at 1100°C in air. 41

Figure 20. Creep strain vs. time curves for N720/AS obtained at applied interlaminar shear stresses in the 2-6 MPa range at 1100°C in air and in steam. 42

Figure 21. Creep strain vs. time curves for N720/AS obtained at applied interlaminar shear stresses in the 2-6 MPa range at 1100°C in air. 43

Figure 22. Creep strain vs. time curves for N720/AS obtained at applied interlaminar shear stresses in the 2-6 MPa range at 1100°C in steam. 44

Figure 23. Minimum creep rate as a function of applied interlaminar shear stress for N720/AS CMC at 1100 °C in air and in steam. 45

Figure 24. Interlaminar shear stress vs. time to rupture for N720/AS CMC at 1100°C in air and in steam. 46

Figure 25. Fracture surface of the DNS specimen tested in compression to failure at 1100 °C in air (test duration < 15 s). 47

Figure 26. SEM micrographs of the fracture surface of the DNS specimen tested in compression to failure at 1100 °C in air (test duration < 15 s). 48

Figure 27. Fracture surface of the DNS specimen tested in creep at 6 MPa at 1100°C in air, tf = 14.1 h. 50

Figure 28. Fracture surface of the DNS specimen tested in creep at 2 MPa at 1100°C in air, tf = 78.3 h. 51

Figure 29. Fracture surface of the DNS specimen tested in creep at 6 MPa at 1100°C in steam, tf = 22.7 h. 54

Figure 30. Fracture surface of the DNS specimen tested in creep at 2 MPa at 1100°C in steam, tf = 96.9 h. 55

Figure 31. Representative compressive stress-compressive strain curve for N720/AS composite obtained at 23°C in air. 57

Figure 32. A schematic of the 45° rectangular strain gauge rosette. 59

Figure 33. Axial stress σ_{yy} vs. axial strain ε_{yy} curve for Specimen A tested in combined tension-torsion with the SR of 1:4. 61

Figure 34. Shear stress τ_{xy} vs. shear strain γ_{xy} curve for specimen A tested in combined tension-torsion with the SR of 1:4. 61

Figure 35. N720/AS specimen A tested in combined tension torsion with the SR of 1:4. 62

Figure 36. Axial stress σ_{yy} vs. axial strain ε_{yy} curves for specimen B tested in combined tension-torsion with the SR of 1:1. 64

Figure 37. Shear stress τ_{xy} vs. shear strain γ_{xy} curves for specimen B tested in combined tension-torsion with the SR of 1:1. 64

Figure 38. N720/AS specimen B tested in combined tension torsion with the SR of 1:1. 65

Figure 39. Axial stress σ_{yy} vs. axial strain ε_{yy} curves for Specimen C tested in combined tension-torsion with the SR of 1:2. 66

Figure 40. Shear stress τ_{xy} vs. shear strain γ_{xy} curves for specimen C tested in combined tension-torsion with the SR of 1:2. 67

Figure 41. N720/AS Specimen B tested in combined tension torsion with the SR of 1:2. 68

Figure 42. A comparison between experimental and predicted failure envelopes for N720/AS composite under combined tension-torsion. Failure stress values from DeRienzo [90] and Buchanan et al [98] are also included. 71

List of Tables

Page

Table 1. Key CMC property goals, controlling factors, and demonstration tests for CMC capabilities. After DiCarlo et al [18]. 8

Table 2. Typical physical properties of N720/AS composite panels. 14

Table 3. Summary of specimen dimensions and loading calculations for uniaxial tests. 22

Table 4. Summary of specimen dimensions and loading calculations for combined tension-torsion tests. 22

Table 5. PIDF values before and after tuning. 39

Table 6. Summary of compression tests to failure for DNS specimens of the N720/AS composite at 1100°C in laboratory air. 40

Table 7. Summary of creep tests in interlaminar shear for N720/AS composite at 1100°C in laboratory air and in steam. 42

Table 8. Determination of the desired creep stress level. 42

Table 9. Summary of the combined tension-torsion tests performed on N720/AS thin-walled tubular specimens at 23°C in laboratory air. 58

EXPERIMENTAL INVESTIGATION OF MECHNICAL BEHAVIOR OF AN OXIDE/OXIDE CERAMIC COMPOSITE IN INTERLAMINAR SHEAR AND UNDER COMBINED TENSION-TORSION LOADING

I. Introduction

1.1 Motivation

Composites are a unique category of materials that can be engineered to meet specific material property requirements. As the study of composites continues, the capability of materials continues to increase. In general, composites are not new; not only have they been made for thousands of years through the reinforcement of mud bricks with straw, they occur naturally in both wood and bone [1]. A composite material consists of at least two constituent materials (or phases) where the combined composite strength is greater than that of the constituent materials acting independently [2]. Typically, one material, the matrix, is weaker while the other phase, the reinforcement, is stiffer and stronger [2]. Composites offer high strength and stiffness combined with relatively low weight, thus providing a class of materials that can excel in many different industrial applications [3].

Of the many industries that composites are now integrated into, the aerospace industry is one of the largest. Since composites can be used to build lightweight stiff structures that allow for reduced fuel consumption and emissions, the high cost associated with composites is outweighed by the benefits they provide [4]. The aircraft composite content has increased by 25-35% over the last 10 years to the point that, now there are aircraft with 50% composite content by weight [5]. By volume, that equates to almost 80% of the entire structure being comprised of composites [6]. Not only are composites used to make aerospace parts lighter, they also can be used for high temperature applications such as engine components. By designing composites that can withstand higher operating temperatures inside an aircraft engine, fuel efficiency is increased leading to less fuel consumption and lower operating costs [7].

Further research is required to develop composites for high temperature and thermal protection applications. At high temperatures, materials experience additional conditions which require specific design considerations and guidance [8]. For example, time dependent inelastic strains, creep, thermal stresses due to temperature gradients, and degradation of a material and its properties due to the high temperature environment must be addressed [8]. In many aerospace applications, materials must operate at high temperatures in oxidizing environment. Assuming the material of interest reacts with oxygen, oxidation reactions can occur more rapidly at higher temperatures causing significant degradation and erosion of the composite material. In thermal protection systems (TPS), one side of the material experiences high temperatures while the other remains cooler thus protecting what resides behind it. The thermal gradients created due to heating only one side of a composite can create large internal stresses due to the thermal mismatch of matrix and reinforcement [9]. All of these conditions, faced by composites at higher temperatures, require further research to address these difficult issues. Ultimately, a thorough understanding of how a material behaves under service operating conditions is required before it can be safely and reliably used in a structural component.

1.2 Problem Statement

Ceramic matrix composites (CMCs) are promising materials for a variety of high temperature applications. However, before CMCs can be used, the structural integrity must be assured in simulated operating environments. Advanced thermal protection systems (TPS) and aircraft engine components require structural materials that have superior long-term mechanical properties under extreme environmental conditions such as high temperature, high pressure, and water vapor. Among the most promising candidate materials for these applications are ceramic matrix composites (CMCs), which exhibit excellent strength and fracture toughness at high temperatures. Before CMCs can be widely used in TPS applications, their structural integrity and long-term environmental durability must be assured. In the TPS applications, CMCs are expected to experience significant interlaminar shear stresses. Hence, a thorough understanding of CMC behavior in interlaminar shear is needed. Characterization of the behavior in interlaminar shear of candidate CMCs in relevant environments is critical to safe and reliable use of these materials in TPS applications.

1.3 Research Objective

The objective of this research is twofold. First, this effort aims to investigate creep behavior in interlaminar shear of an oxide-oxide CMC at elevated temperature in laboratory air and in steam using double notch shear (DNS) specimens. In addition, the research explores failure of the candidate CMC under combined tension-torsion loading. The Nextel™720/ aluminosilicate (N720/AS) oxide-oxide CMC studied in this research consists of an aluminosilicate matrix reinforced with laminated Nextel™720 alumina-mullite fibers woven in an eight harness satin weave (8HSW). The N720/AS is currently being considered for use in aerospace TPS.

In this work, the behavior of N720/AS in interlaminar shear is characterized at a maximum use temperature of 1100°C. The effects of steam environment on the performance in interlaminar shear are identified. The understanding of the composite behavior in interlaminar shear gained in this effort also provides insight into failure modes likely under combined tension-torsion loading of the N720/AS thin-walled tubular specimens fabricated using a novel involute ply lay-up. Exploratory tension-torsion tests conducted in this effort advance the state of the art for biaxial testing of CMCs. These exploratory tests also provide valuable information regarding failure modes and failure stresses associated with combined tension-torsion loading. Finally, results of the biaxial tests and of the uniaxial compression tests performed in this work together with data from literature are used to evaluate the efficacy of existing failure theories in predicting failure of the N720/AS CMC under biaxial tension-torsion loading. Ultimately, this research effort will advance the key technologies essential for insertion of CMCs into TPS and/or aircraft engine applications in the near future.

1.4 Methodology

1.4.1 Perform monotonic compression to failure tests on double notch shear (DNS) specimens to determine the interlaminar shear strength (ILSS)

1.4.2 Perform creep tests at various levels of interlaminar shear stress on DNS specimens at 1100°C in laboratory air to study creep behavior of the N720/AS in interlaminar shear at the maximum use temperature.

1.4.3 To assess the effects of environment on high-temperature creep performance in interlaminar shear of N720/AS, perform creep tests in interlaminar shear at

1100°C in steam. Compare results obtained in steam to those produced in air. Determine whether steam has a degrading or beneficial effect on creep resistance and/or lifetimes of the N720/AS at 1100°C.

1.4.4 Perform exploratory tension-torsion tests on thin-walled tubular specimens at room temperature in laboratory air to gain initial insight into the complex material response under multiaxial loading. Measure failure stresses produced under proportional tension-torsion loading with various ratios of axial stress to shear stress.

1.4.5 Perform compression to failure tests on straight-sided uniaxial specimens at room temperature in laboratory air to measure compressive strength of N720/AS.

1.4.6 Use failure stresses measured in tension-torsion tests and in compression tests together with data from literature to construct a preliminary failure envelope for N720/AS CMC.

1.4.7 Assess applicability of existing multiaxial failure theories (i.e. Tsai-Hill and Tsai-Wu failure theories) to predicting failure of N720/AS composite under combined tension-torsion loading.

II. Background

2.1 Ceramics

Ceramics are a material class with the potential to fulfill the design requirements of the cutting edge high temperature thermal protection systems and aerospace engine applications. While monolithic ceramics have excellent high temperature properties, they have significant drawbacks that must be considered. Monolithic ceramics have higher strength and modulus of elasticity than metals and polymers while having lower densities and thermal expansion coefficients [9]. However, the largest disadvantage of ceramics is their low fracture toughness and their propensity to catastrophic failure [9]. For example, when a ceramic cup is dropped, it shatters catastrophically while a metal mug would absorb the impact by forming a dent (i.e. through plastic deformation). The strength of a ceramic is dependent on and very sensitive to the flaw population. The flaws that are inherent in all ceramic materials can grow to a critical size during use in extreme environments. Once the flaw grows to a critical size, the ceramic fails in a catastrophic manner [9]. While lowering the flaw population can improve durability of monolithic ceramics, research into increasing the fracture toughness of ceramic materials has led to development of ceramic matrix composites [9].

2.2 Ceramic Matrix Composites

The objective behind development of CMCs is to create a material system that exhibits graceful failure while retaining the superior properties of monolithic ceramics. The design philosophies behind CMCs focus on ensuring that cracks initiating in the matrix are deflected around the fibers [10]. Ceramic matrix composites have already been employed in the aerospace industry. Because the CMCs offer superior high-temperature strength combined with low weight compared to high-temperature alloys, they are promising candidate materials for use in combustion turbine sections of an aircraft engine [11]. It is believed that a 1-lb reduction in turbine weight will results in weight reduction of up to 3-lb in the supporting structure [11]. Presently, GE is testing CMCs in the new GE LEAP jet engine [11], the new Air Force Joint Strike Fighter uses CMCs in the turbine vanes of the engine [12], and the Air Force is replacing seals on older F-16 engine exhaust nozzles with new CMC seals [13].

The main advantage of CMCs over monolithic ceramics is their superior toughness, tolerance to the presence of cracks and defects, and non-catastrophic mode of failure. It is recognized that in order to avoid brittle fracture behavior in CMCs and improve the damage tolerance, a weak fiber/matrix interface is needed, which serves to deflect matrix cracks and to allow subsequent fiber pullout [14-16]. A schematic of a composite material showing fibers, matrix and fiber/matrix interface is presented in Figure 1.

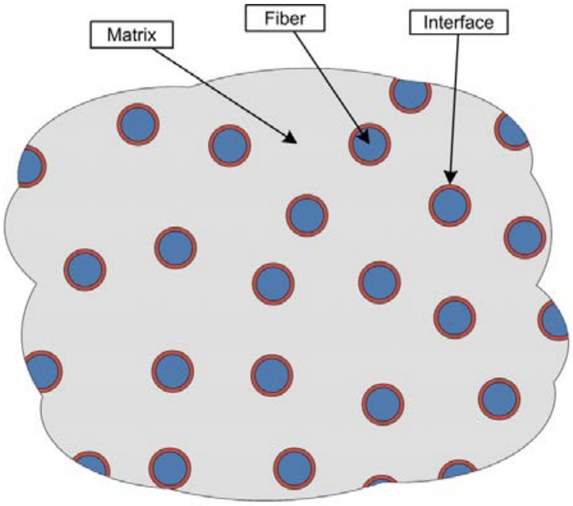

Figure 1. Schematic of the matrix surrounding the fibers in a composite. After Figure 1.1 in [2].

Over the last 30 years extensive research at NASA has been devoted to development of CMCs for hot-section engine components [17]. NASA researchers have summarized goals and requirements for CMCs for engine applications (Table 1) [10]. Because of the high operating temperature of the hydrogen fuel engines of interest to NASA [10], research efforts at NASA have focused on SiC fiber-reinforced SiC matrix (SiC/SiC) CMC systems. The SiC/SiC CMCs offer numerous attractive properties. The SiC/SiC have lower density and higher temperature capability compared to metal superalloys as well as higher toughness and capacity for graceful failure compared to monolithic ceramics. Furthermore, SiC/SiC CMCs have higher strength, temperature capability, and creep resistance compared to oxide/oxide CMCs [17].

Table 1. Key CMC property goals, controlling factors, and demonstration tests for CMC capabilities. After DiCarlo et al [18].

Key CMC Property Goals	Key Controlling Constituent Factors	CMC Demonstration Test
High tensile Proportional Limit Stress after CMC processing	Matrix Porosity, Fiber Content	Tensile stress-strain behavior in fiber direction at room temp and upper use temp
High UTS and strain after CMC processing	Fiber Strength, Fiber Content	Tensile stress-strain behavior in fiber direction at room temp and upper use temp
High UTS retention after interphase exposure at intermediat temperatures in wet oxygen	Fiber Coating Composition	Tensile stress-strain behavior after burner rig near 800oC Rupture behavior of cracked CMC near 800oC in air
High creep resistance at upper use temperature under high tensil stresss	Matrix Creep, Fiber Creep	Creep behavior in air at upper use temperature under a constant tensile stress ~60% fo matrix cracking stress
Long Rupture life at upper use temperature under high tensile stress	Matrix Rupture, Fiber-Rupture	Rupture life in air at upper use temperature under a constant tensile stress ~60% fo matrix cracking stress
High thermal conductivity at all service temperatures	Fiber-Coating-Matrix Conductivity, Matrix Porosity	Thermal conductivity from room temperature to upper use temperature

In many advanced aerospace applications, the fiber-reinforced CMCs will be exposed to elevated temperatures and oxidizing environments. Therefore, the thermodynamic stability and oxidation resistance of CMCs have become important issues. While the SiC fiber-reinforced SiC matrix composites exhibit many excellent properties, their constituents are intrinsically oxidation-prone. Oxidation embrittlement is the most significant problem hindering SiC/SiC composites [19]. Typically, the embrittlement occurs once oxygen enters through the matrix cracks and reacts with the fibers and the fiber coatings [20-22]. The degradation of fibers and fiber coatings is generally accelerated in the presence of moisture [23]. Several studies investigated performance of CMCs consisting of both nonoxide and oxide constituents. Nonoxide fiber/oxide matrix composites or oxide fiber/nonoxide matrix composites were found to exhibit low oxidation resistance. For nonoxide/oxide CMCs, the high permeability constant for the diffusion of oxygen causes rapid oxygen permeation through the oxide matrix [24]. These considerations motivated the development of CMCs based on environmentally stable oxide constituents [25-33].

A CMC can be designed to exhibit improved damage tolerance and graceful failure by introducing a weak fiber/matrix interface which serves to deflect matrix cracks and to allow subsequent fiber pull-out [14, 15, 34]. It is now widely accepted that similar crack-deflecting behavior can also be achieved by means of a finely distributed porosity in the matrix instead of a separate interface between matrix and fibers [35]. This microstructural design philosophy accepts the formation of strong fiber-matrix interfaces. A concept of utilizing a porous matrix to provide for crack deflection in a CMC is based on previous studies of porous interlayers as crack deflection paths [35, 36]. This concept has been successfully demonstrated for oxide-oxide composites [25, 29, 33, 37-42]. Resulting oxide/oxide continuous fiber ceramic composites (CFCCs) exhibit damage tolerance combined with inherent oxidation resistance. An extensive review of the mechanisms and mechanical properties of porous-matrix CMCs is given in [43, 44].

2.3 Previous Research

Numerous recent studies investigated mechanical behavior of high-performance SiC/SiC composites at elevated temperature [45-55]. Likewise, various research efforts studied mechanical performance of oxide-oxide CMCs at elevated temperature [56-65]. The majority of efforts to assess the life-limiting behaviors of the CMCs have been focused mainly on the fiber-dominated properties. However, due to the inherent material defects in the matrix-rich or fiber-matrix interface regions, fiber-reinforced woven CMCs are often susceptible to failure under interlaminar tensile or shear stress. The interlaminar failure or delamination may cause the loss of stiffness and accelerate structural failure of the CMC component [66, 67]. Therefore, a thorough understanding of the performance of the CMCs under interlaminar stresses in service environments is critical to design and life prediction for these materials.

Several authors have examined the high-temperature behavior in interlaminar shear of various 2D woven CMCs. Choi et al [66-70] evaluated high-temperature behavior in interlaminar shear of SiC/BSAS, SiC/MAS, C/SiC, and Hi-Nicalon™/SiC composites using double notch shear (DNS) specimens. Interlaminar shear strength (ILSS) values of 30-50 MPa were reported. Choi and co-workers established the ILSS as a function of loading rate and demonstrated that the ILSS degraded with decreasing loading rate. It was concluded that the life of these CMCs in shear was limited by slow crack growth (SCG) or damage accumulation. A phenomenological, power-law crack growth model was proposed to account for the degradation of ILSS. Model predictions were in good agreement with experimental results. All experimental data reported by Choi and co-workers were obtained at elevated temperature in air. Recently Ruggles-Wrenn and Laffey [62] studied creep behavior in interlaminar shear of an oxide/oxide composite (Nextel™720/alumina) CMC at 1200°C in air and in steam. The creep lifetimes were drastically reduced in the presence of steam.

Numerous research efforts have been devoted to studying the biaxial behavior of and evaluating failure theories for fiber-reinforced polymer matrix laminates. Excellent surveys of these studies can be found elsewhere [2, 71-79]. Recently the international World-Wide Failure Exercise (WWFE) was carried out to assess the accuracy of current predictive theories and theoretical methods of failure prediction for composite laminates with polymer matrix [80-84]. The leading failure theories were explored in great detail to assess their efficacy in predicting structural failure of composite laminates under complex states of stress. Notably these studies focused on polymer matrix composites.

In contrast, only a few studies investigated performance of structural ceramics under complex state of stress. Petrovic and Stout performed combined tension-torsion tests on solid alumina (Al_2O_3) round bars. Principal tensile and compressive stresses were calculated for all test conditions. Results revealed that the tensile principal stress at fracture increased with increasing compressive principal stress. It was found that Al_2O_3 was stronger in torsion than in uniaxial tension. Petrovic and Stout also reported that the results were influenced by the test method. [85]. In a follow-on effort, Stout and Petrovic tested alumina thin-walled tubular specimens under axial tension, hoop tension, combined tension and internal pressure, combined compression and internal pressure and pure torsion. Slight weakening was observed in combined tension-internal pressure compared to axial tension. Conversely, the strength in pure torsion was found to be 16% higher than the axial strength. [86].

Nohut et al performed tension-torsion tests on alumina solid round bar specimens. The experimental results were compared with the effective volume and effective surface values calculated according to different multiaxial failure criteria. The following failure criteria were employed: (i) normal stress criterion, (ii) first principal stress criterion, (iii) von Mises stress criterion, (iv) coplanar energy release rate criterion, (v) maximum non-coplanar energy release rate criterion, (vi) the maximum energy hoop stress criterion and (vii) Richard empirical criterion (based on fitting a large set of experimental data obtained under multiaxial loading). Nohut et al concluded that failure was due to the presence of surface flaws and that the normal stress criterion successfully predicted strength of alumina under multiaxial stress state. [87].

Kawai et al examined performance of silicon nitride under multiaxial stress state. Combined compression–torsion tests were performed on solid round bars. This study emphasized the influence of prior heat treatment on specimen strength. [88]

Liao et al proposed a method for testing ceramic composite tubes under multiaxial loading. Thin-walled tubular specimens were fabricated by winding continuous Almax alumina-based fibers into a preform with a ±45 fiber orientation. The preform was infiltrated with the alumina matrix material using a sol-gel infiltration technique. The preform was dried and fired after each infiltration. Typically, 15 or more infiltration cycles were required to obtain matrix porosity of no more than 26%. Tensile and shear (in this case torsional) strength of the specimens were critically affected by the fiber tow cross over regions. Redesigning the architecture of the tubular specimen was recommended. Fatigue loading under 50% of ultimate tensile or shear strength did not significantly reduce the retained axial stiffness or strength. However, superimposing out-of-phase cyclic torsion onto cyclic tension significantly reduced fatigue lifetimes. [89].

A recent study by DeRienzo at AFIT explored failure of N720/AS thin-walled tubular specimens under combined tension-torsion loading. Two successful experiments were performed at room temperature in laboratory air environment. Shear strength was determined as 32.7 MPa in a pure torsion test. Another thin-walled tubular specimen was subjected to proportional tension-torsion loading. In this test, the ratio of applied axial stress to applied shear stress targeted 100% of the ultimate tensile strength (UTS = 228 MPa) and 50% of the ultimate shear strength (USS = 32.7 MPa). Hence, the ratio of applied axial stress to applied shear stress was determined as $\sigma/\tau = 14$. The failure stresses were measured as $\sigma_f = 171.7$ MPa and $\tau_f = 11.8$ MPa. An attempt was made to construct a failure envelope in the $\sigma-\tau$ space using existing data (three data points). [90].

III. Material and Specimen Geometry

3.1 Nextel^{TM} 720/Aluminosilicate (N720/AS) Ceramic Matrix Composite

Three types of specimens were employed in this research: (1) the double notch shear (DNS) specimen, (2) the straight-sided uniaxial compression specimen and (3) the thin-walled tubular specimen.

The material studied was Nextel^{TM}720/Aluminosilicate (N720/AS), an oxide-oxide CMC (manufactured by COI Ceramics, San Diego, CA) consisting of a porous alumina matrix reinforced with Nextel^{TM}720 fibers. There is no fiber coating. The DNS specimens as well as the compression specimens were cut from panels comprised of 18 0°/90° woven layers. The fiber fabric was infiltrated with the matrix in a sol-gel process. The laminate was dried with a "vacuum bag" technique under low pressure and low temperature, and then pressureless sintered [91]. Typical N720/AS composite panel physical properties of the type used in this research are summarized in Table 2. The optical micrograph (side view) of the composite panel is shown in Figure 2.

Table 2. Typical physical properties of N720/AS composite panels.

Density (g/cm3)	Fiber Volume (%)	Matrix Volume (%)	Matrix Porosity (%)
2.67	47.2	31.1	21.7

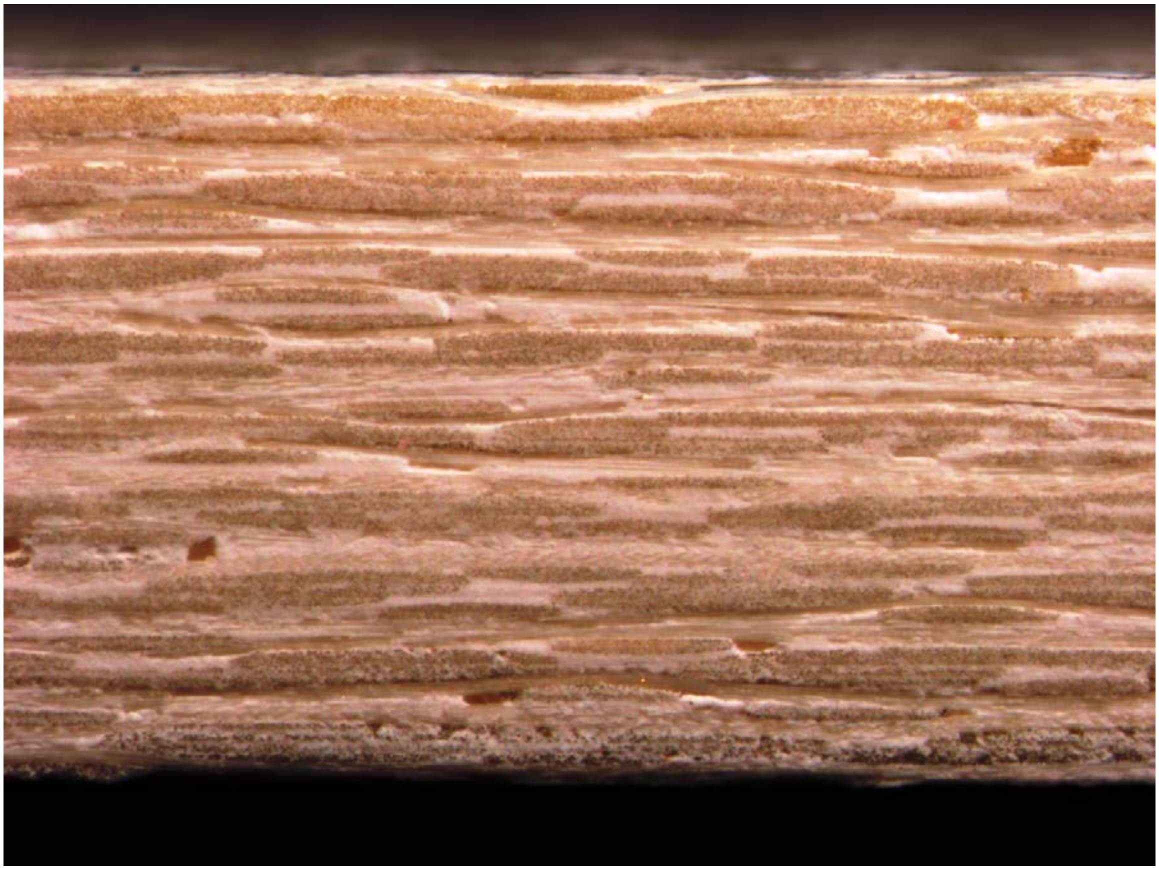

Figure 2. Optical micrograph (side view) of the N720/AS panels comprised of 18 0/90 layers.

The thin-walled tubular specimens were fabricated by COI Ceramics (San Diego, CA) using a novel involute layup schematically shown in Figure 3. In this process, N720/AS plies were cut into 2-in wide strips were assembled such that one end of the ply resided on the outer surface of the tube and the other end, on the inner surface. The walls of the final involute tube were nominally comprised of 16 plies. Such lay-up is readily machinable to desired specifications. Furthermore, the involute lay-up resists defects caused by ply wrinkling. Fiber architecture of the involute tubes is designed with 0° fibers directed along the axis (length) of the tube. Thus, the tube is expected to exhibit fiber-dominated behavior under axial loading. Note that the involute lay-up creates a matrix-dominated interlaminar path from the outer surface to the inner surface of the tube. Hence, the involute tube is expected to fail through interlaminar shear when subjected to pure torsion. Each involute tube was machined to produce the thin-walled tubular test specimens. The total length of the thin-walled tubular specimen was 9 in. The ID of the tubular specimen was 1.5 in. The reduced gage section was 3.4-in long reduced and had an OD of 1.61 in. The gripping sections were each 2.3-in. long and had an OD = 1.75 in. Smooth transition from a gripping section to the gage section occurred over 0.51 in.

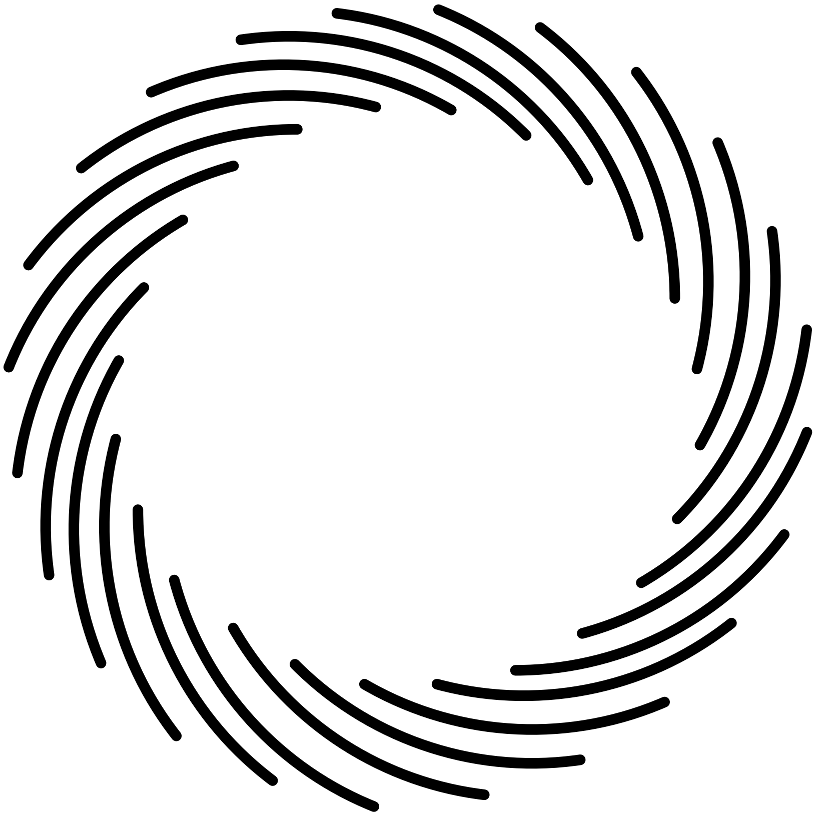

Figure 3. Simplified schematic of the novel involute ply layup used to fabricate thin-walled tubular specimens.

3.2 Specimen Geometry

3.2.1 Double Notch Shear (DNS) Specimen

The DNS specimens of uniform width were used in all interlaminar shear tests. The interlaminar shear strength was measured by loading the DNS specimens in compression in accordance with ASTM Standard C1425-13[92]. Creep tests in interlaminar shear were performed by subjecting the DNS specimens to sustained compressive loading. Per ASTM Standard C1425-13, design of the DNS specimen ensures that failure occurs in interlaminar shear between the two centrally located notches cut halfway through the thickness of the DNS specimen and spaced a fixed distance apart on opposite faces of the specimen.

The DNS specimens used in this work measured 152 mm x 18 mm x 4 mm. The notches of 0.5 mm width were extended to the mid-plane of each test specimen so that shear failure occurred on the plane between the notch tips. The distance between the notches was 13 mm. The DNS specimen and loading mode are schematically shown in Figure 4. The 13 mm distance between the notches permits the measurement of compressive strain between the notch tips with an MTS high-temperature extensometer of 12.5 mm gage length. For strain measurement, the extensometer rods were placed as close to the notch tips of the specimen as possible. All DNS specimens were loaded in compression along the specimen axis (Figure 4) to produce failure by interlaminar shear along the shear plane between the notches (Figure 5).

The shear stress, τ, between the notches along the shear plane was calculated in accordance with the ASTM Standard C1425-13 [92] as:

$$\tau = \frac{P}{Wh} \tag{1}$$

Here P is the applied force, W is the specimen width, and h is the distance between the notches. While the shear stress distribution between the notches is not uniform, the average shear stresses provided by Eq. (1) are useful when evaluating interlaminar shear strength values and comparing creep behavior of specimens subjected to identical mechanical tests in different environments. It is noteworthy that in all tests reported here, the DNS specimens failed in the shear mode along the shear plane.

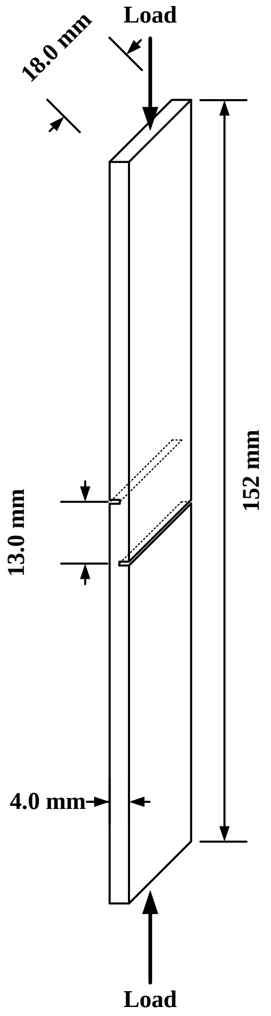
Load
18.0 mm
152 mm
13.0 mm
4.0 mm
Load

Figure 4. Schematic of the DNS specimen and the loading mode.

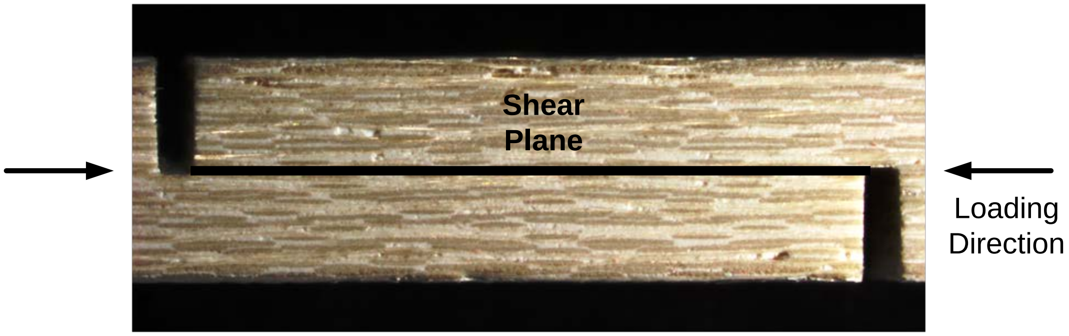
Shear
Plane
Loading
Direction

Figure 5. Optical micrograph of a typical DNS after failure in interlaminar shear. Note that failure occurs along the shear plane.

3.2.2 Uniaxial compression specimen

Straight-sided specimens measuring 152 mm x 18 mm x 4 mm were used in all compression tests to failure. Note that compression tests were performed in order to determine compressive strength of the N720/AS composite. This property is required to exercise the Tsai-Wu and/or Tsai-Hill multiaxial failure criteria. Compressive stress was calculated using the standard expression:

$$\sigma = \frac{P}{A} \tag{2}$$

where P is the applied force and A is the area of the specimen cross section.

3.2.3 Thin-Walled Tubular Specimens

The thin walled tubular specimens were used in all combined tension-torsion tests. In real world applications, materials frequently are subject to complex multiaxial state of stress. Therefore, multiaxial failure analysis is critical to the fundamental understanding material behavior and performance in service. The exploratory tension-torsion tests provide preliminary insight into multiaxial failure modes of the CMC specimens with the involute lay-up. The thin-walled tubular specimens had an average ID of 37.2 mm. The reduced gauge section had the OD of 40.9 mm. A schematic depicting the thin-walled tubular specimen is presented in Figure 6. Axial stresses were calculated using the standard formula:

$$\sigma = \frac{F}{A} \tag{3}$$

where σ is the axial stress, F is the axial force, and A is the crossectional area. Shear stresses were calculated using the following equation

$$\tau = \frac{Tr}{J} \tag{4}$$

where τ is the shear stress, T is the applied torque, r is the outer gage section radius and J is the polar moment of inertia calculated as:

$$J = \frac{\pi}{32}\left(D_o^4 - D_i^4\right) \tag{5}$$

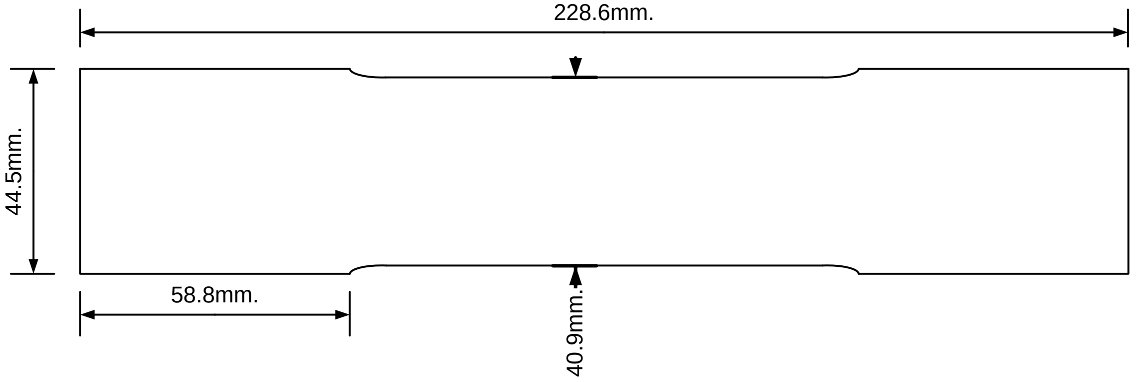

Figure 6. Schematic of the thin walled tubular specimen showing approximate dimensions.

Dimensions of the DNS specimens and compression specimens (CS) used in this work are summarized in Table 3 together with the loading calculations.

Table 3. Summary of specimen dimensions and loading calculations for uniaxial tests.

Specimen	Panel	Type	Avg Width (mm)	Avg Gage Height/Thickness (mm)	Cross Area (m^2)	N/s	MPa/s	N	MPa
1	P11149-E	DNS	18.017	12.094	2.179E-04	444.82	2.041		
2	P11149-D	DNS	18.073	12.638	2.284E-04	444.82	1.948		
3	P11149-E	DNS	18.020	12.738	2.295E-04	344.30	1.500		
4	P11149-D	DNS	17.953	12.810	2.300E-04	344.99	1.500	1379.90	6.000
5	P11149-E	DNS	18.030	12.618	2.275E-04	341.25	1.500	1365.00	6.000
6	P11149-D	CS	18.050	4.020	7.256E-05	1088.40	15.000		
7	P11149-D	DNS	18.057	12.773	2.306E-04	345.95	1.500	922.52	4.000
8	P11149-D	CS	18.057	4.023	7.265E-05	1089.70	15.000		
9	P11149-E	DNS	18.020	12.760	2.299E-04	229.94	1.000	459.88	2.000
10	P11149-D	DNS	18.070	12.760	2.306E-04	345.86	1.500	1383.50	6.000
11	P11149-E	DNS	18.037	12.805	2.310E-04	346.44	1.500	1385.80	6.000
12	P11149-D	DNS	18.060	12.748	2.302E-04	345.33	1.500	920.88	4.000
13	P11149-E	DNS	18.037	12.768	2.303E-04	230.29	1.000	460.57	2.000
14	P11149-E	DNS	18.020	12.738	2.295E-04	229.53	1.000	459.06	2.000
15	P11149-D	DNS	18.050	12.725	2.297E-04	229.69	1.000	459.38	2.000
16	P11149-D	DNS	17.993	3.967	7.137E-05	1070.60	15.000		
17		DNS	15.062	12.635	1.903E-04	285.47	1.500		

Dimensions of the thin-walled tubular specimens used in this work are presented in Table 4 together with the load calculations.

Table 4. Summary of specimen dimensions and loading calculations
for combined tension-torsion tests.

		DIMENSIONS		
Specimen	Tube #	Outer Diameter Average, Do (mm)	Outer Radius Average, r (mm)	Inner Diameter Average, Di
A	1	40.872	20.436	37.24
B	2	40.902	20.451	37.218
C	3	40.864	20.432	37.212
		AXIAL FORCE		
Specimen	Tube #	Axial Stress, σ (MPa)	Area, A (m^2)	Axial Force, P (N)
A	1	212	2.228E-04	47238
B	2	212	2.260E-04	47919
C	3	212	2.239E-04	47476
		TORQUE		
Specimen	Tube #	Desired Shear Stress, τ (MPa)	Polar Moment of Inertia (m^4)	Torque, T (N-m)
A	1	132	8.515E-08	550.03
B	2	33	8.641E-08	139.42
C	3	66	8.551E-08	276.21

IV. Experimental Set-Up and Test Procedures

4.1 Mechanical Test Equipment

Uniaxial mechanical testing was conducted using an MTS 810 Material Test Systems servohydraulic machine with 22.2 kN (5 kip) capacity. The testing system was equipped with hydraulic wedge grips (model MTS 647) cooled with 15^oC deionized water by a Thermo Scientific Neslab HX-75 chiller. An MTS FlexTest 40 digital controller and a PC with MTS FlexTest 40 Software (version 5.2A 2865) were used in all tests to generate input signal and to collect data. The grip pressure was 5 MPa for testing the DNS specimens and 5.75 MPa for testing straight-sided compression specimens. For strain measurement, a uniaxial low contact force high-temperature MTS extensometer (model 632.53E-14) with 1.27 cm gauge length was used in all uniaxial tests. Figure 7 shows the test setup.

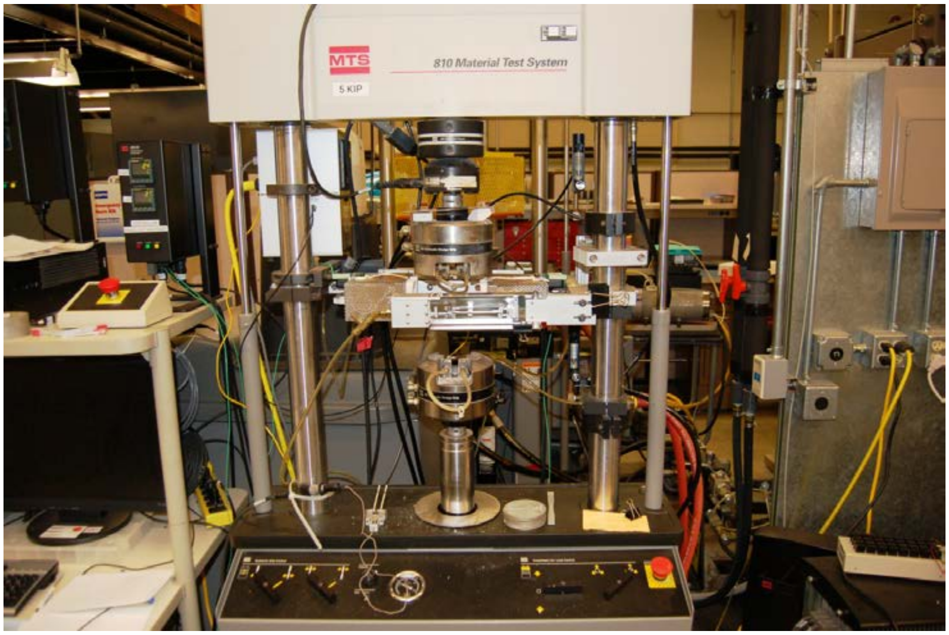

Figure 7. MTS 810 load frame.

Biaxial tension-torsion tests were conducted using an MTS 809 Axial/Torsional test system equipped with MTS 646 hydraulic collet grips. The MTS 809 Axial/Torsional test system has the axial capacity of 98 kN (22,000 lbs) and the torsional capacity of 1130 N-m (10,000 in-lbs). An MTS TestStar IIm digital controller and a PC with TestStar IIm Station Manager Software (version 5.3B 3243) were used for input signal generation and data acquisition. Test setup is shown in Figure 8. The grip pressure in all tests was set to 5 MPa. To accomplish strain measurement, thin-walled tubular specimens were instrumented with strain gauges, which were connected to a rack of 11 Vishay Precision Group 2300 Signal Conditioning Amplifiers (SCAs) seen in Figure 9. The SCAs applied a 0.5 V excitation to the 350 Ω strain gages to condition the signal for proper recording by the MTS system. During the tests, damage development and failure of each specimen were recorded with a Dantec Dynamics Nanosense MkII high speed camera (Figure 10).

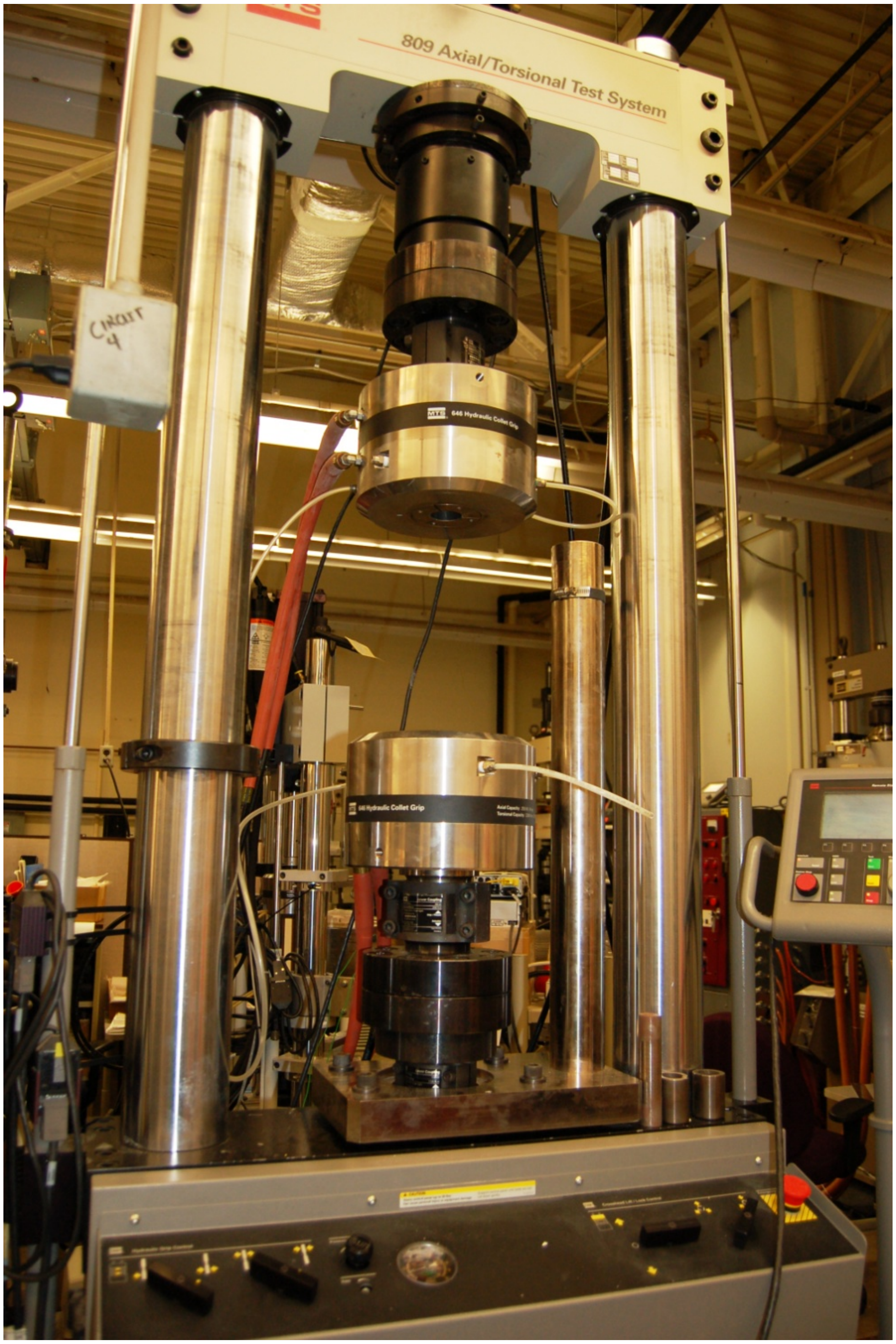
809 Axial/Torsional Test System
CIRCUIT 4
646 Hydraulic Collet Grip
646 Hydraulic Collet Grip

Figure 8. MTS 809 load frame.

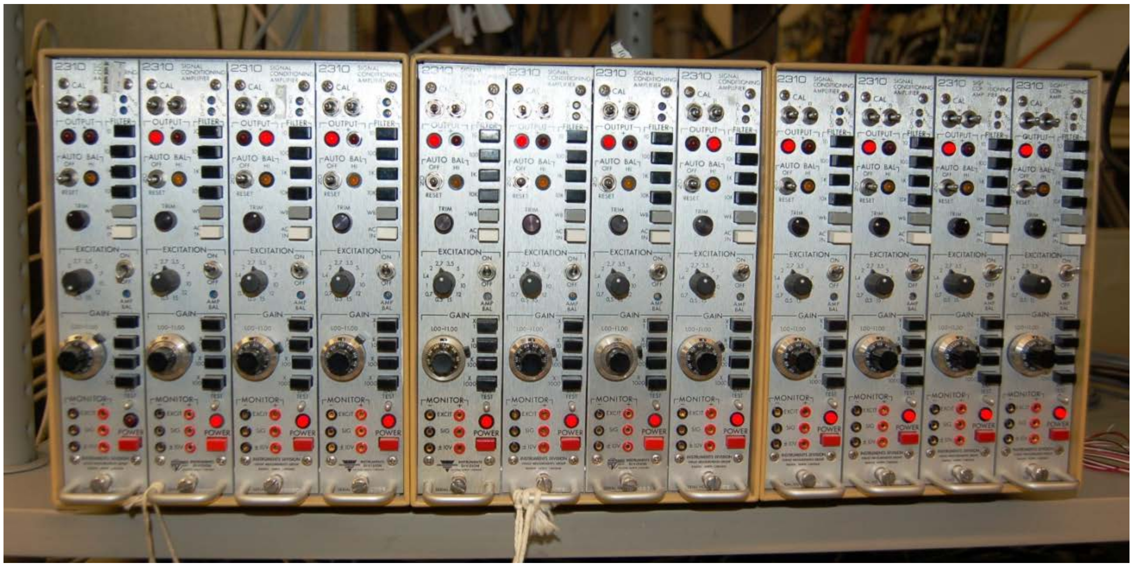

Figure 9. Rack mounted Vishay 2310 strain gage SCAs.

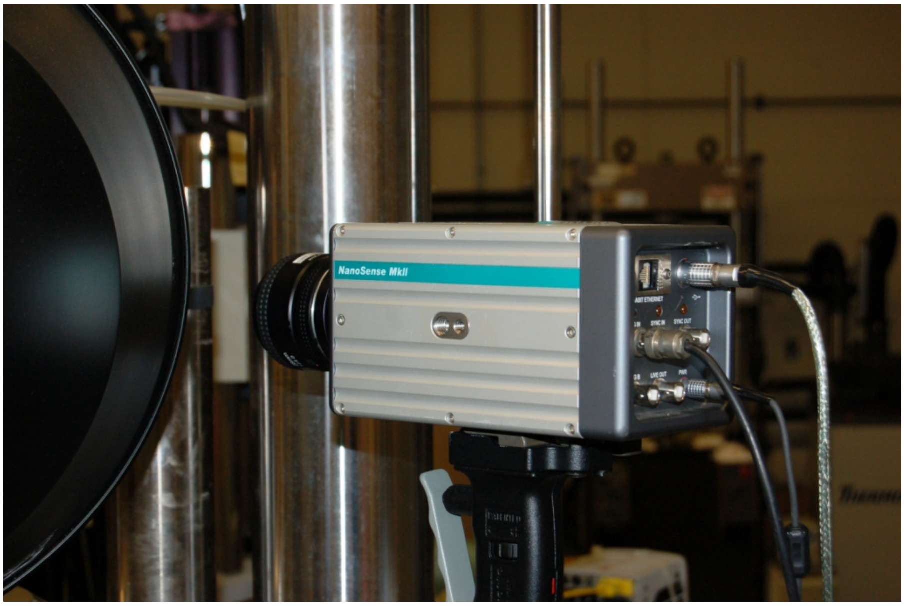
NanoSense MkII

Figure 10. High speed camera setup.

4.1.1 Environmental Test Equipment

Most of the uniaxial tests were performed at 1100°C in laboratory air or in steam. A two-zone AMTECO Hot Rail resistance heated furnace (Figure 11) and two MTS 409.83B temperature controllers were used in all high-temperature tests. An AMTECO HRFS-STMGEN steam generator (Figure 11) and an alumina susceptor were used for testing in steam. The susceptor (tube with endcaps) fits inside the AMTECO furnace. The specimen gage section resides inside the susceptor while the ends of the specimen pass through openings in the susceptor. Steam is supplied to the susceptor through a feeding tube in a continuous stream with low positive pressure, expelling the dry air and creating a near 100% steam environment around the gage section of the specimen.

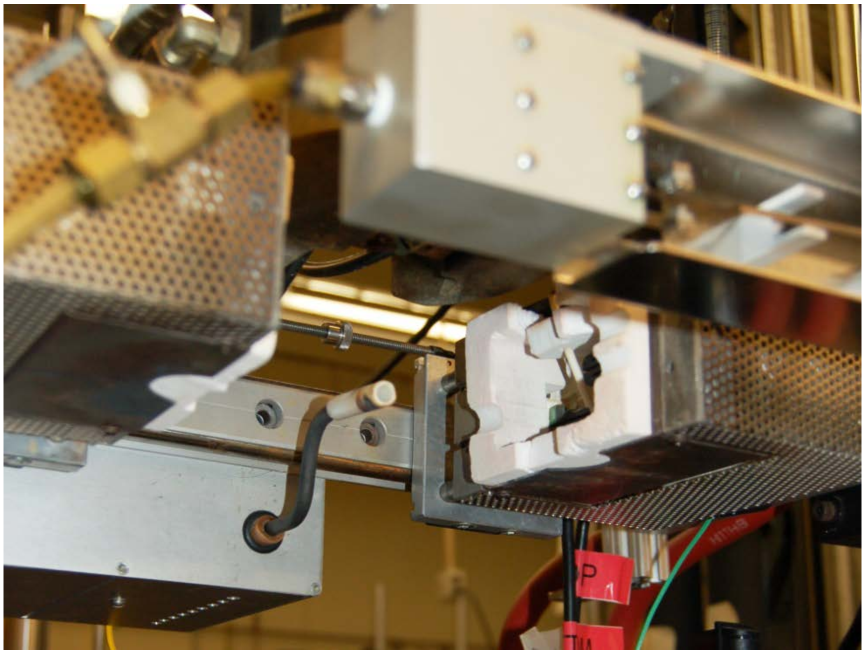

Figure 11. AMTECO hot rail furnace and steam generator.

4.1.2 Temperature Calibration

Temperature calibration for elevated temperature testing in air and in steam was performed on regular basis. For calibration, two R-type thermocouples were attached to a specimen and connected to an Omega CL3515A digital hand thermometer. The set points on the furnace controllers (using non-contacting thermocouples exposed to the environment in the vicinity of the test specimen) were adjusted until a uniform temperature of 1100°C was achieved on both sides of the test specimen. The temperature controller settings determined in this manner were used in the actual tests. For testing in steam, the temperature controller setting were determined by placing the specimen instrumented with thermocouples in steam and repeating the calibration procedure. During tests in laboratory air, temperature of the test specimen was within ±3°C of the nominal test temperature. During tests in steam, temperature of the test specimen was within ±5°C of the desired test temperature. In all elevated temperature tests the specimens was heated to test temperature at the rate of 1°C/s and held at the test temperature for at least 30 min prior to testing. Note that the temperature calibration procedure was performed prior to each test to ensure that the desired test temperature was achieved.

4.2 Test Preparation

4.2.1 Uniaxial Tests

Before each test the MTS testing machine was warmed up for at least 30 min using a cyclic command with a sine waveform in displacement control. Gripping sections of each test specimen were outfitted with fiberglass tabs, which were attached to the specimen using M-Bond 200 adhesive. Note that in the case of CMCs, the specimen surface does not require extensive preparation, unlike metals where oxidation needs to be removed. Prior to gripping in the MTS testing machine, the test specimen was inserted into the susceptor. Then the testing machine is placed in displacement control and the top portion of the specimen is gripped. The next step is to switch control to force, command zero force and grip the bottom portion of the specimen. Once the test specimen is gripped, the furnace is placed around the specimen and the extensometer is mounted. Note that in the case of the DNS specimens, the extensometer rods were placed as close to the root of the notches as possible (Figure 12).

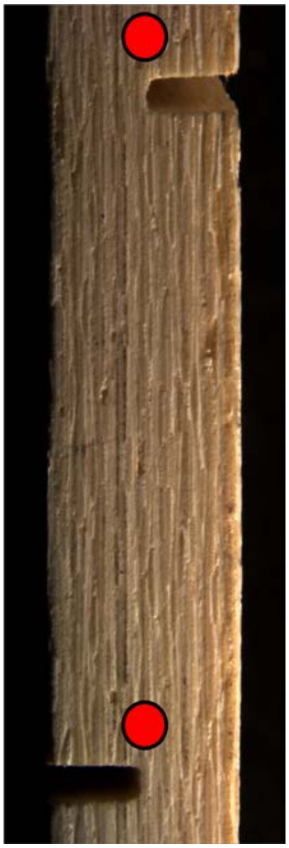

Figure 12. Extensometer positioning on the DNS specimen.

4.2.2 Biaxial Tension-Torsion Tests

Prior to biaxial tension-torsion testing, the axial-torsional MTS machine was warmed for at least 60 min using a cyclic command with a sine waveform in combined displacement/angle of rotation mode. It was necessary to reinforce the gripping sections of the tubular specimens to prevent them from being crushed in the grips. Therefore, two end inserts were machined from aluminum alloy for each test specimen according to specifications in Figure 13. The inserts were placed inside the gripping sections of the tubular specimen and bonded to the specimen using epoxy adhesive. Each specimen was then carefully instrumented with strain gages using M-Bond 200 adhesive. Procedure for attaching the strain gages to the specimen is outlined in Section 4.3 below. The strain gages provided 11 strain measurements that were carefully monitored and recorded. A schematic showing placement of strain gages on a thin-walled tubular specimen is presented in Figure 14. Two 45° rectangular rosettes (C2A-03-250LR-350) accounted for 6 channels of strain signal, while the remaining five channels were used by linear strain gages (L2A-03-250LW-350). Note that 3 linear strain gages were used to construct another 45° rectangular rosette. Each direction on the rosette is represented with a strain direction as seen in Figure 15. A separate signal conditioner was employed to process the signal of each strain gage. Naturally, three signal conditioners were utilized to process signals produced by a strain gage rosette. The conditioned strain signals were sent directly to the MTS Test Star IIm digital controller and recorded in data files. The high speed cameras were prepositioned to provide the best view of the specimen. Initiation of the test procedure with the MTS software also triggered the operation of the high speed cameras.

The testing system was placed in displacement/rotation control and the top portion of the test specimen was gripped. Then the control mode was changed to force/torque, commanding zero force and zero torque, and the bottom portion of the specimen was gripped. Testing is now ready to begin.

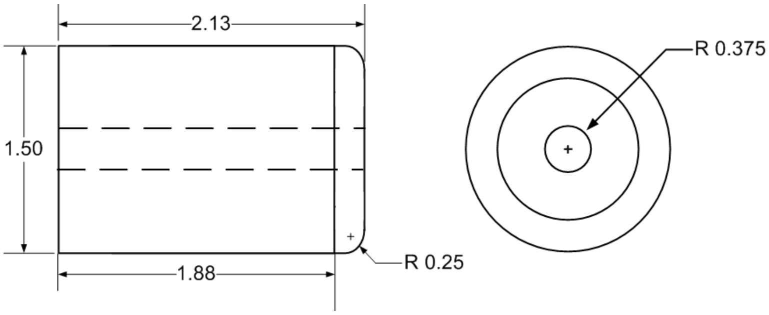

Figure 13. Schematic of the end inserts for thin-walled tubular specimens. All dimensions are in inches.

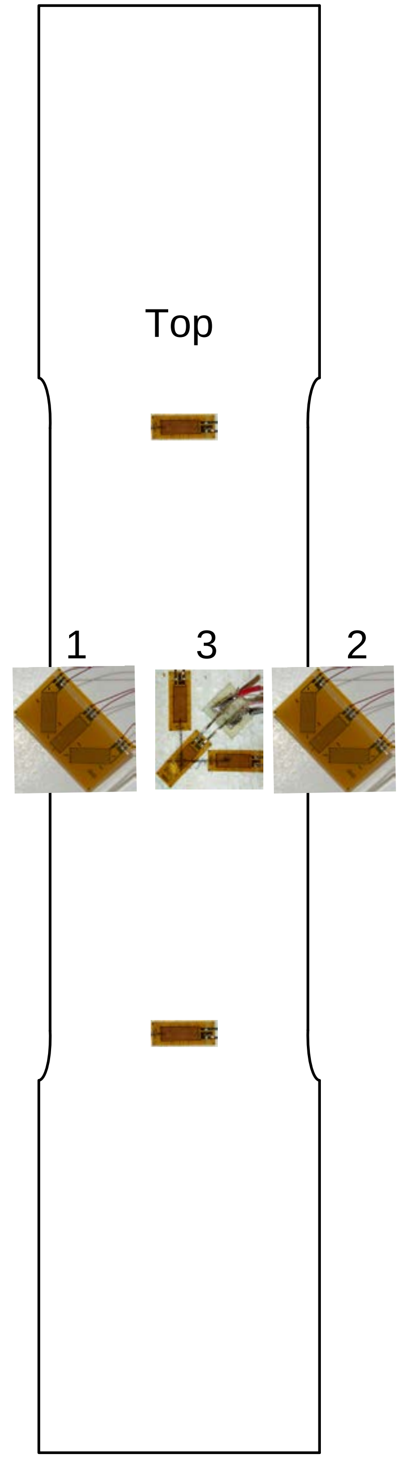

Figure 14. Schematic showing placement of strain gages on a thin-walled tubular specimen. Gage 1 and 2 were 180^{o} apart, gage 3 was 90^{o} with respect to gage 1.

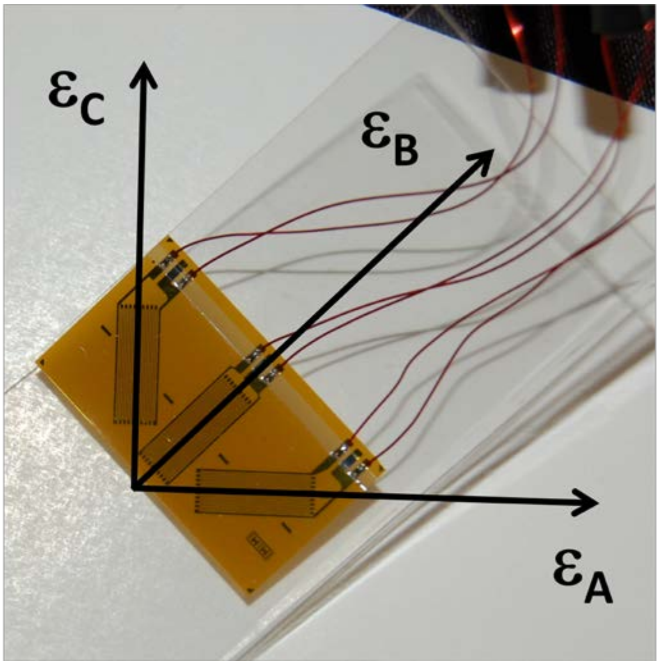

Figure 15. Diagram showing the strain directions on a rosette.

4.3 Specimen Preparation

After machining all uniaxial specimens were cleaned in an ultrasonic bath (Branson 5510 Sonic Bath) using isopropyl alcohol, and then dried in an oven (Quincy Labs Inc. 40 GC Lab Oven). Steps of the specimen cleaning procedure are outlined below:

1. Rinse with isopropyl alcohol
2. Immerse in Ultrasonic Bath of isopropyl alcohol for 20 minutes
3. Soak in a separate isopropyl alcohol bath for 10 minutes
4. Rinse with isopropyl alcohol
5. Dry in an oven for 12-15 h at 100-150 °C.

The thin-walled tubular specimens were instrumented with strain gages using M-Bond 200 adhesive and catalyst. The following procedure was employed:

1. Mark the strain gage locations on the specimen surface. Use pencil to mark center and/or orientation of each strain gage.
2. Do not sand the specimen surface.
3. Clean the specimen surface with isopropyl alcohol.
4. Remove the strain gage from package and place face up on a smooth, flat, clean glass surface.
5. Apply Vishay PCT-2M tape over the top of the gage with at least 1 additional length of tape on both sides of the gage.
6. Remove the tape with the gage from the clean surface and apply the gage to the marked specimen surface, aligning the arrows on the strain gage with the pencil marks made previously.
7. Adjust the position of the gage by moving the tape as needed for proper alignment.
8. Peel back the tape with attached gage until the entire gage is separated from the specimen surface.
9. Apply a small amount of M-Bond 200 catalyst to the back of the gage; allow to dry for 1 min.
10. Apply one drop of M-Bond 200 adhesive to the specimen surface where it meets the tape and align the gage just off the surface using the tape.
11. In a single motion, slide a thumb over the lifted gage and apply thumb pressure for 30 sec. and leave tape on for a minimum of 5 min.
12. Tape down the leads after soldering to provide strain relief
13. Apply glue over solder pads to protect the connections

4.4 Test Procedures

The test method employed for interlaminar shear tests is based on the ASTM Standard C 1425-13 [92]. Note that the aforementioned ASTM standard is generally used for testing small specimens. Recent research efforts at AFIT [93, 94] adapted the standardized test method for testing of 6 in long DNS specimens. The modified test method, which permits interlaminar shear testing using a uniaxial testing machine, was demonstrated to produce successful results. The modified test method was used in this work. The test procedure programmed using the MTS software is shown in Appendix A. Special consideration was taken to ensure that the test was stopped as soon as the specimen failure was reached. This was accomplished through the use of a failure detector set at 85% of Minimum Load with a sensitivity of 85 N. As a result, the tests were stopped and the fracture surfaces were not damaged by continued compression.

Compression tests on straight-sided specimens were performed in accordance with the ASTM Standard C 1358-13 [95]. The test procedure programmed with the MTS software is given in Appendix A.

The biaxial tension torsion test method was based on the ASTM Standard E2207-08(2013) e1 [96]. The test procedure was programmed using the MTS software and is shown in Appendix A. The procedure for the high speed cameras was programmed using the camera software such that the start of the MTS test procedure also initiated the camera recording.

4.5 Microstructural Characterization

Fracture surfaces of the tested specimens were analyzed using a Zeiss Discovery.V12 stereoscopic optical microscope equipped with a Zeiss AxioCam HRc digital camera (Figure 16) and a Quanta 450 Scanning Electron Microscope (SEM) (Figure 17). In preparation for SEM examination, specimens were cut on a Buehler IsoMet 5000 Linear Precision Saw (Figure 18).

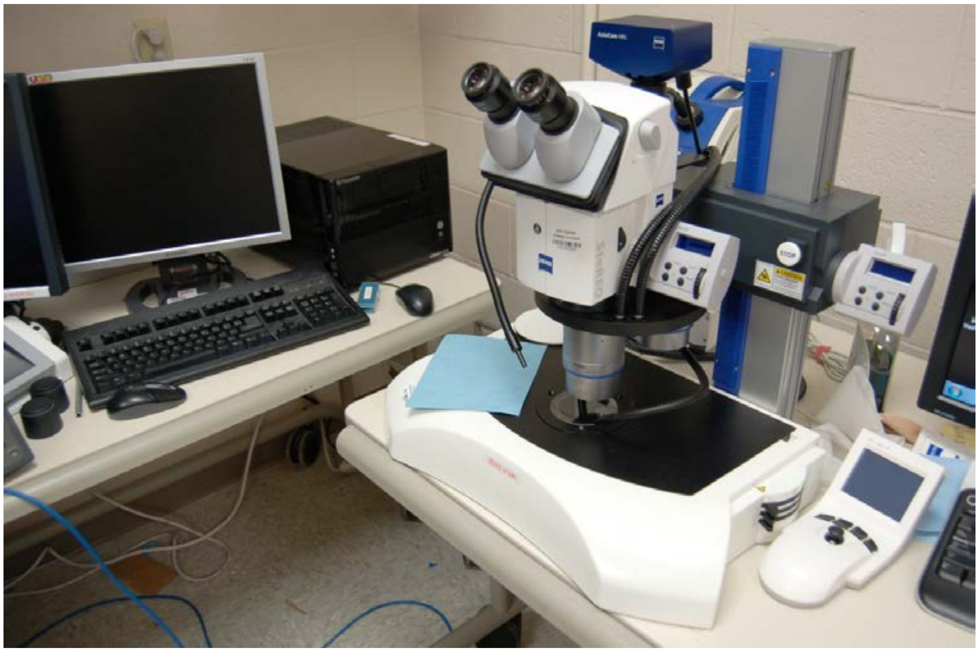

Figure 16. Zeiss Discovery.V12 stereoscopic optical microscope.

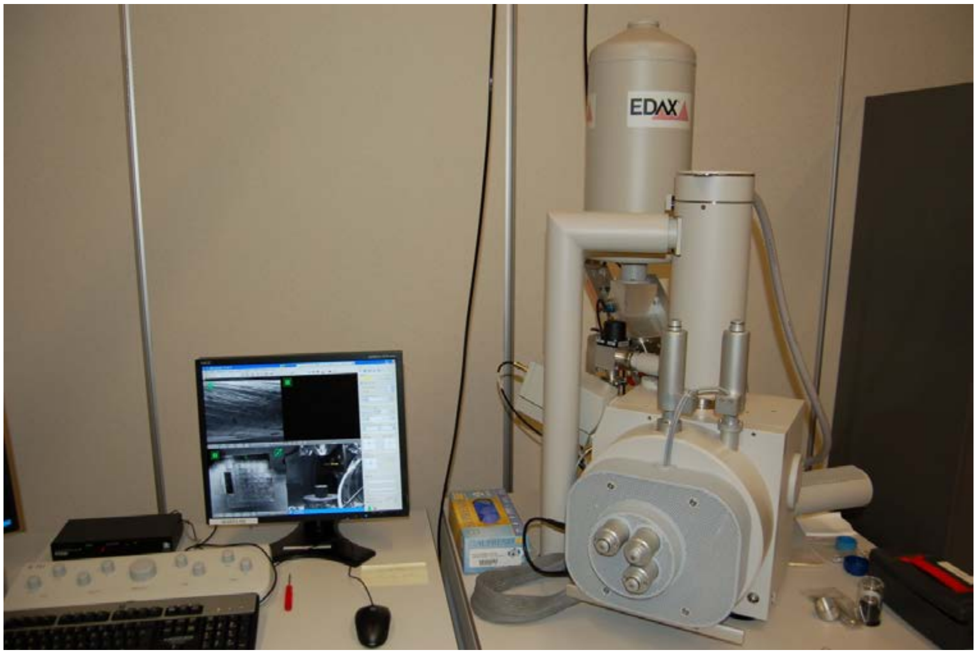

Figure 17. Quanta 450 scanning electron microscope.

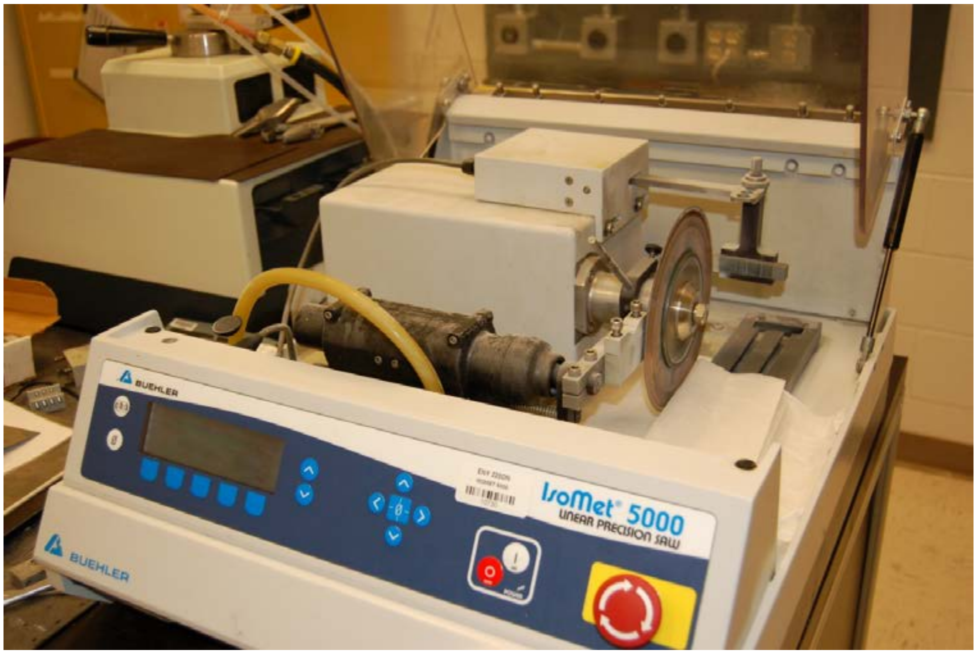
BUEHLER
IsoMet® 5000
LINEAR PRECISION SAW
BUEHLER

Figure 18. Buehler IsoMet 5000 linear precision saw.

4.6 Tuning Adjustment of the MTS TestStar IIm controller for Tension-Torsion Biaxial Loading

Careful review of prior tension-torsion tests performed at AFIT [90] revealed a significant lag between that the axial load feedback and command. The MTS 793 Tuning and Calibration manual provided basic knowledge of tuning parameters and of the resultant effects of changing the values of proportional gain (P), integral gain (I), derivative gain (D), and feed forward gain (F) [97]. It is recognized that to properly tune the system in load/torque control for a given test specimen geometry and material, an actual specimen is required. It should be noted, that the specimen used for tuning may fail during the tuning exercise. Due to a very limited number and high cost of the N720/AS thin-walled tubular specimens, a specimen could not be sacrificed to tune the load control mode. Instead, a thin-walled tubular specimen of identical geometry but made from alumina was used to adjust the gain settings to improve the machine performance. The alumina tubes were subjected to tension-torsion loading, but not loaded to failure. While there was no noticeable lag between torque feedback and command, there was a delay between axial load feedback and command. The gain settings were adjusted to improve the performance of the axial load channel. This procedure was repeated twice and was terminated after the alumina specimen failed. As a result only a small correction was made to the P-gain as seen in Table 5. It should be noted that while the geometry of the alumina specimen is the same as that of the N720/AS specimens, its compliance is different. Hence we cannot expect the two materials to offer the same response under load. Whereas some improvement in axial force response was noted when the N720/AS specimen was tested, both the axial and torque response could still be improved.

Sacrificial N720/AS specimens would be required to perform the proper tuning of the axial force and torque modes.

Table 5. PIDF values before and after tuning.

Axial Channel				
	P	I	D	F
Pre-Tuning	0.8000	0.4004	0.000	0.000
Post-Tuning	0.8300	0.4004	0.000	0.000

V. Results and Discussion

In this work N720/AS specimens of three different types were tested under various loading and environmental conditions. Due to a limited number of specimens, the test results provide a qualitative rather than quantitative assessment of the material behavior. Additional testing should be performed to provide quantitative results with statistical significance.

5.1 Creep Behavior in Interlaminar Shear of N720/AS CMC at 1100°C

5.1.1 Interlaminar Shear Strength

Double notch shear specimens were tested in compression to failure, at 1100°C in laboratory air, to determine the Interlaminar Shear Strength (ILSS). Test results are summarized in Table 6. The ILSS values, with an average of 7.65 MPa, were comparable to ILSS values reported by DeRienzo [90]. A representative stress-strain curve obtained for a DNS specimen in compression test to failure is shown in Figure 19. Note that the shear stress-compressive strain curve is nearly linear to failure.

Table 6. Summary of compression tests to failure for DNS specimens of the N720/AS composite at 1100°C in laboratory air.

	Specimen 1	Specimen 2	Specimen 3	Average
Loading Rate (MPa/s)	2	1.9	1.5	N/A
ILSS (MPa)	7.32	8.50	7.12	7.65
Strain at Failure (%)	0.038	0.071	0.084	0.064

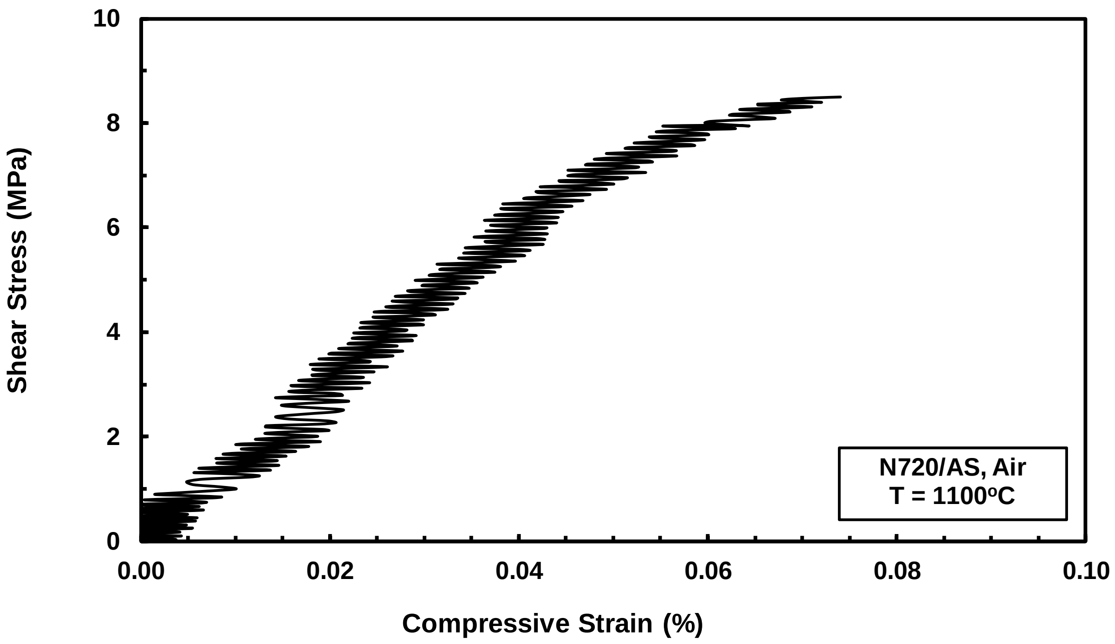

Figure 19. Interlaminar shear stress vs. compressive strain curve obtained for N720/AS at 1100°C in air.

5.1.2 Creep Behavior in Interlaminar Shear

Creep behavior in interlaminar shear was investigating in compression creep tests conducted on DNS specimens at 1100°C in laboratory air and in steam. Test results are summarized in Table 7. The creep stress levels were chosen to represent percentages of the experimentally obtained ILSS of 7.65 MPa (Table 8). Creep curves obtained at 1100^{o}C in air and in steam are presented in Figures 20-22. All creep curves produced at stress levels ≤ 4 MPa exhibit primary and secondary creep regimes, but no tertiary creep. Conversely, creep curves at 6 MPa exhibit some tertiary creep. Primary creep transitions to secondary creep early in creep life, within the first 5 hours of the creep test. Notably, creep run-out defined as 100 h at creep stress was not achieved in this study.

Table 7. Summary of creep tests in interlaminar shear for N720/AS composite at 1100°C in laboratory air and in steam.

Specimen #	Enviroment	Creep Stress (MPa)	Creep Strain (%)	Time to Rupture (h)	Creep Rate (1/s)	Coefficient of Thermal Expansion (10^{-6} 1/^{o}C)
5	Air	6	0.435	14.1	5.5E-08	6.59
7	Air	4	0.396	64.1	8.4E-09	6.50
9	Air	2	0.156	78.3	4.4E-09	6.41
11	Steam	6	1.440	22.7	1.4E-07	5.76
12	Steam	4	1.050	71.9	1.5E-08	6.31
13	Steam	2	0.229	96.9	5.8E-09	6.22

Table 8. Determination of the desired creep stress level.

Percentage of Avg ILSS	80%	55%	25%
Stress Level (MPa)	6.12	4.21	1.91
Stress Level Chosen (MPa)	6.0	4.0	2.0

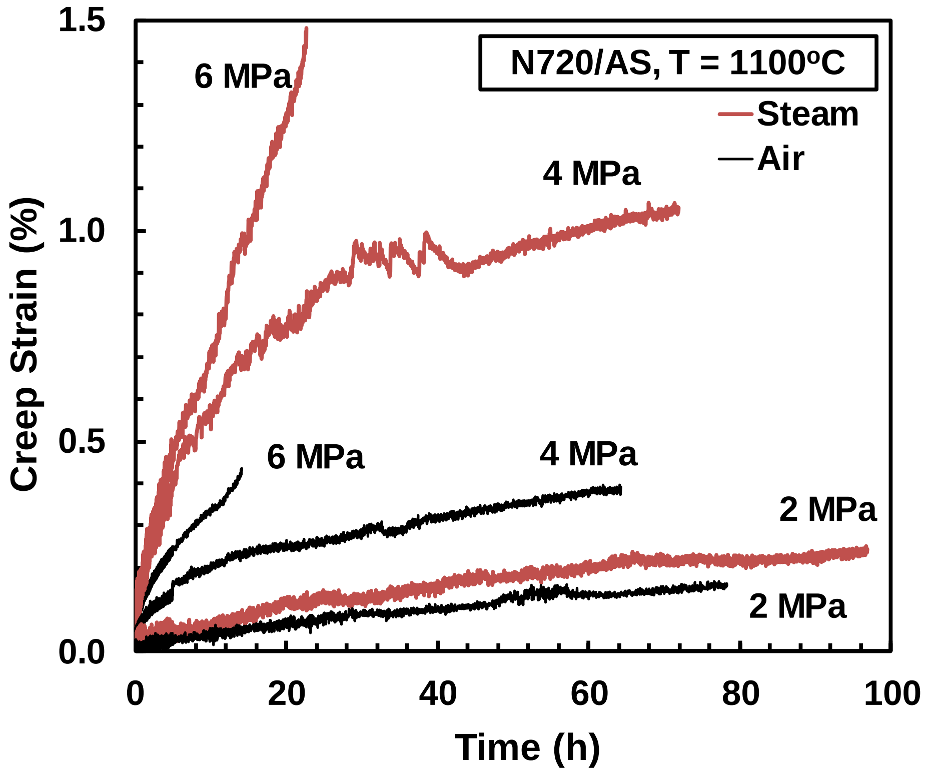

Figure 20. Creep strain vs. time curves for N720/AS obtained at applied interlaminar shear stresses in the 2-6 MPa range at 1100°C in air and in steam.

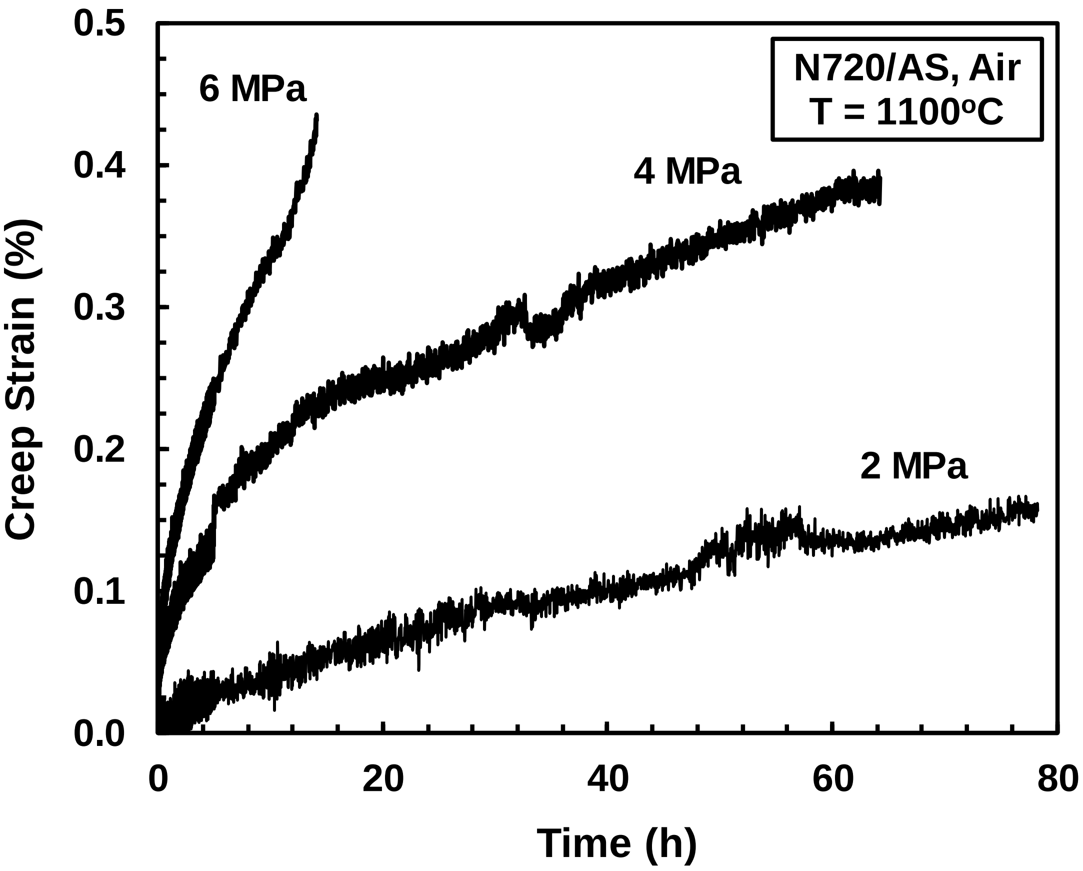

Figure 21. Creep strain vs. time curves for N720/AS obtained at applied interlaminar shear stresses in the 2-6 MPa range at 1100°C in air.

As expected, larger creep strains were accumulated at higher creep stress levels in both air and steam environments. Creep strain accumulated in air at 4 MPa was more than two times that accumulated at 2 MPa. Creep strain produced at 6 MPa was more than three times the creep strain at 2 MPa. While the creep curves produced in steam are qualitatively similar to those produced in air, much larger creep strains were accumulated in steam. As seen in Table 7, creep strains obtained in steam are 2 to 3 times the creep strains obtained in air. As mentioned above, 100-h creep run-out was not achieved in this work.

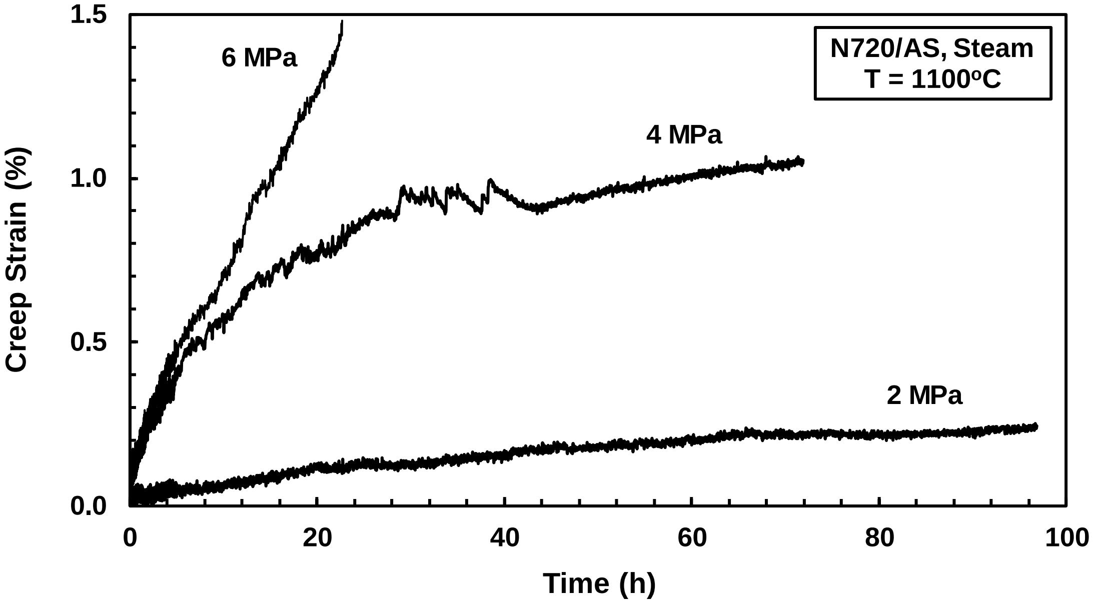

Figure 22. Creep strain vs. time curves for N720/AS obtained at applied interlaminar shear stresses in the 2-6 MPa range at 1100°C in steam.

Minimum creep rate was measured in all tests. Creep strain rate as a function of applied interlaminar shear stress is shown in Figure 23. In air as well as in steam, the minimum creep rate increases by at least an order of magnitude when the applied stress increases from 2 to 6 MPa. The creep strain rates produced in steam are higher than those obtained in air. Still, the overall effect of steam on secondary creep rate does not appear to be dramatic. Creep results obtained at 1100°C in air and in steam were fitted with a temperature-independent Norton-Bailey equation:

$$\dot{\epsilon} = A\tau^n \tag{6}$$

Where $\dot{\epsilon}$ is the minimum creep rate, A is a temperature-dependent coefficient that accounts for the activation energy and other variables, and τ is the applied interlaminar shear stress. The stress exponent was $n = 2.2$ in air and $n = 2.6$ in steam. These values of the stress exponent are lower than the stress exponent of $n = 3$ reported by Buchanan et al

[98]. However, Buchanan et al evaluated tensile creep performance of the composite with ±45° fiber orientation. While the fibers do not dominate tensile creep behavior of a ±45 cross-ply, they do contribute to the material response. Conversely, composite behavior in interlaminar shear is matrix-dominated. Hence, a different value of the stress exponent is not unreasonable. Still, additional interlaminar shear creep tests must be performed before a definitive conclusion regarding the stress exponent and corresponding creep mechanisms can be reached.

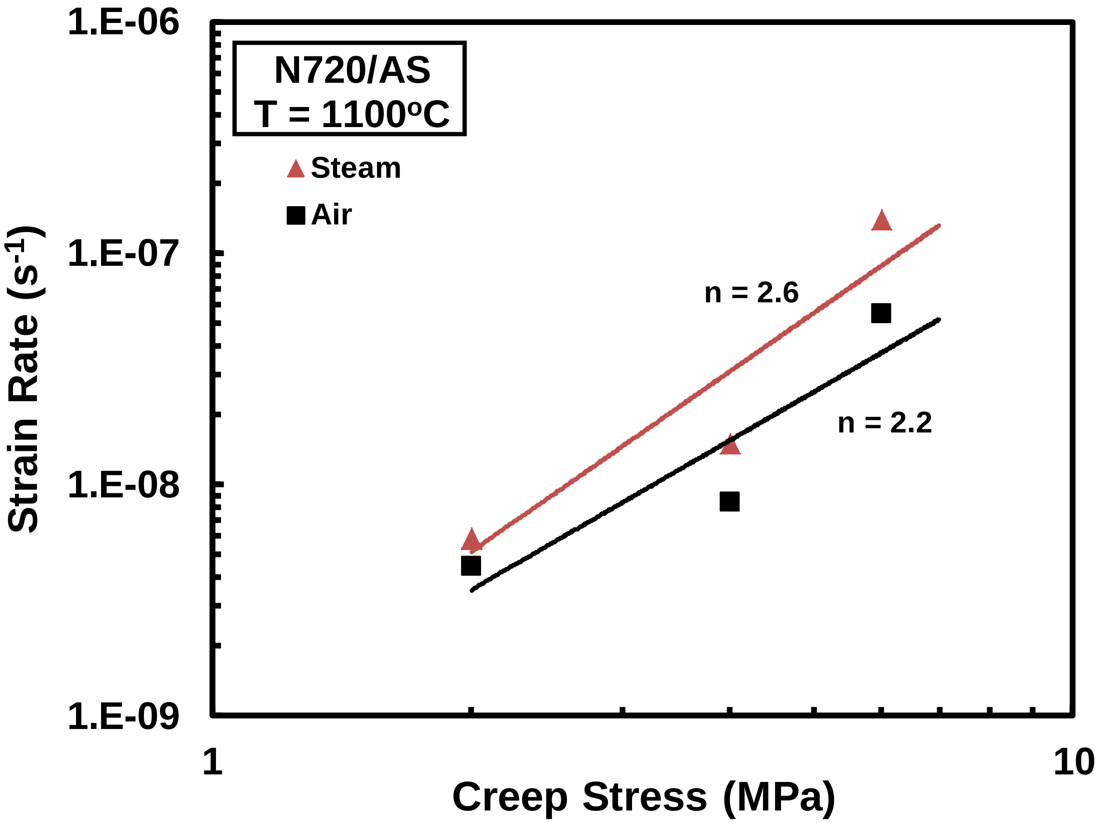

Figure 23. Minimum creep rate as a function of applied interlaminar shear stress for N720/AS CMC at 1100 °C in air and in steam.

Stress-rupture behavior is summarized in Figure 24, where the applied interlaminar shear stress is plotted vs. time to rupture at 1100°C in air and in steam. As expected, creep lifetimes decrease with increasing applied stress. Surprisingly, the presence of steam at 1100 °C appears to be beneficial. Creep lifetimes produced in steam are consistently longer than those obtained in air. Recall that creep behavior in interlaminar shear is dominated by matrix behavior. Matrix strengthening may be occurring at 1100°C in steam under load, which would account for improved lifetimes in steam.

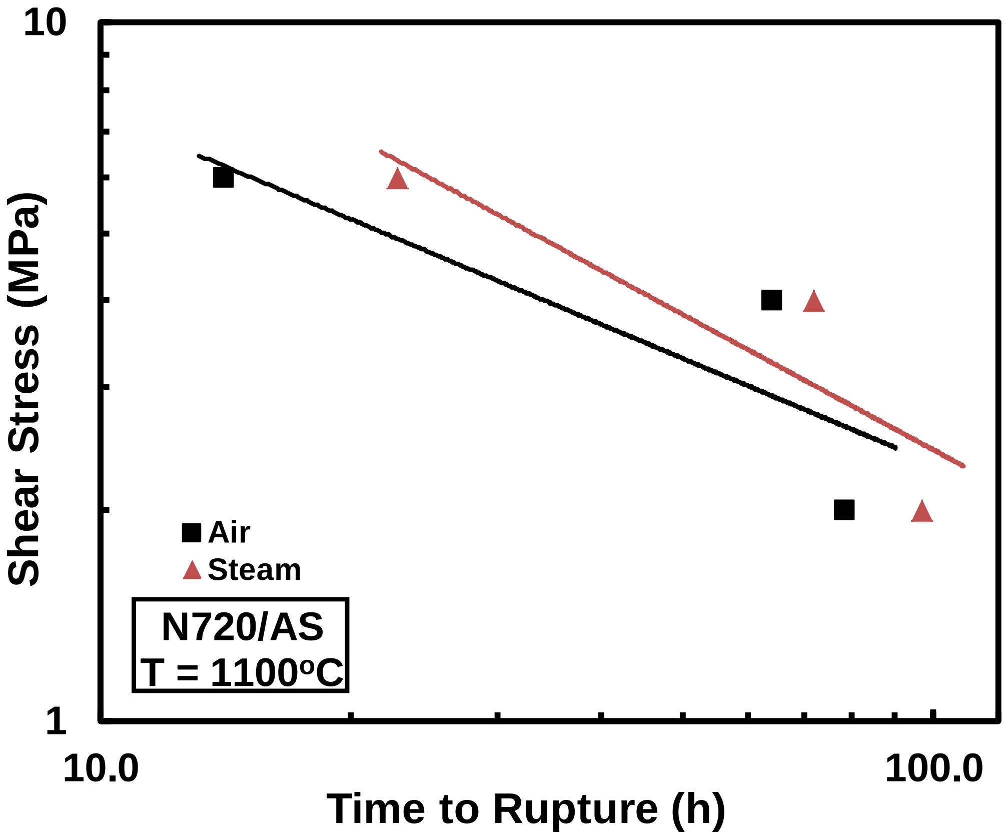

Figure 24. Interlaminar shear stress vs. time to rupture for N720/AS CMC at 1100°C in air and in steam.

5.1.3 Fractography

To better understand the microstructural phenomena behind the results of interlaminar shear tests performed at 1100°C in air and in steam fracture surfaces of the tested specimens were examined first under the optical microscope and then with an SEM. The representative optical micrographs and SEM images are presented below. Additional optical micrographs can be seen in Appendices B-P. Additional SEM images can be viewed in Appendices Q-U.

A representative fracture surface of the DNS specimen tested in compression to failure at 1100 °C in air (test duration < 15 s) is presented in Figure 25. It is seen that fracture occurs along the shear plane mainly through delamination of woven 0/90 fiber layers from the matrix-rich regions, with only minimal fiber fracture. The fracture surface in Figure 25 is largely clean and smooth, suggesting that a single fiber layer is involved in delamination. While virtually no rough areas can be seen in Figure 25, higher magnification views in Figure 26 reveal some debris and fiber breakage. The SEM micrographs in Figure 26 also show small amounts of the matrix material that remain bonded to the fibers exposed during delamination.

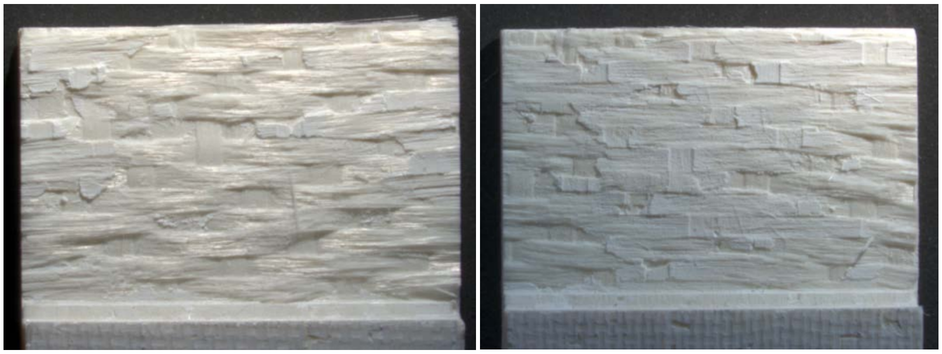

Figure 25. Fracture surface of the DNS specimen tested in compression to failure at 1100 °C in air (test duration < 15 s).

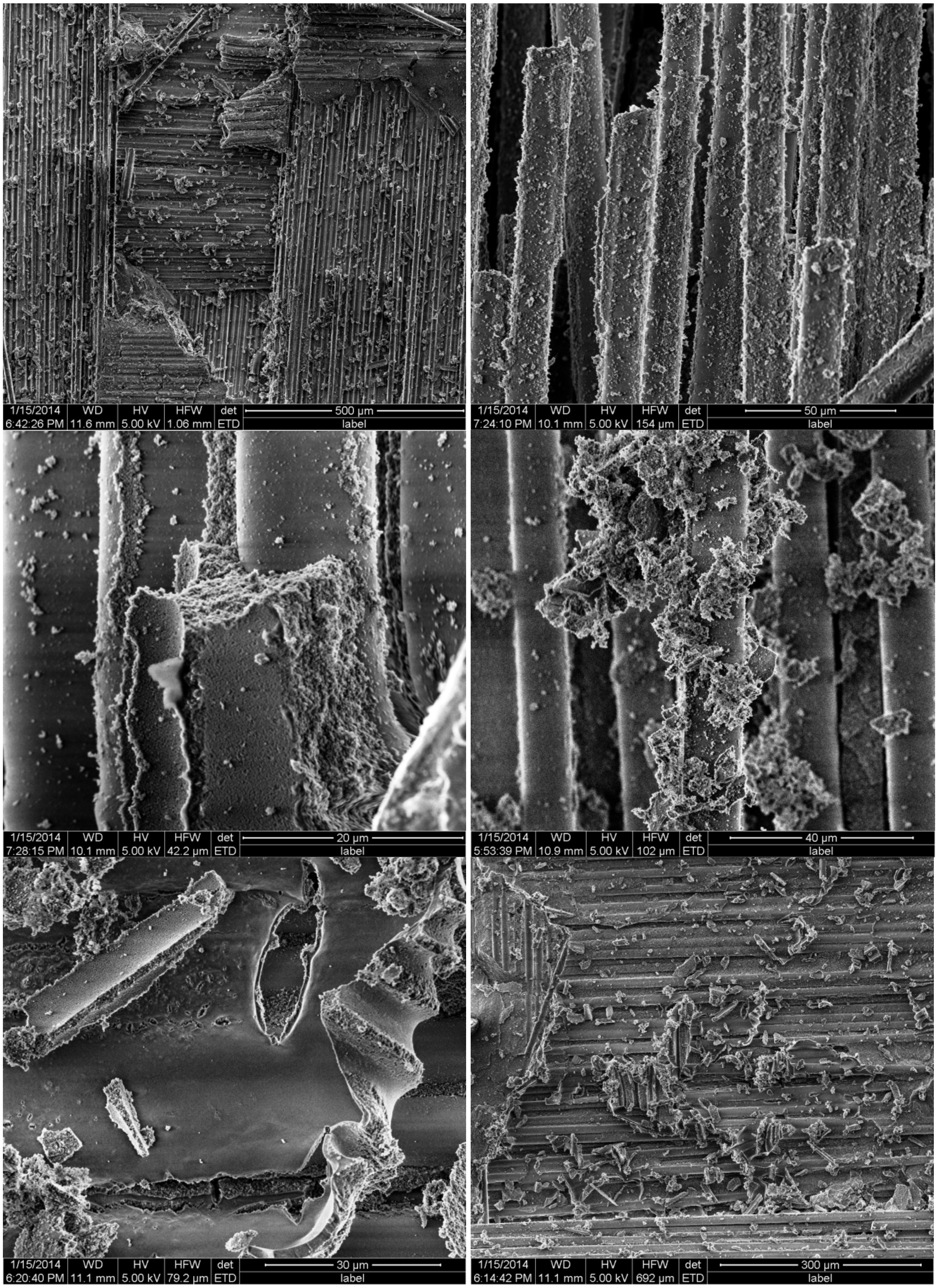
1/15/2014 WD HV HFW det 500 μm
6:42:26 PM 11.6 mm 5.00 kV 1.06 mm ETD label
1/15/2014 WD HV HFW det 50 μm
7:24:10 PM 10.1 mm 5.00 kV 154 μm ETD label
1/15/2014 WD HV HFW det 20 μm
7:28:15 PM 10.1 mm 5.00 kV 42.2 μm ETD label
1/15/2014 WD HV HFW det 40 μm
5:53:39 PM 10.9 mm 5.00 kV 102 μm ETD label
1/15/2014 WD HV HFW det 30 μm
6:20:40 PM 11.1 mm 5.00 kV 79.2 μm ETD label
1/15/2014 WD HV HFW det 300 μm
6:14:42 PM 11.1 mm 5.00 kV 692 μm ETD label

Figure 26. SEM micrographs of the fracture surface of the DNS specimen tested in compression to failure at 1100 °C in air (test duration < 15 s).

The SEM micrographs of the fracture surfaces of the DNS specimens tested in creep at 6 MPa (test duration 14.1 h) and at 2 MPa (test duration 78.3 h) at 1100 °C in air are shown on Figures 27 and 28, respectively. The fracture surfaces in Figures 27 and 28 demonstrate that with increasing test duration the failure mechanism changes from interplay delamination to fracture of fiber tows. The fracture surface contains multiple rough areas showing increased damage in fiber tows and exposing multiple 0°/90° fiber layers. Nevertheless, a few areas show clean delamination of a single fiber layer from the matrix-rich regions. For example: see a higher magnification image in Figure 27, which shows grooves left in the matrix by the fibers in the course of delamination.

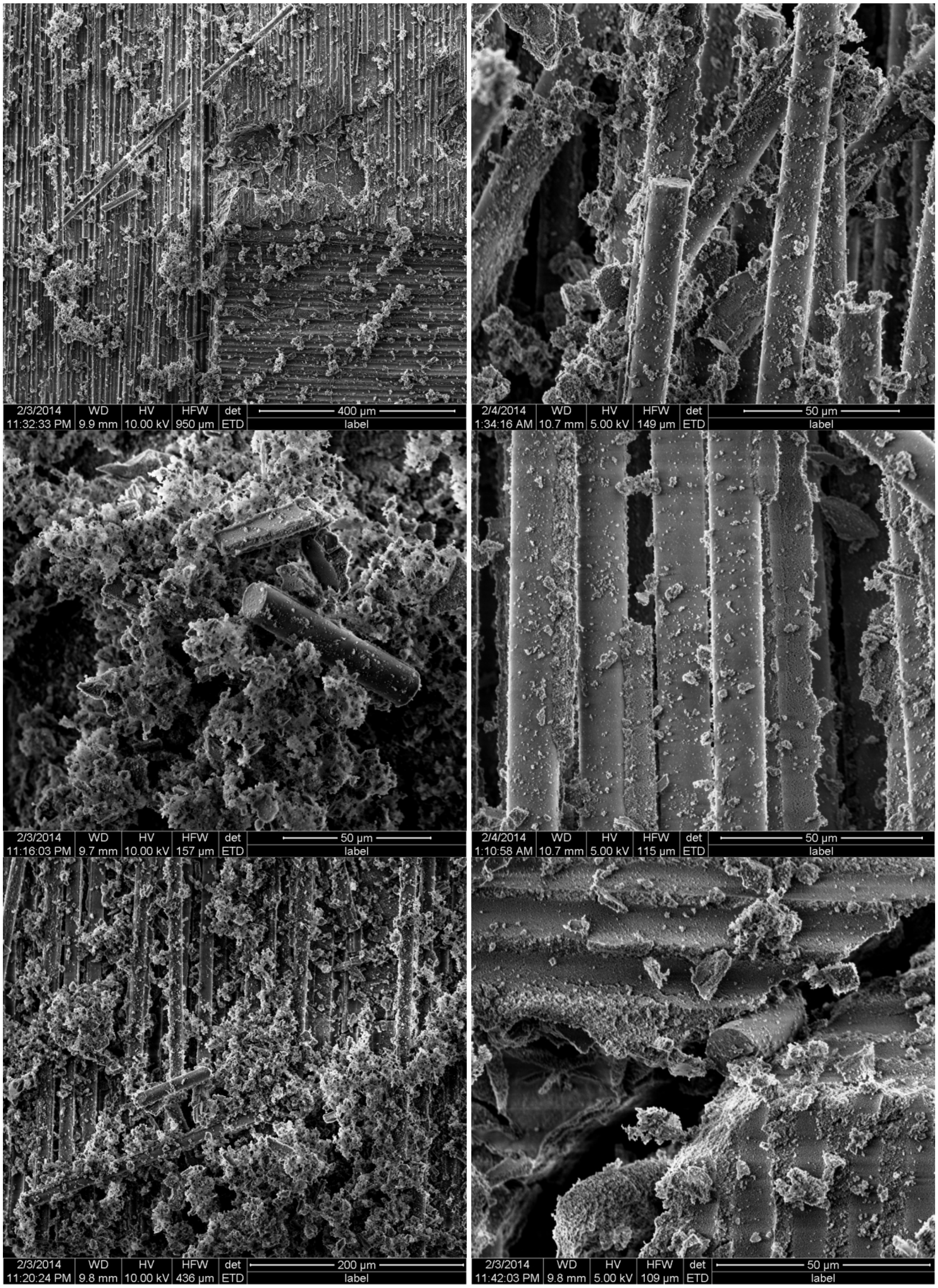
2/3/2014 11:32:33 PM | WD 9.9 mm | HV 10.00 kV | HFW 950 µm | det ETD | 400 µm | label
2/4/2014 1:34:16 AM | WD 10.7 mm | HV 5.00 kV | HFW 149 µm | det ETD | 50 µm | label
2/3/2014 11:16:03 PM | WD 9.7 mm | HV 10.00 kV | HFW 157 µm | det ETD | 50 µm | label
2/4/2014 1:10:58 AM | WD 10.7 mm | HV 5.00 kV | HFW 115 µm | det ETD | 50 µm | label
2/3/2014 11:20:24 PM | WD 9.8 mm | HV 10.00 kV | HFW 436 µm | det ETD | 200 µm | label
2/3/2014 11:42:03 PM | WD 9.8 mm | HV 5.00 kV | HFW 109 µm | det ETD | 50 µm | label

Figure 27. Fracture surface of the DNS specimen tested in creep at 6 MPa at 1100°C in air, tf = 14.1 h.

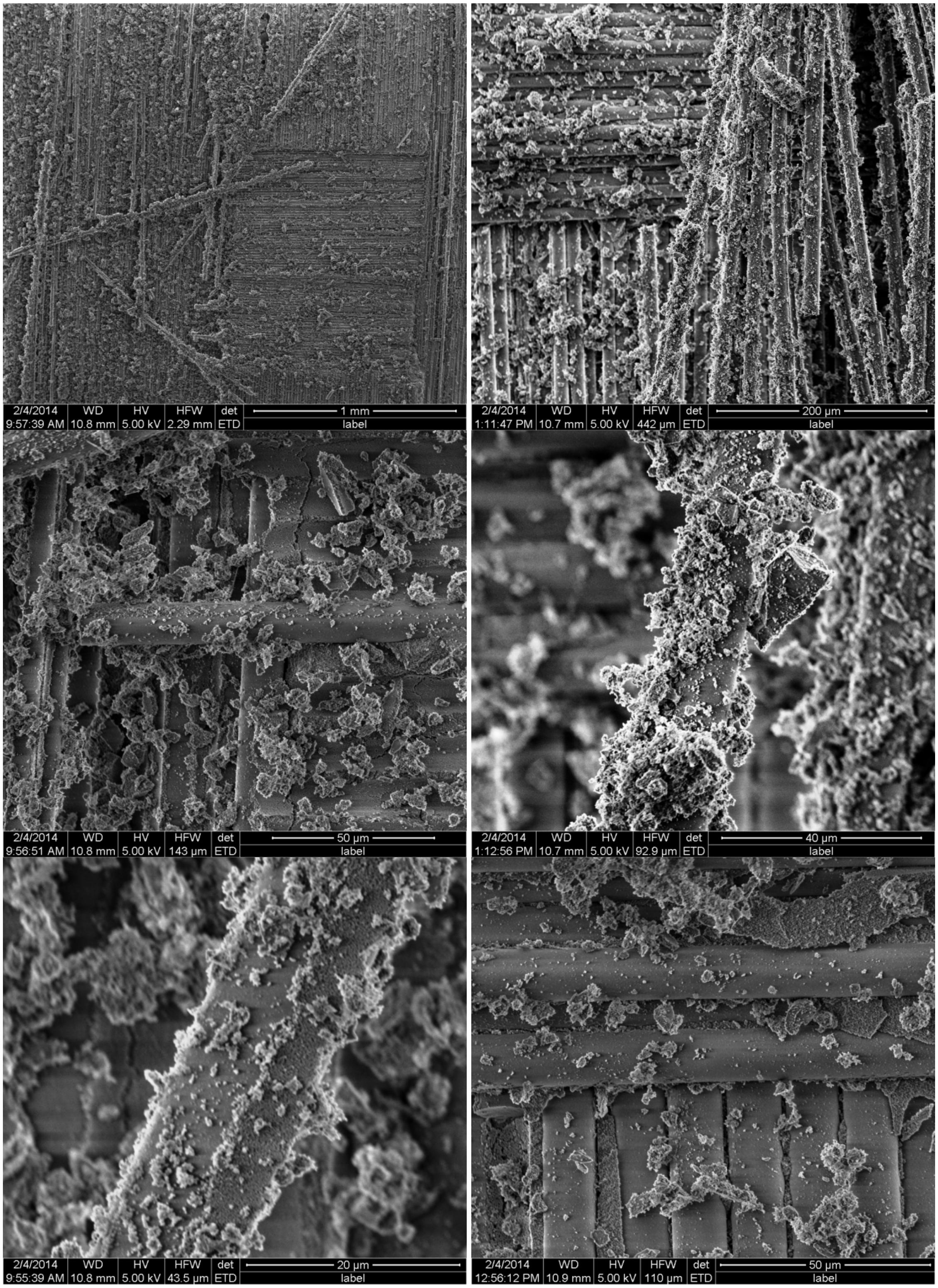
2/4/2014 | WD | HV | HFW | det | 1 mm
9:57:39 AM | 10.8 mm | 5.00 kV | 2.29 mm | ETD | label
2/4/2014 | WD | HV | HFW | det | 200 µm
1:11:47 PM | 10.7 mm | 5.00 kV | 442 µm | ETD | label
2/4/2014 | WD | HV | HFW | det | 50 µm
9:56:51 AM | 10.8 mm | 5.00 kV | 143 µm | ETD | label
2/4/2014 | WD | HV | HFW | det | 40 µm
1:12:56 PM | 10.7 mm | 5.00 kV | 92.9 µm | ETD | label
2/4/2014 | WD | HV | HFW | det | 20 µm
9:55:39 AM | 10.8 mm | 5.00 kV | 43.5 µm | ETD | label
2/4/2014 | WD | HV | HFW | det | 50 µm
12:56:12 PM | 10.9 mm | 5.00 kV | 110 µm | ETD | label

Figure 28. Fracture surface of the DNS specimen tested in creep at 2 MPa at 1100°C in air, tf = 78.3 h.

At 1100°C prolonged exposure to steam environment under load has dramatic effects on composite microstructure. The fracture surfaces of the DNS specimens subjected to creep at 6 MPa (test duration 22.7 h) and at 2 MPa (test duration 96.9 h) at 1100 °C in steam are shown on Figures 29 and 30, respectively. As seen in Figures 29 and 30, the presence of steam causes the change in failure mechanism from interplay delamination to fiber fracture. Extending test duration in steam further intensifies this change in failure mechanism. The fracture surfaces in Figures 29 and 30 exhibit massive fiber fracture. No areas of clean interplay delamination are visible. Areas of violent failure exposing multiple fiber layers are seen throughout both fracture surfaces. Extensive fiber-matrix bonding is also observed. Note large amounts of matrix bonded to the fibers. The fiber tows become bonded together by the matrix material. Extensive failure of fiber bundles is evident. The failure also involves widespread damage to the matrix.

As mentioned above, the results of the creep tests in interlaminar shear were somewhat surprising. Recall that larger creep strains were accumulated in steam. Yet, the presence of steam also appeared to have a beneficial effect on creep lifetimes. Because composite behavior in interlaminar shear is dominated by the behavior of the matrix, it is reasonable to conjecture that changes in the matrix, caused by exposure to steam at 1100°C under load, are behind the creep behavior in steam. Indeed, the SEM micrographs in Figures 26-30 reveal changes in the appearance of the aluminosilicate matrix. After prolonged exposure in steam the matrix material appears to be less porous. Recall that the aluminosilicate matrix of the N720/AS composite is comprised of the alumina (Al_2O_3) particles bonded together by a continuous silica (SiO_2) film. The aluminosilicate matrix derives its porosity from incomplete filling of the interparticle voids. The SiO_2 film in the aluminosilicate matrix is under a three-dimensional nearly hydrostatic constraint from the tightly packed Al_2O_3 grains and the surrounding N720 fibers. Under this constraint, exposure to elevated temperature causes coarsening of the pore-size distribution, rather than the densification of the matrix [99]. Pore-coarsening occurs as the regions of high capillary pressure (namely small pores) contract causing larger pores to expand [100]. The total volume of the composite cannot change because it is dimensionally constrained by the fiber skeleton. At the same time the smaller matrix pores shrink forcing the larger ones to grow. As a result some matrix regions densify while others dilate forming large voids [59].

Earlier studies [99, 101-103] showed that the rate of pore coarsening is related to the viscosity of SiO_2. Parikh [104] found that at elevated temperature water vapor significantly lowered the surface tension of soda-lime silica glass, causing a decrease in viscosity. It is likely that decreased viscosity of SiO_2 in the aluminosilicate matrix is responsible for larger creep strains accumulated in steam in this effort. At the same time, it is possible that the decrease in SiO_2 viscosity also enhanced the process of pore coarsening and localized densification of the aluminosilicate matrix. Matrix densification and strengthening, albeit confined to small regions may contribute to longer creep lifetimes in interlaminar shear of the N720/AS composite at 1100°C in steam.

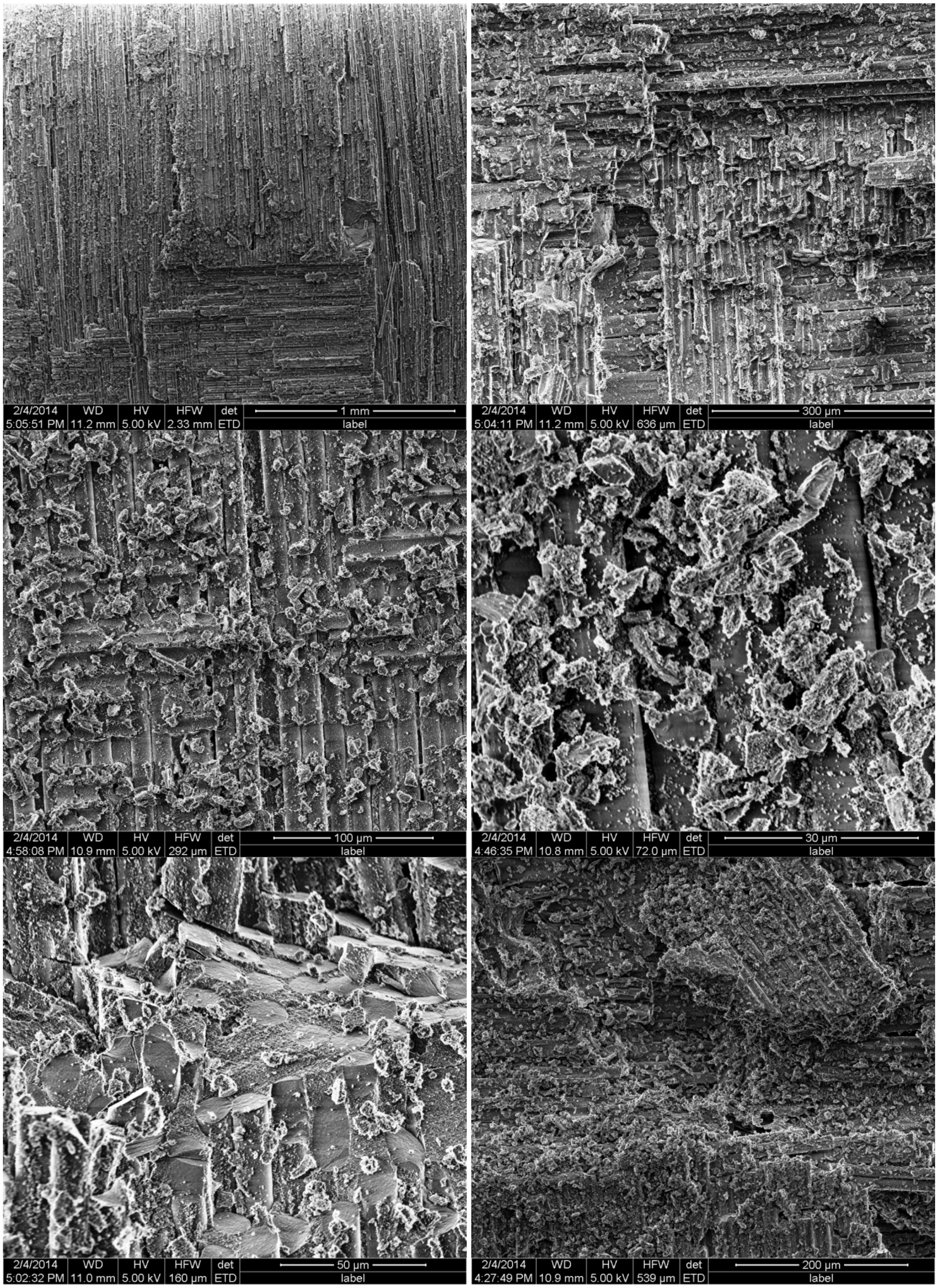
2/4/2014 5:05:51 PM WD 11.2 mm HV 5.00 kV HFW 2.33 mm det ETD 1 mm label
2/4/2014 5:04:11 PM WD 11.2 mm HV 5.00 kV HFW 636 µm det ETD 300 µm label
2/4/2014 4:58:08 PM WD 10.9 mm HV 5.00 kV HFW 292 µm det ETD 100 µm label
2/4/2014 4:46:35 PM WD 10.8 mm HV 5.00 kV HFW 72.0 µm det ETD 30 µm label
2/4/2014 5:02:32 PM WD 11.0 mm HV 5.00 kV HFW 160 µm det ETD 50 µm label
2/4/2014 4:27:49 PM WD 10.9 mm HV 5.00 kV HFW 539 µm det ETD 200 µm label

Figure 29. Fracture surface of the DNS specimen tested in creep at 6 MPa at 1100°C in steam, tf = 22.7 h.

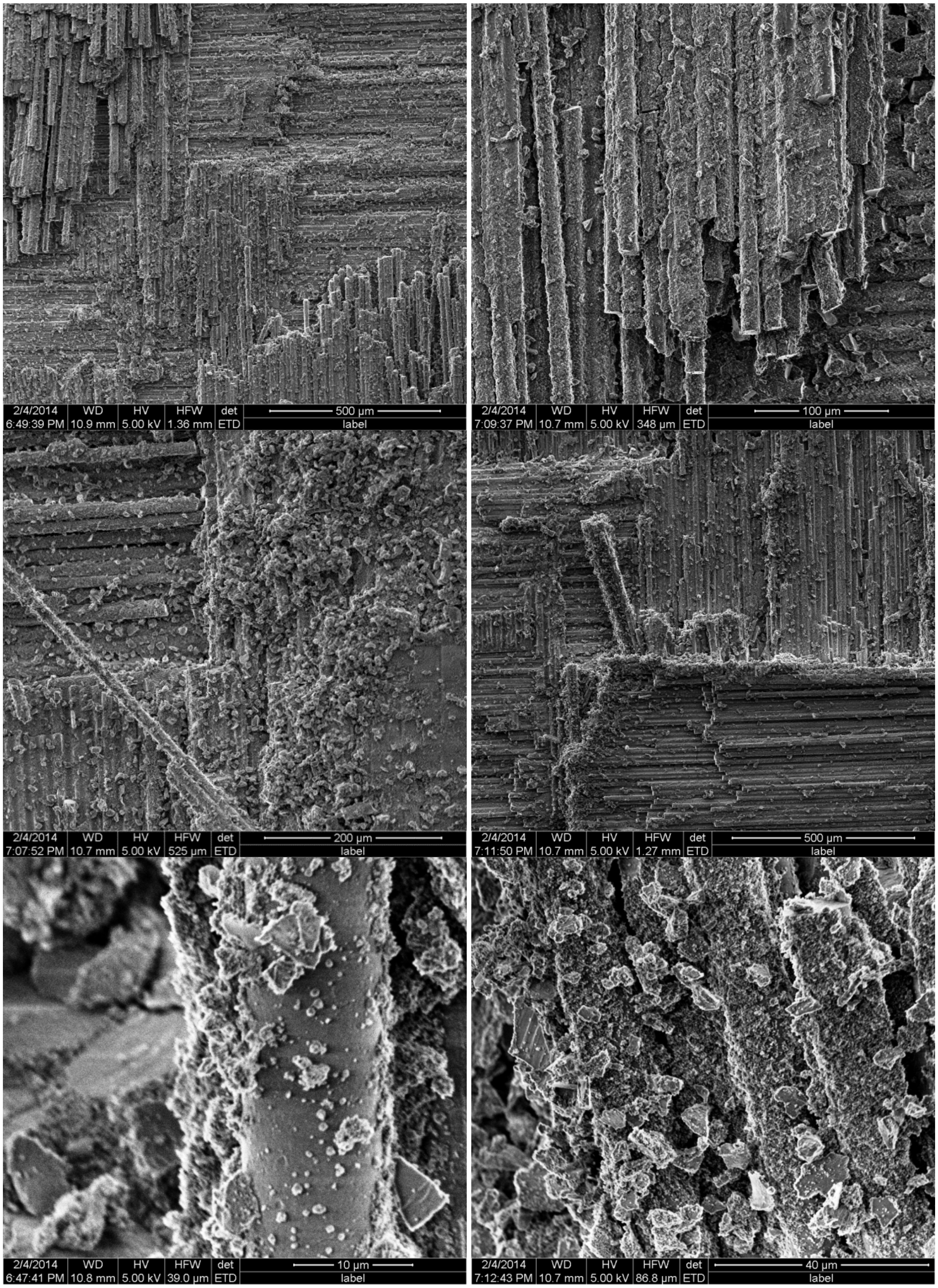
2/4/2014 6:49:39 PM WD 10.9 mm HV 5.00 kV HFW 1.36 mm det ETD 500 µm label
2/4/2014 7:09:37 PM WD 10.7 mm HV 5.00 kV HFW 348 µm det ETD 100 µm label
2/4/2014 7:07:52 PM WD 10.7 mm HV 5.00 kV HFW 525 µm det ETD 200 µm label
2/4/2014 7:11:50 PM WD 10.7 mm HV 5.00 kV HFW 1.27 mm det ETD 500 µm label
2/4/2014 6:47:41 PM WD 10.8 mm HV 5.00 kV HFW 39.0 µm det ETD 10 µm label
2/4/2014 7:12:43 PM WD 10.7 mm HV 5.00 kV HFW 86.8 µm det ETD 40 µm label

Figure 30. Fracture surface of the DNS specimen tested in creep at 2 MPa at 1100°C in steam, tf = 96.9 h.

5.2 Compressive Stress-Strain Behavior and Compressive Properties of N720/AS CMC

A limited number of N720/A specimens were tested in compression to failure at room temperature in laboratory air. The main objective of these tests was to determine compressive strength that could be used in conjunction with the Tsai-Wu and/or Tsai-Hill multiaxial failure theories. Compressive stress-strain behavior is typified in Figure 31, where stress magnitude is plotted vs strain magnitude. Typical compressive stress vs. compressive strain curves are nearly linear to failure. The average compressive strength was 132.5 MPa and the average compressive failure strain was 0.14%. Notably, the average compressive strength of 132.5 MPa is considerably less than the N720/AS tensile strength values of 179-204 MPa reported by Antti et al [105] or the tensile strength value of 212 MPa reported by DeRienzo [90]. Note that Ruggles-Wrenn and Szymczak [64] obtained similar values of compressive strength for a N720/alumina composite at 1200°C in air. Furthermore, in the case of N720/A composite the average compressive strength of 128 MPa reported by Ruggles-Wrenn and Szymczak was also significantly lower than the corresponding tensile strength value of 181 MPa reported in [106]. The fracture surfaces produced in compression to failure tests can be seen in Appendices Q-U.

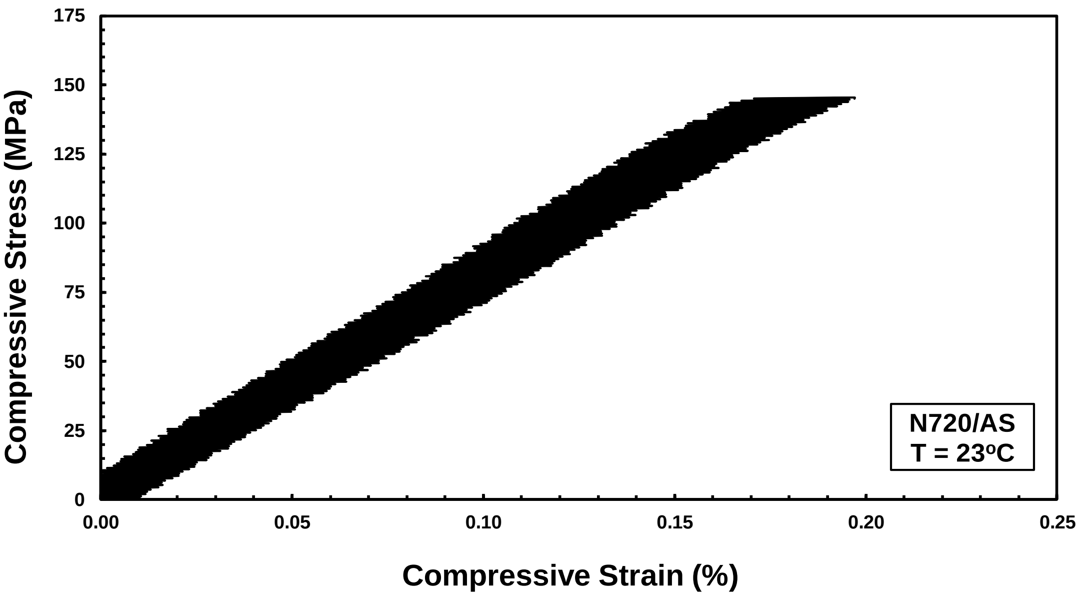

Figure 31. Representative compressive stress-compressive strain curve for N720/AS composite obtained at 23°C in air.

5.3 Stress-Strain Behavior and Failure of N720/AS Composite under Combined Tension-Torsion Loading

Mechanical behavior of fiber reinforced composites under biaxial loading is clearly more complex than that under the uniaxial loading due to a “stress coupling effect” experienced in biaxial loading conditions [107]. Thin-walled tubular N720/AS specimens fabricated using a novel involute ply lay-up were tested in proportional tension-torsion. All tests were performed at 23°C in laboratory air. The objective of this effort was to gain initial insight into deformation and failure of this composite and, especially this type of specimen under multiaxial loading. In addition, failure stresses produced in various tension-torsion tests were measured and used to assess the applicability of existing failure theories. Tension-torsion tests performed on thin-walled tubular specimens are summarized in Table 9.

Note that in the case of proportional tension-torsion tests the ratio of normal stress to shear stress was defined using the values of UTS = 212 MPa and USS = 33 MPa reported by DeRienzo [90]. Thus in the case of specimen A, the stress ratio was SR = ¼ , which translates into the ratio of normal stress to shear stress σ/τ = UTS/(4xUSS) = 212/132 = 1.6. For specimen B, the stress ratio was SR = 1, implying that the specimen was loaded simultaneously to the normal stress of 212 MPa and the shear stress of 33 MPa. Finally, in the case of specimen C, the ratio was SR = ½, signifying that the ratio of normal stress to shear stress σ/τ = UTS/(2xUSS) = 212/66 = 3.2. All tension-torsion tests were performed in stress control. Axial stress rate and shear stress rate are shown in Table 9 for each test.

Table 9. Summary of the combined tension-torsion tests performed on N720/AS thin-walled tubular specimens at 23°C in laboratory air.

Specimen	Stress Ratio SR	Axial Stress Rate (MPa/s)	Shear Stress Rate (MPa/s)	Axial Failure Stress (MPa)	Axial Strain at Failure (%)	Shear Failure Stress (MPa)	Shear Strain at Failure (%)
A	1/4	0.8	0.5	44.7	0.04	27.3	0.29
B	1/1	3.21	0.05	123	0.12	18.6	0.22
C	1/2	1.61	0.05	66.5	0.09	19.5	0.27

Axial stress vs. axial strain curves and shear stress vs. shear strain curves are presented in Figures 33-39. Axial strains ε_{yy} were measured by the strain gauges aligned parallel to the specimen axis. Each 45° rectangular strain gauge rosette provided the following measurements: $\varepsilon_A = \varepsilon_{xx}$ (measured by gage A in Figure 32), $\varepsilon_C = \varepsilon_{yy}$ (measured by gage C in Figure 32) and $\varepsilon_B = \varepsilon_{45}$ (measured by gage B in Figure 32), which were employed to calculate the shear strains as:

$$\gamma_{xy} = 2\epsilon_B - \epsilon_A - \epsilon_C \tag{7}$$

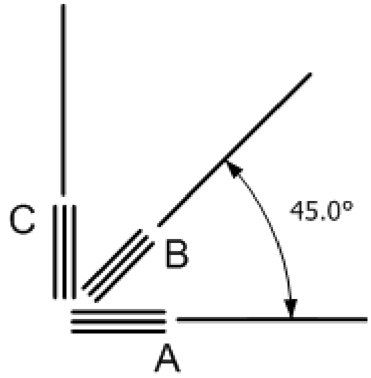

Figure 32. A schematic of the 45° rectangular strain gauge rosette.

Strains plotted in Figures 33, 34, 36, 37, 39, and 40 are the averages calculated using measurements produced by several strain gages and/or strain gage rosettes. It is noteworthy, that measurements of a given strain obtained from different strain gages were nearly the same with very few exceptions. In some cases, crack growth and failure occurred in the immediate vicinity of a strain gage or a strain gage rosette, rendering strains measured by these gages unreliable. Therefore, strain measurements obtained from strain gages located at or near the crack path were not used in calculating average strain. Thus measurements obtained from rosettes 2 and 3 were omitted in the case of specimen A. The measurements produced by rosette 2 were omitted in the case of specimens B and C. Locations of rosettes 1, 2 and 3 on a thin-walled tubular specimen is shown in Figure 14 of Section 4.2.2 above.

Specimen A was loaded to failure in combined tension-torsion with a SR of 1:4. The failure stresses were σ_{yy} = 44.7 MPa and τ_{xy} = 27.3 MPa. The axial stress - axial strain curve and the shear stress – shear strain curve obtained in this test are shown in Figures 33 and 34, respectively. The axial stress – axial strain curve in Figure 33 becomes slightly nonlinear when the axial stress exceeds 20 MPa. Axial strain produced in this test remains very small, below 0.04%. Conversely, the shear stress – shear strain curve in Figure 34 remains linear only up to about 10 MPa. Considerable nonlinear stress-strain behavior is observed at stresses exceeding 10 MPa. Note that shear strain at failure (0.29%) is approximately an order of magnitude higher than the axial strain (0.04%) at failure. The strong nonlinearity of the shear stress-strain response, dominated by the matrix behavior in interlaminar shear is in strong contrast to the nearly linear axial stress-strain response, dominated by the N720 fibers. As seen in Figure 35, the failure surface of specimen A is nearly perpendicular to the loading axis. Notably, the failure mode is similar to that observed in a combined tension-torsion test of N720/AS involute tubular specimen by DeRienzo [90]. Fibrous fracture appears to dominate the fracture surface, indicating crack deflection around the fibers.

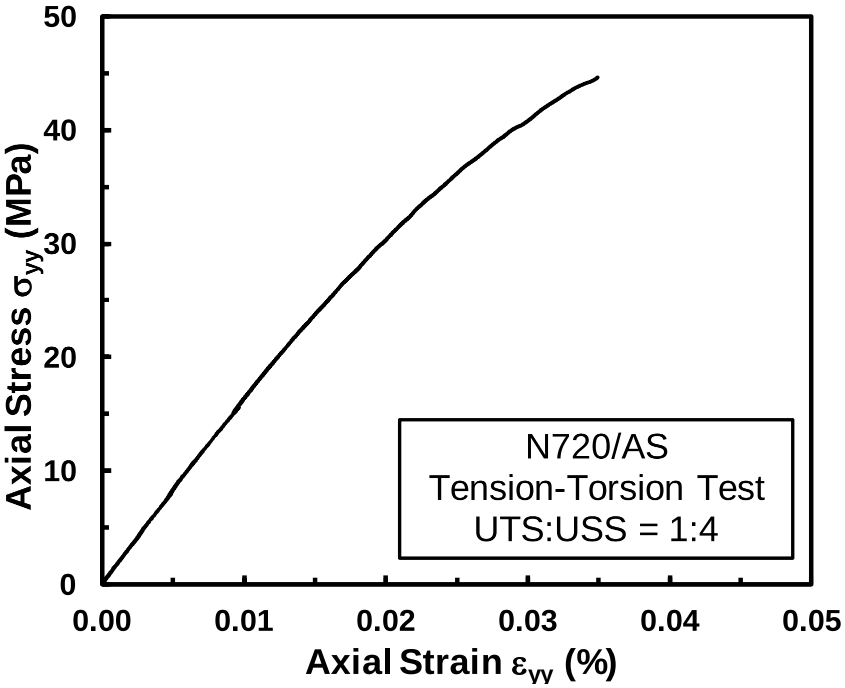

Figure 33. Axial stress σ_{yy} vs. axial strain ε_{yy} curve for Specimen A tested in combined tension-torsion with the SR of 1:4.

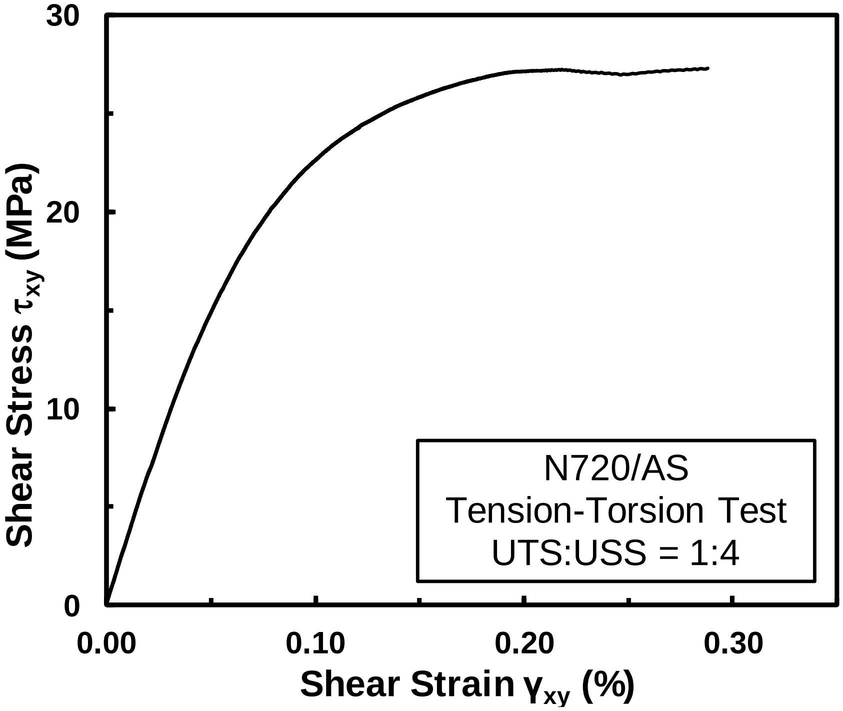

Figure 34. Shear stress τ_{xy} vs. shear strain γ_{xy} curve for specimen A tested in combined tension-torsion with the SR of 1:4.

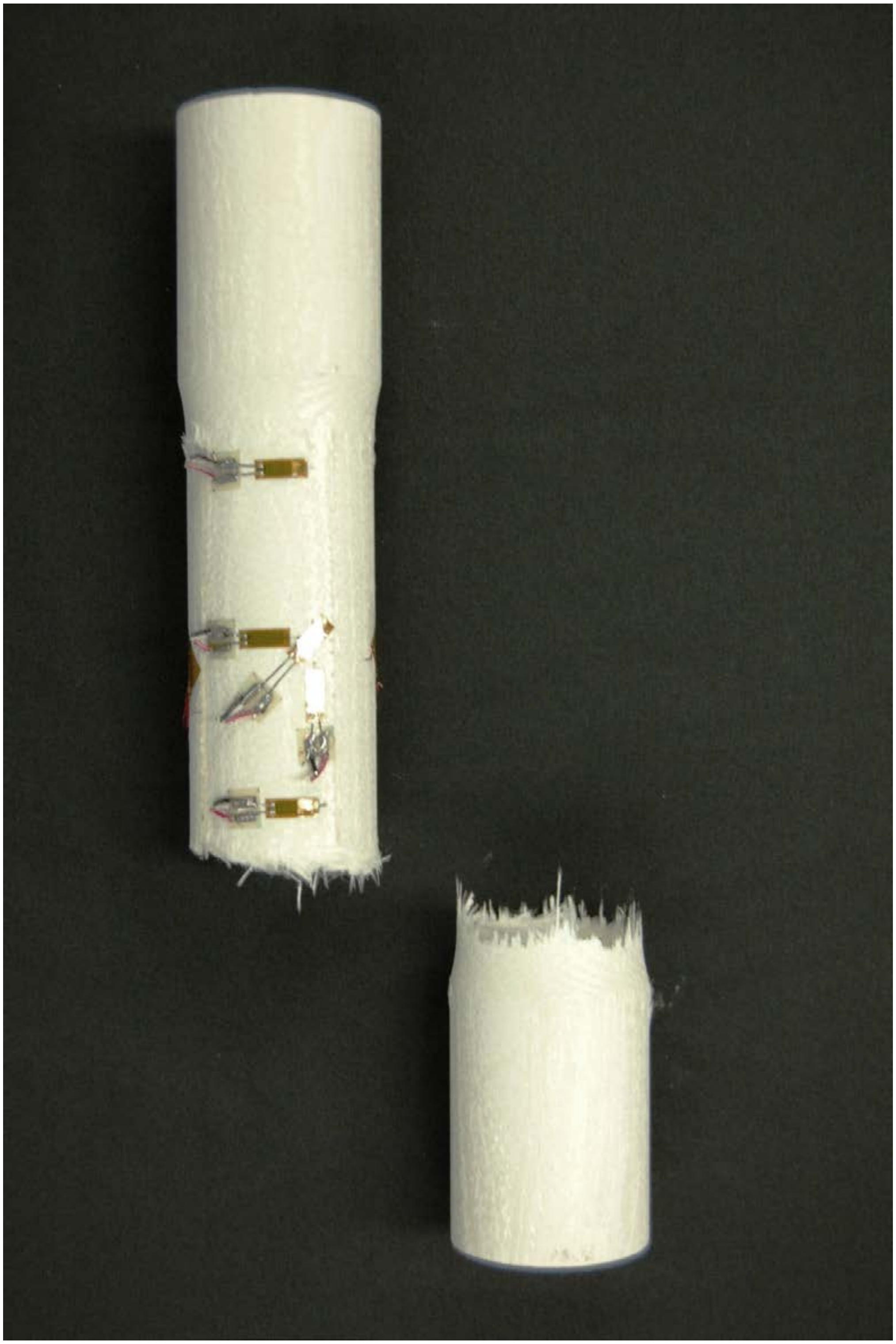

Figure 35. N720/AS specimen A tested in combined tension torsion with the SR of 1:4.

Specimen B was loaded to failure in combined tension-torsion with the SR of 1:1. The failure stresses were σ_{yy} = 123 MPa and τ_{xy} = 18.6 MPa. The axial stress – axial strain curve and the shear stress – shear strain curve obtained in this test are shown in Figures 36 and 37, respectively. As in the case of specimen A, the axial stress-strain curve is nearly linear to failure, while the shear stress-strain curve exhibits strong nonlinearity. As in the case of specimen A, the slight nonlinearity of the axial stress-strain response of specimen B becomes apparent as the axial stress exceeds 20 MPa. Conversely, the shear stress-strain response of specimen B departs from linearity at a lower stress of approximately 5 MPa. In test B axial stress at failure (123 MPa) is nearly three times that produced in test A. Yet the shear stress at failure in test B is (18.6 MPa) is not drastically lower than that in test A. It is noteworthy that the axial strain at failure (0.12%) is nearly an order of magnitude higher than that obtained for specimen A (0.04%). In contrast, shear strain at failure (0.28%) is not dramatically different from that produced by specimen A (0.22%). The failure surface of specimen B is depicted in Figure 38. It is seen that the failure surface has a portion that is nearly perpendicular to the specimen axis and a portion that is at a well-defined 45° angle to the specimen axis.

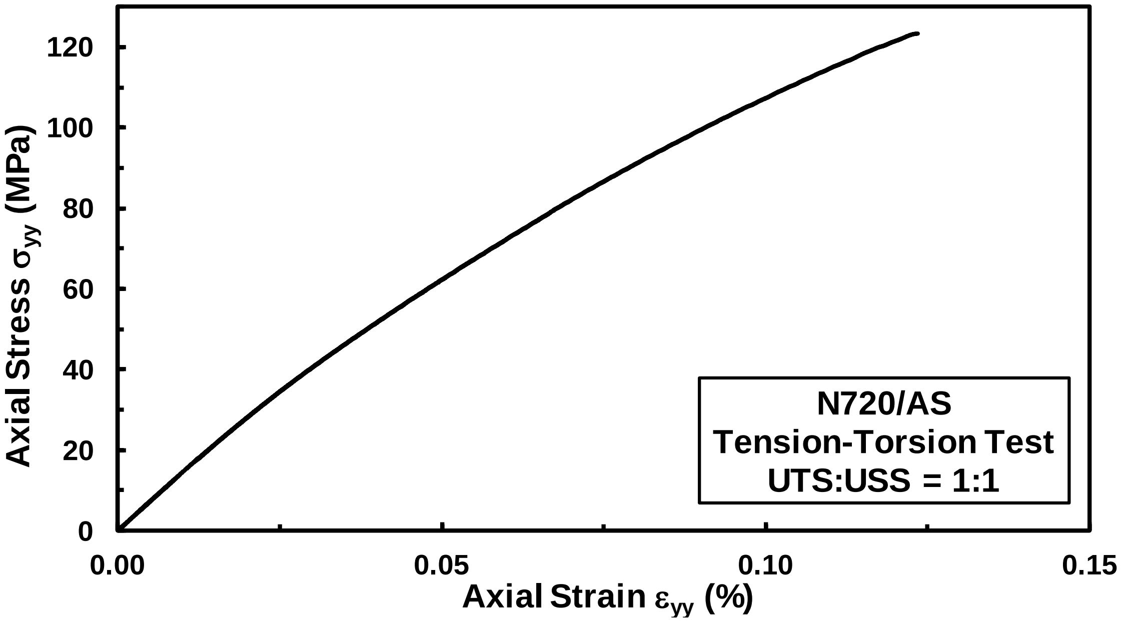

Figure 36. Axial stress σ_{yy} vs. axial strain ε_{yy} curves for specimen B tested in combined tension-torsion with the SR of 1:1.

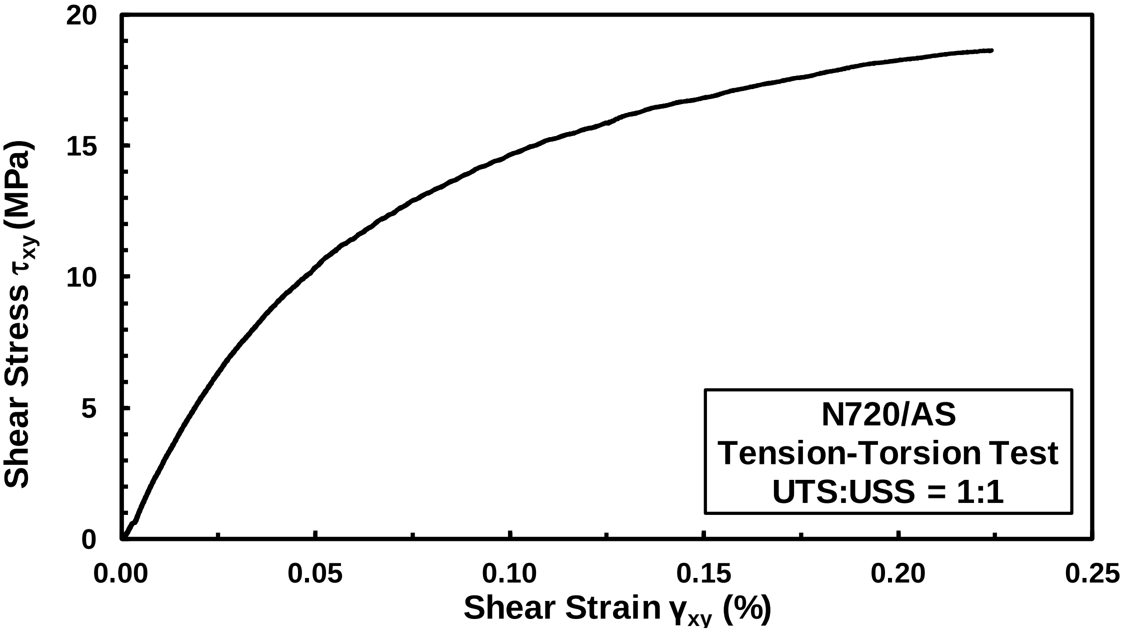

Figure 37. Shear stress τ_{xy} vs. shear strain γ_{xy} curves for specimen B tested in combined tension-torsion with the SR of 1:1.

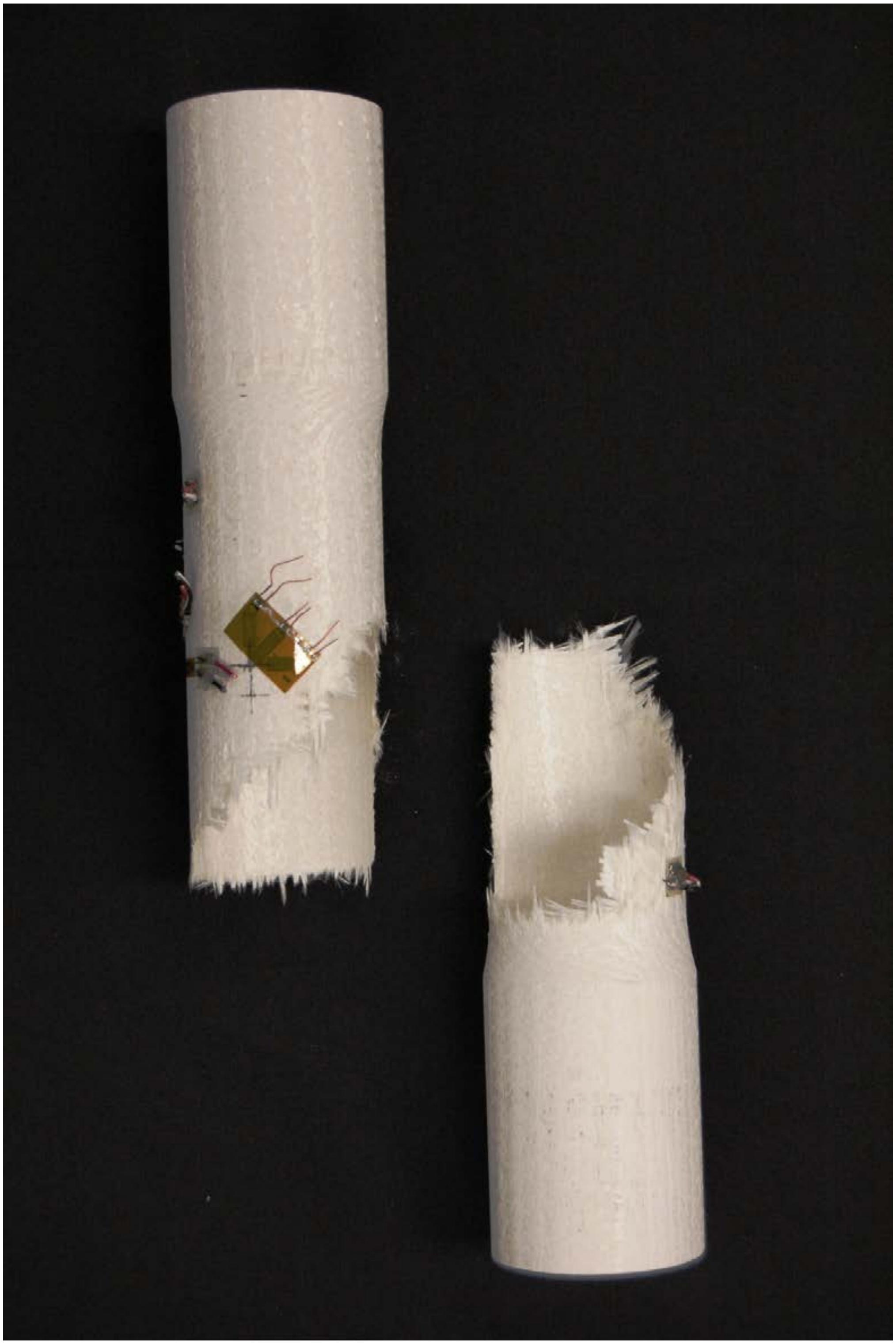

Figure 38. N720/AS specimen B tested in combined tension torsion with the SR of 1:1.

Specimen C was loaded to failure in combined tension-torsion with the SR of 1:2. The failure stresses were σ_{yy} = 66.5 MPa and τ_{xy} = 19.5 MPa. The axial stress – axial strain curve and the shear stress – shear strain curve obtained in this test are shown in Figures 39 and 40, respectively. Note that the failure stresses obtained in this test fall between the corresponding failure stresses produced in tests A and B. The same observation can be made regarding axial and shear strains at failure. The shear stress-strain behavior of specimen C remains similar to those exhibited by specimens A and B. However, the axial stress-strain curve obtained for specimen C show considerably stronger nonlinearity than those obtained for specimens A and B. This difference may be due to specimen-to-specimen variability. Additional tension-torsion test must be performed before a definitive conclusion can be attempted.

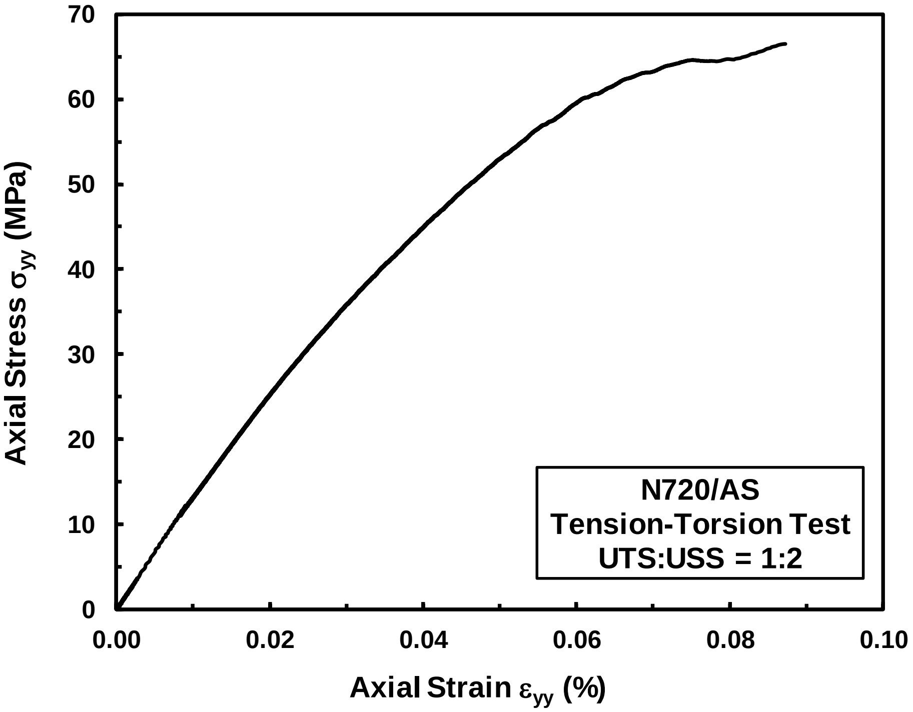

Figure 39. Axial stress σ_{yy} vs. axial strain ε_{yy} curves for Specimen C tested in combined tension-torsion with the SR of 1:2.

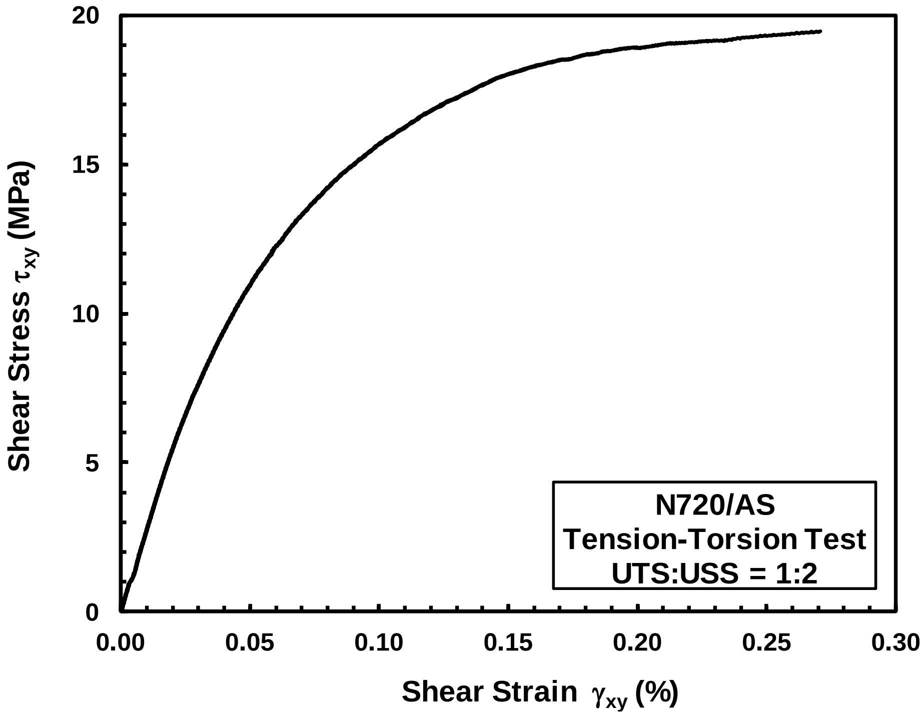

Figure 40. Shear stress τ_{xy} vs. shear strain γ_{xy} curves for specimen C tested in combined tension-torsion with the SR of 1:2.

A post-test photograph of specimen C is shown in Figure 41. Note an unusual failure mode of Specimen C, where parts of the failure surface are nearly perpendicular to the specimen axis. Yet, failure path also propagates parallel to the specimen axis throughout most of the specimen gage section.

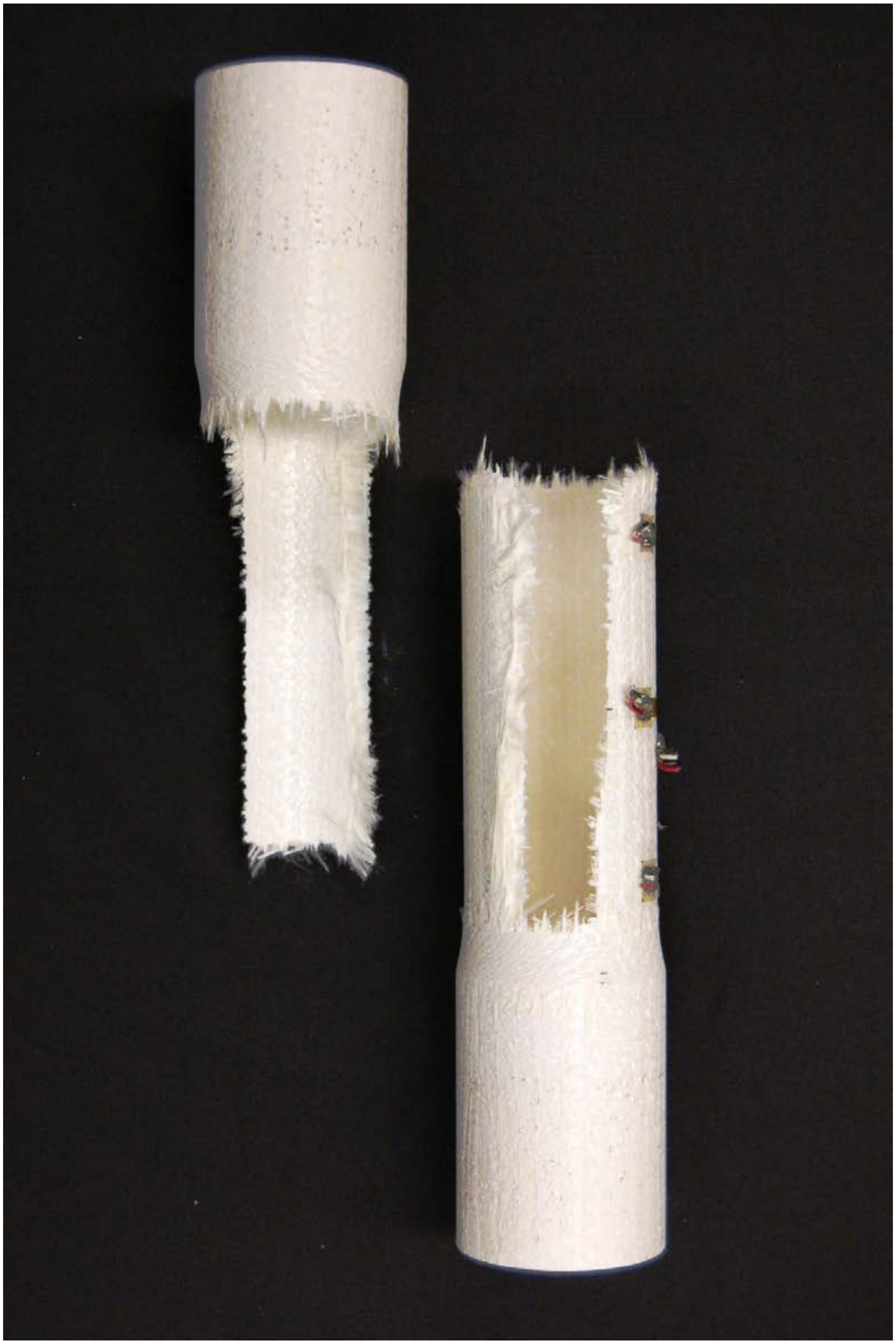

Figure 41. N720/AS Specimen B tested in combined tension torsion with the SR of 1:2.

5.4 Experimental Failure Envelope vis-à-vis Some Failure Theories

Data scatter due to specimen-to-specimen variability is inevitable in any experimental investigation. Hence, multiple specimens should be tested per condition. However, only very few specimens were available for this effort. To construct a reliable experimental failure envelope for the N720/AS thin-walled tubular specimen with involute lay-up, results obtained in this effort should be augmented by additional testing. The values of axial and shear failure stresses obtained in this research are plotted in the σ_{yy}-τ_{xy} space in Figure 42 together with the failure stress values obtained from literature [90]. Failure stresses obtained in tension-torsion tests in this work are also compared with the predictions of the Tsai-Hill and Tsai-Wu failure theories. The purpose of this exercise is to assess the applicability of the aforementioned failure theories to predicting failure in CMCs. It is recognized that due to a limited amount of data, only preliminary conclusions can be offered. As was pointed out by Liu and Tsai [108], “a criterion is only as good as the data available”.

The Tsai-Hill failure theory is given by [2]:

$$A\sigma_1^2 + B\sigma_2^2 + C\sigma_1\sigma_2 + D\tau_6 = 1 \tag{8}$$

which under tension-torsion loading reduces to

$$A\sigma_1^2 + D\tau_6^2 = 1 \tag{9}$$

Here σ_1 is the axial stress and τ_6 is the shear stress. Constants A and D are determined as:

$$A = \frac{1}{\mathrm{F}_1^2}; \quad D = \frac{1}{\mathrm{F}_6^2} \tag{10}$$

The constant A was calculated using (i) the tensile strength F_1= 212 MPa reported by DeRienzo [90] and (ii) the tensile strength F_1= 180 MPa reported by Buchanan et al [98]. The constant D was calculated using the shear strength F_6 = 33 MPa reported by DeRienzo [90]. Solid lines in Figure 42 represent the Tsai-Hill failure envelopes calculated using the two values of constant A.

The Tsai-Wu failure criterion is given by [2]:

$$f_i\sigma_i + f_{ij}\sigma_i\sigma_j = 1 \tag{11}$$

For the case of tension-torsion, the equation (13) reduces to:

$$f_1\sigma_1 + f_{11}\sigma_1^2 + f_{66}\tau_6^2 = 1 \tag{12}$$

where σ_1 is the axial stress and τ_6 is the shear stress and the constants f_1, f_{11}, and f_6 are determined as:

$$f_1 = \frac{1}{F_{1t}} - \frac{1}{F_{1c}}; \qquad f_{11} = \frac{1}{F_{1t}F_{2c}}; \qquad f_{66} = \frac{1}{F_6^2} \tag{13}$$

The tensile strength values of F_{1t} = 212 MPa (from DeRienzo [90]) and F_{1t} = 180 MPa (from Buchanan et al [98]) were used to calculate two values of f_1. Compressive strength F_{1c} = 133 MPa and shear strength F_6 = 33 MPa (from DeRienzo [90]) were also used. Dashed lines in Figure 42 represent the Tsai-Wu failure envelopes calculated using the two values of constant f_1.

As seen in Figure 42, the failure stresses obtained in tension-torsion tests for the N720/AS composite appear to follow a trend similar to those predicted by the Tsai-Hill and Tsai-Wu failure theories. Further comments on the efficacy of these or any other failure theories in representing failure of the N720/AS composite should be reserved until considerably more experimental data are available. It is particularly recommended, that more accurate values of tensile strength, compressive strength and shear strength be obtained from multiple additional tests. It is also recommended that effects of fiber architecture (i. e. involute lay-up vs. 0/90 cross-ply) on tensile, compressive and shear strengths be investigated.

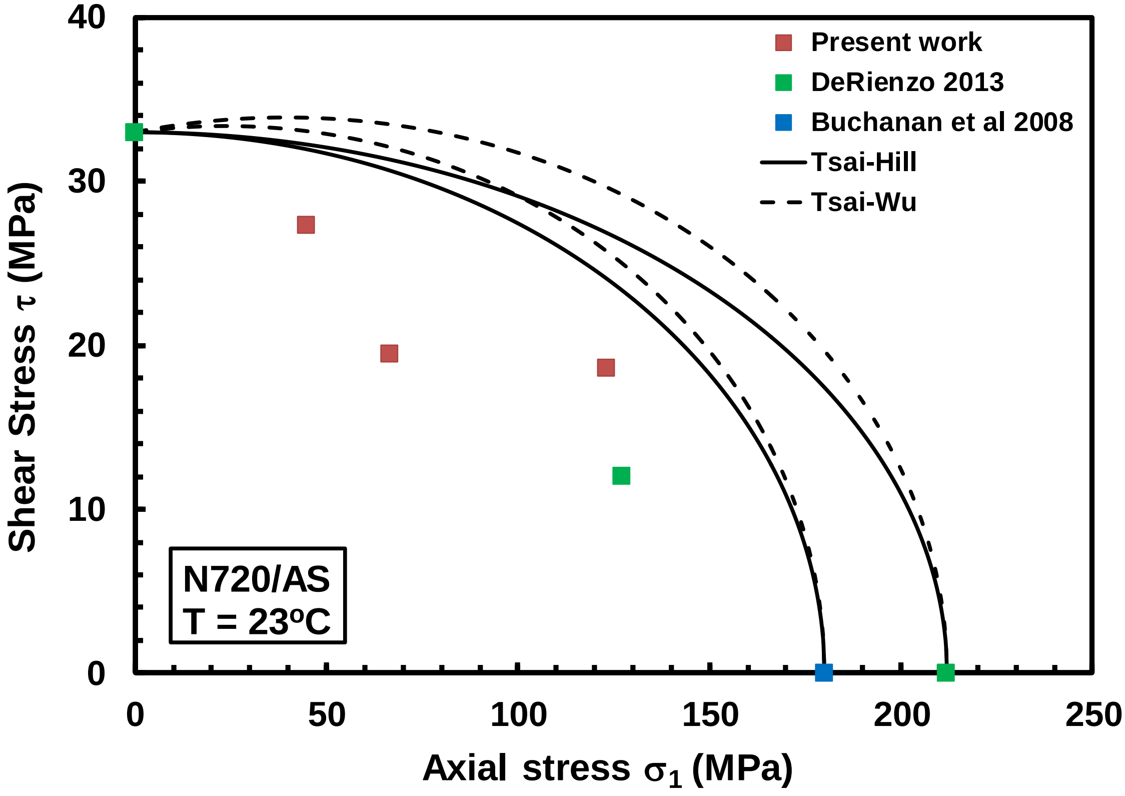

Figure 42. A comparison between experimental and predicted failure envelopes for N720/AS composite under combined tension-torsion. Failure stress values from DeRienzo [90] and Buchanan et al [98] are also included.

VI. Conclusions and Recommendations

The creep behavior in interlaminar shear of N720/AS composite was investigated and interlaminar shear properties measured at 1100°C in laboratory air. Double notch shear specimens were employed. The interlaminar shear strength (ILSS) was 7.65 MPa. The creep-rupture behavior was characterized for interlaminar shear stresses ranging from 2 MPa to 6 MPa. The influence of steam environment was assessed in creep tests performed at 1100°C in steam. In air as well as in steam, the composite exhibits primary and secondary creep regimes at creep stresses below 6 MPa. In contrast, at 6 MPa tertiary creep regime was also observed in both environments. Creep run-out defined as 100 h at creep stress was not achieved in air or in steam. Larger creep strains were accumulated at a given creep stress in steam than in air. Secondary creep rates obtained in steam were also higher than those produced in air. Surprisingly, creep lifetimes were longer in steam than in air. Longer creep lifetimes obtained in steam are attributed to localized densification and strengthening of the aluminosilicate matrix caused by coarsening of the matrix porosity at 1100°C in steam.

The ultimate compressive strength (UCS) of the N720/AS composite was measured in a limited number of compression tests to failure performed at room temperature in laboratory air. The average UCS value was 132.5 MPa and the average compressive failure strain was 0.14%. The UCS value represents a critical composite property required for failure prediction using the Tsai-Wu failure theory.

Exploratory tension-torsion tests of thin-walled tubular specimens were performed at room temperature in laboratory air. The tubular N702/AS specimens were fabricated using a novel involute ply lay-up. The thin-walled tubular specimens were tested in combined tension-torsion to failure with three different stress ratios: 1:4, 1:1 and 1:2. The axial and shear failure stresses obtained in the combined tension-torsion tests and the UCS values determined in compression to failure tests were plotted together with data from literature in the σ_{yy}-τ_{xy} coordinate space. The experimental failure envelope was compared with predictions obtained using the Tsai-Hill and Tsai-Wu failure theories. The experimental values appear to exhibit a trend consistent with the Tsai-Hill and Tsai-Wu failure envelopes. However, due a very limited amount of experimental data, no definitive conclusions regarding the applicability of the aforementioned failure theories to representing multiaxial failure of the N720/AS composite can be made at this time.

Future efforts should focus on augmenting the experimental data produced in this research effort. Additional DNS specimens should be tested in creep in interlaminar shear to validate the results presented above. Multiple specimens should be tested per test condition. Additional results would permit better evaluation of the stress exponents and associated creep mechanisms. A more detailed analysis of the composite microstructure is needed to understand the mechanisms behind the matrix changes occurring under load at 1100°C in steam.

Further testing of thin-walled tubular specimens is needed. In addition to obtaining additional results under combined tension-torsion loading, it is imperative that the effects of fiber architecture (involute lay-up vs traditional 0/90 cross-ply) on basic tensile, compressive and shear strength properties be studied. Testing additional specimens, and performing multiple tests per test condition will provide better experimental basis for formulating a multiaxial failure criterion as well as for assessing the applicability of existing failure theories.

Appendix A: Procedures

Monotonic Compression to Failure of DNS Specimens

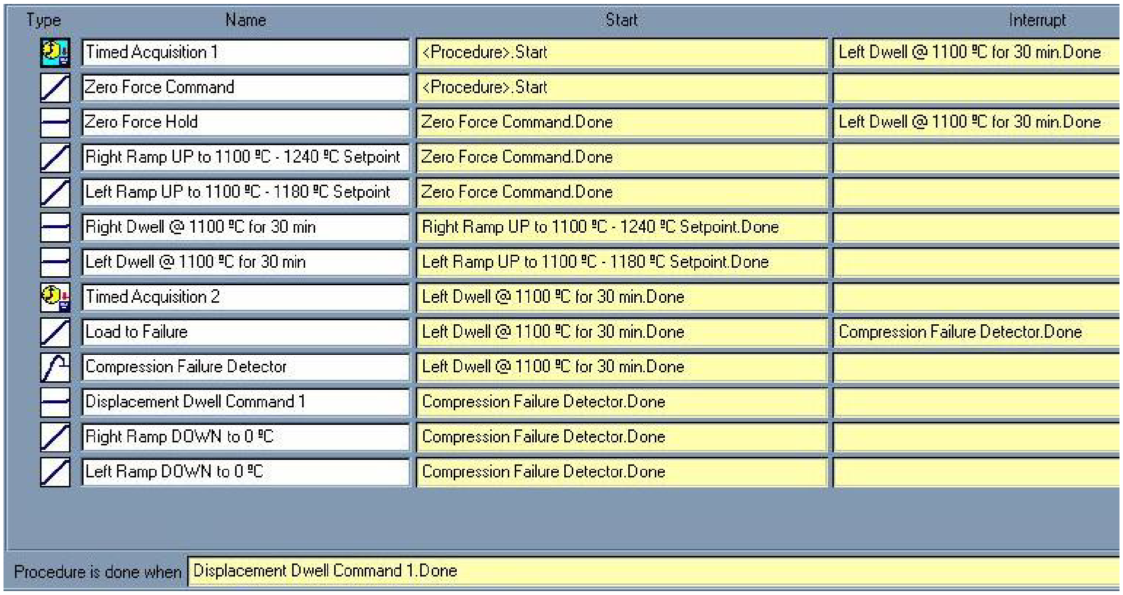

Type	Name	Start	Interrupt
⏰	Timed Acquisition 1	<Procedure>.Start	Left Dwell @ 1100 °C for 30 min.Done
╱	Zero Force Command	<Procedure>.Start	
—	Zero Force Hold	Zero Force Command.Done	Left Dwell @ 1100 °C for 30 min.Done
╱	Right Ramp UP to 1100 °C - 1240 °C Setpoint	Zero Force Command.Done	
╱	Left Ramp UP to 1100 °C - 1180 °C Setpoint	Zero Force Command.Done	
—	Right Dwell @ 1100 °C for 30 min	Right Ramp UP to 1100 °C - 1240 °C Setpoint.Done	
—	Left Dwell @ 1100 °C for 30 min	Left Ramp UP to 1100 °C - 1180 °C Setpoint.Done	
⏰	Timed Acquisition 2	Left Dwell @ 1100 °C for 30 min.Done	
╱	Load to Failure	Left Dwell @ 1100 °C for 30 min.Done	Compression Failure Detector.Done
⌒	Compression Failure Detector	Left Dwell @ 1100 °C for 30 min.Done	
—	Displacement Dwell Command 1	Compression Failure Detector.Done	
╱	Right Ramp DOWN to 0 °C	Compression Failure Detector.Done	
╱	Left Ramp DOWN to 0 °C	Compression Failure Detector.Done	

Procedure is done when Displacement Dwell Command 1.Done

Monotonic Compression to Failure of Straightsided Specimens

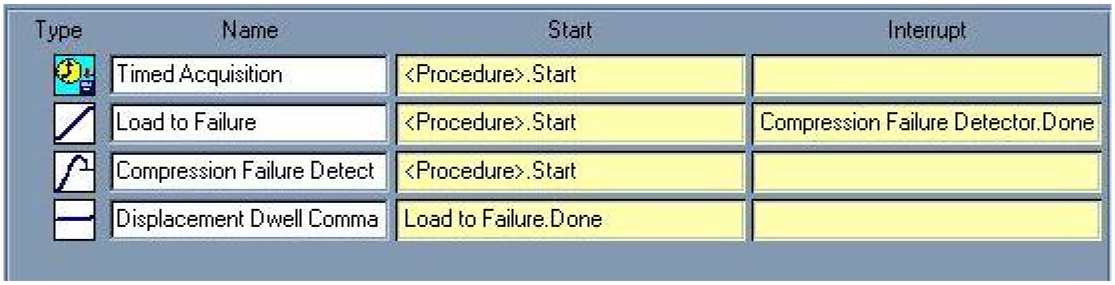

Type	Name	Start	Interrupt
⏰	Timed Acquisition	<Procedure>.Start	
╱	Load to Failure	<Procedure>.Start	Compression Failure Detector.Done
⌒	Compression Failure Detect	<Procedure>.Start	
—	Displacement Dwell Comma	Load to Failure.Done	

Biaxial Loading of Tension-Torsion Thin Walled Tubes

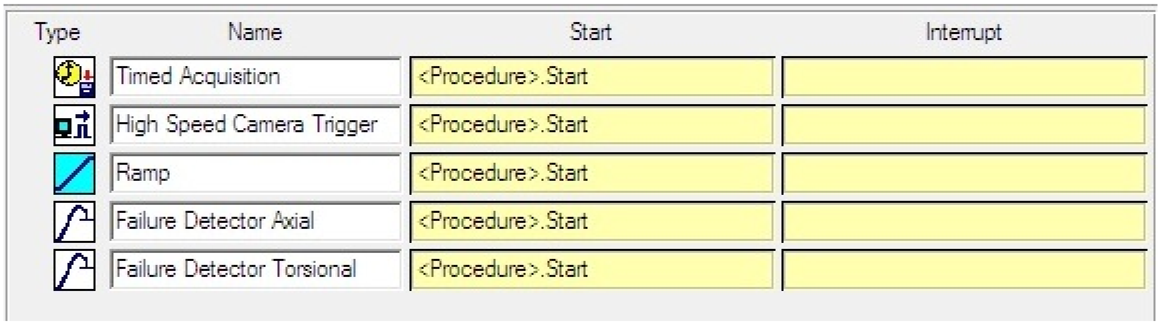

Type	Name	Start	Interrupt
	Timed Acquisition	<Procedure>.Start	
	High Speed Camera Trigger	<Procedure>.Start	
	Ramp	<Procedure>.Start	
	Failure Detector Axial	<Procedure>.Start	
	Failure Detector Torsional	<Procedure>.Start	

DNS Specimens tested in Interlaminar Compressive Creep

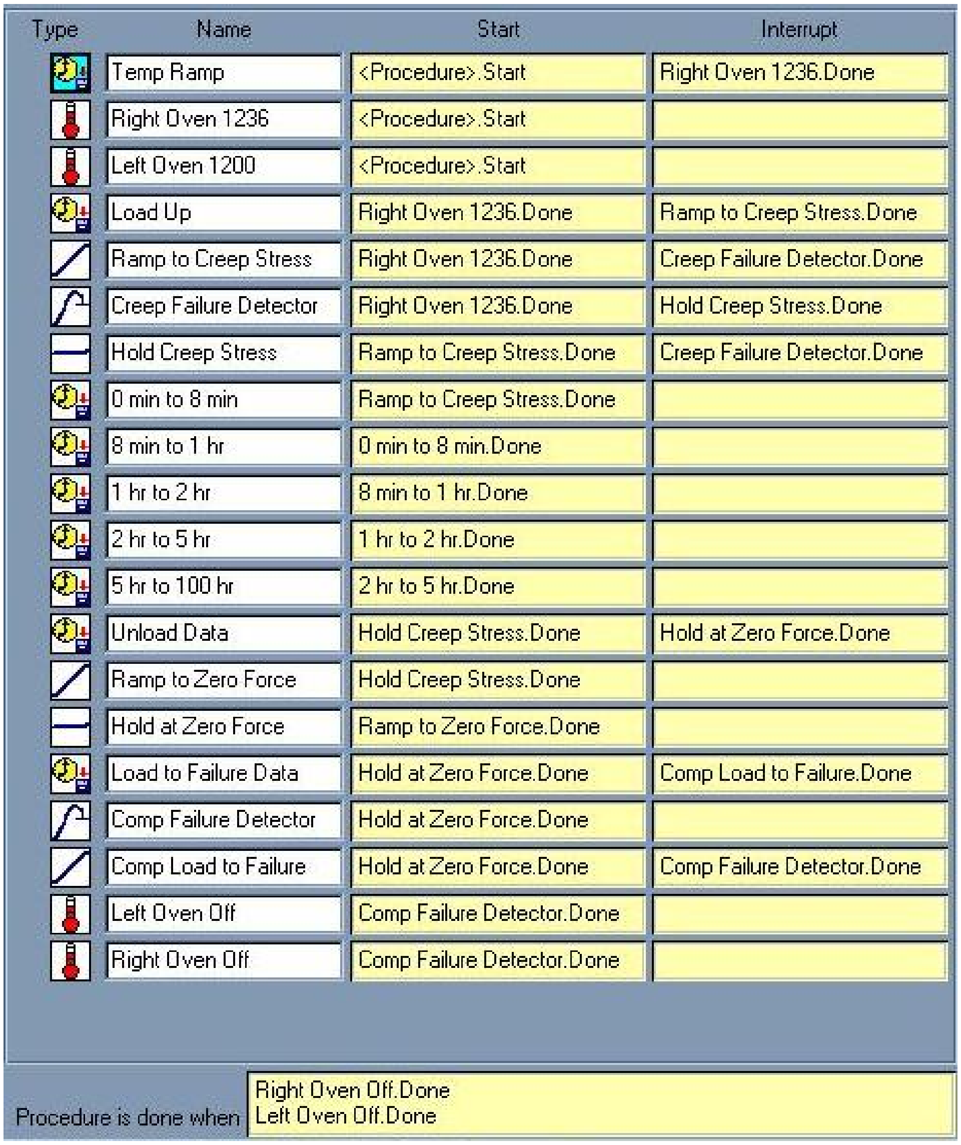

Type	Name	Start	Interrupt
	Temp Ramp	<Procedure>.Start	Right Oven 1236.Done
	Right Oven 1236	<Procedure>.Start	
	Left Oven 1200	<Procedure>.Start	
	Load Up	Right Oven 1236.Done	Ramp to Creep Stress.Done
	Ramp to Creep Stress	Right Oven 1236.Done	Creep Failure Detector.Done
	Creep Failure Detector	Right Oven 1236.Done	Hold Creep Stress.Done
	Hold Creep Stress	Ramp to Creep Stress.Done	Creep Failure Detector.Done
	0 min to 8 min	Ramp to Creep Stress.Done	
	8 min to 1 hr	0 min to 8 min.Done	
	1 hr to 2 hr	8 min to 1 hr.Done	
	2 hr to 5 hr	1 hr to 2 hr.Done	
	5 hr to 100 hr	2 hr to 5 hr.Done	
	Unload Data	Hold Creep Stress.Done	Hold at Zero Force.Done
	Ramp to Zero Force	Hold Creep Stress.Done	
	Hold at Zero Force	Ramp to Zero Force.Done	
	Load to Failure Data	Hold at Zero Force.Done	Comp Load to Failure.Done
	Comp Failure Detector	Hold at Zero Force.Done	
	Comp Load to Failure	Hold at Zero Force.Done	Comp Failure Detector.Done
	Left Oven Off	Comp Failure Detector.Done	
	Right Oven Off	Comp Failure Detector.Done	

Procedure is done when
Right Oven Off.Done
Left Oven Off.Done

Appendix B: Optical Micrographs of Specimen 1

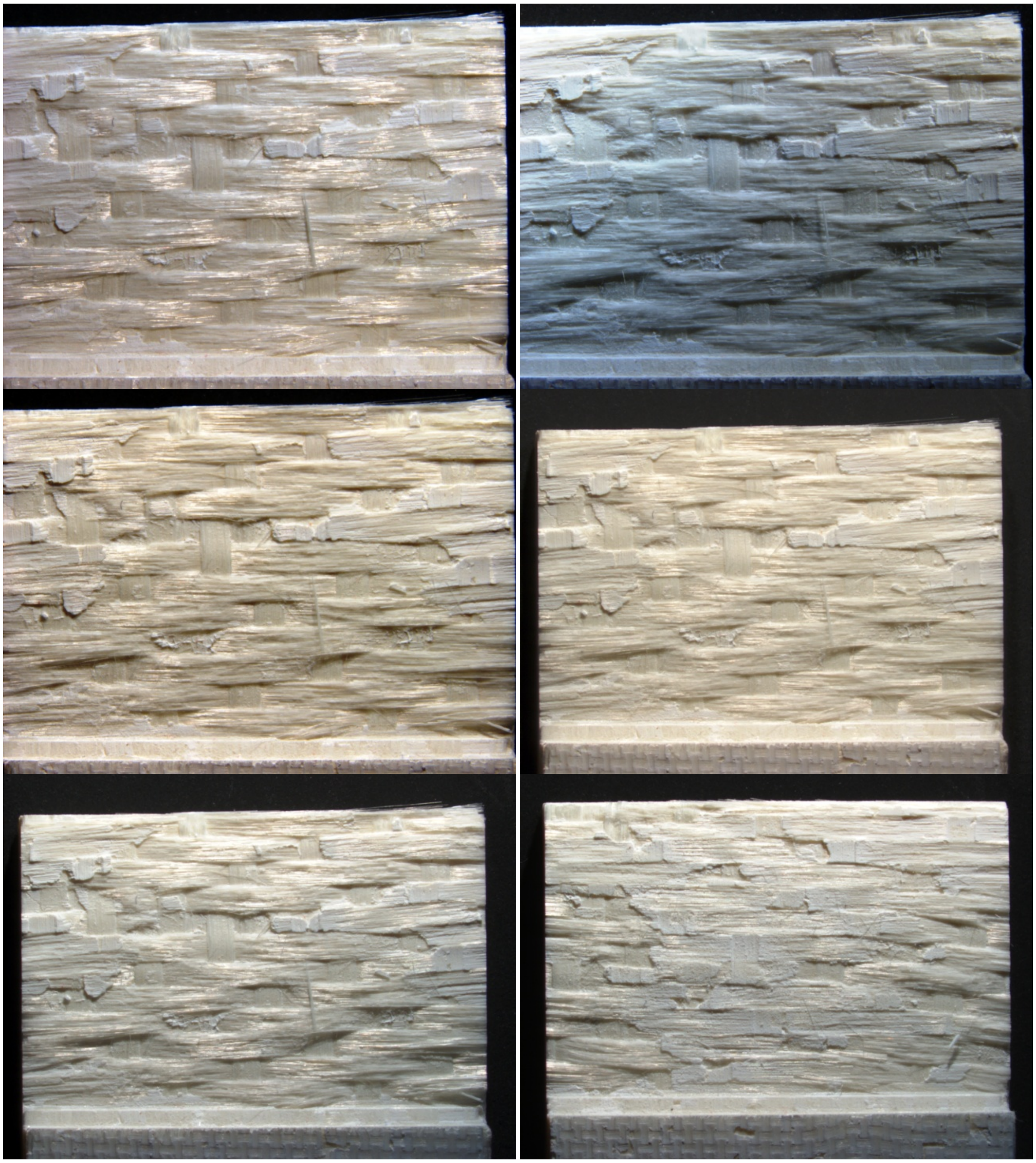

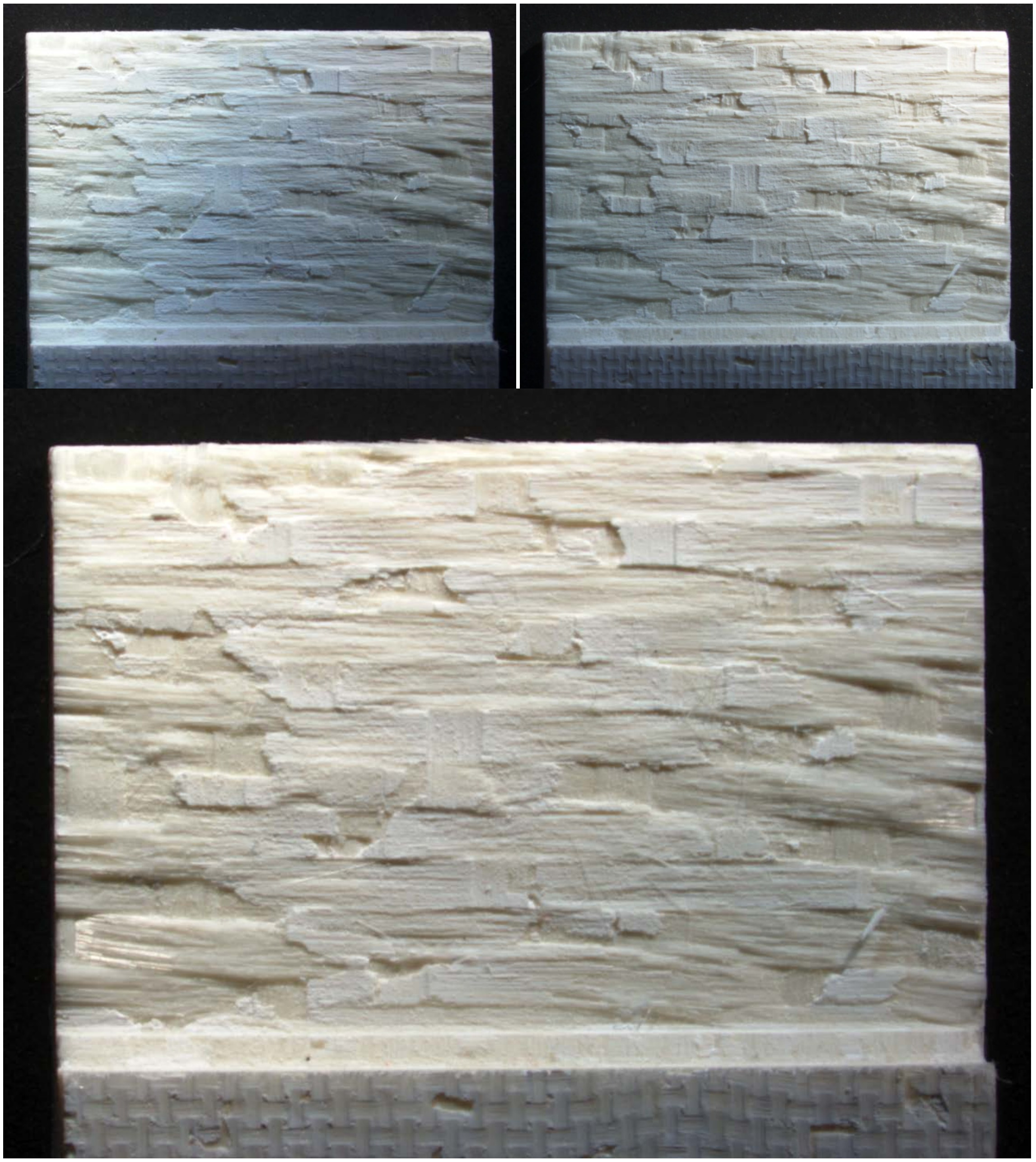

Appendix C: Optical Micrographs of Specimen 2

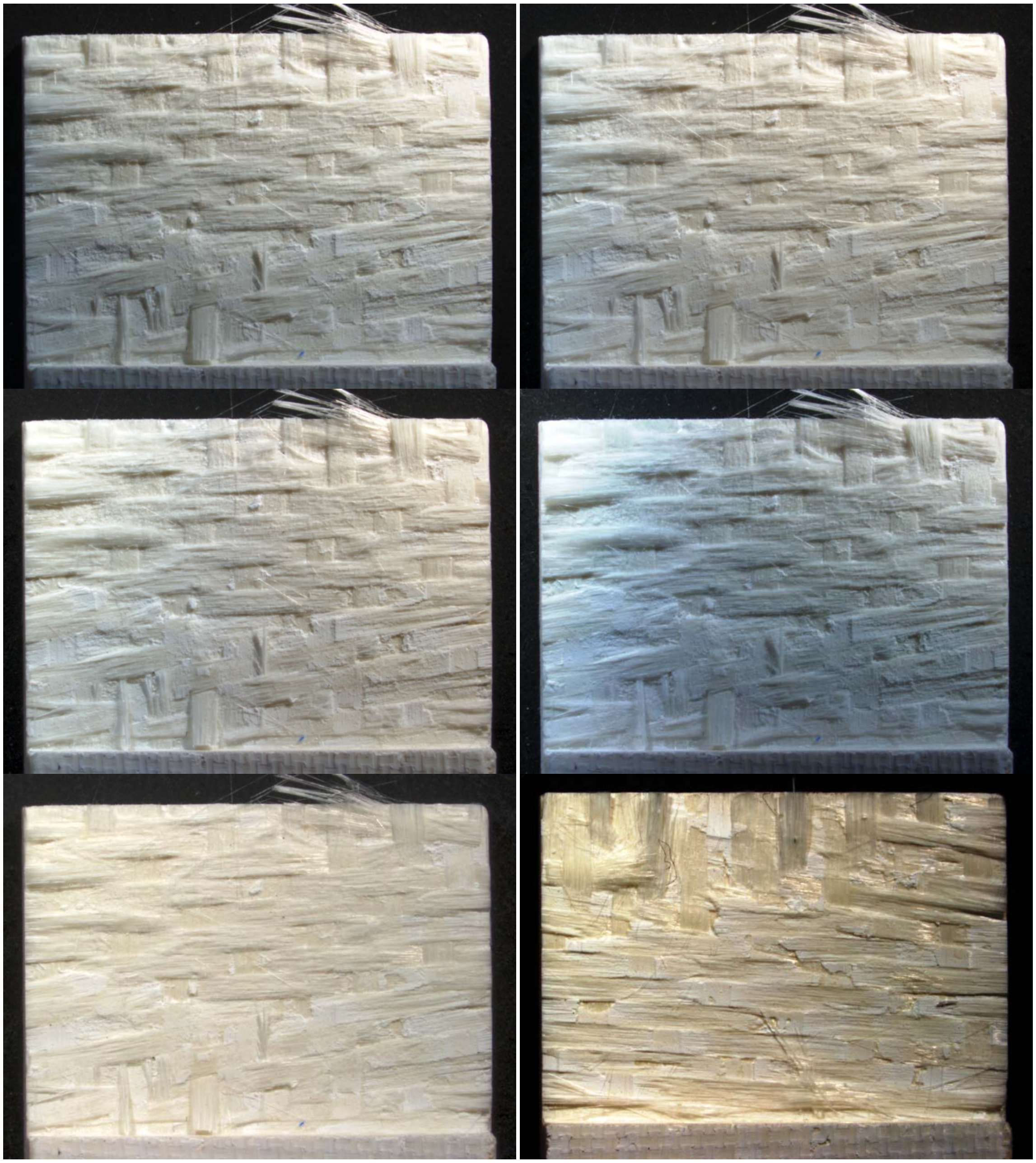

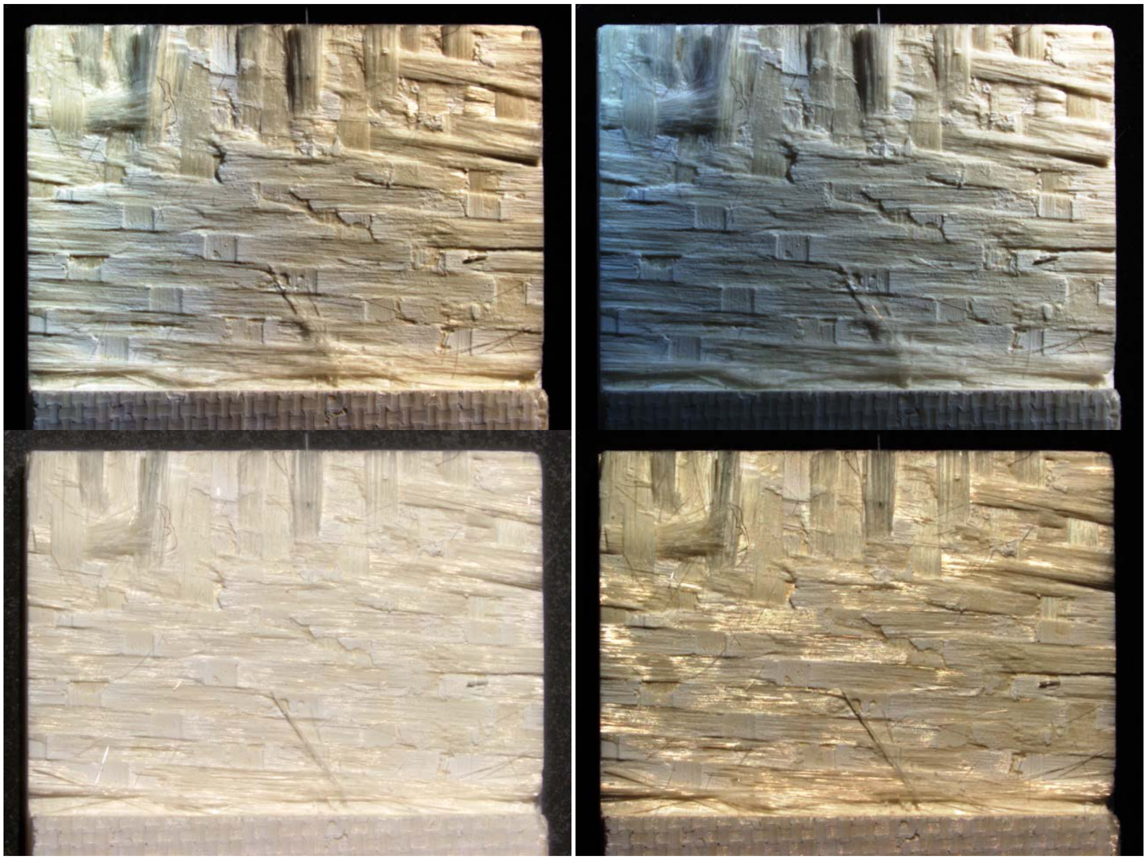

Appendix D: Optical Micrographs of Specimen 3

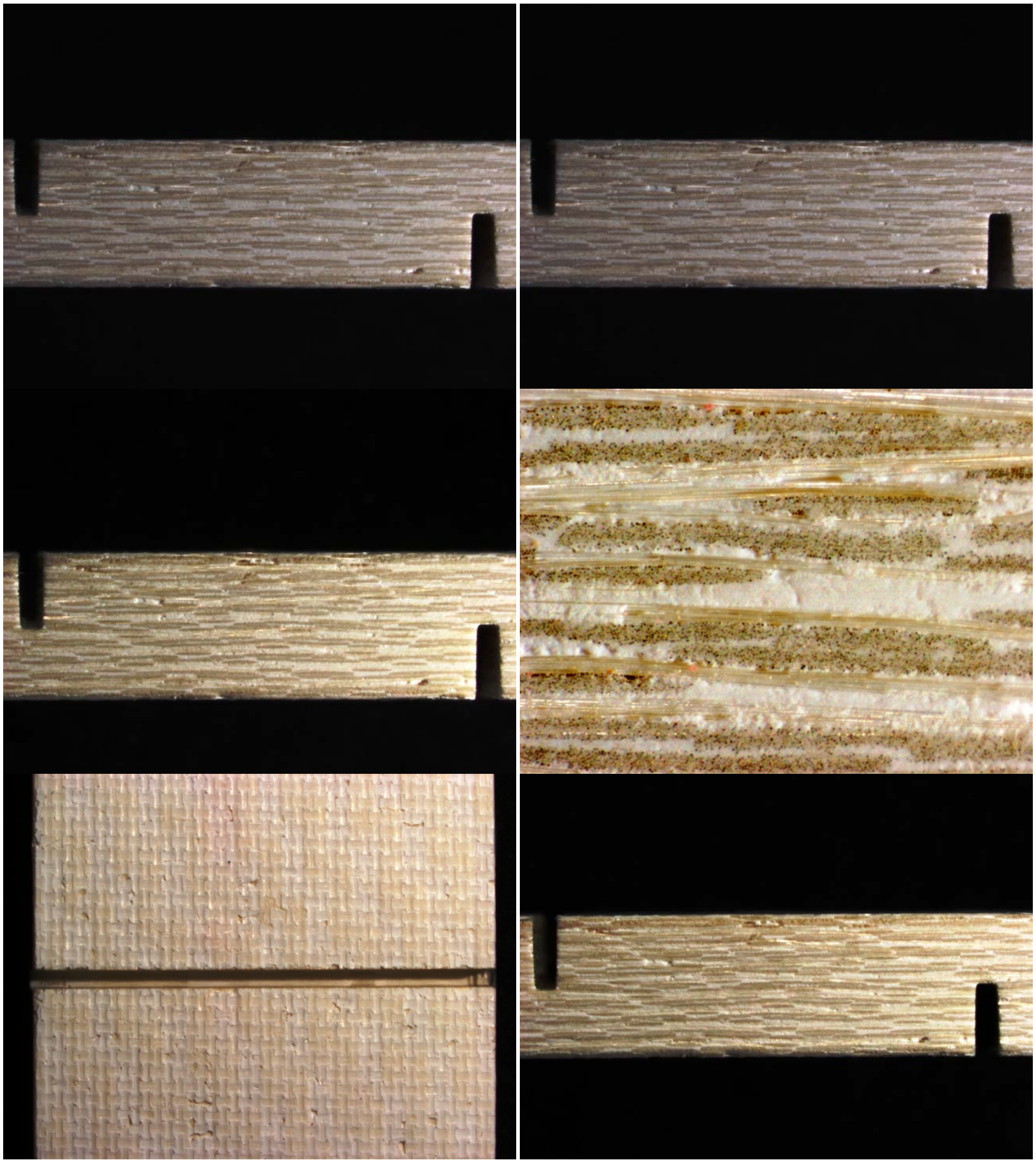

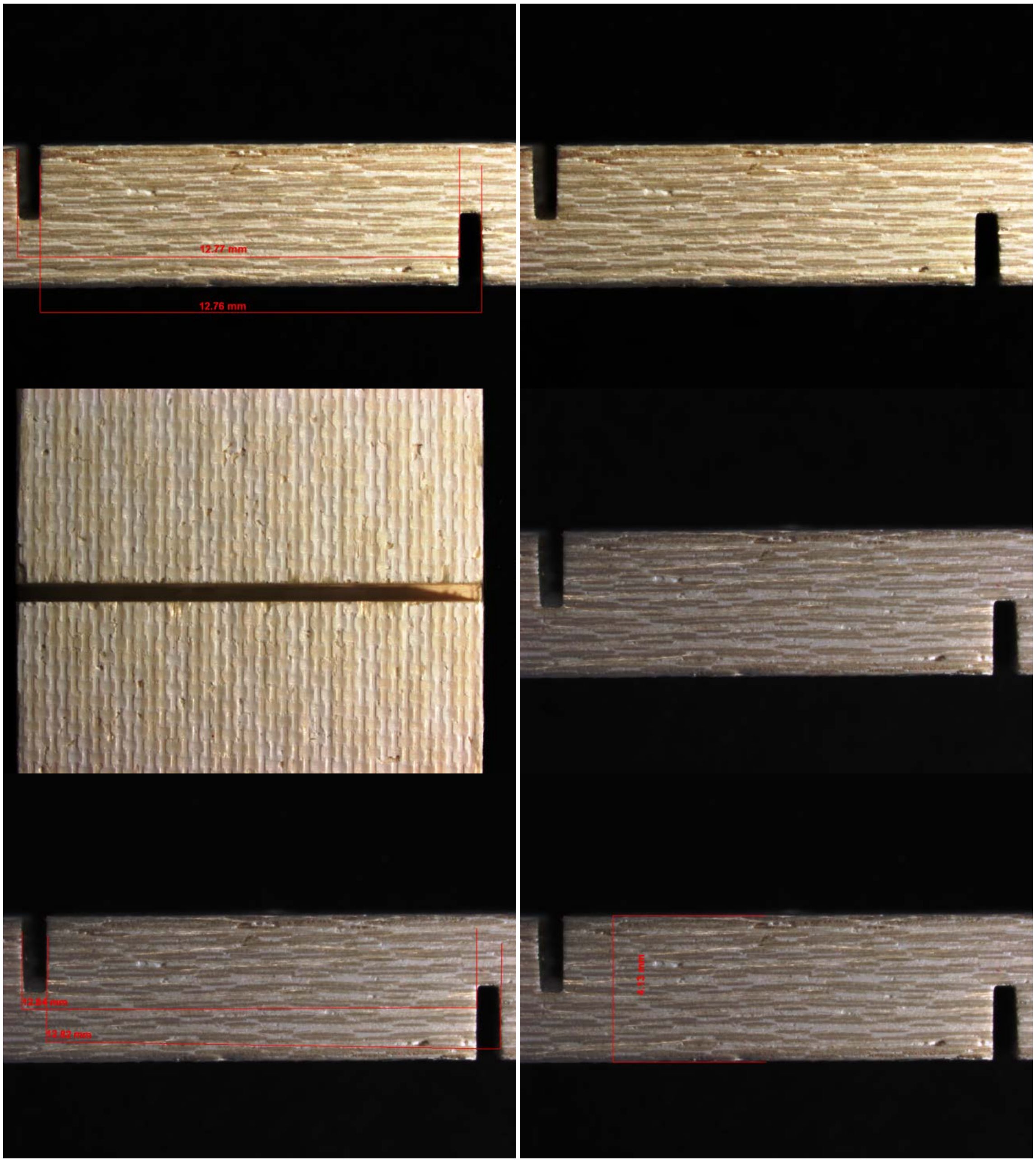
12.77 mm
12.76 mm
12.84 mm
12.82 mm
4.13 mm

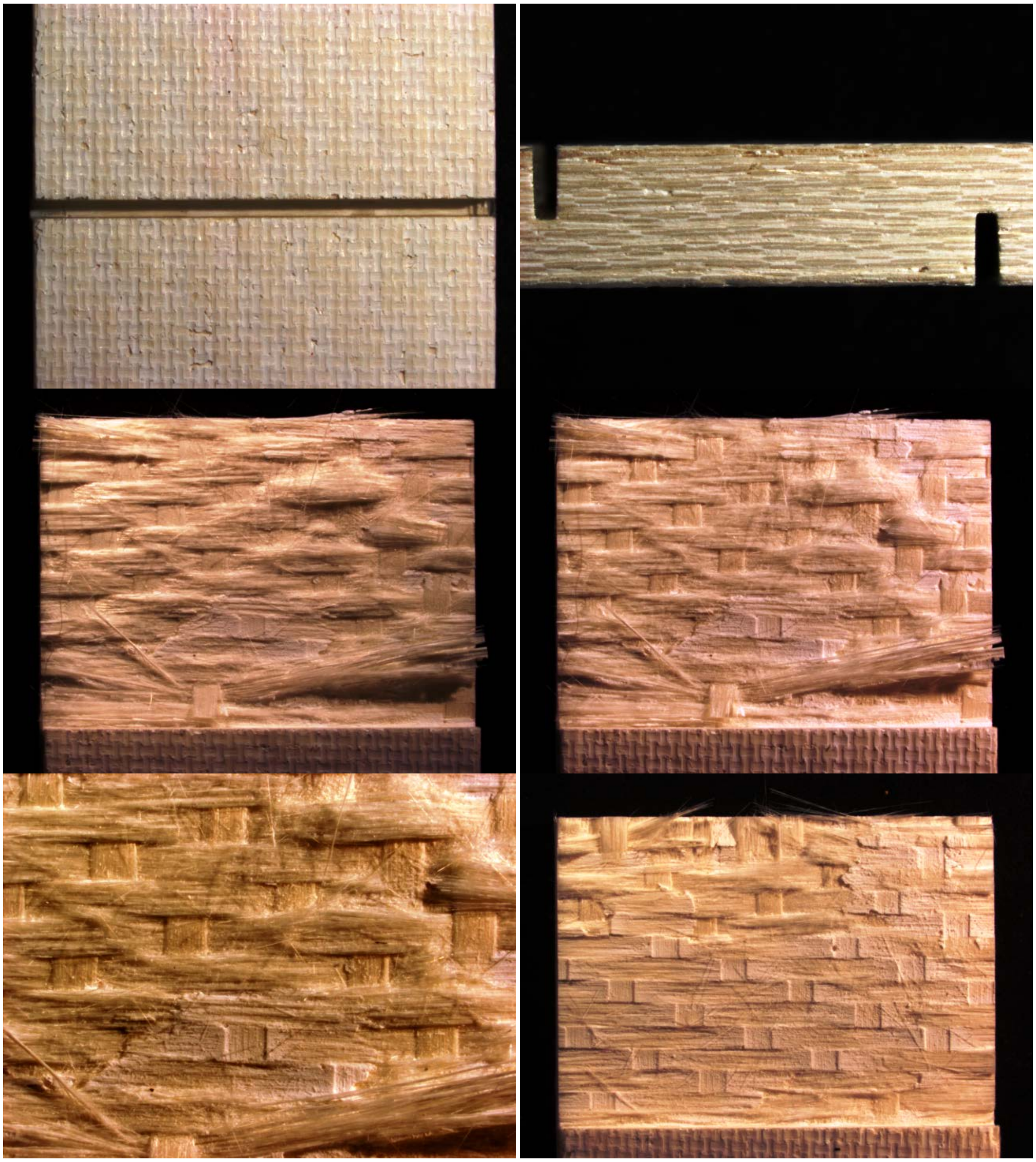

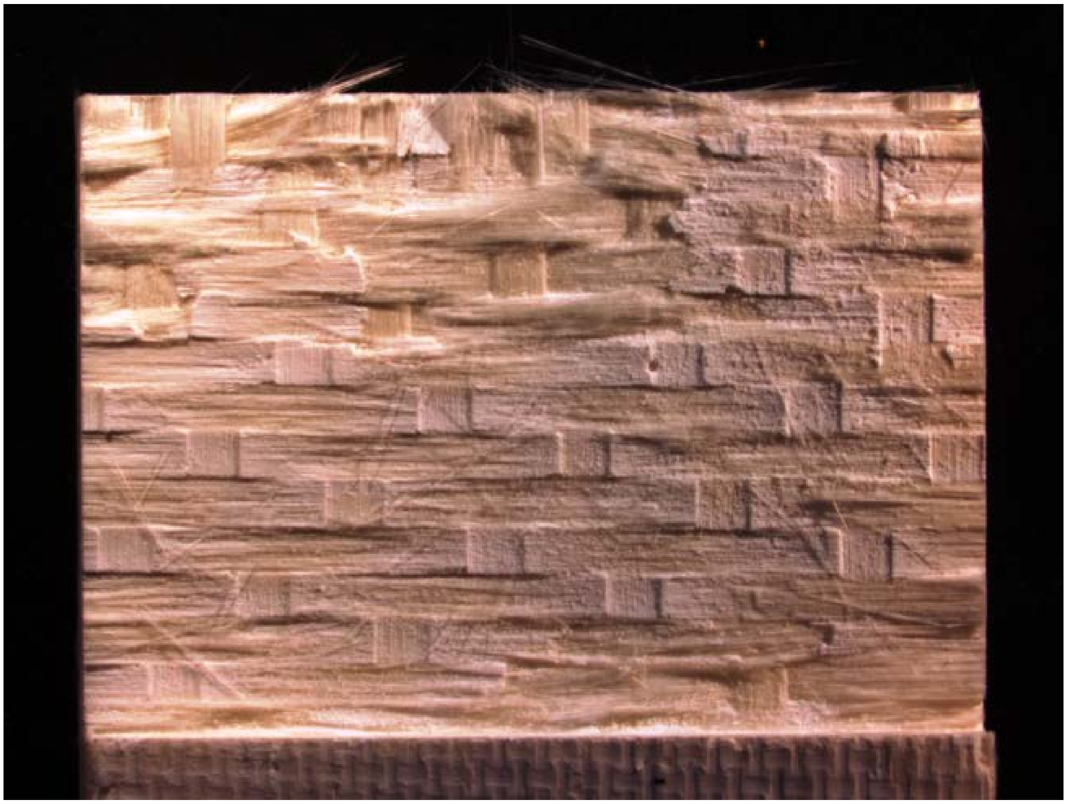

Appendix E: Optical Micrographs of Specimen 4

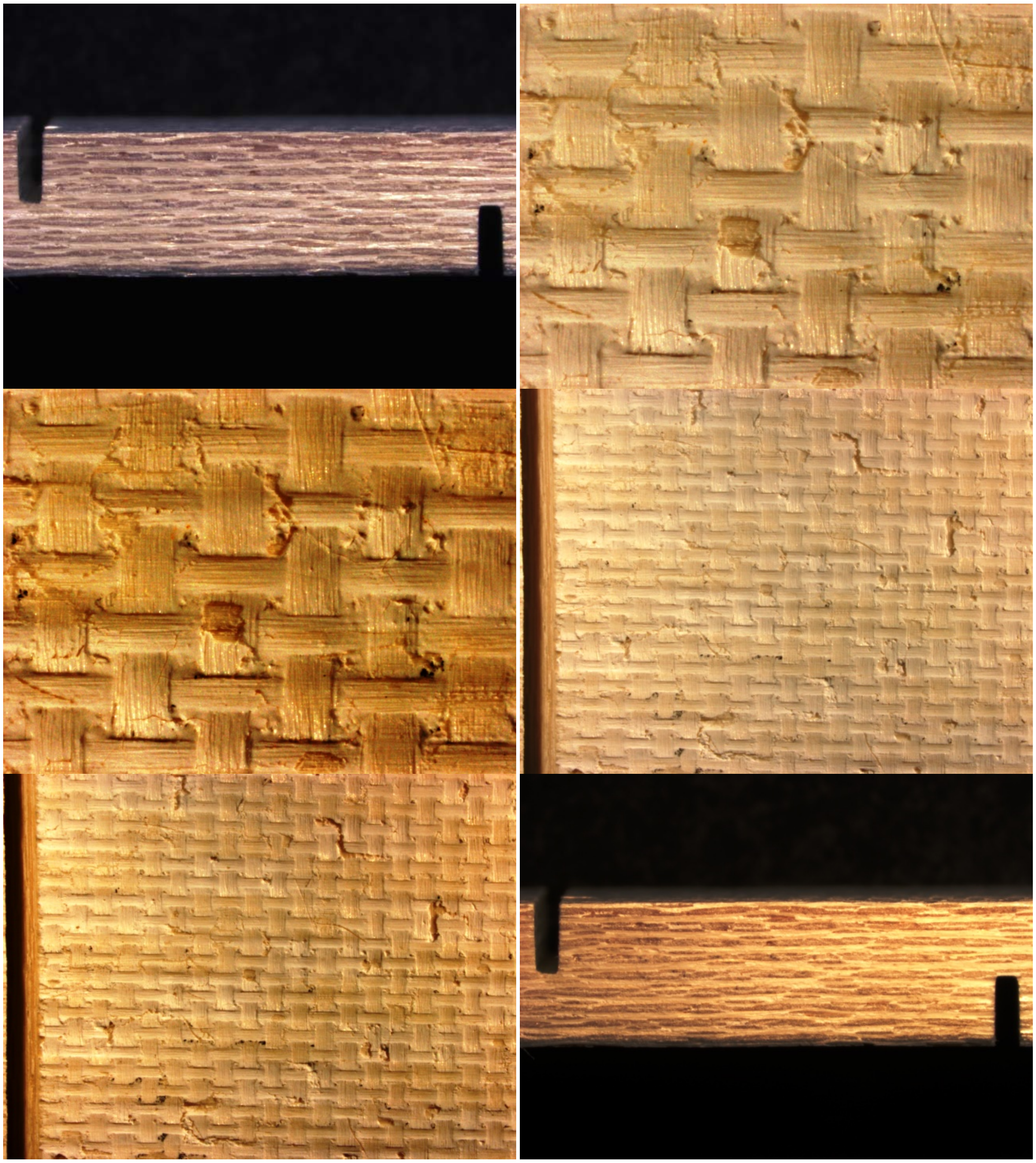

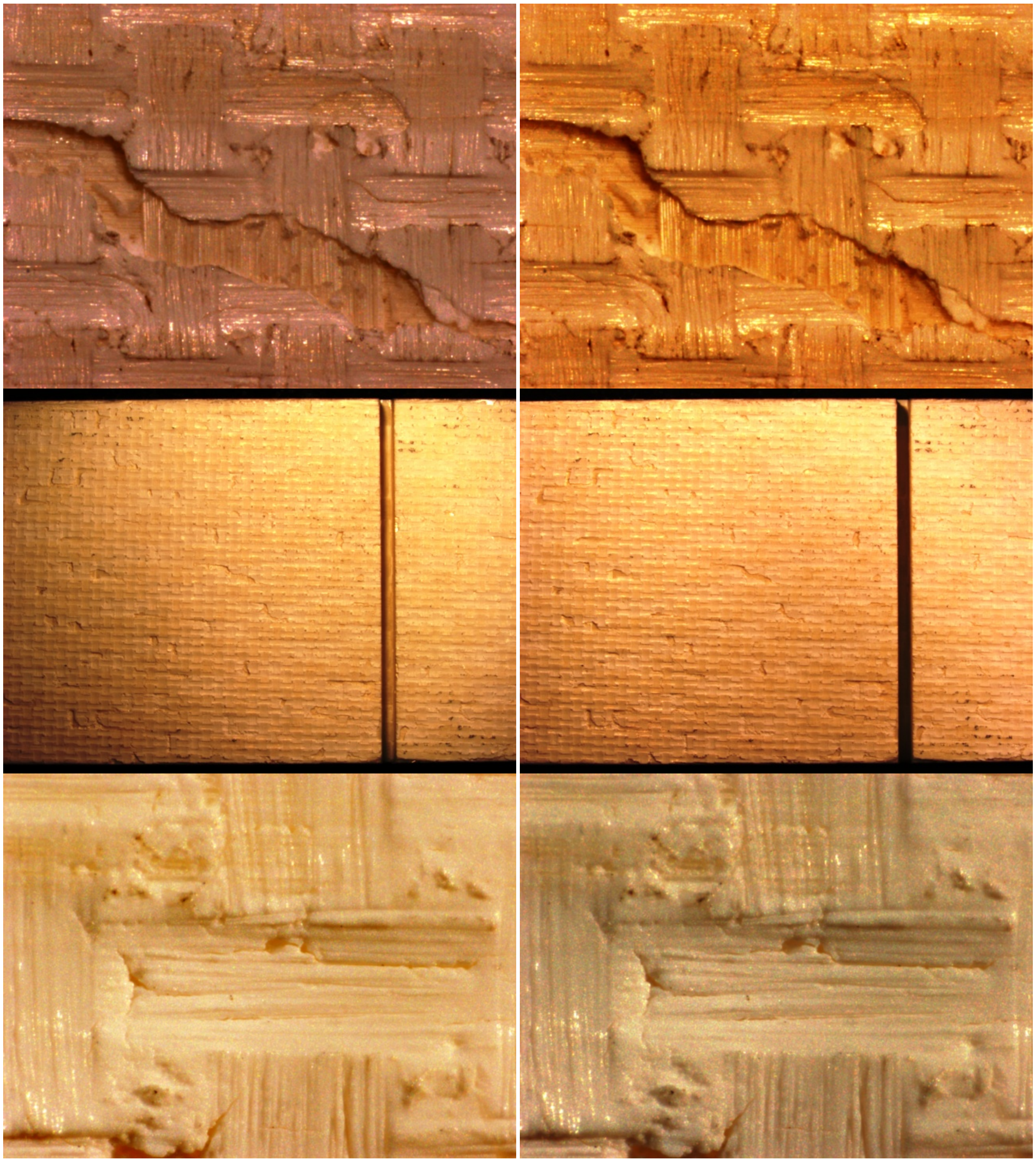

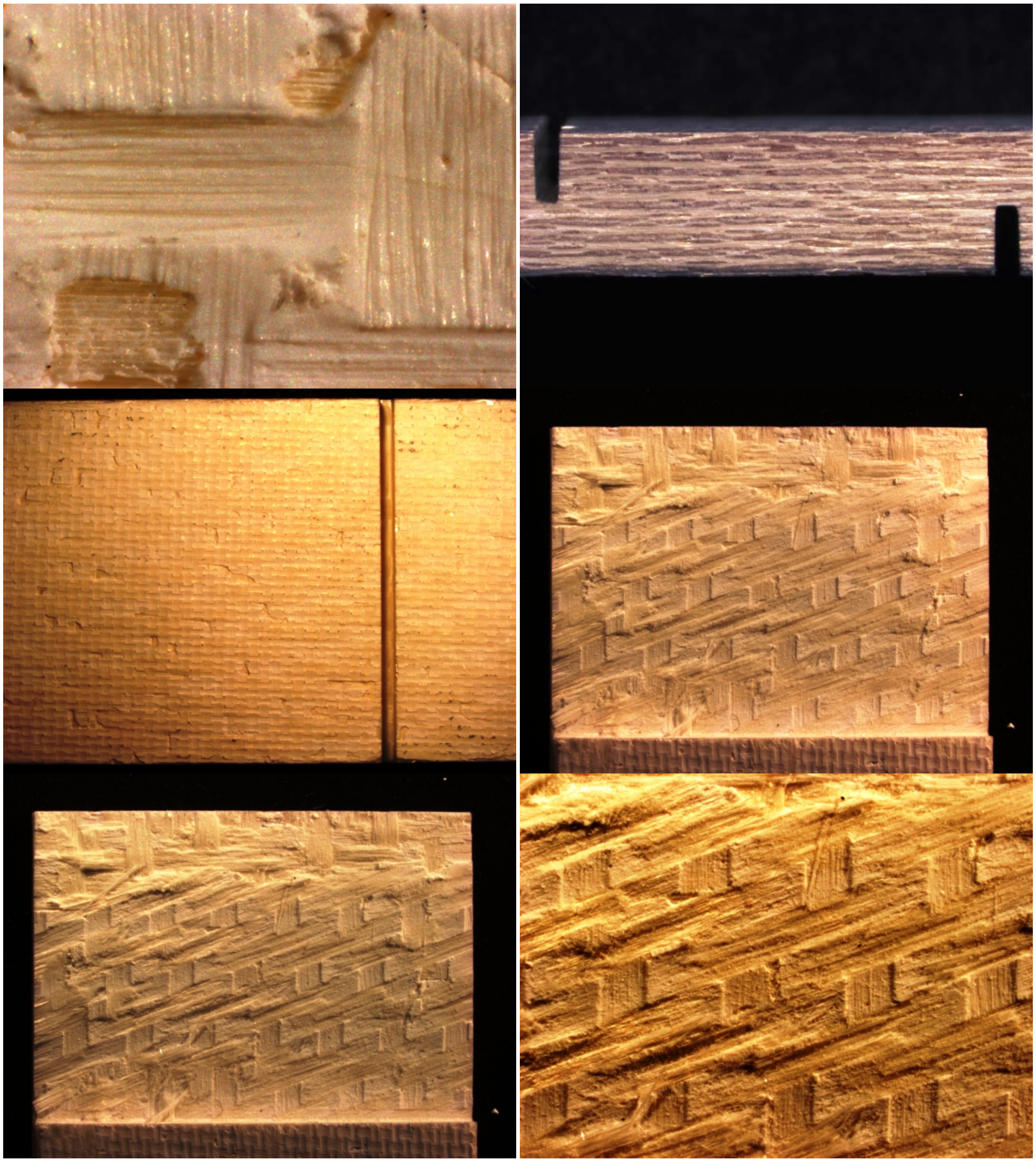

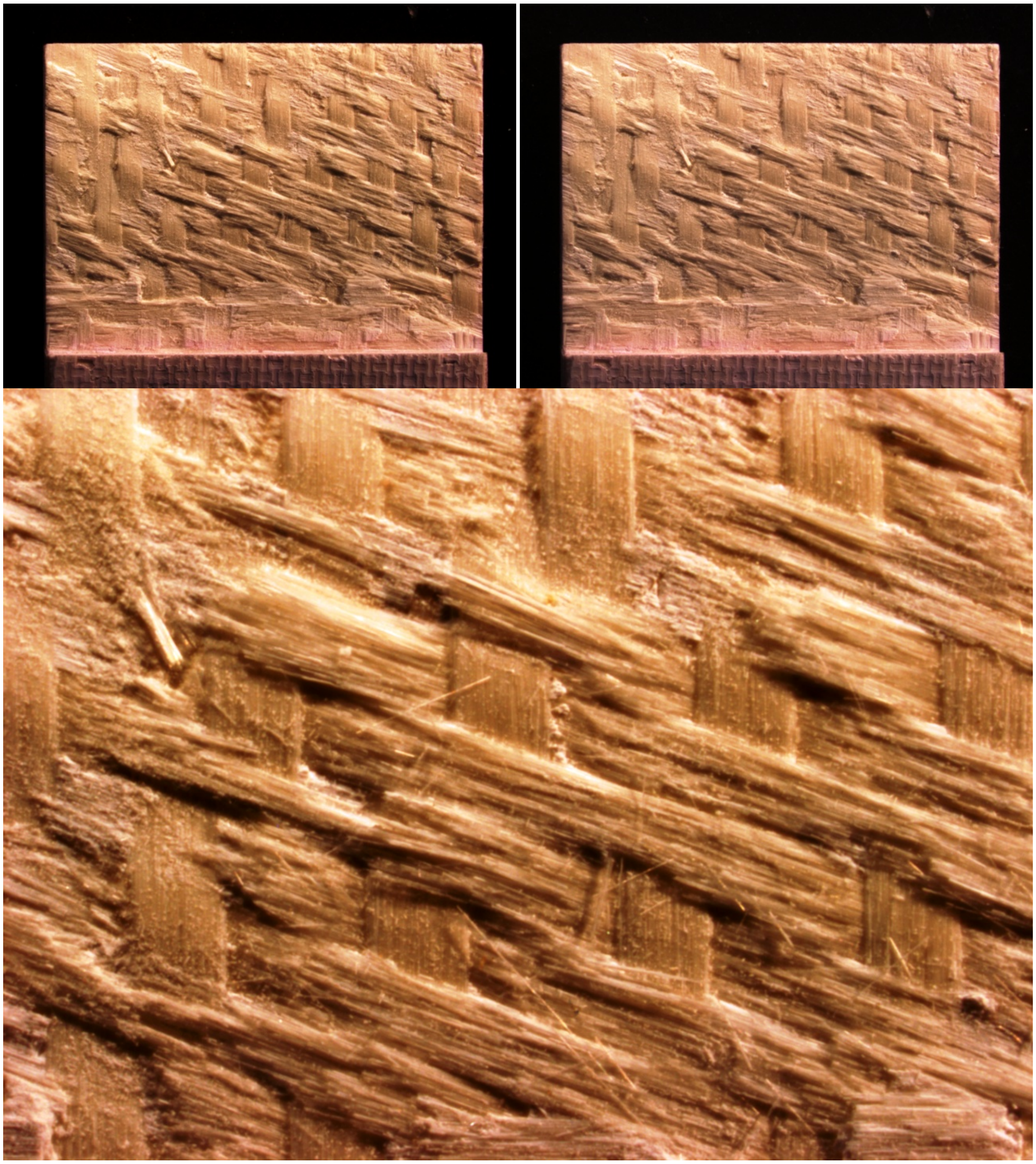

Appendix F: Optical Micrographs of Specimen 5

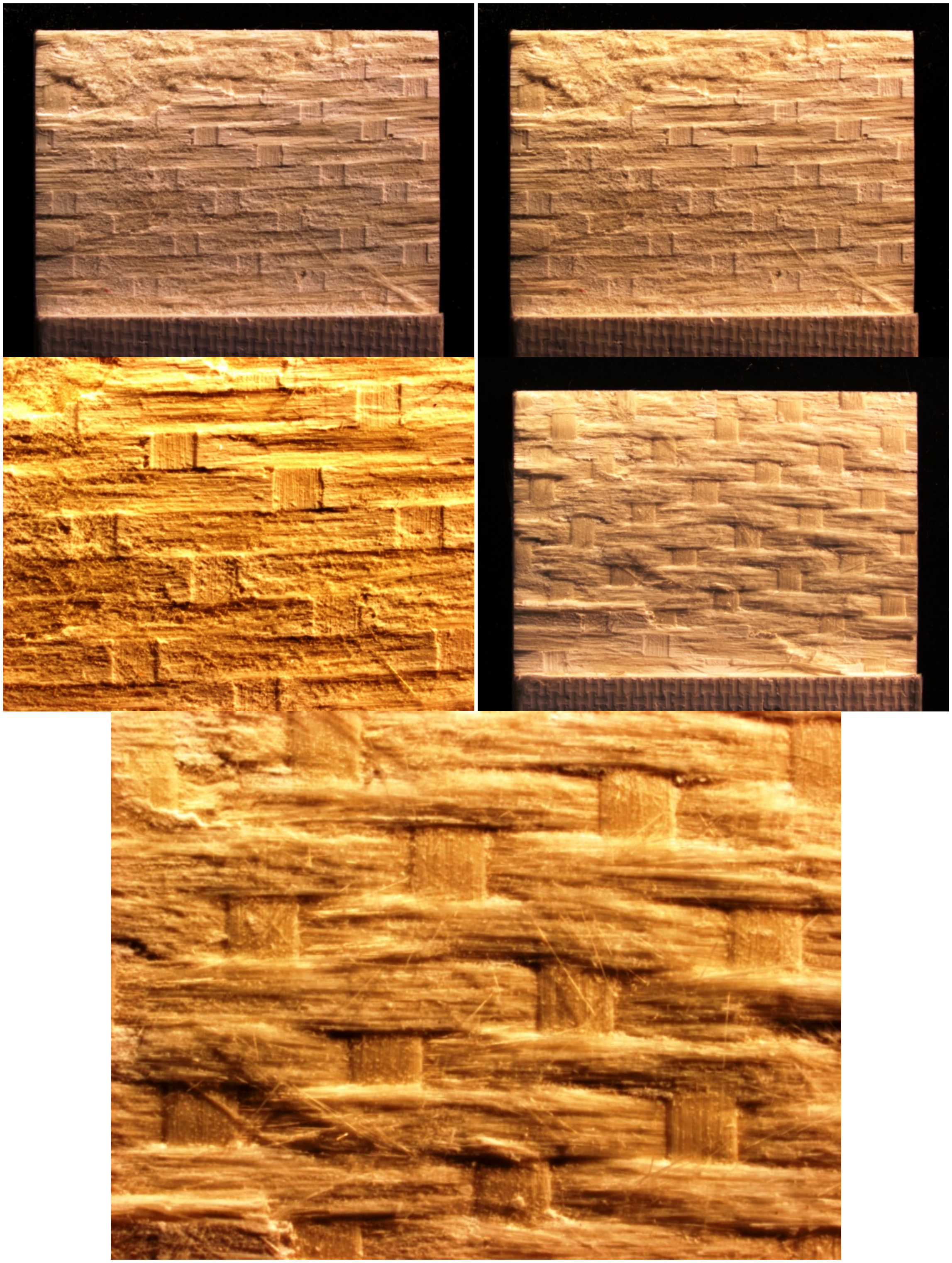

Appendix G: Optical Micrographs of Specimen 6

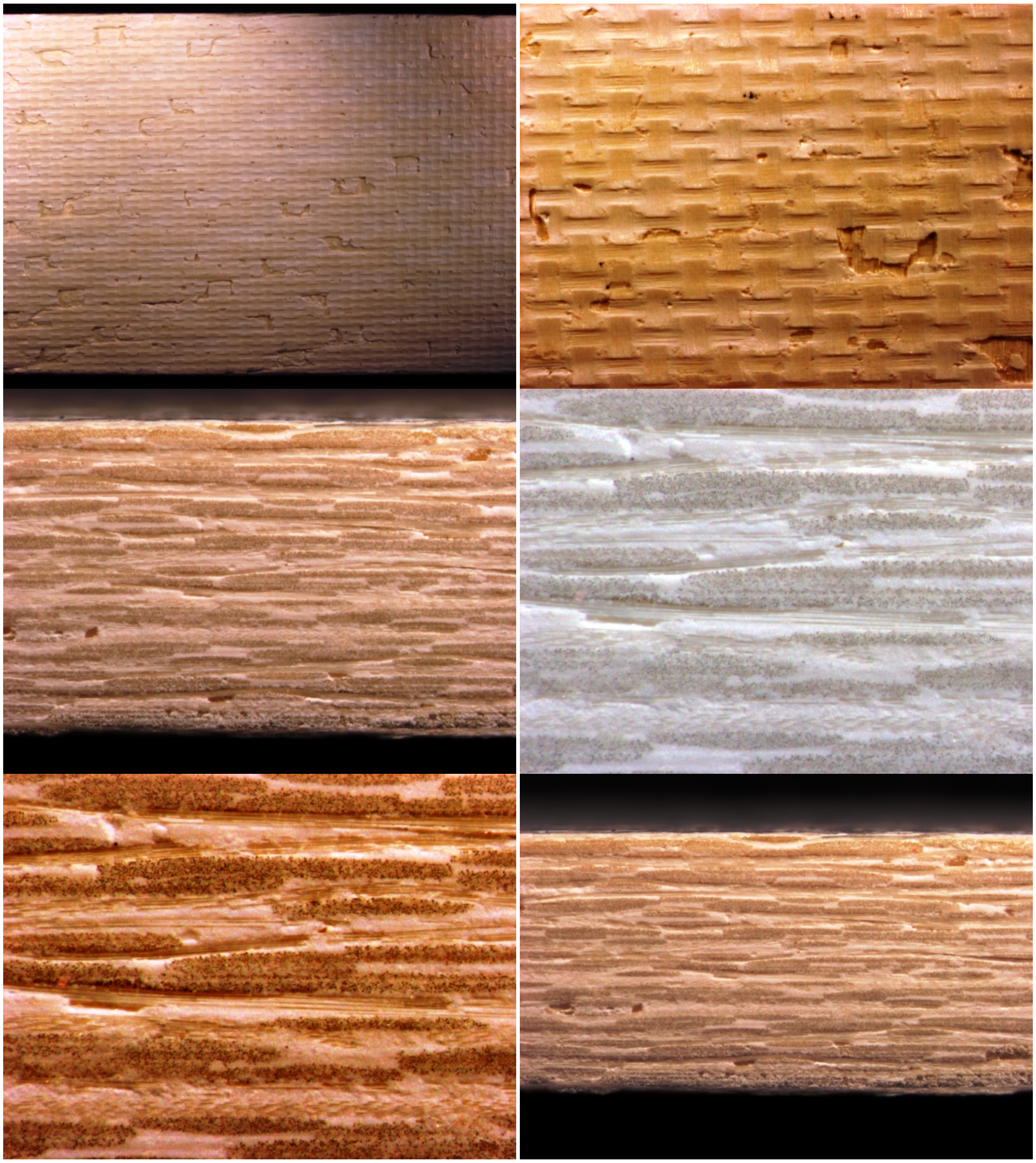

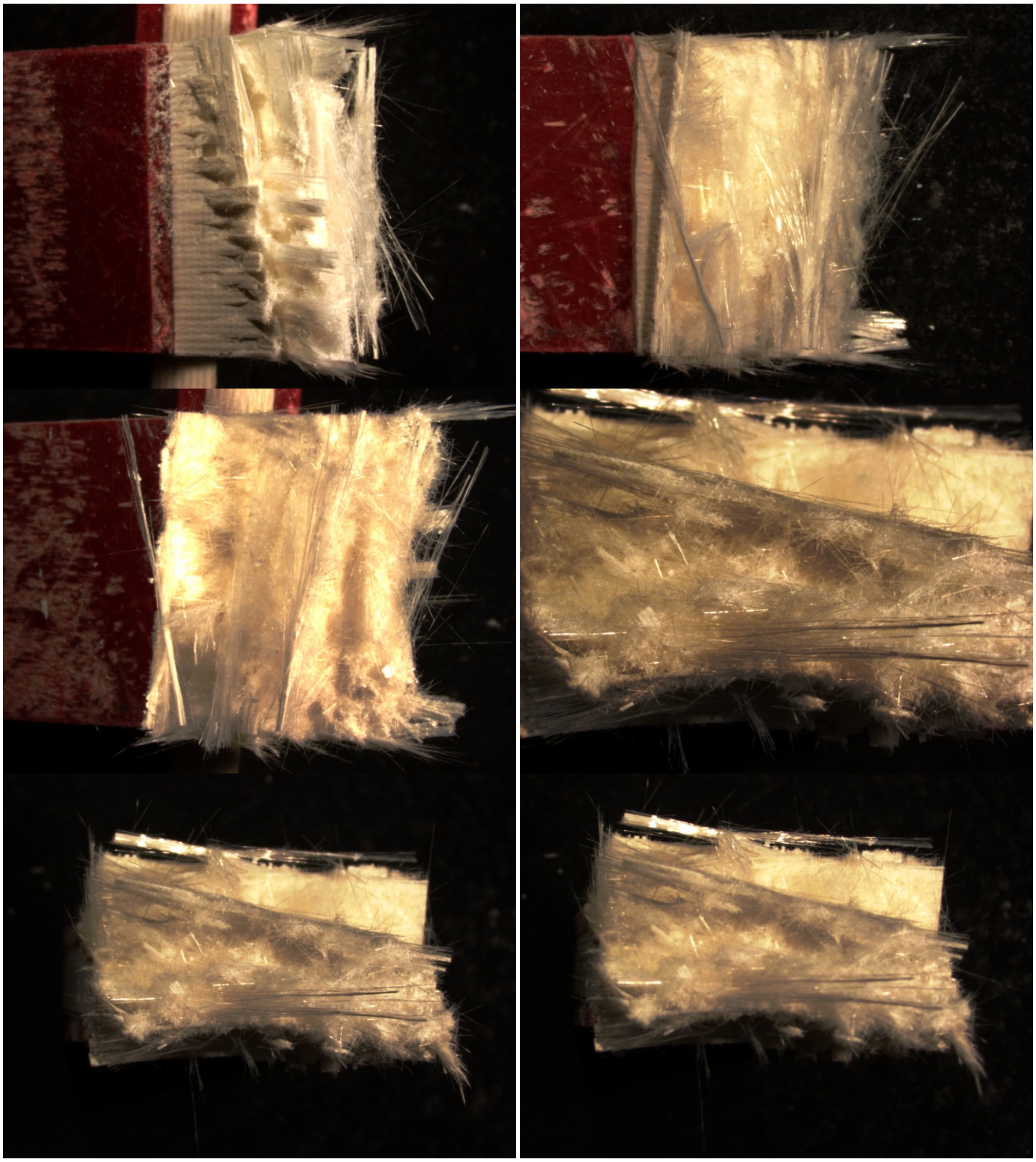

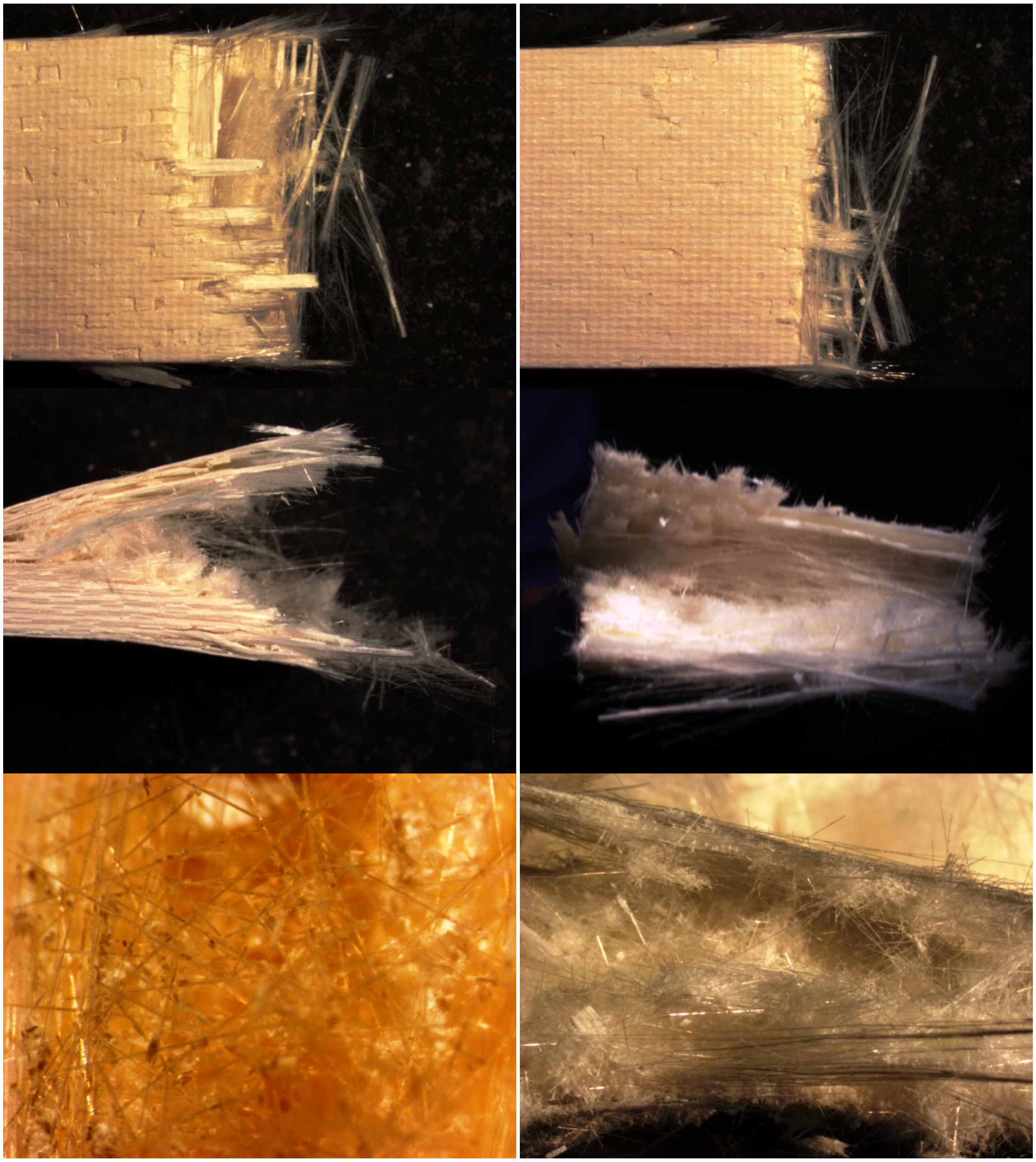

Appendix H: Optical Micrographs of Specimen 7

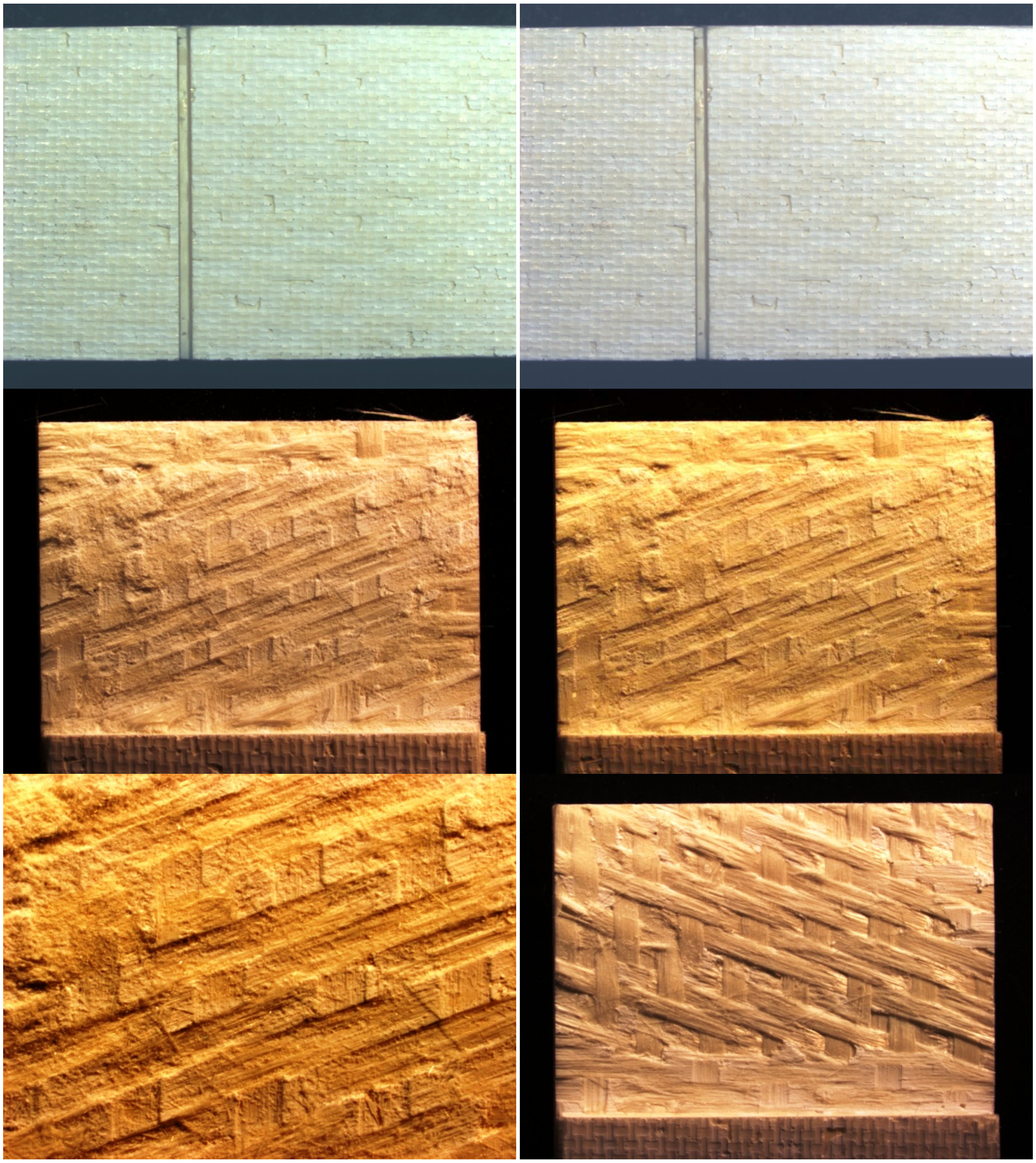

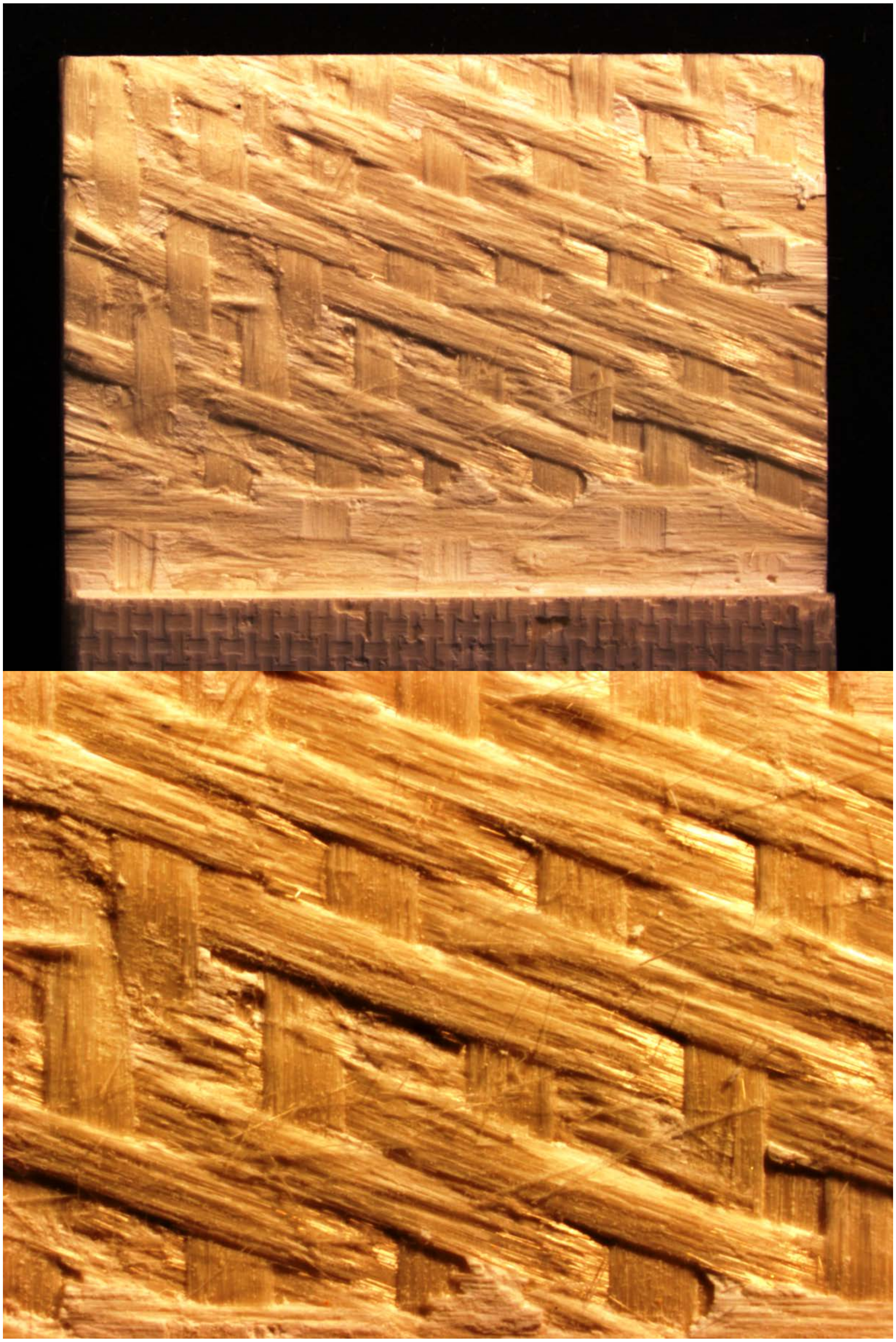

Appendix I: Optical Micrographs of Specimen 8

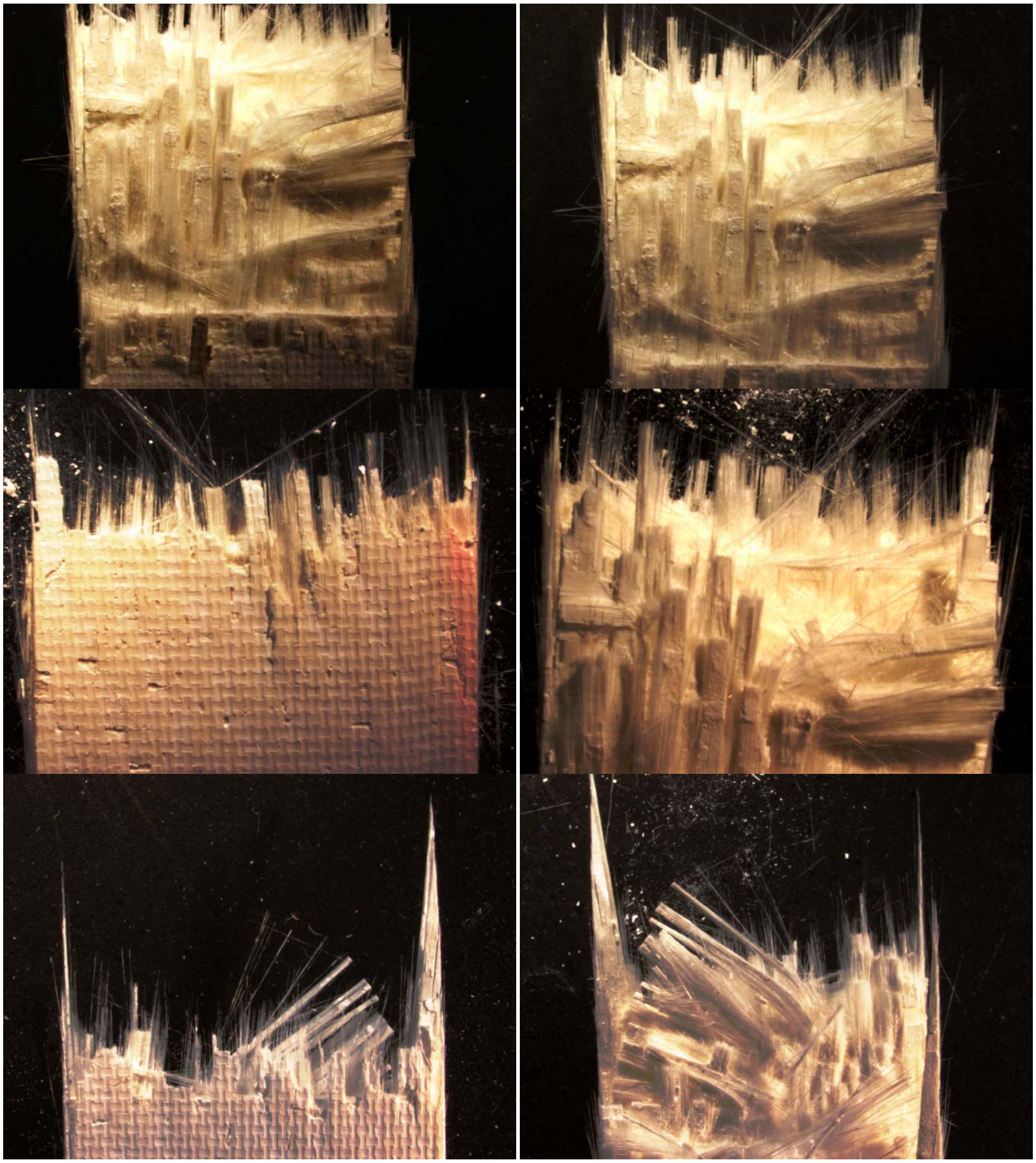

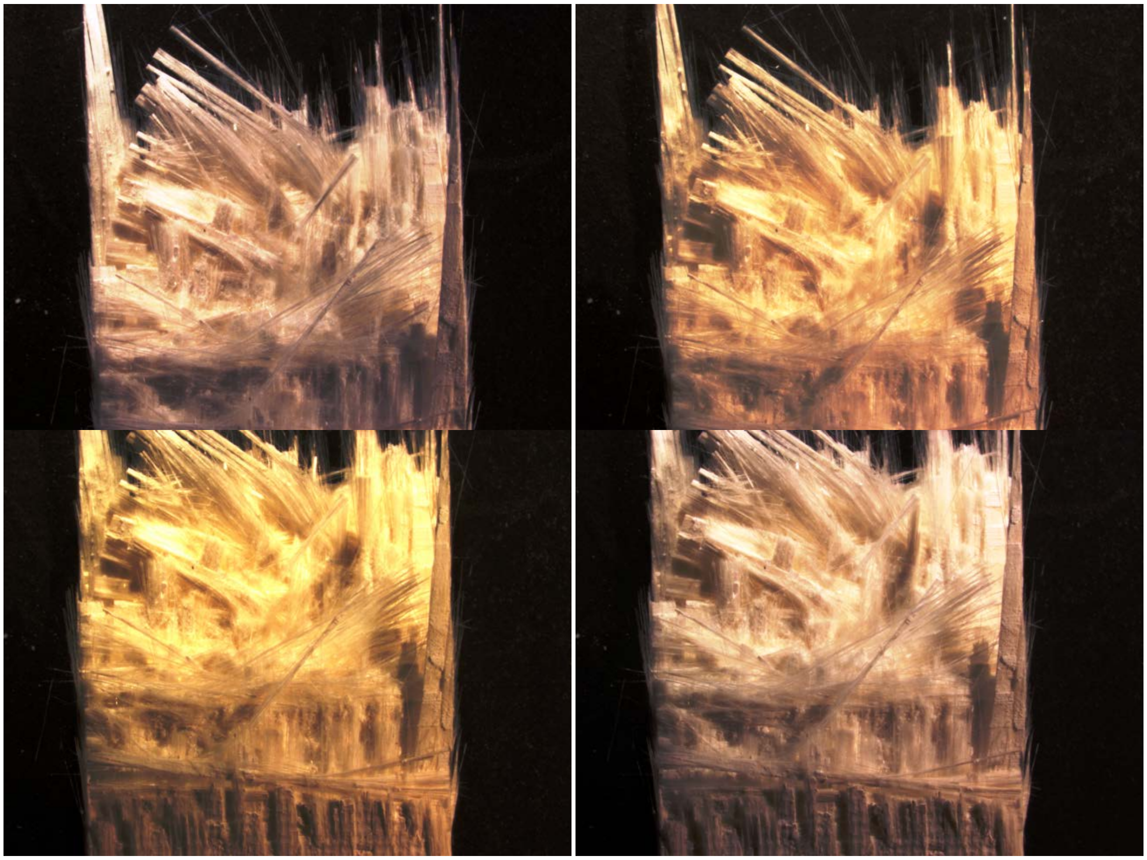

Appendix J: Optical Micrographs of Specimen 9

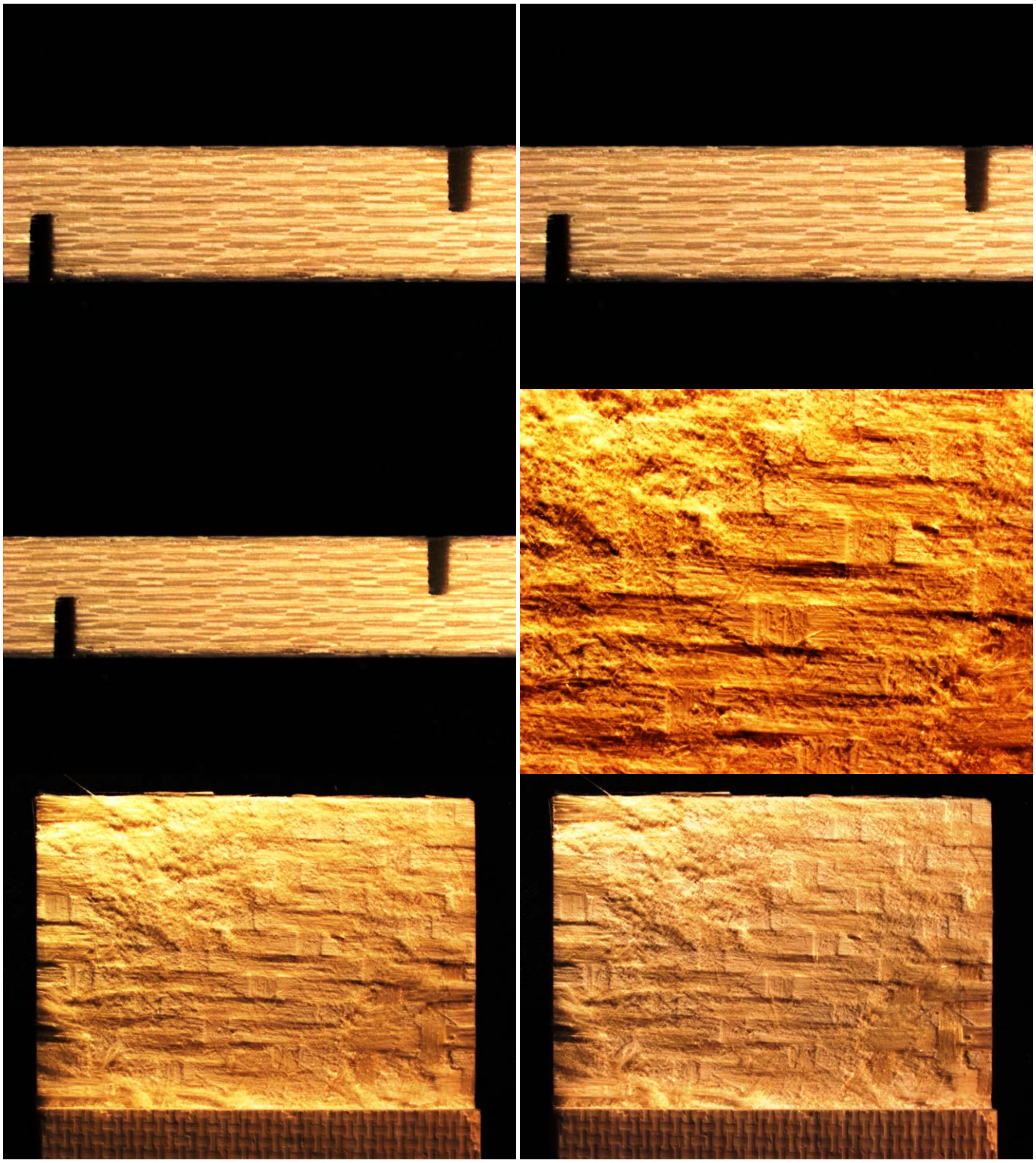

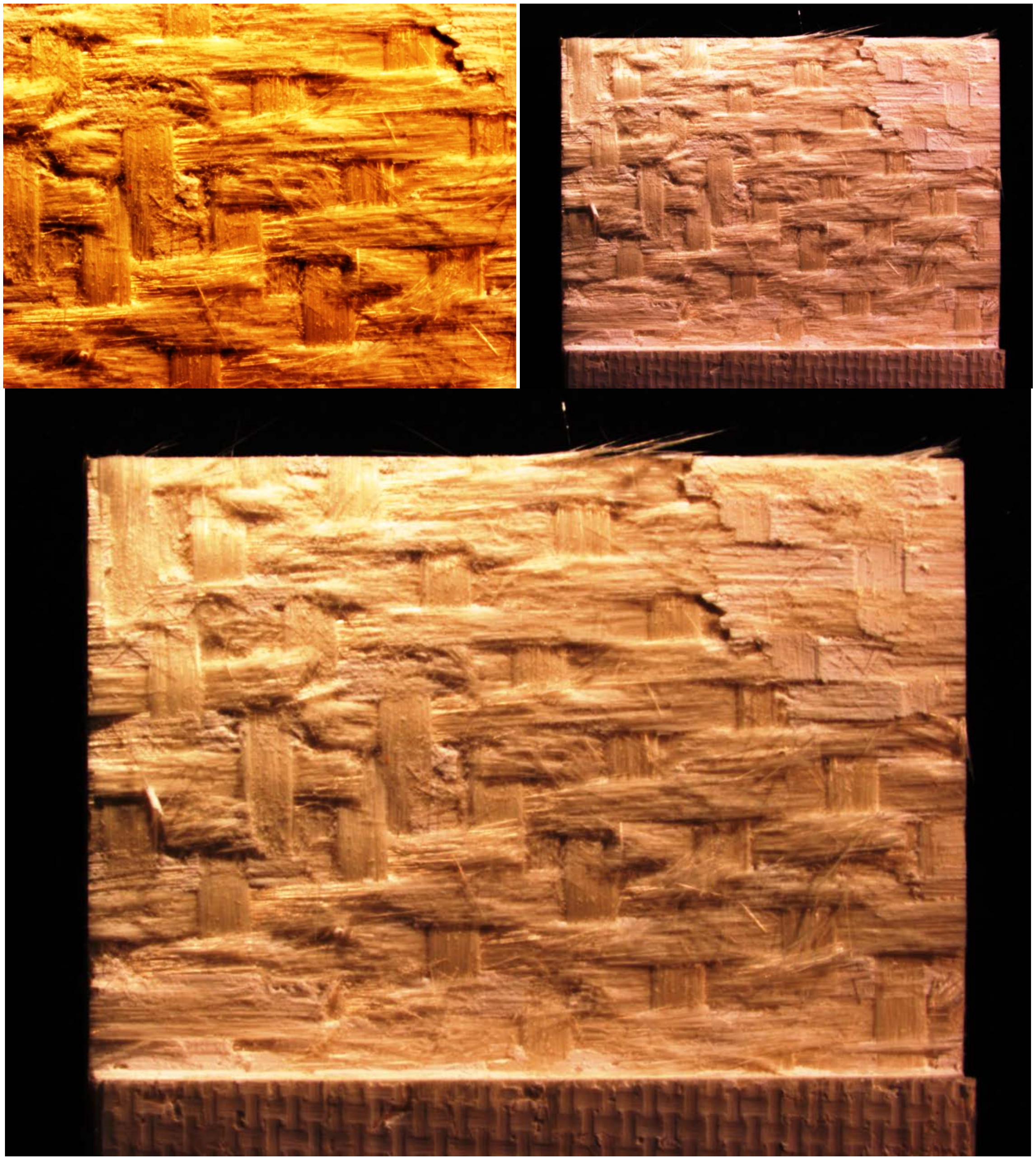

Appendix K: Optical Micrographs of Specimen 10

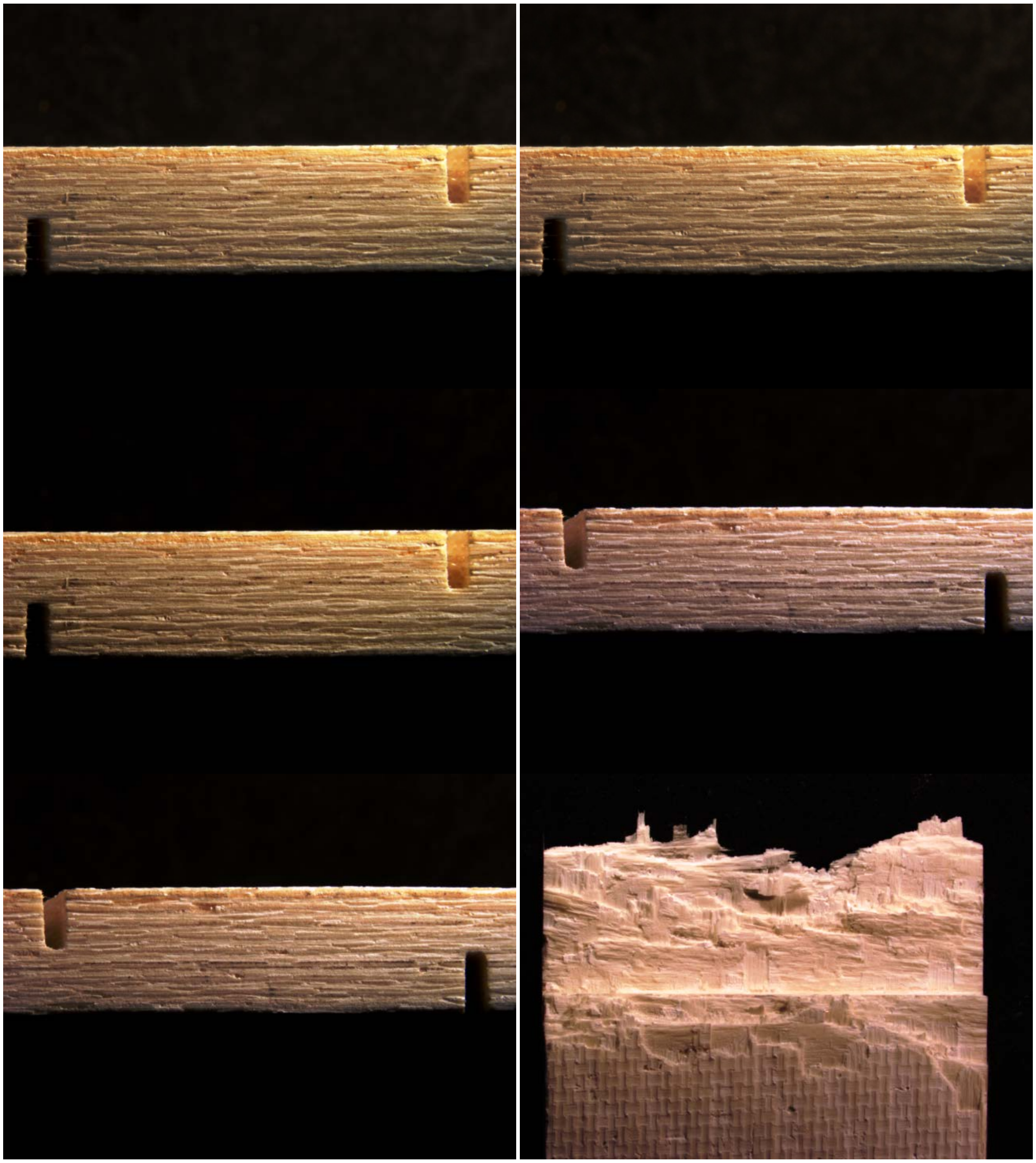

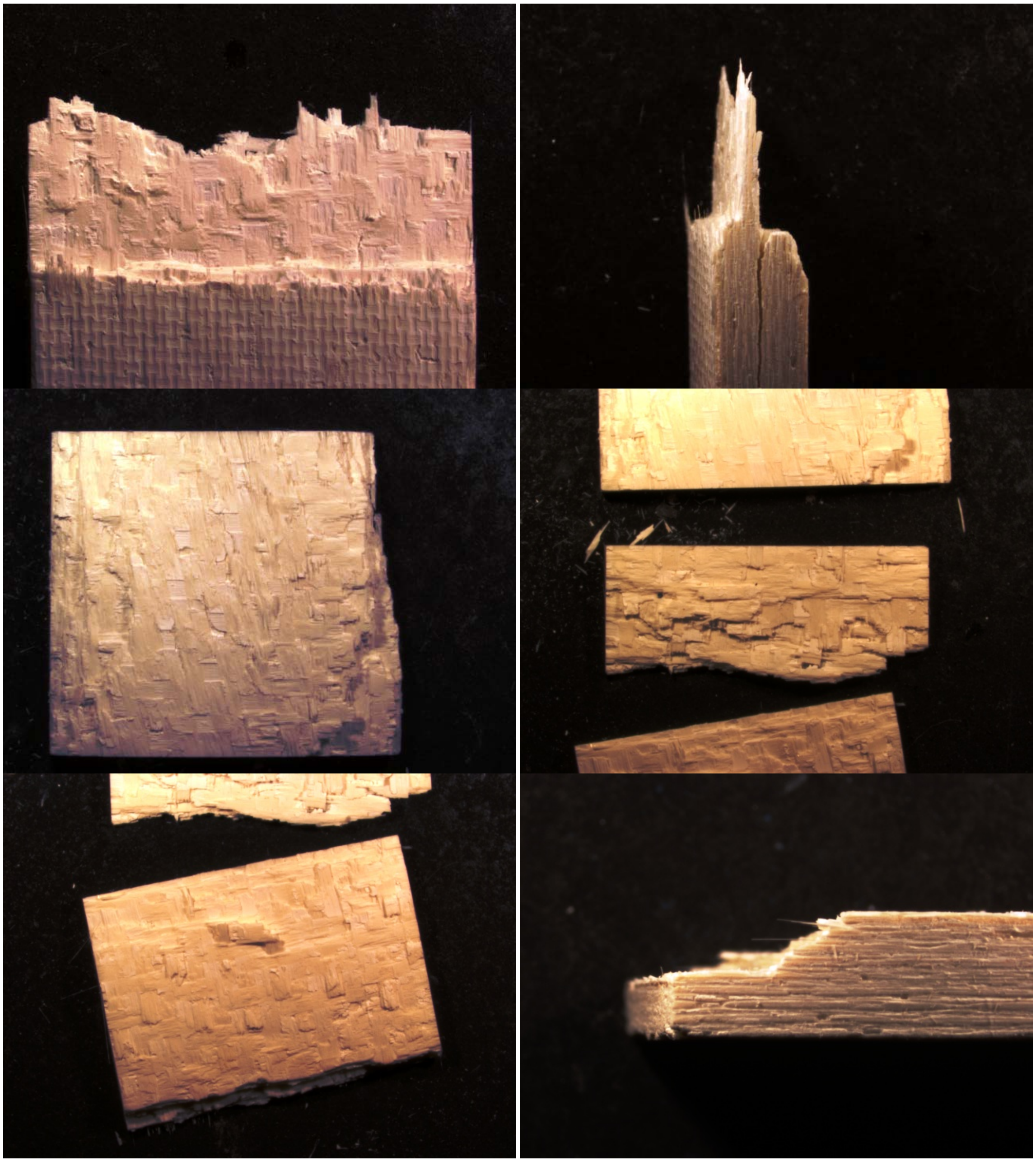

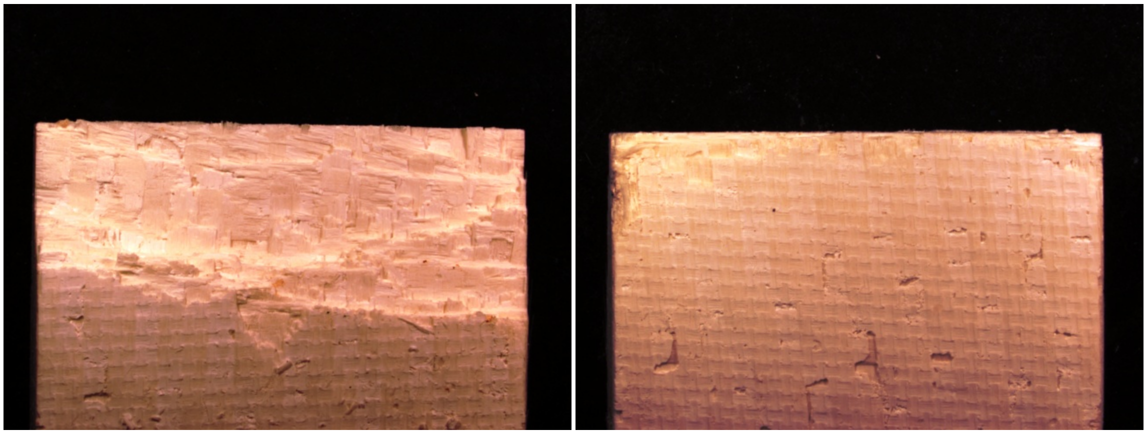

Appendix L: Optical Micrographs of Specimen 11

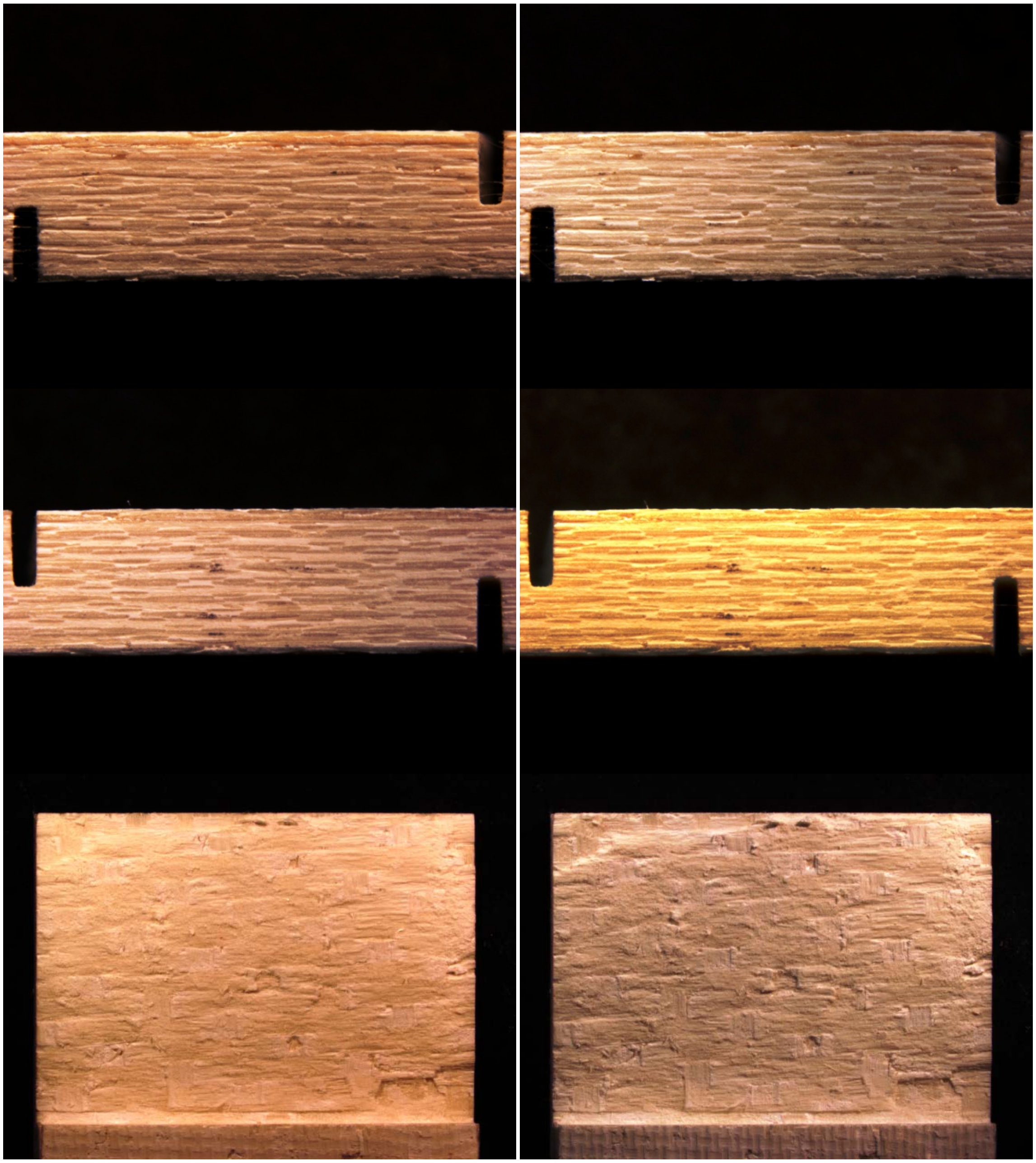

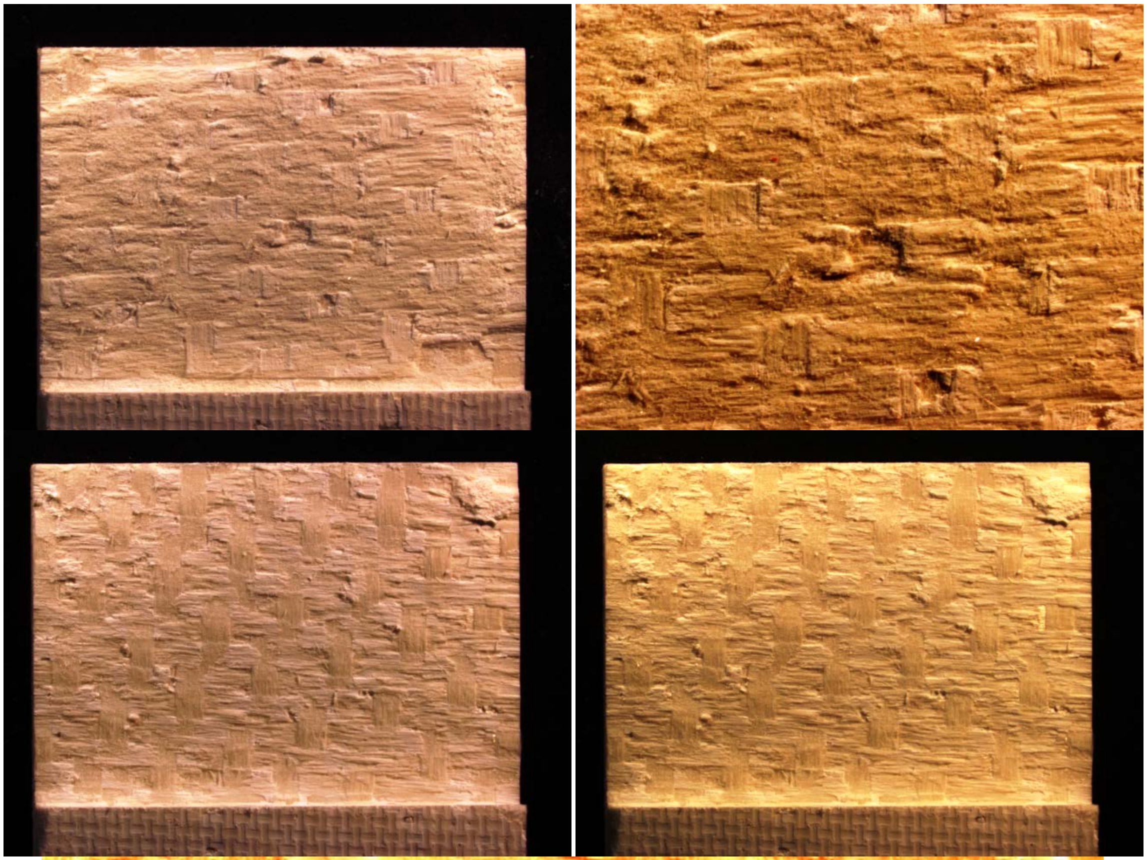

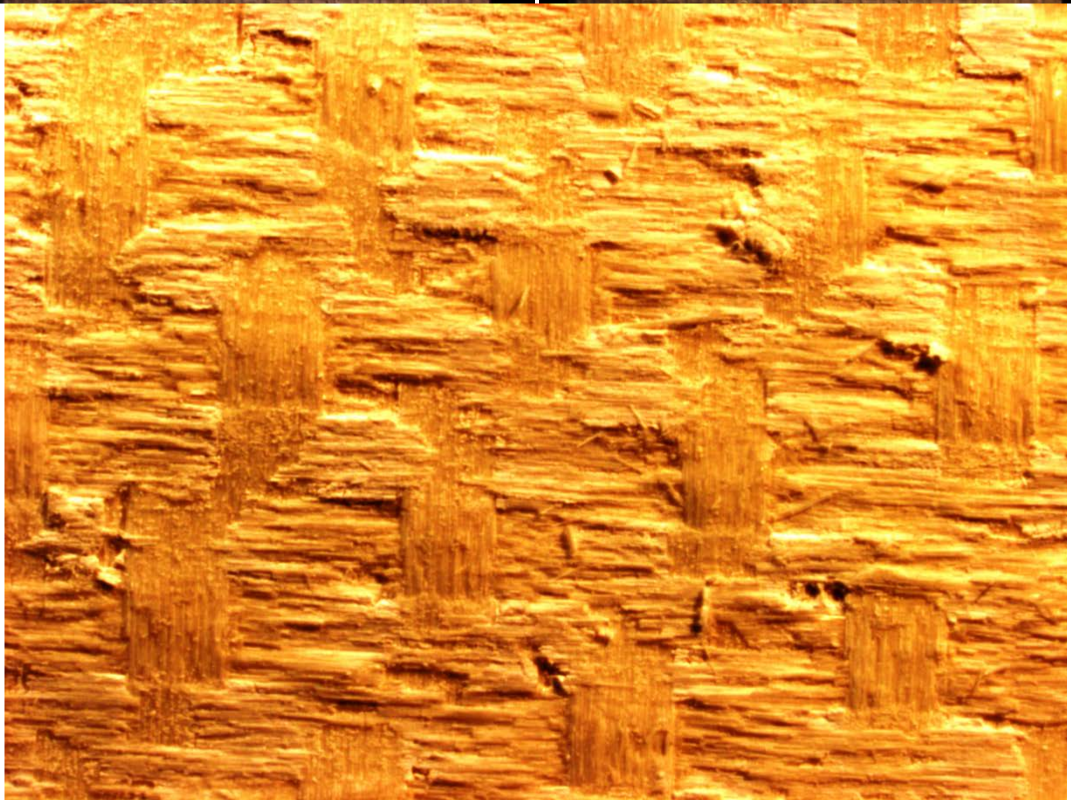

Appendix M: Optical Micrographs of Specimen 12

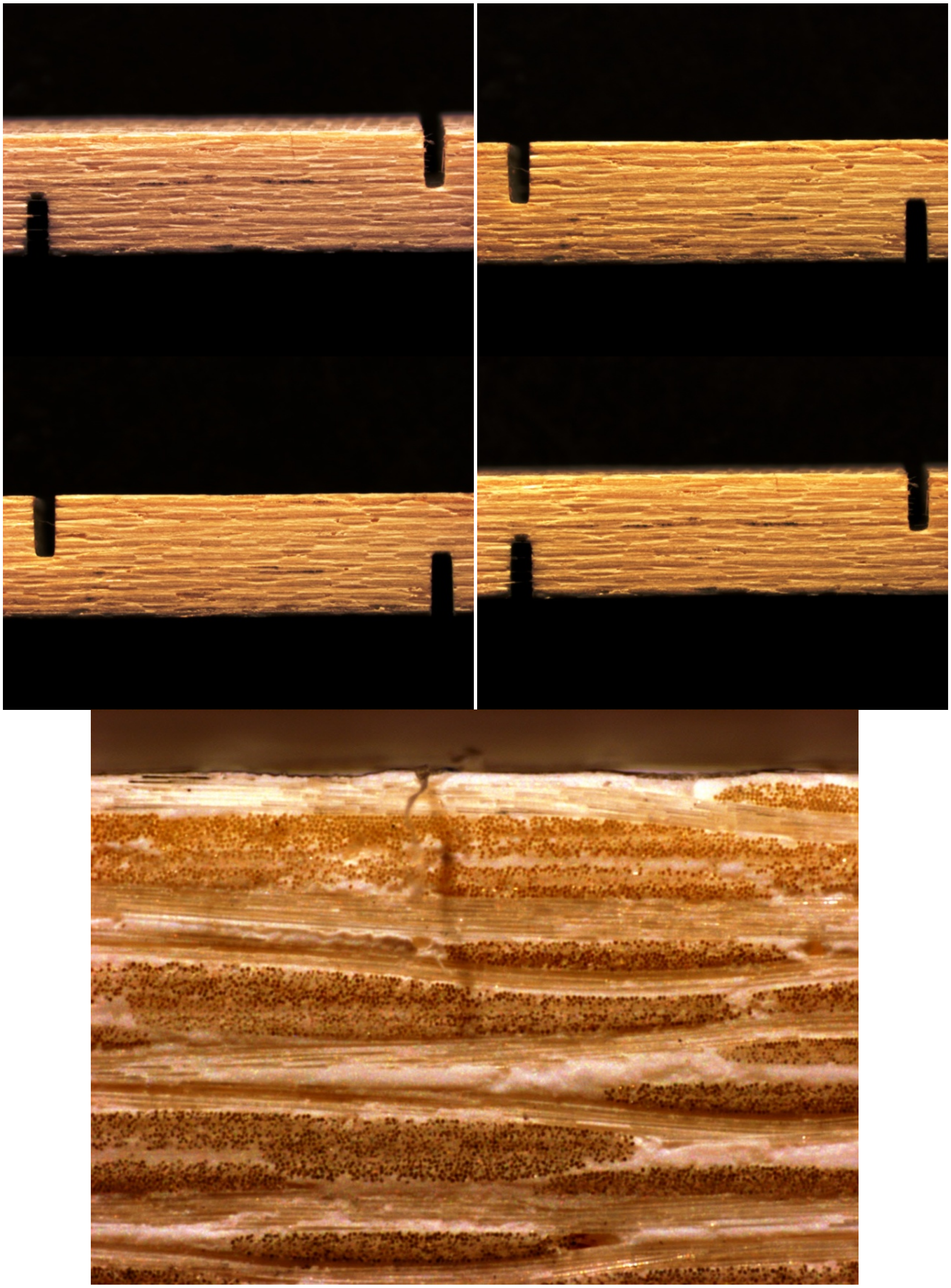

Appendix N: Optical Micrographs of Specimen 13

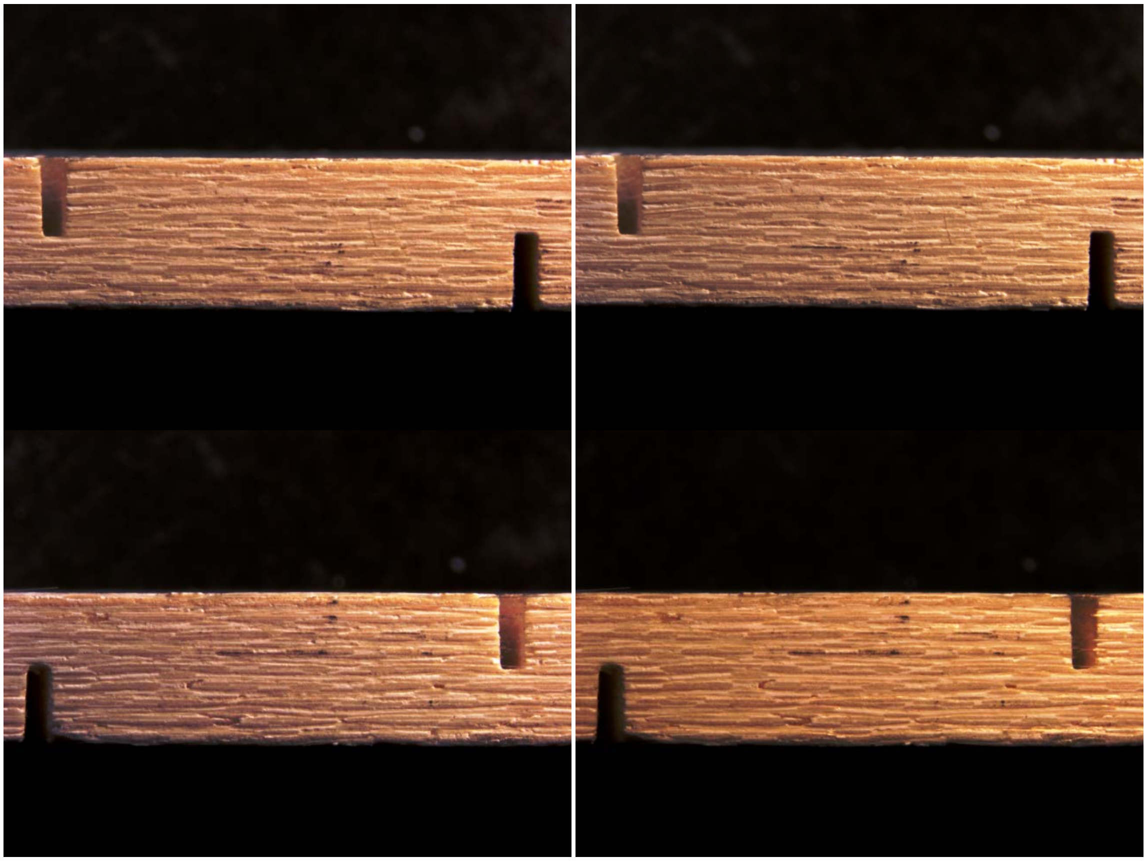

Appendix O: Optical Micrographs of Specimen 14

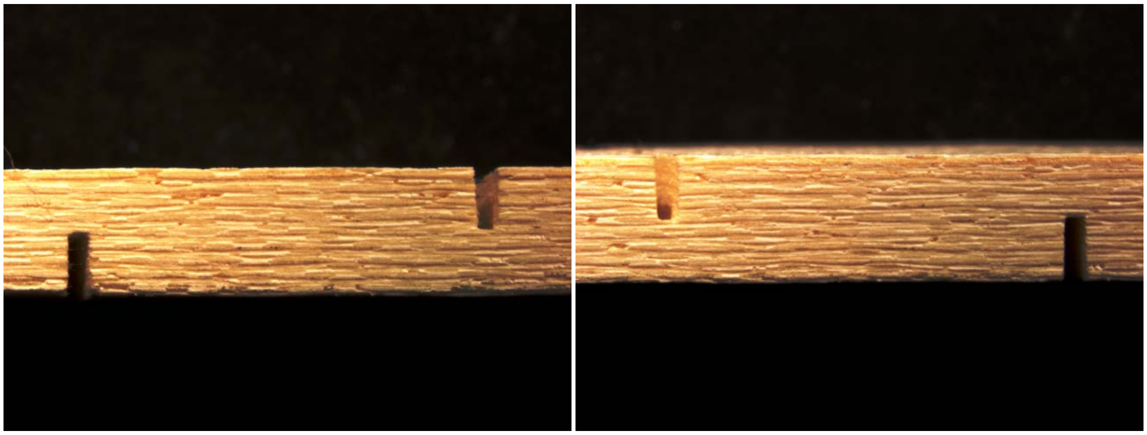

Appendix P: Optical Micrographs of Specimen 15

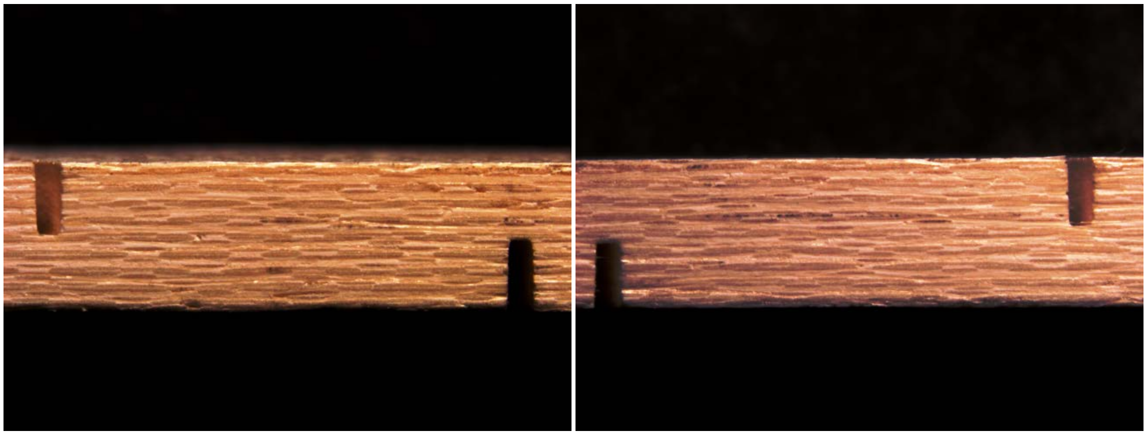

Appendix Q: SEM Images of Specimen 1 – DNS Compression to Failure in Air at 1100^{o}C

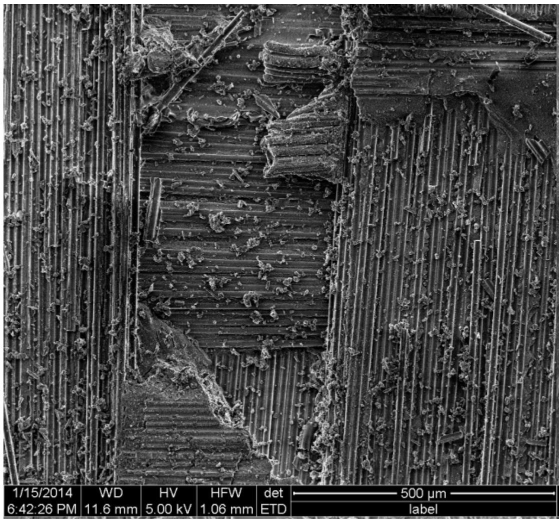
1/15/2014 6:42:26 PM
WD 11.6 mm
HV 5.00 kV
HFW 1.06 mm
det ETD
500 µm
label

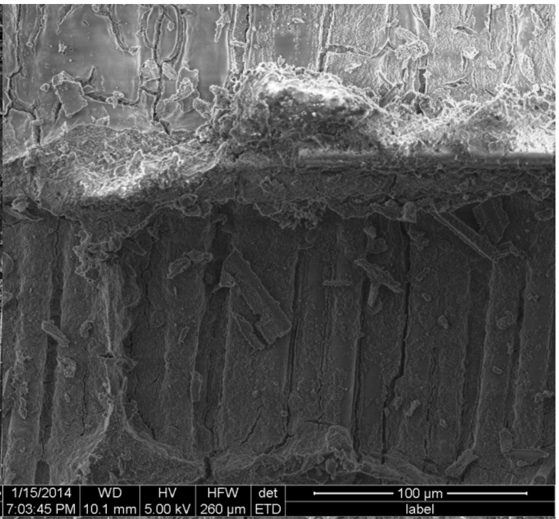
1/15/2014 7:03:45 PM
WD 10.1 mm
HV 5.00 kV
HFW 260 µm
det ETD
100 µm
label

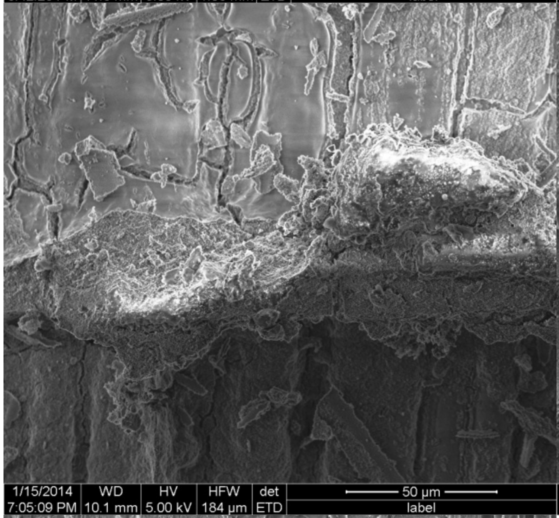
1/15/2014 7:05:09 PM
WD 10.1 mm
HV 5.00 kV
HFW 184 µm
det ETD
50 µm
label

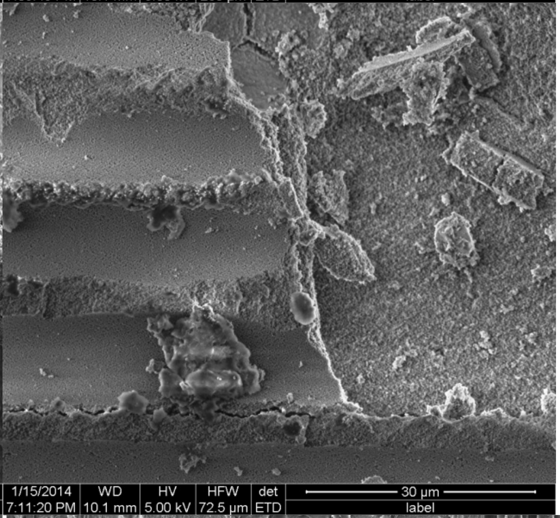
1/15/2014 7:11:20 PM
WD 10.1 mm
HV 5.00 kV
HFW 72.5 µm
det ETD
30 µm
label

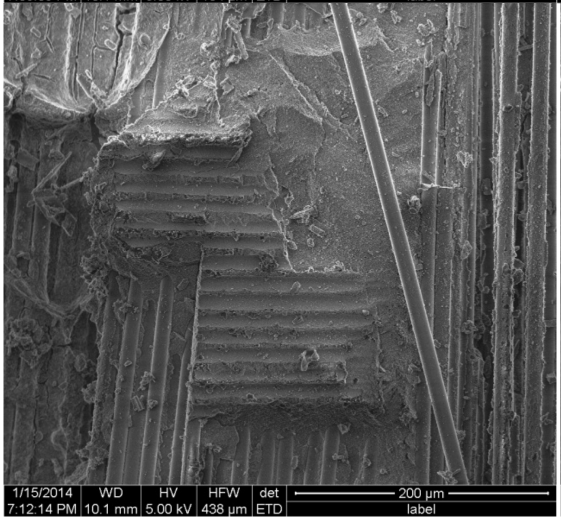
1/15/2014 7:12:14 PM
WD 10.1 mm
HV 5.00 kV
HFW 438 µm
det ETD
200 µm
label

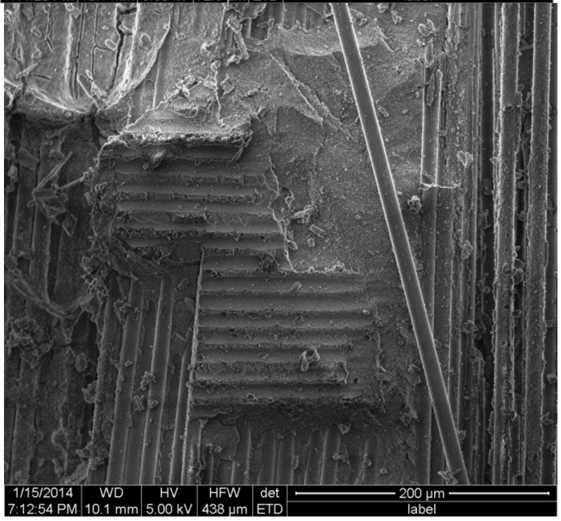
1/15/2014 7:12:54 PM
WD 10.1 mm
HV 5.00 kV
HFW 438 µm
det ETD
200 µm
label

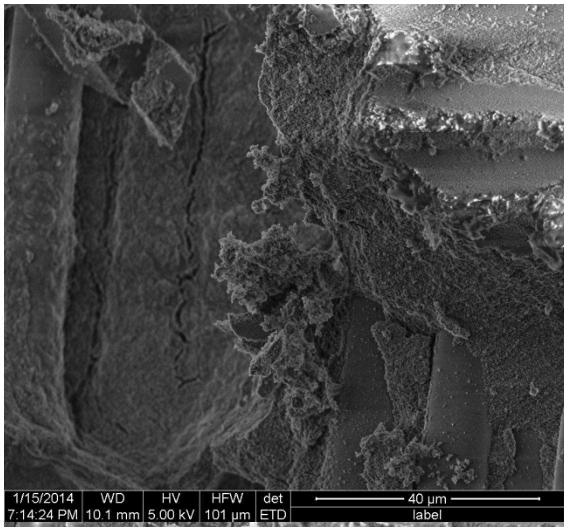
1/15/2014
7:14:24 PM
WD
10.1 mm
HV
5.00 kV
HFW
101 µm
det
ETD
40 µm
label

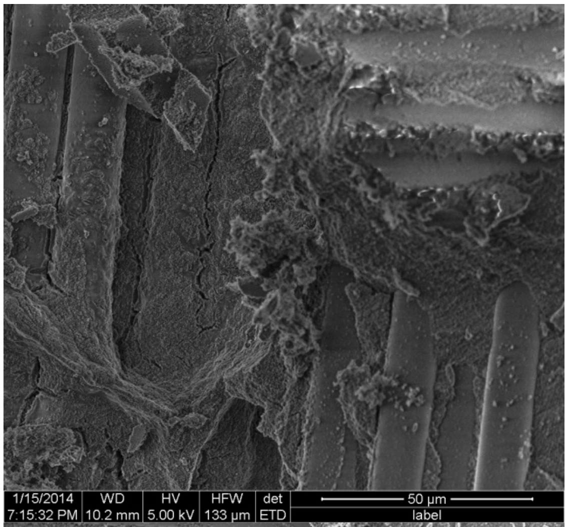
1/15/2014
7:15:32 PM
WD
10.2 mm
HV
5.00 kV
HFW
133 µm
det
ETD
50 µm
label

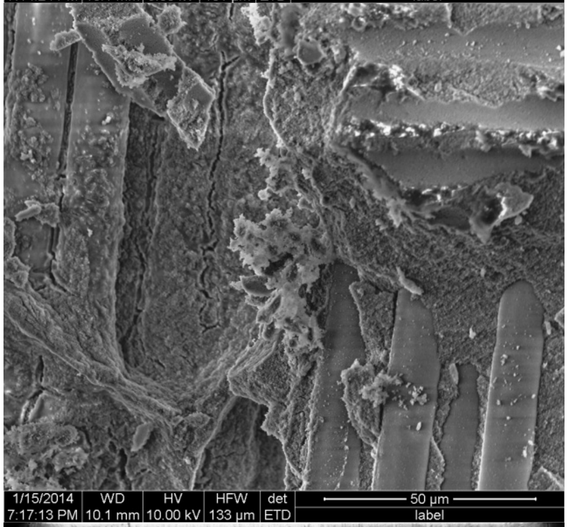
1/15/2014
7:17:13 PM
WD
10.1 mm
HV
10.00 kV
HFW
133 µm
det
ETD
50 µm
label

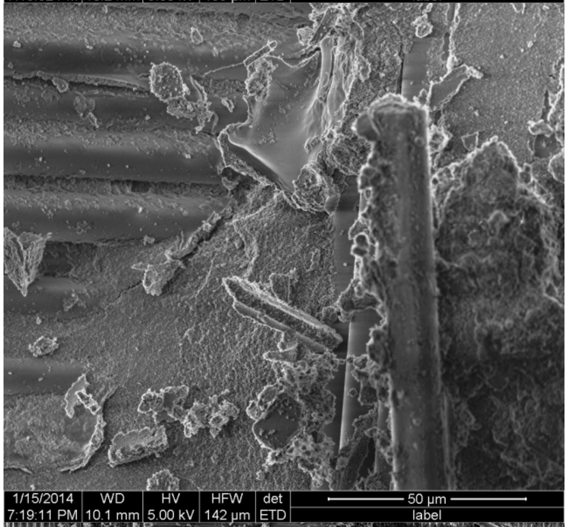
1/15/2014
7:19:11 PM
WD
10.1 mm
HV
5.00 kV
HFW
142 µm
det
ETD
50 µm
label

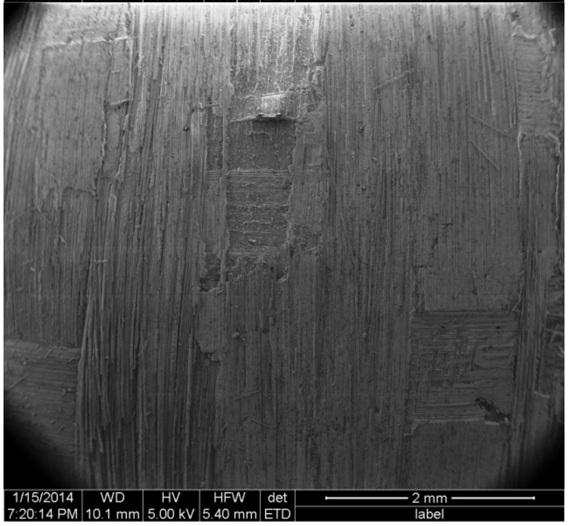
1/15/2014
7:20:14 PM
WD
10.1 mm
HV
5.00 kV
HFW
5.40 mm
det
ETD
2 mm
label

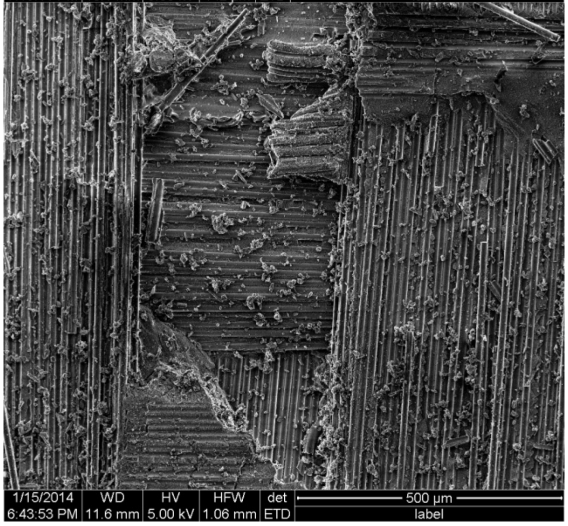
1/15/2014
6:43:53 PM
WD
11.6 mm
HV
5.00 kV
HFW
1.06 mm
det
ETD
500 µm
label

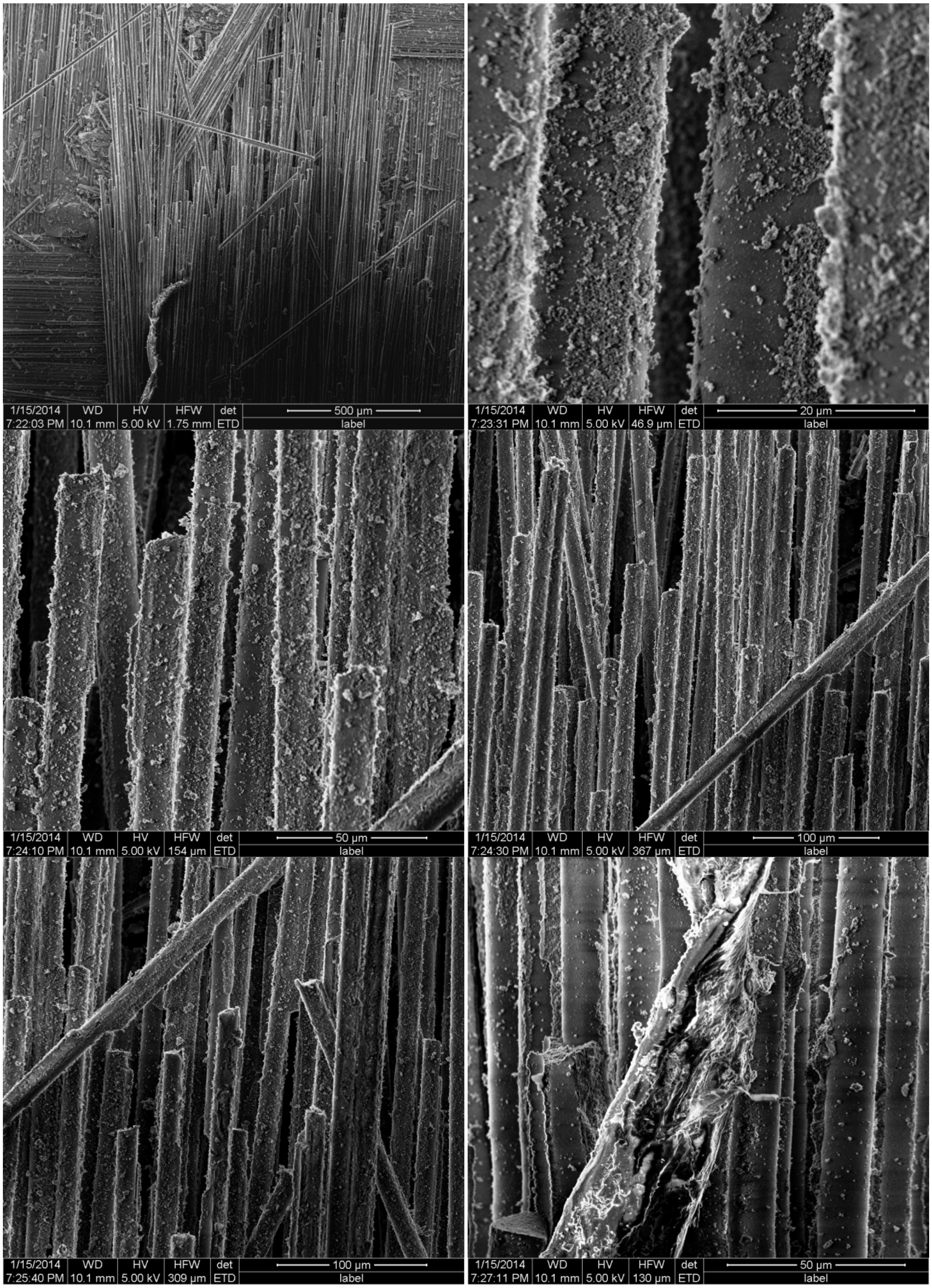
1/15/2014 7:22:03 PM | WD 10.1 mm | HV 5.00 kV | HFW 1.75 mm | det ETD | 500 µm | label
1/15/2014 7:23:31 PM | WD 10.1 mm | HV 5.00 kV | HFW 46.9 µm | det ETD | 20 µm | label
1/15/2014 7:24:10 PM | WD 10.1 mm | HV 5.00 kV | HFW 154 µm | det ETD | 50 µm | label
1/15/2014 7:24:30 PM | WD 10.1 mm | HV 5.00 kV | HFW 367 µm | det ETD | 100 µm | label
1/15/2014 7:25:40 PM | WD 10.1 mm | HV 5.00 kV | HFW 309 µm | det ETD | 100 µm | label
1/15/2014 7:27:11 PM | WD 10.1 mm | HV 5.00 kV | HFW 130 µm | det ETD | 50 µm | label

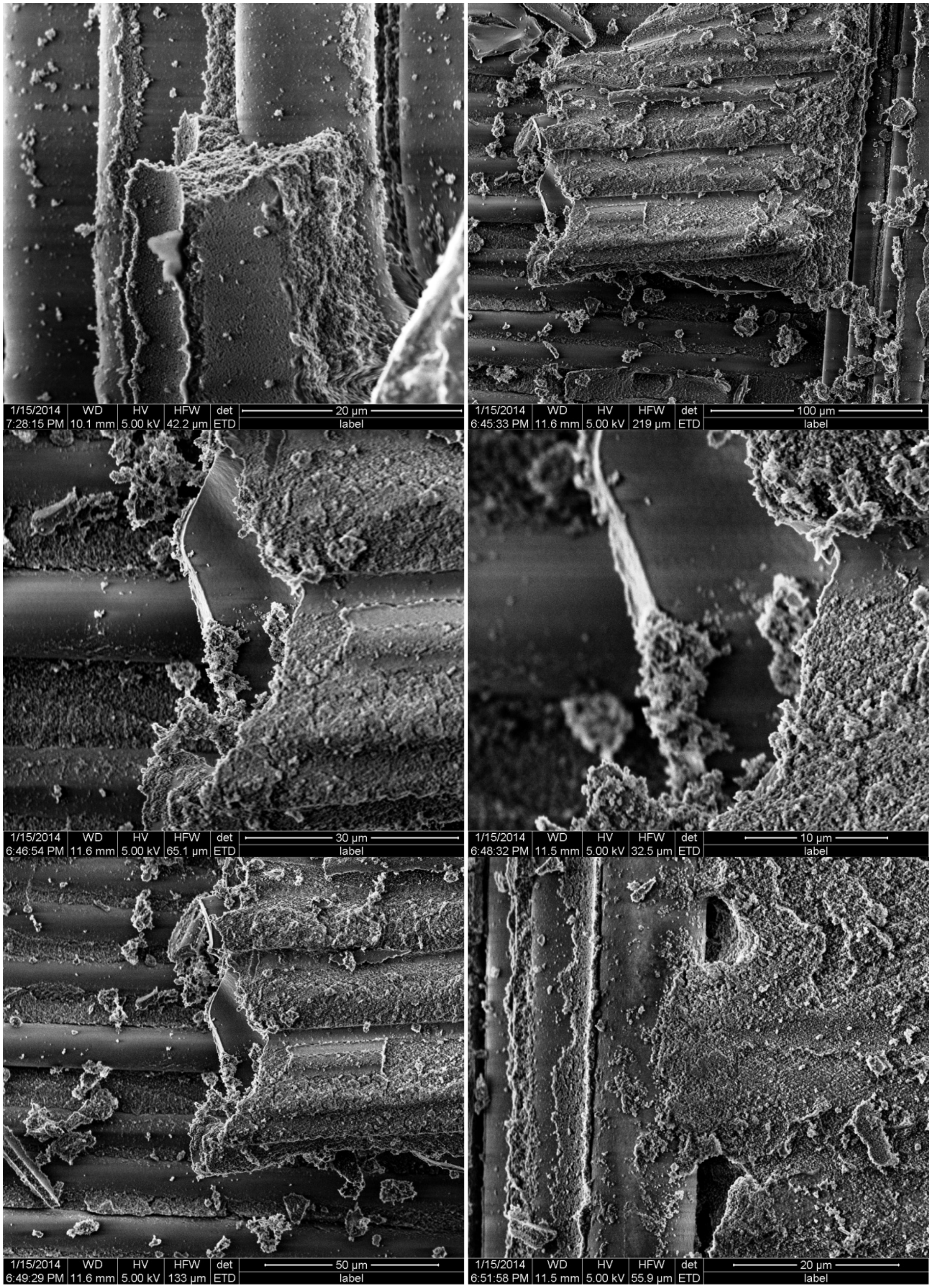
1/15/2014 7:28:15 PM | WD 10.1 mm | HV 5.00 kV | HFW 42.2 µm | det ETD | 20 µm | label
1/15/2014 6:45:33 PM | WD 11.6 mm | HV 5.00 kV | HFW 219 µm | det ETD | 100 µm | label
1/15/2014 6:46:54 PM | WD 11.6 mm | HV 5.00 kV | HFW 65.1 µm | det ETD | 30 µm | label
1/15/2014 6:48:32 PM | WD 11.5 mm | HV 5.00 kV | HFW 32.5 µm | det ETD | 10 µm | label
1/15/2014 6:49:29 PM | WD 11.6 mm | HV 5.00 kV | HFW 133 µm | det ETD | 50 µm | label
1/15/2014 6:51:58 PM | WD 11.5 mm | HV 5.00 kV | HFW 55.9 µm | det ETD | 20 µm | label

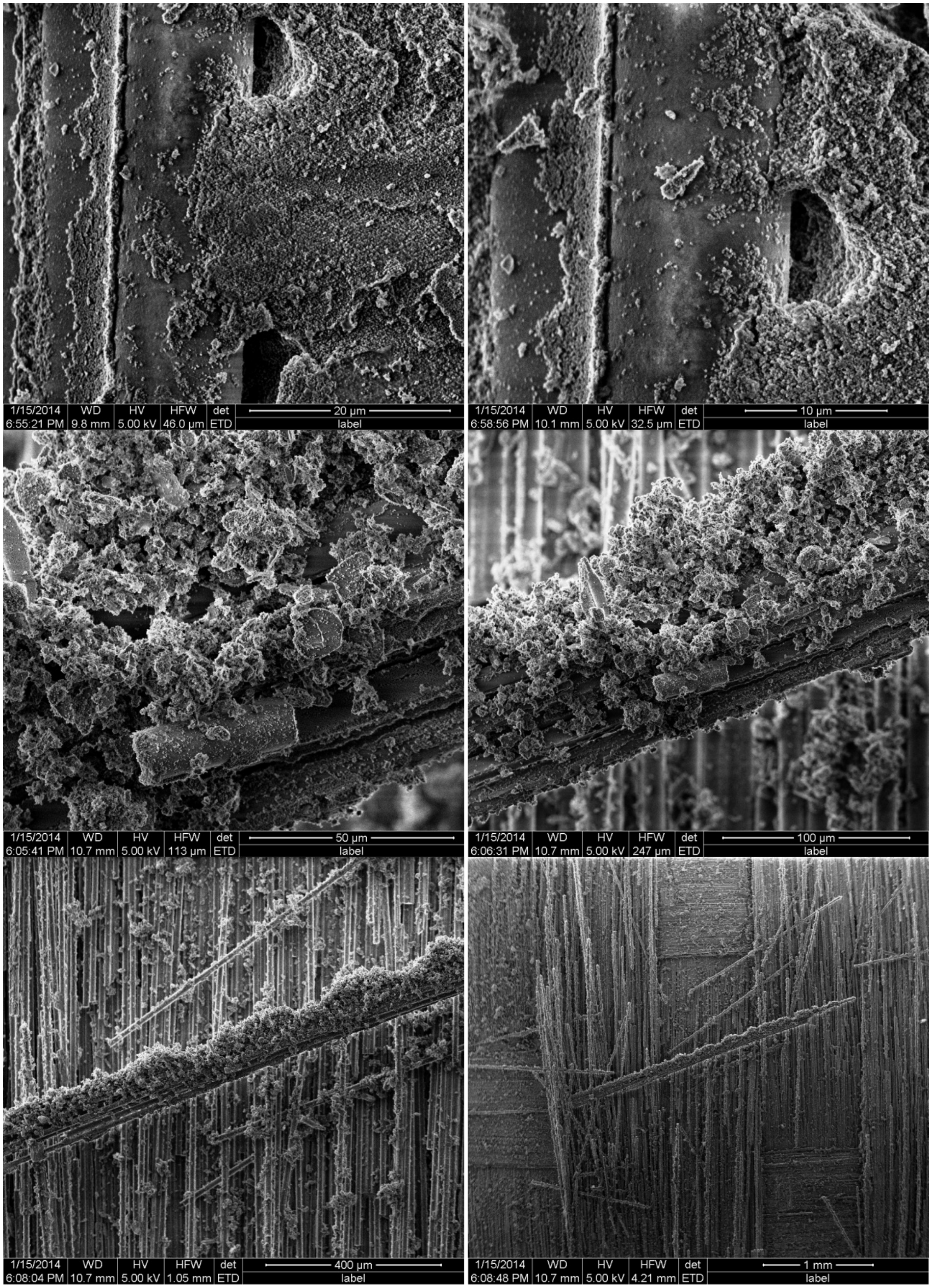
1/15/2014 6:55:21 PM WD 9.8 mm HV 5.00 kV HFW 46.0 µm det ETD 20 µm label
1/15/2014 6:58:56 PM WD 10.1 mm HV 5.00 kV HFW 32.5 µm det ETD 10 µm label
1/15/2014 6:05:41 PM WD 10.7 mm HV 5.00 kV HFW 113 µm det ETD 50 µm label
1/15/2014 6:06:31 PM WD 10.7 mm HV 5.00 kV HFW 247 µm det ETD 100 µm label
1/15/2014 6:08:04 PM WD 10.7 mm HV 5.00 kV HFW 1.05 mm det ETD 400 µm label
1/15/2014 6:08:48 PM WD 10.7 mm HV 5.00 kV HFW 4.21 mm det ETD 1 mm label

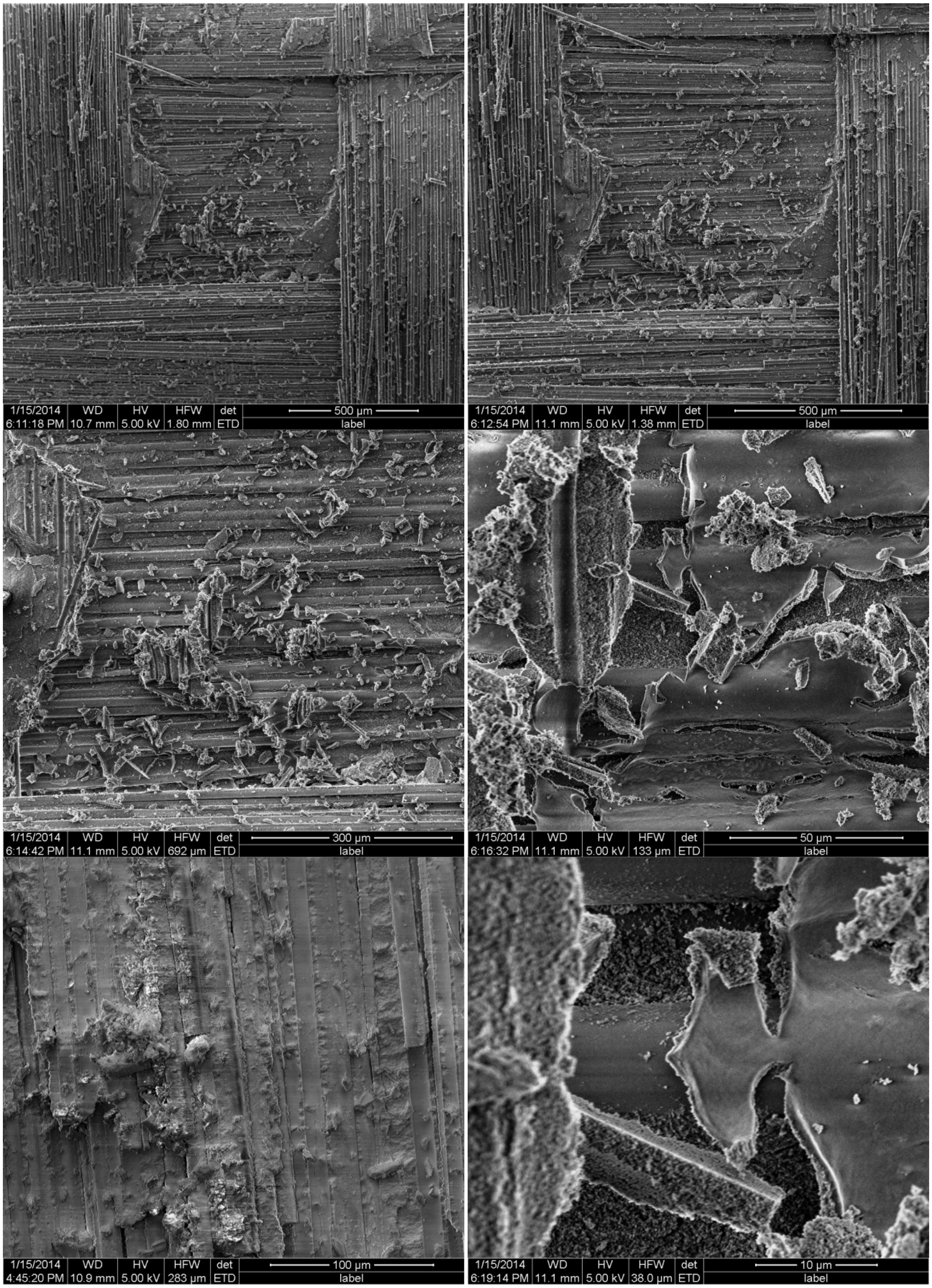
1/15/2014 6:11:18 PM | WD 10.7 mm | HV 5.00 kV | HFW 1.80 mm | det ETD | 500 µm | label
1/15/2014 6:12:54 PM | WD 11.1 mm | HV 5.00 kV | HFW 1.38 mm | det ETD | 500 µm | label
1/15/2014 6:14:42 PM | WD 11.1 mm | HV 5.00 kV | HFW 692 µm | det ETD | 300 µm | label
1/15/2014 6:16:32 PM | WD 11.1 mm | HV 5.00 kV | HFW 133 µm | det ETD | 50 µm | label
1/15/2014 4:45:20 PM | WD 10.9 mm | HV 5.00 kV | HFW 283 µm | det ETD | 100 µm | label
1/15/2014 6:19:14 PM | WD 11.1 mm | HV 5.00 kV | HFW 38.0 µm | det ETD | 10 µm | label

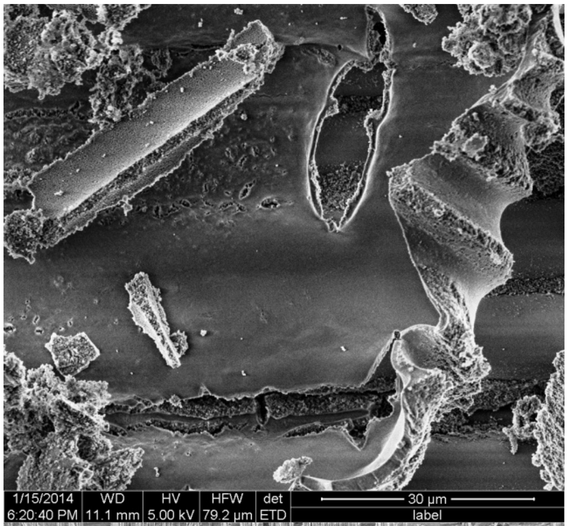
1/15/2014
6:20:40 PM
WD
11.1 mm
HV
5.00 kV
HFW
79.2 µm
det
ETD
30 µm
label

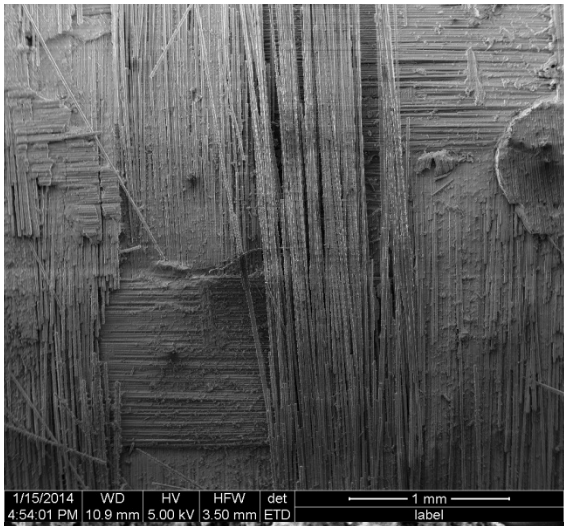
1/15/2014
4:54:01 PM
WD
10.9 mm
HV
5.00 kV
HFW
3.50 mm
det
ETD
1 mm
label

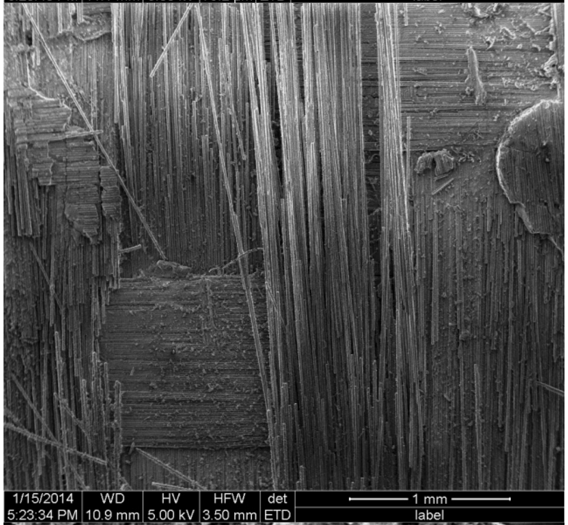
1/15/2014
5:23:34 PM
WD
10.9 mm
HV
5.00 kV
HFW
3.50 mm
det
ETD
1 mm
label

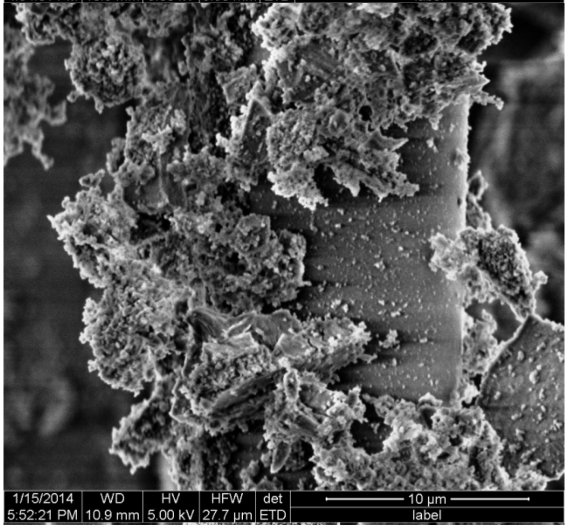
1/15/2014
5:52:21 PM
WD
10.9 mm
HV
5.00 kV
HFW
27.7 µm
det
ETD
10 µm
label

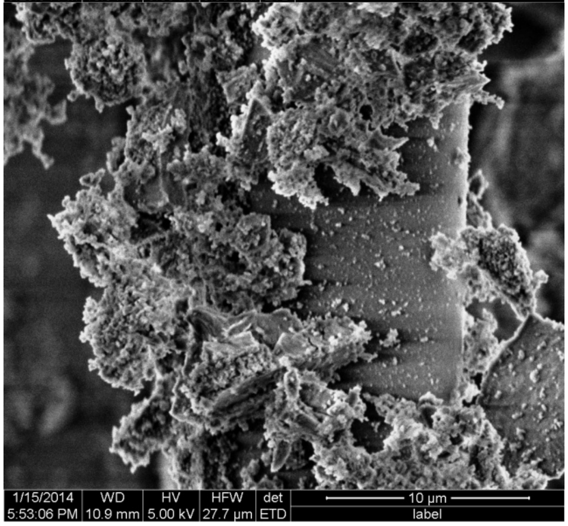
1/15/2014
5:53:06 PM
WD
10.9 mm
HV
5.00 kV
HFW
27.7 µm
det
ETD
10 µm
label

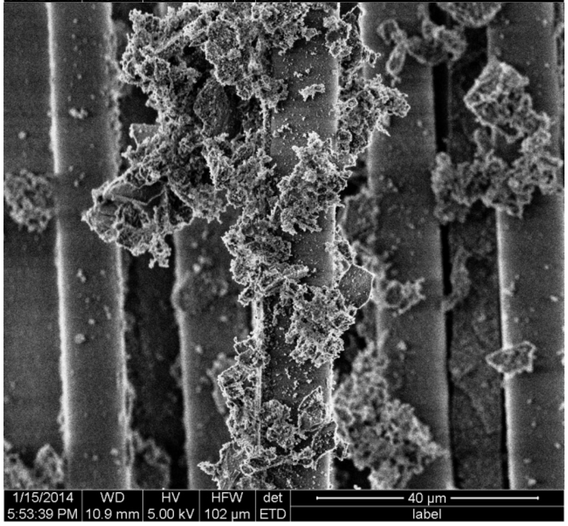
1/15/2014
5:53:39 PM
WD
10.9 mm
HV
5.00 kV
HFW
102 µm
det
ETD
40 µm
label

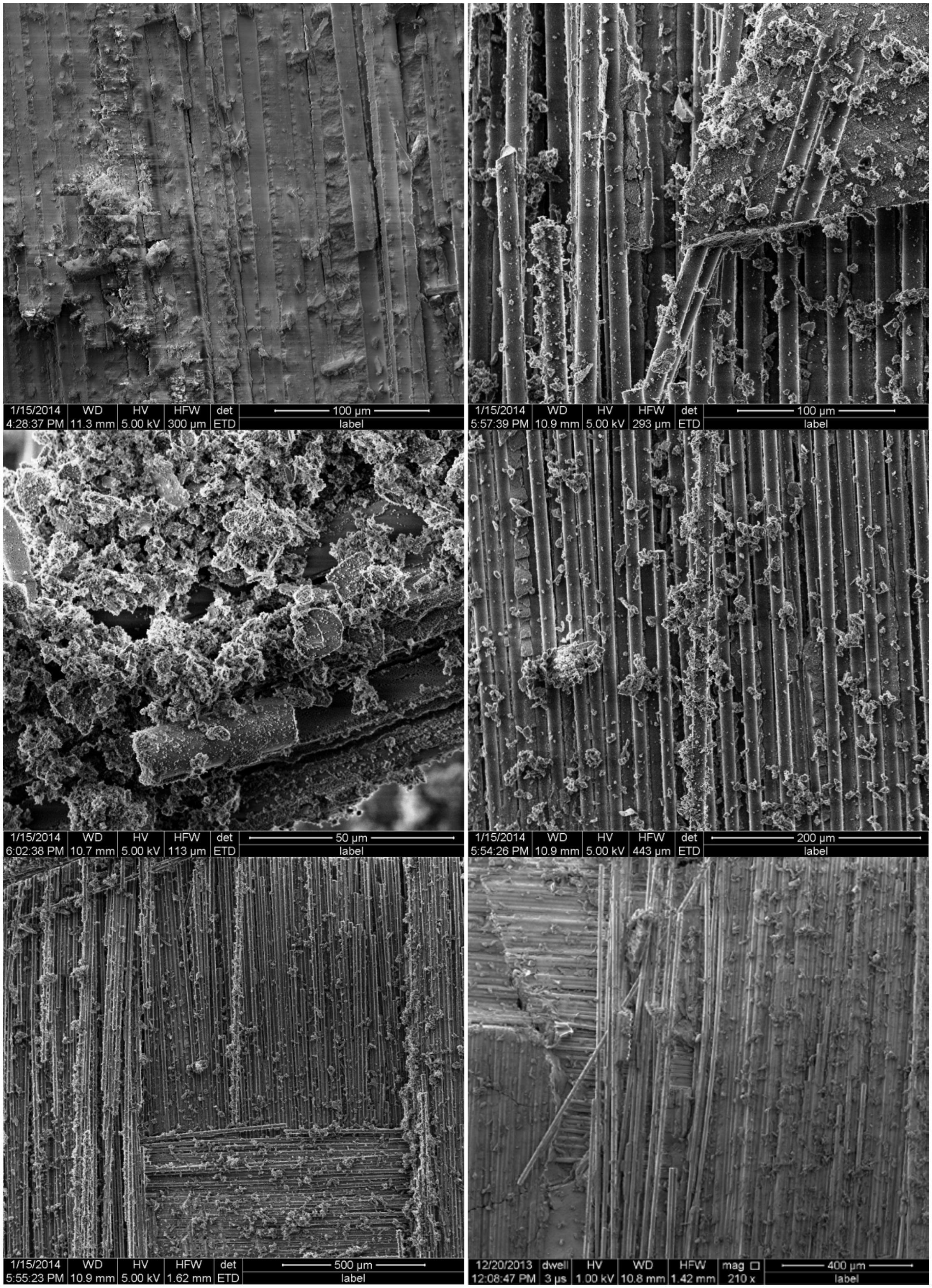
1/15/2014 4:28:37 PM | WD 11.3 mm | HV 5.00 kV | HFW 300 µm | det ETD | 100 µm | label
1/15/2014 5:57:39 PM | WD 10.9 mm | HV 5.00 kV | HFW 293 µm | det ETD | 100 µm | label
1/15/2014 6:02:38 PM | WD 10.7 mm | HV 5.00 kV | HFW 113 µm | det ETD | 50 µm | label
1/15/2014 5:54:26 PM | WD 10.9 mm | HV 5.00 kV | HFW 443 µm | det ETD | 200 µm | label
1/15/2014 5:55:23 PM | WD 10.9 mm | HV 5.00 kV | HFW 1.62 mm | det ETD | 500 µm | label
12/20/2013 12:08:47 PM | dwell 3 µs | HV 1.00 kV | WD 10.8 mm | HFW 1.42 mm | mag □ 210 x | 400 µm | label

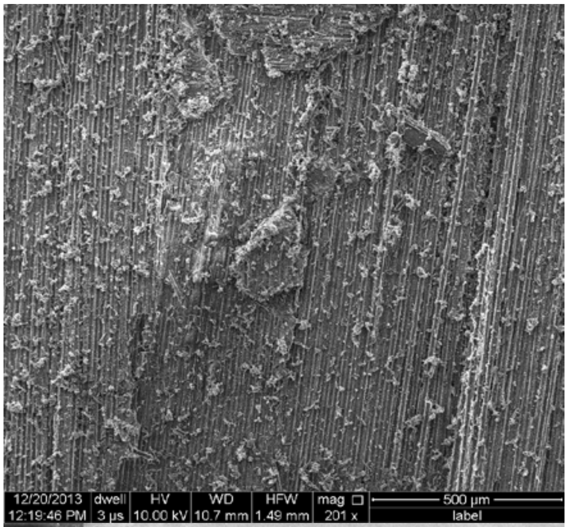
12/20/2013
dwell
HV
WD
HFW
mag □
500 µm
12:19:46 PM
3 µs
10.00 kV
10.7 mm
1.49 mm
201 x
label

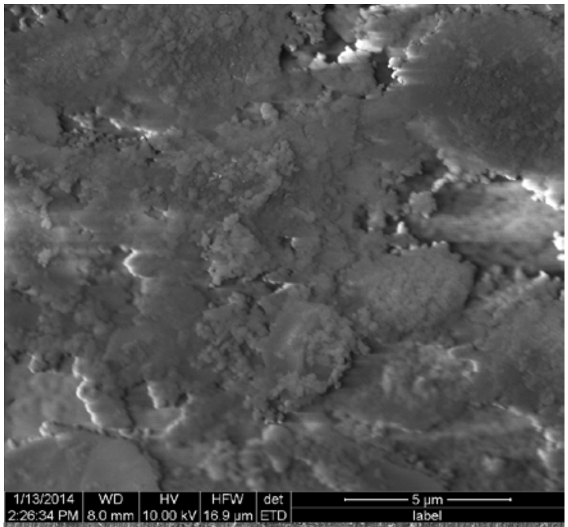
1/13/2014
WD
HV
HFW
det
5 µm
2:26:34 PM
8.0 mm
10.00 kV
16.9 µm
ETD
label

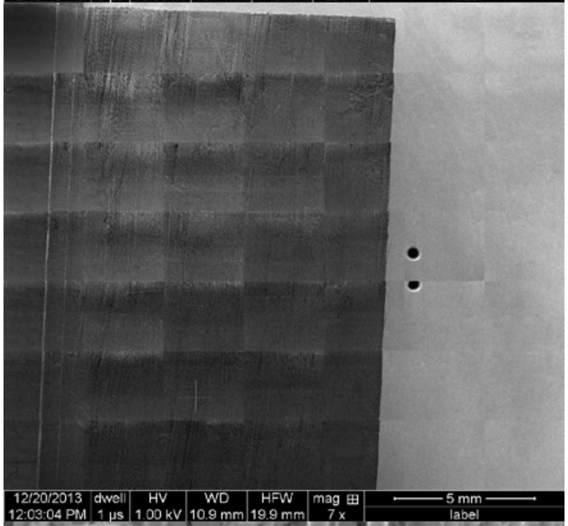
12/20/2013
dwell
HV
WD
HFW
mag ⊞
5 mm
12:03:04 PM
1 µs
1.00 kV
10.9 mm
19.9 mm
7 x
label

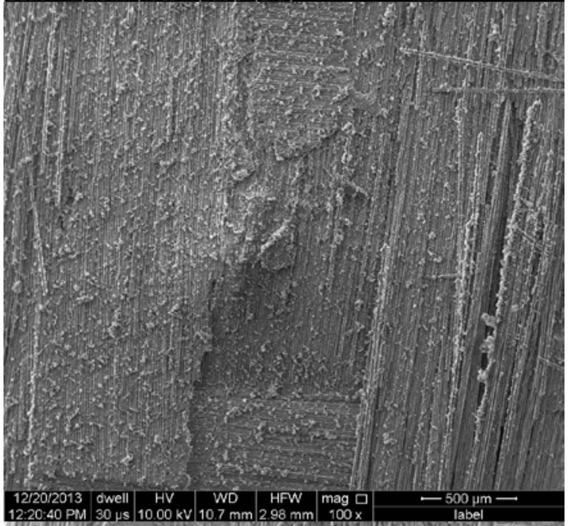
12/20/2013
dwell
HV
WD
HFW
mag □
500 µm
12:20:40 PM
30 µs
10.00 kV
10.7 mm
2.98 mm
100 x
label

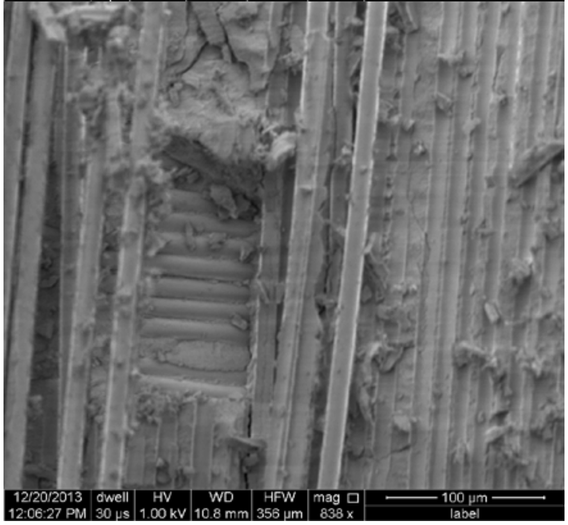
12/20/2013
dwell
HV
WD
HFW
mag □
100 µm
12:06:27 PM
30 µs
1.00 kV
10.8 mm
356 µm
838 x
label

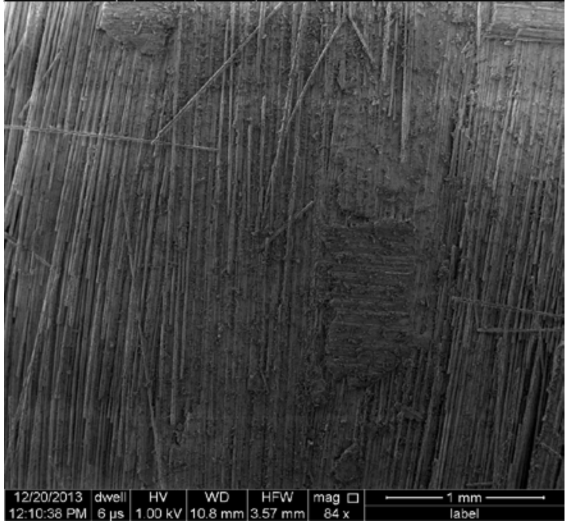
12/20/2013
dwell
HV
WD
HFW
mag □
1 mm
12:10:38 PM
6 µs
1.00 kV
10.8 mm
3.57 mm
84 x
label

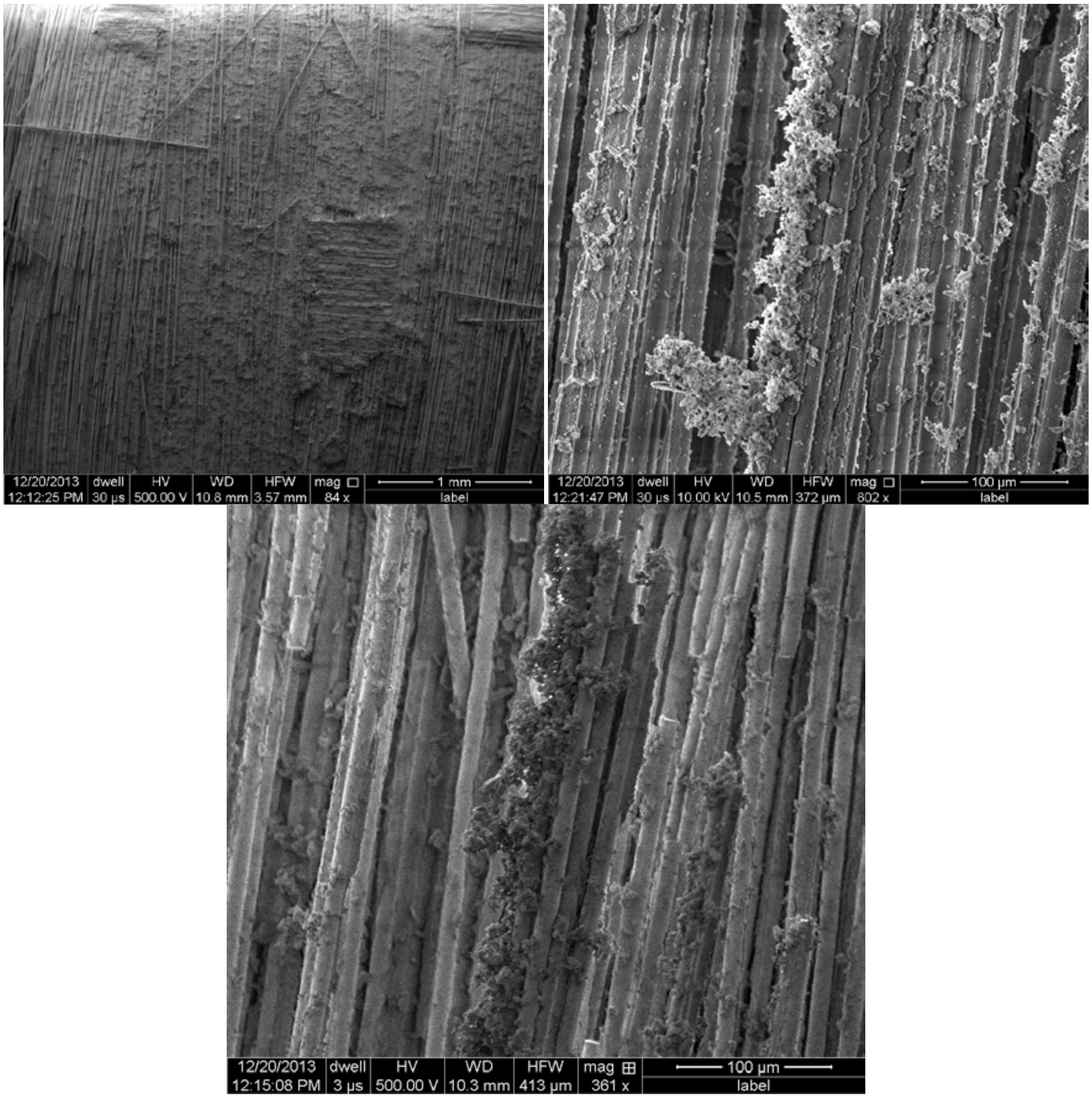
12/20/2013 12:12:25 PM | dwell 30 µs | HV 500.00 V | WD 10.8 mm | HFW 3.57 mm | mag □ 84 x | 1 mm | label
12/20/2013 12:21:47 PM | dwell 30 µs | HV 10.00 kV | WD 10.5 mm | HFW 372 µm | mag □ 802 x | 100 µm | label
12/20/2013 12:15:08 PM | dwell 3 µs | HV 500.00 V | WD 10.3 mm | HFW 413 µm | mag ⊞ 361 x | 100 µm | label

Appendix R: SEM Images of Specimen 5 – DNS Creep at 6 MPa in Air at 1100^{o}C.

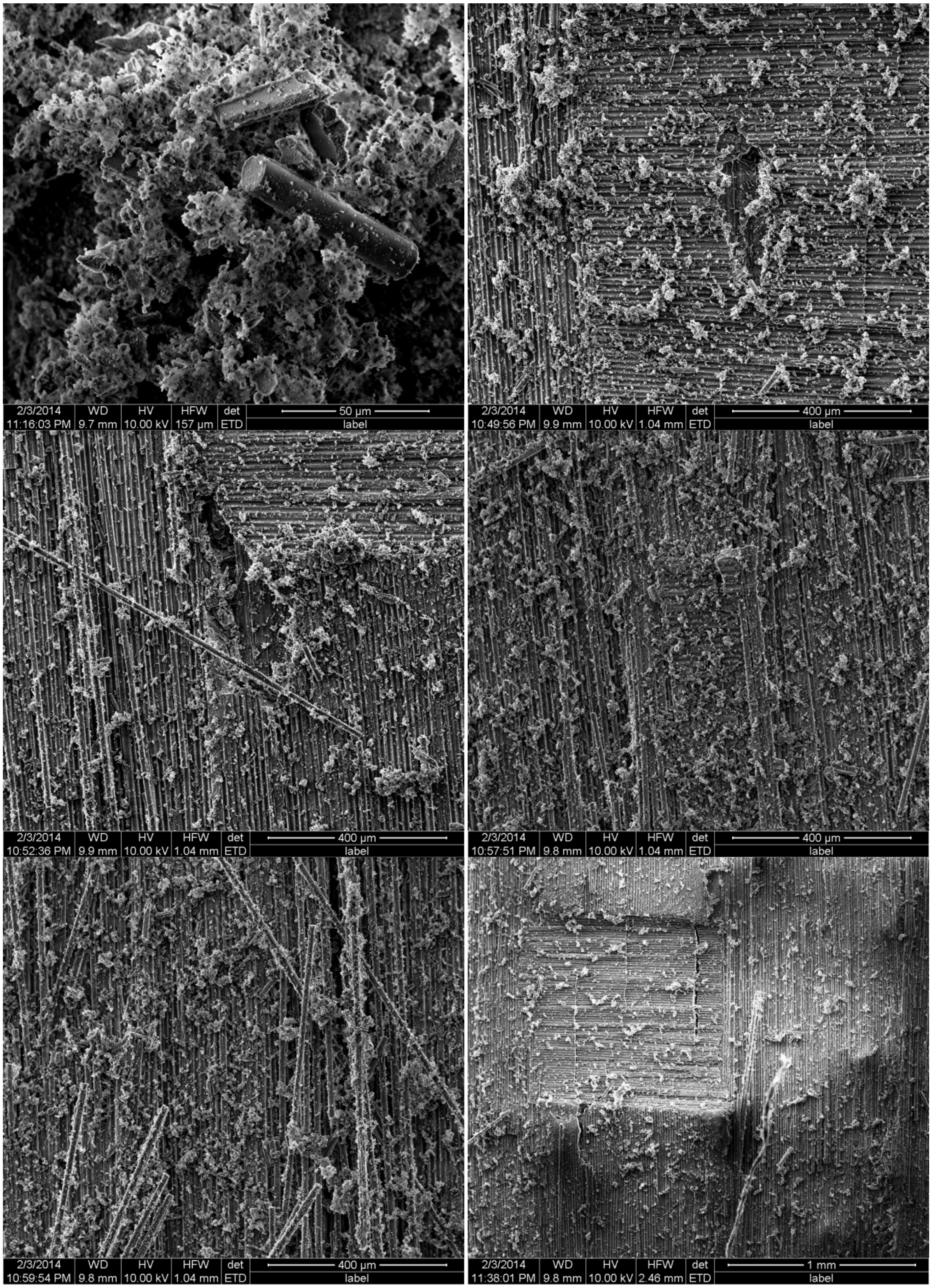
2/3/2014 11:16:03 PM | WD 9.7 mm | HV 10.00 kV | HFW 157 µm | det ETD | 50 µm | label
2/3/2014 10:49:56 PM | WD 9.9 mm | HV 10.00 kV | HFW 1.04 mm | det ETD | 400 µm | label
2/3/2014 10:52:36 PM | WD 9.9 mm | HV 10.00 kV | HFW 1.04 mm | det ETD | 400 µm | label
2/3/2014 10:57:51 PM | WD 9.8 mm | HV 10.00 kV | HFW 1.04 mm | det ETD | 400 µm | label
2/3/2014 10:59:54 PM | WD 9.8 mm | HV 10.00 kV | HFW 1.04 mm | det ETD | 400 µm | label
2/3/2014 11:38:01 PM | WD 9.8 mm | HV 10.00 kV | HFW 2.46 mm | det ETD | 1 mm | label

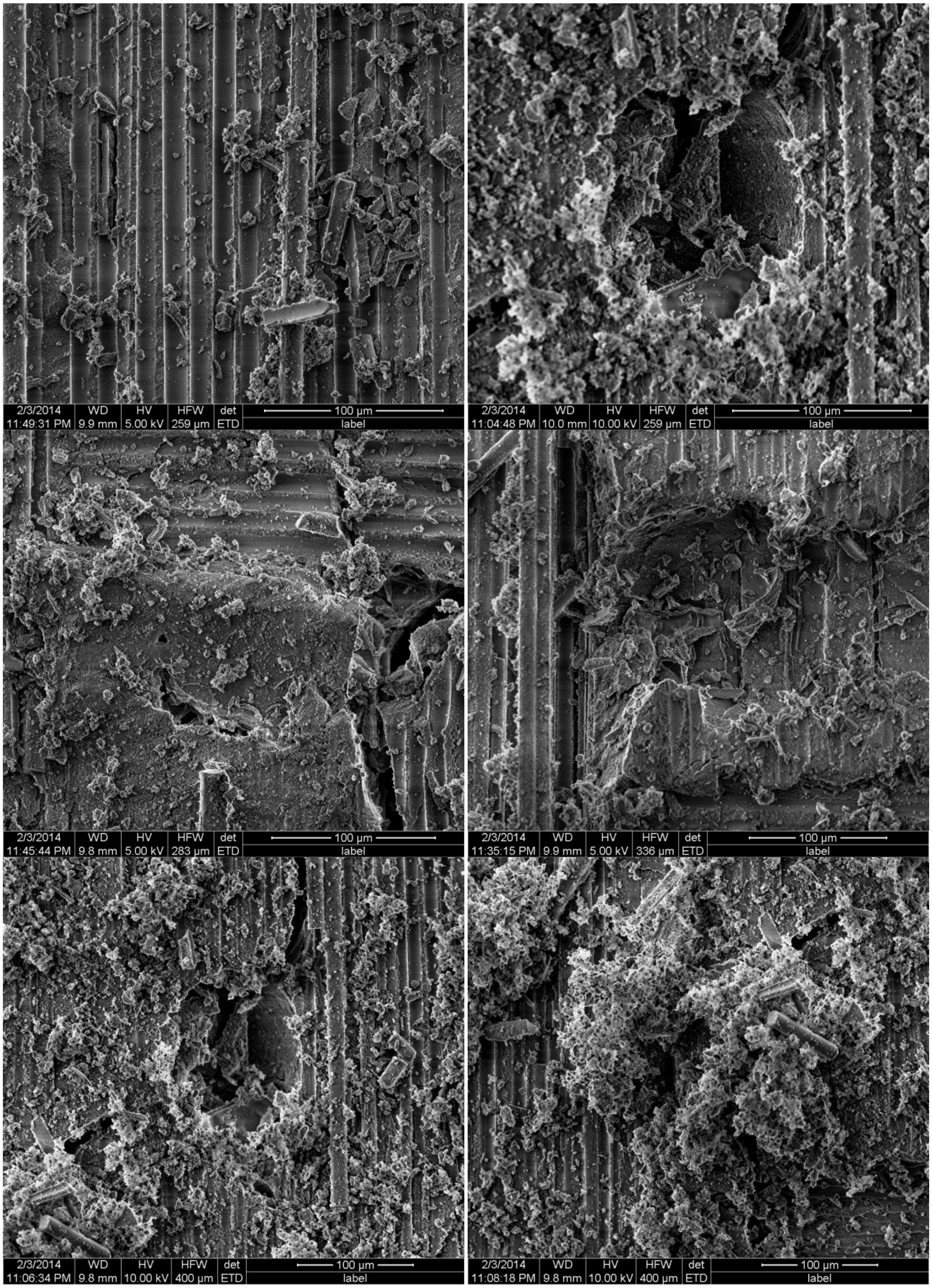
2/3/2014 11:49:31 PM | WD 9.9 mm | HV 5.00 kV | HFW 259 µm | det ETD | 100 µm | label
2/3/2014 11:04:48 PM | WD 10.0 mm | HV 10.00 kV | HFW 259 µm | det ETD | 100 µm | label
2/3/2014 11:45:44 PM | WD 9.8 mm | HV 5.00 kV | HFW 283 µm | det ETD | 100 µm | label
2/3/2014 11:35:15 PM | WD 9.9 mm | HV 5.00 kV | HFW 336 µm | det ETD | 100 µm | label
2/3/2014 11:06:34 PM | WD 9.8 mm | HV 10.00 kV | HFW 400 µm | det ETD | 100 µm | label
2/3/2014 11:08:18 PM | WD 9.8 mm | HV 10.00 kV | HFW 400 µm | det ETD | 100 µm | label

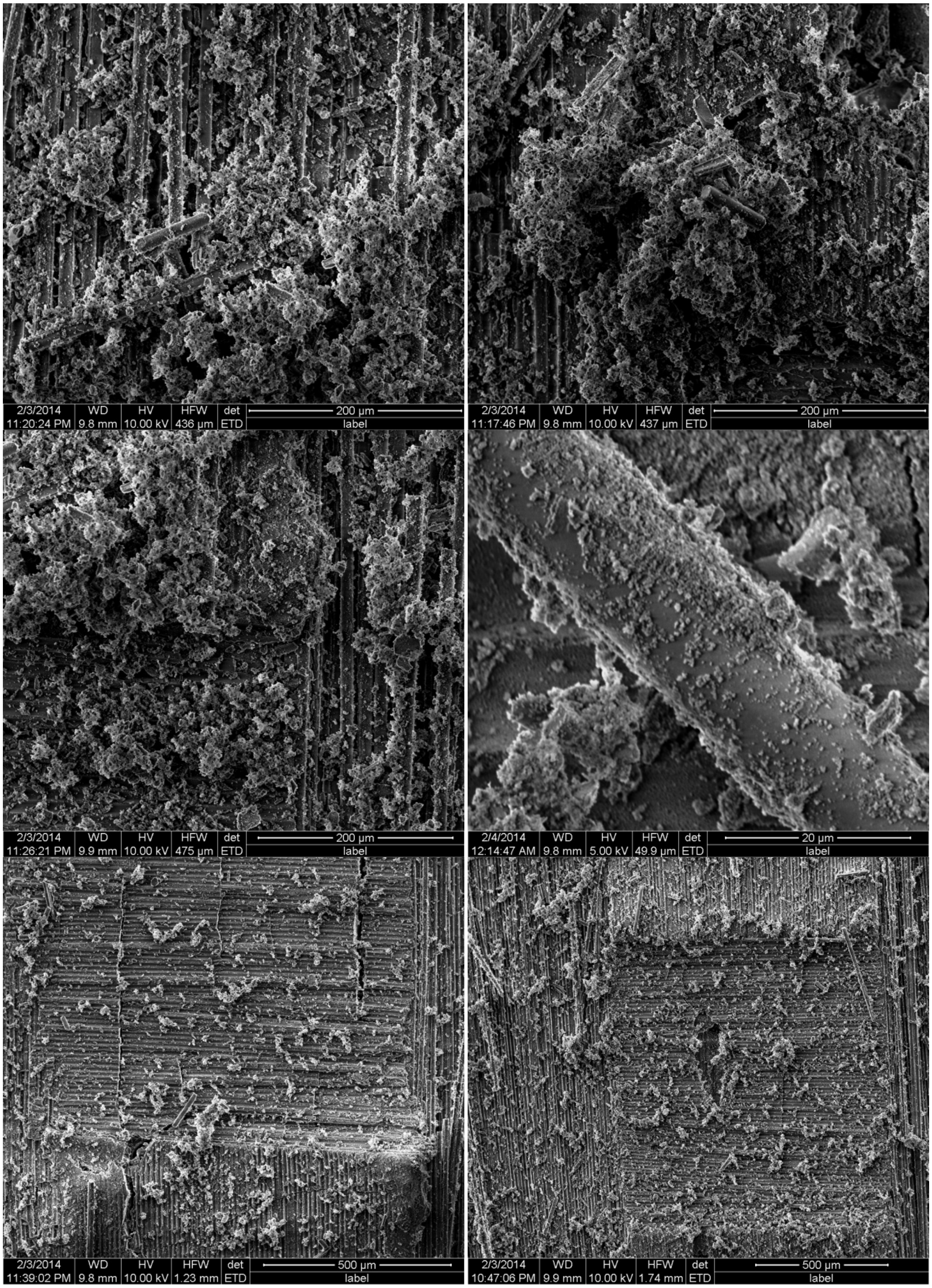
2/3/2014 11:20:24 PM WD 9.8 mm HV 10.00 kV HFW 436 μm det ETD 200 μm label
2/3/2014 11:17:46 PM WD 9.8 mm HV 10.00 kV HFW 437 μm det ETD 200 μm label
2/3/2014 11:26:21 PM WD 9.9 mm HV 10.00 kV HFW 475 μm det ETD 200 μm label
2/4/2014 12:14:47 AM WD 9.8 mm HV 5.00 kV HFW 49.9 μm det ETD 20 μm label
2/3/2014 11:39:02 PM WD 9.8 mm HV 10.00 kV HFW 1.23 mm det ETD 500 μm label
2/3/2014 10:47:06 PM WD 9.9 mm HV 10.00 kV HFW 1.74 mm det ETD 500 μm label

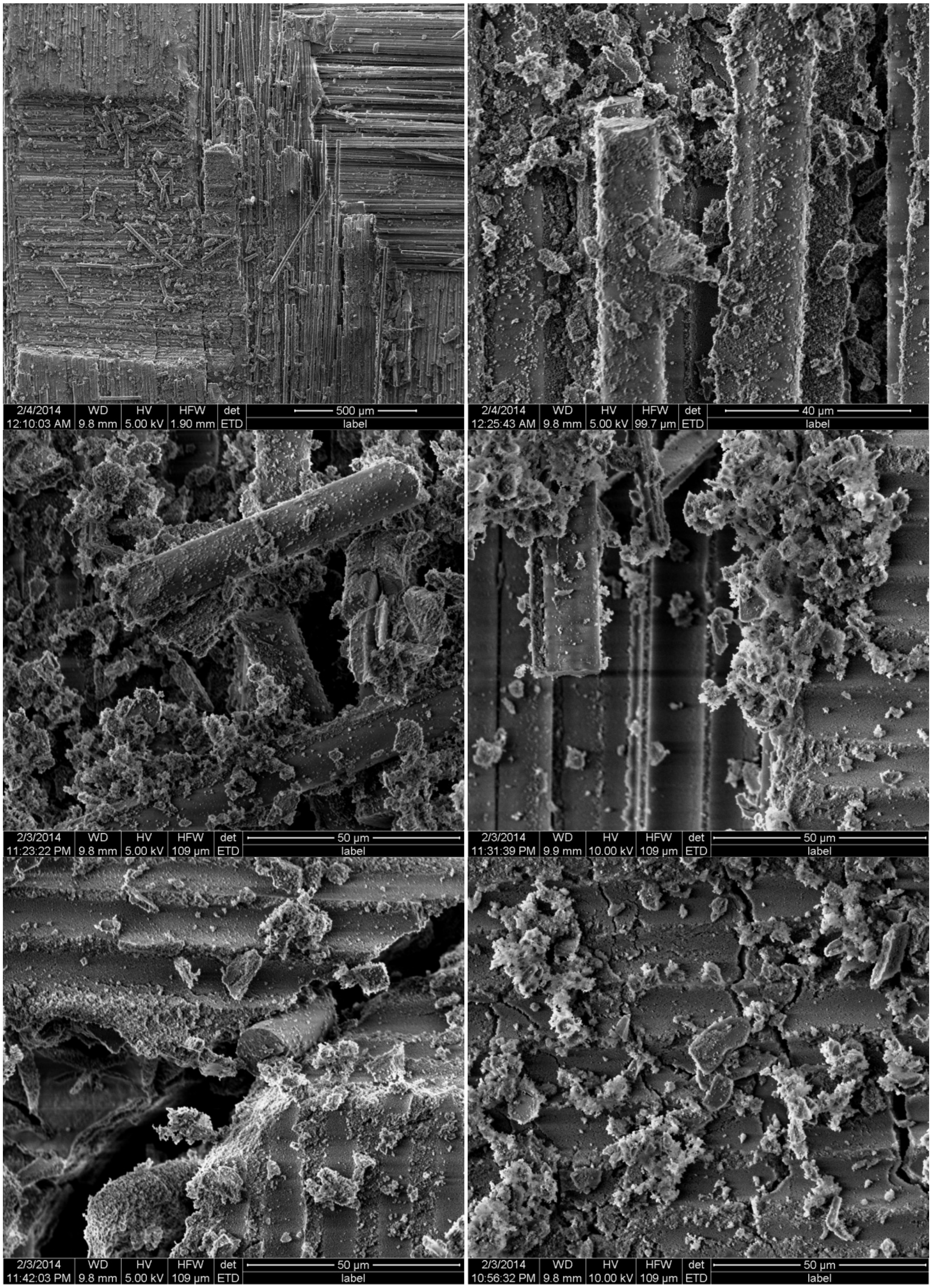
2/4/2014 12:10:03 AM WD 9.8 mm HV 5.00 kV HFW 1.90 mm det ETD 500 μm label
2/4/2014 12:25:43 AM WD 9.8 mm HV 5.00 kV HFW 99.7 μm det ETD 40 μm label
2/3/2014 11:23:22 PM WD 9.8 mm HV 5.00 kV HFW 109 μm det ETD 50 μm label
2/3/2014 11:31:39 PM WD 9.9 mm HV 10.00 kV HFW 109 μm det ETD 50 μm label
2/3/2014 11:42:03 PM WD 9.8 mm HV 5.00 kV HFW 109 μm det ETD 50 μm label
2/3/2014 10:56:32 PM WD 9.8 mm HV 10.00 kV HFW 109 μm det ETD 50 μm label

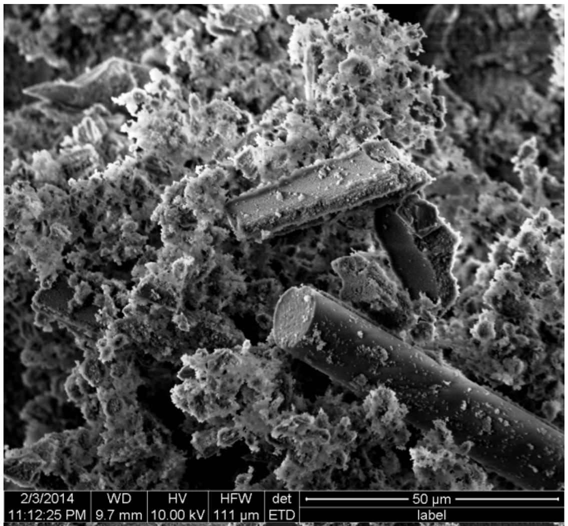
2/3/2014
11:12:25 PM
WD
9.7 mm
HV
10.00 kV
HFW
111 µm
det
ETD
50 µm
label

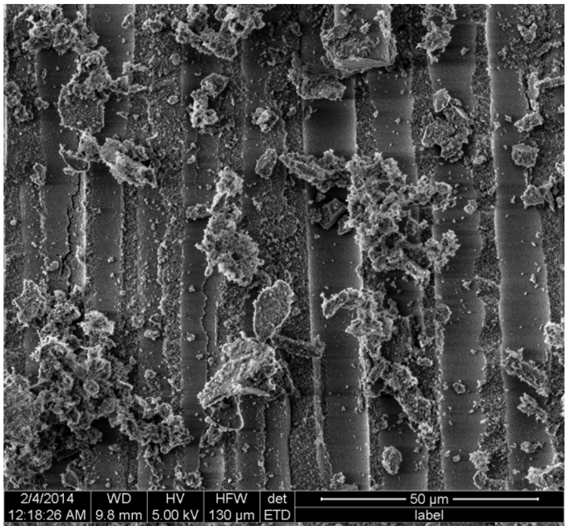
2/4/2014
12:18:26 AM
WD
9.8 mm
HV
5.00 kV
HFW
130 µm
det
ETD
50 µm
label

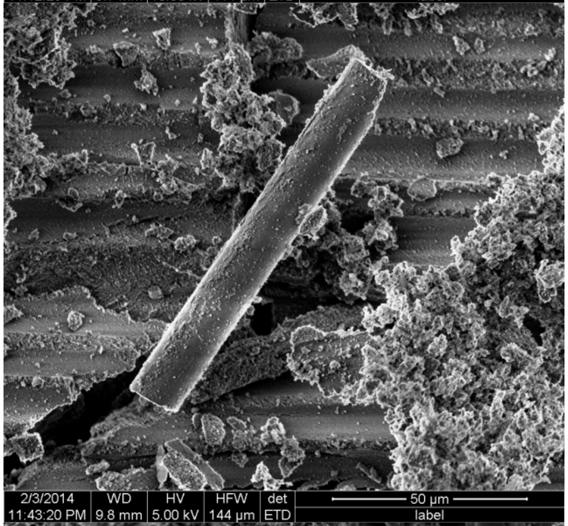
2/3/2014
11:43:20 PM
WD
9.8 mm
HV
5.00 kV
HFW
144 µm
det
ETD
50 µm
label

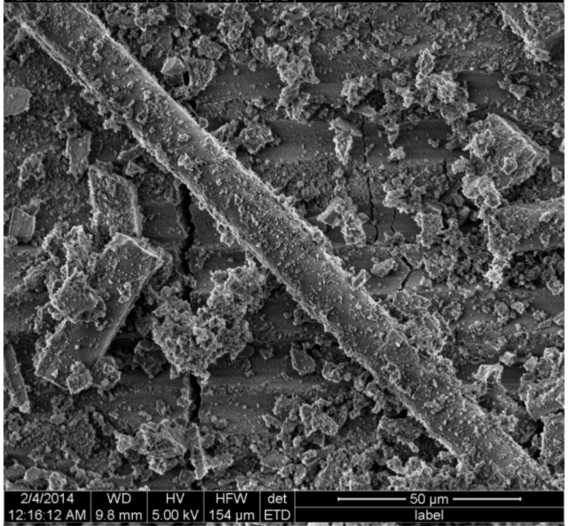
2/4/2014
12:16:12 AM
WD
9.8 mm
HV
5.00 kV
HFW
154 µm
det
ETD
50 µm
label

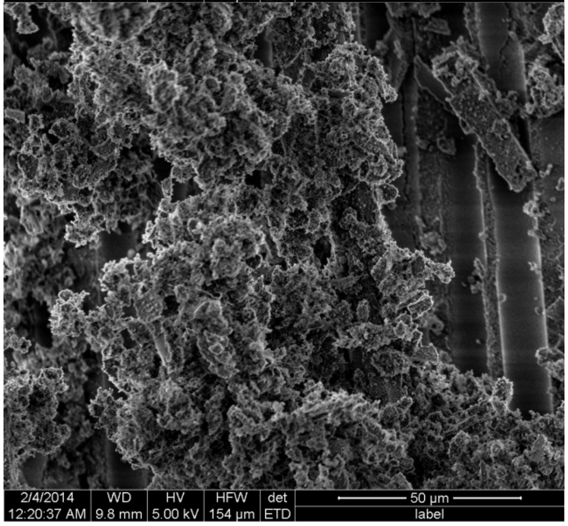
2/4/2014
12:20:37 AM
WD
9.8 mm
HV
5.00 kV
HFW
154 µm
det
ETD
50 µm
label

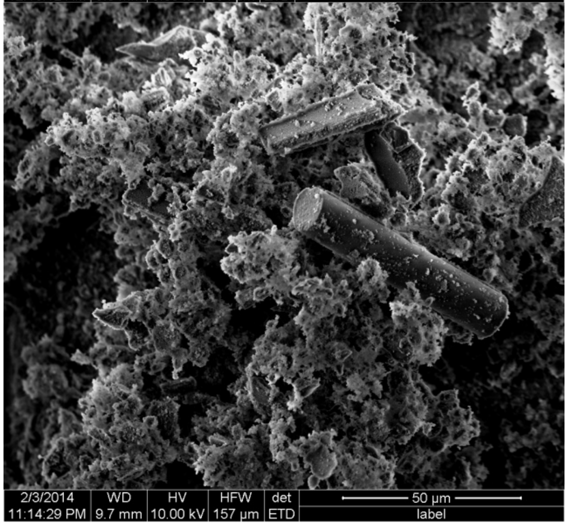
2/3/2014
11:14:29 PM
WD
9.7 mm
HV
10.00 kV
HFW
157 µm
det
ETD
50 µm
label

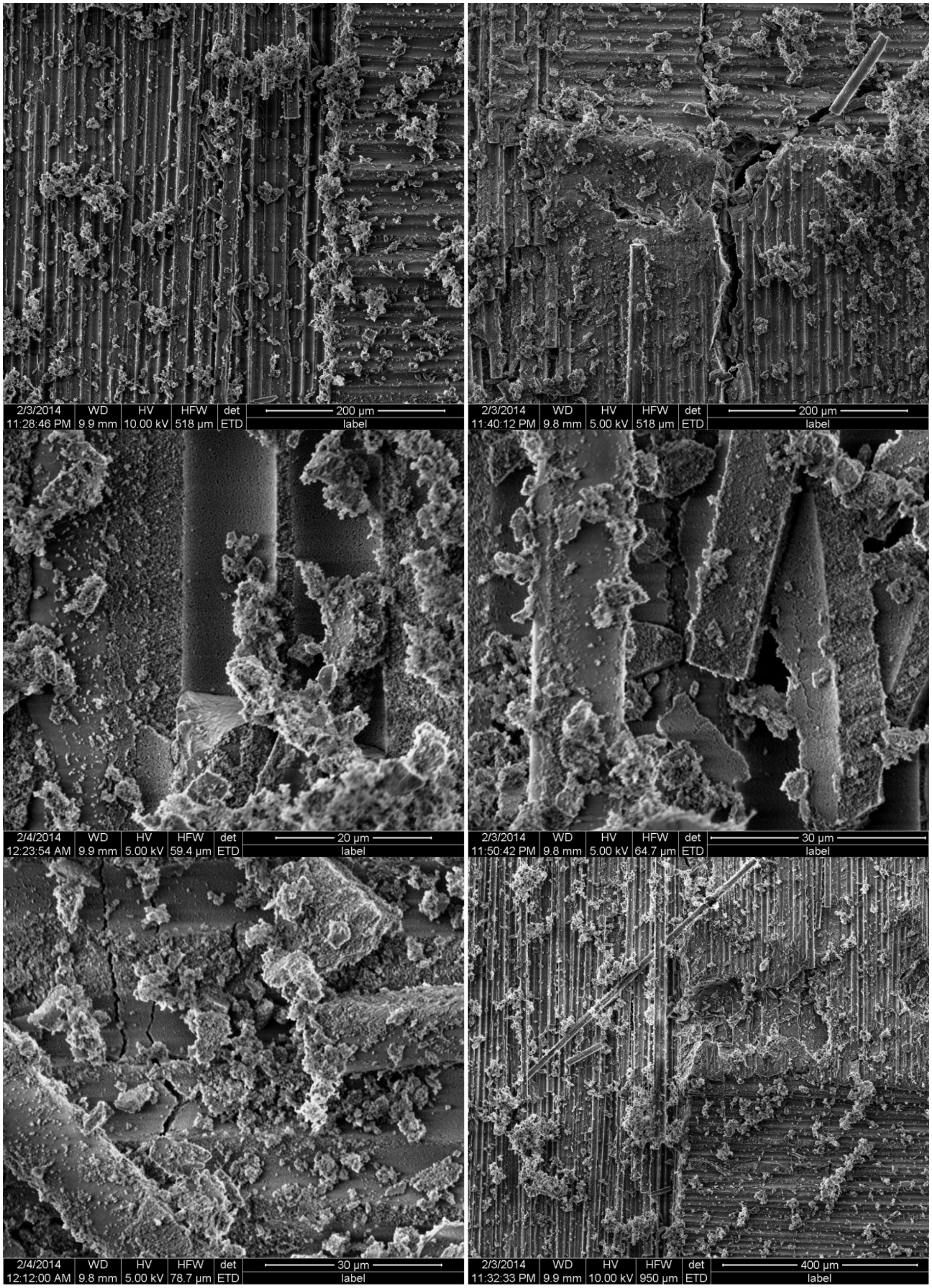
2/3/2014 11:28:46 PM
WD 9.9 mm
HV 10.00 kV
HFW 518 µm
det ETD
200 µm
label
2/3/2014 11:40:12 PM
WD 9.8 mm
HV 5.00 kV
HFW 518 µm
det ETD
200 µm
label
2/4/2014 12:23:54 AM
WD 9.9 mm
HV 5.00 kV
HFW 59.4 µm
det ETD
20 µm
label
2/3/2014 11:50:42 PM
WD 9.8 mm
HV 5.00 kV
HFW 64.7 µm
det ETD
30 µm
label
2/4/2014 12:12:00 AM
WD 9.8 mm
HV 5.00 kV
HFW 78.7 µm
det ETD
30 µm
label
2/3/2014 11:32:33 PM
WD 9.9 mm
HV 10.00 kV
HFW 950 µm
det ETD
400 µm
label

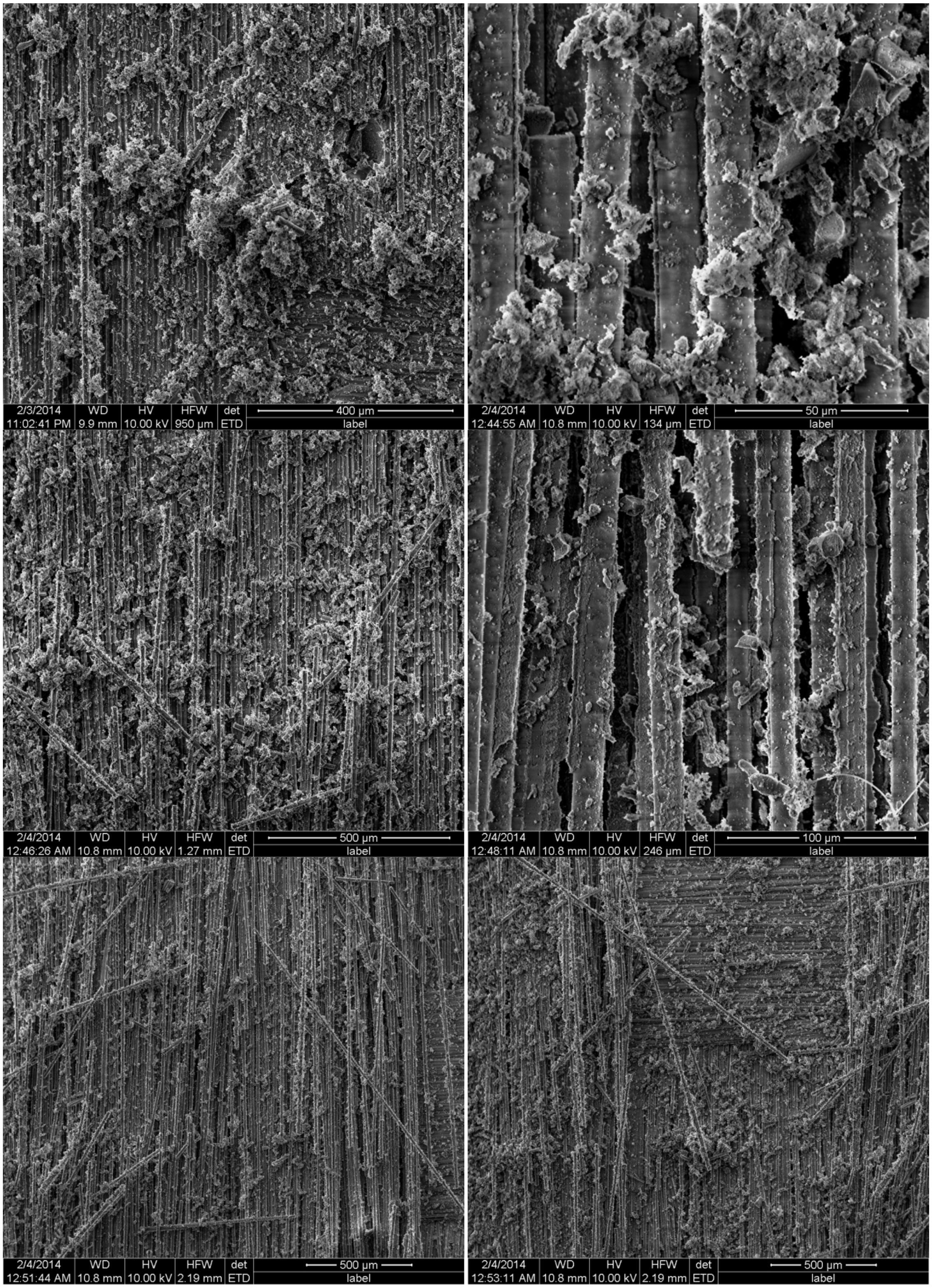
2/3/2014 11:02:41 PM WD 9.9 mm HV 10.00 kV HFW 950 µm det ETD 400 µm label
2/4/2014 12:44:55 AM WD 10.8 mm HV 10.00 kV HFW 134 µm det ETD 50 µm label
2/4/2014 12:46:26 AM WD 10.8 mm HV 10.00 kV HFW 1.27 mm det ETD 500 µm label
2/4/2014 12:48:11 AM WD 10.8 mm HV 10.00 kV HFW 246 µm det ETD 100 µm label
2/4/2014 12:51:44 AM WD 10.8 mm HV 10.00 kV HFW 2.19 mm det ETD 500 µm label
2/4/2014 12:53:11 AM WD 10.8 mm HV 10.00 kV HFW 2.19 mm det ETD 500 µm label

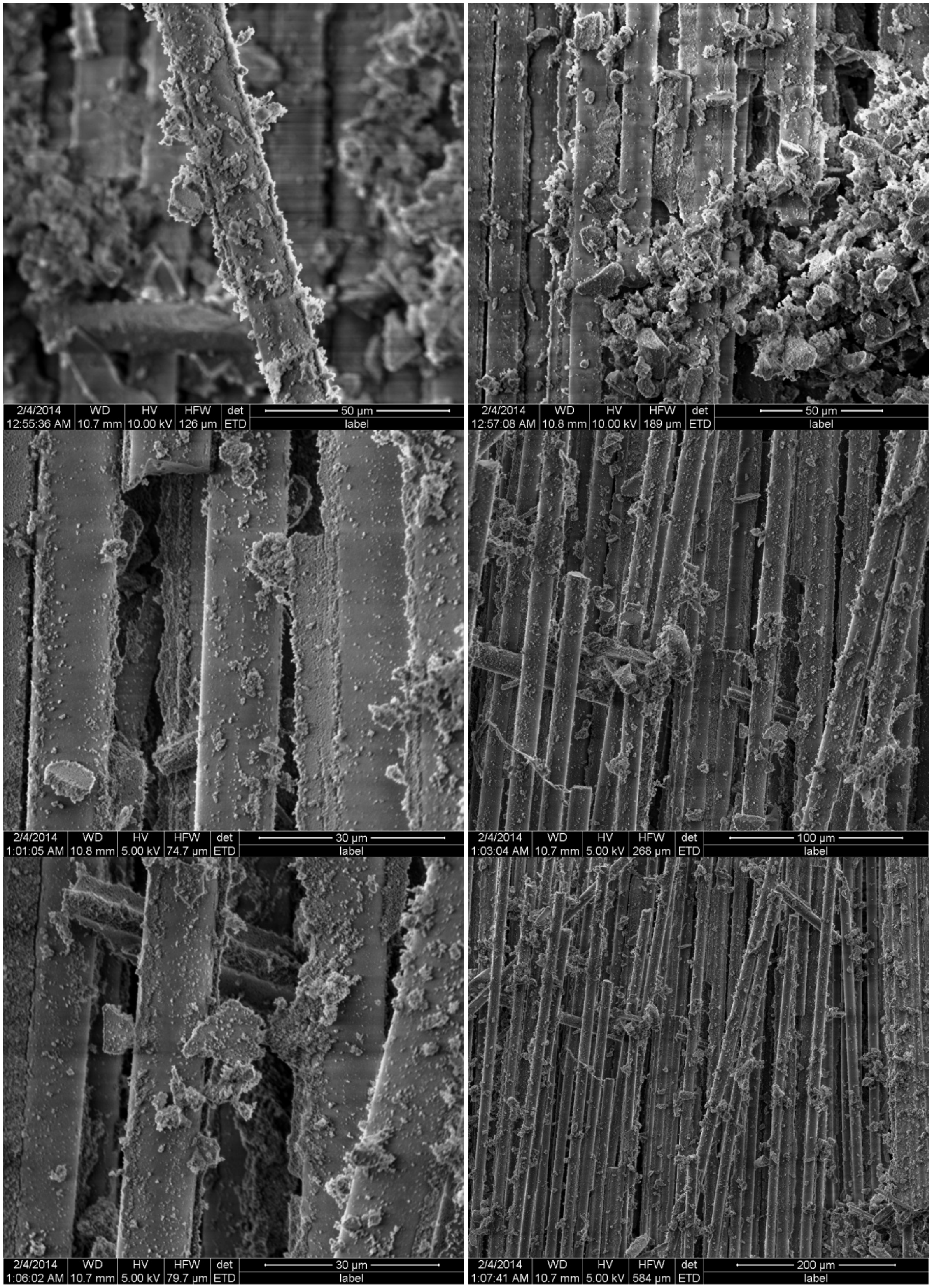
2/4/2014 12:55:36 AM | WD 10.7 mm | HV 10.00 kV | HFW 126 µm | det ETD | 50 µm | label
2/4/2014 12:57:08 AM | WD 10.8 mm | HV 10.00 kV | HFW 189 µm | det ETD | 50 µm | label
2/4/2014 1:01:05 AM | WD 10.8 mm | HV 5.00 kV | HFW 74.7 µm | det ETD | 30 µm | label
2/4/2014 1:03:04 AM | WD 10.7 mm | HV 5.00 kV | HFW 268 µm | det ETD | 100 µm | label
2/4/2014 1:06:02 AM | WD 10.7 mm | HV 5.00 kV | HFW 79.7 µm | det ETD | 30 µm | label
2/4/2014 1:07:41 AM | WD 10.7 mm | HV 5.00 kV | HFW 584 µm | det ETD | 200 µm | label

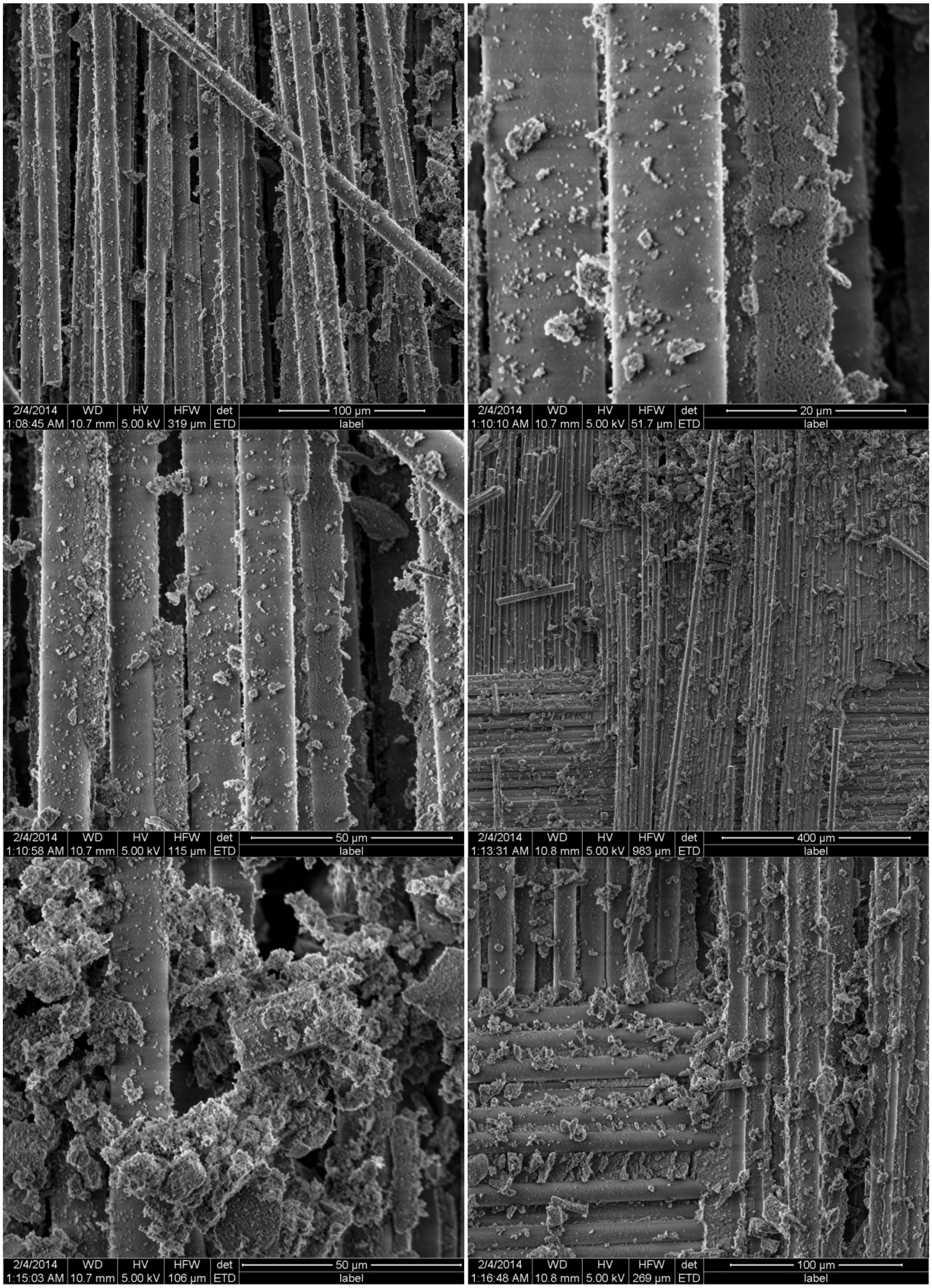
2/4/2014 1:08:45 AM
WD 10.7 mm
HV 5.00 kV
HFW 319 µm
det ETD
100 µm
label
2/4/2014 1:10:10 AM
WD 10.7 mm
HV 5.00 kV
HFW 51.7 µm
det ETD
20 µm
label
2/4/2014 1:10:58 AM
WD 10.7 mm
HV 5.00 kV
HFW 115 µm
det ETD
50 µm
label
2/4/2014 1:13:31 AM
WD 10.8 mm
HV 5.00 kV
HFW 983 µm
det ETD
400 µm
label
2/4/2014 1:15:03 AM
WD 10.7 mm
HV 5.00 kV
HFW 106 µm
det ETD
50 µm
label
2/4/2014 1:16:48 AM
WD 10.8 mm
HV 5.00 kV
HFW 269 µm
det ETD
100 µm
label

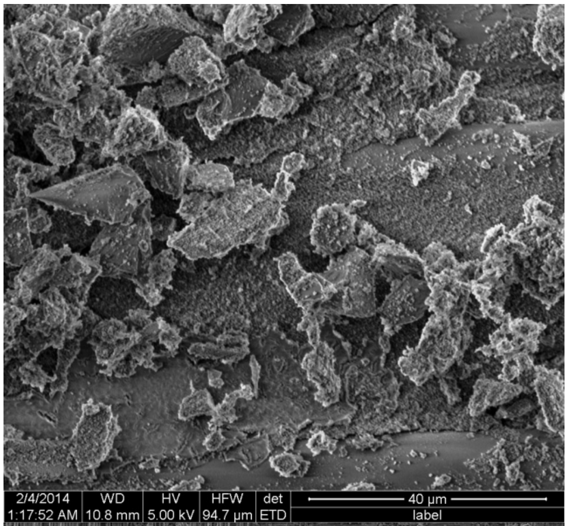
2/4/2014
1:17:52 AM
WD
10.8 mm
HV
5.00 kV
HFW
94.7 µm
det
ETD
40 µm
label

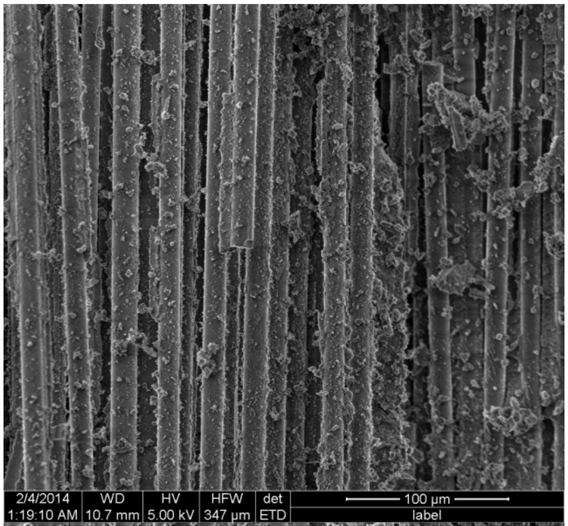
2/4/2014
1:19:10 AM
WD
10.7 mm
HV
5.00 kV
HFW
347 µm
det
ETD
100 µm
label

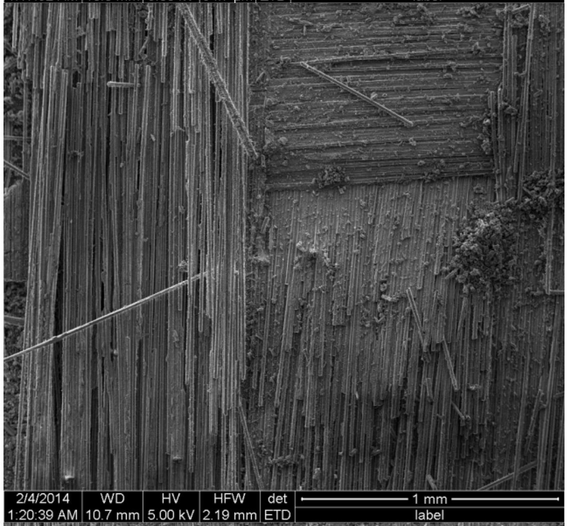
2/4/2014
1:20:39 AM
WD
10.7 mm
HV
5.00 kV
HFW
2.19 mm
det
ETD
1 mm
label

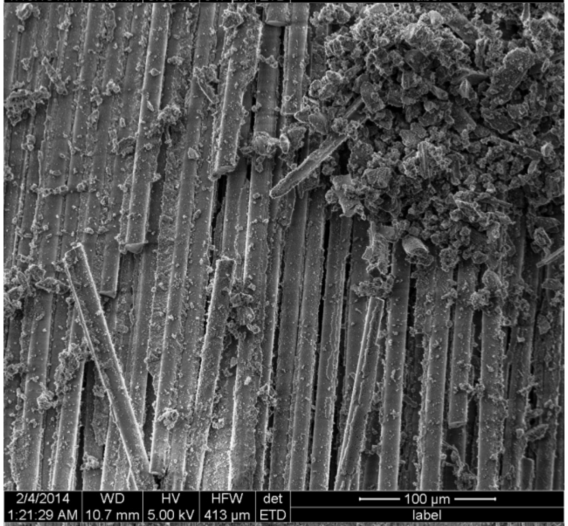
2/4/2014
1:21:29 AM
WD
10.7 mm
HV
5.00 kV
HFW
413 µm
det
ETD
100 µm
label

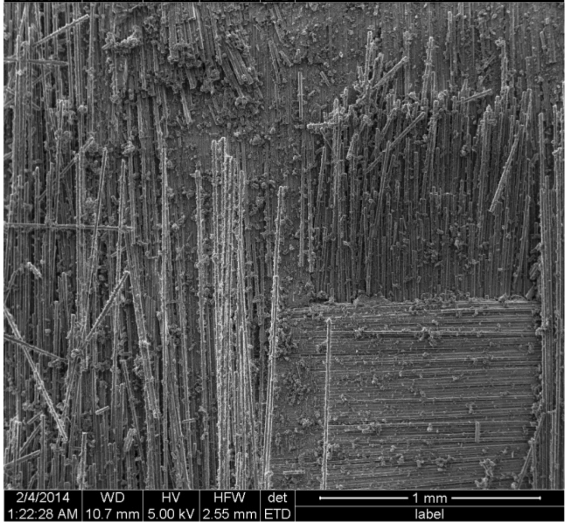
2/4/2014
1:22:28 AM
WD
10.7 mm
HV
5.00 kV
HFW
2.55 mm
det
ETD
1 mm
label

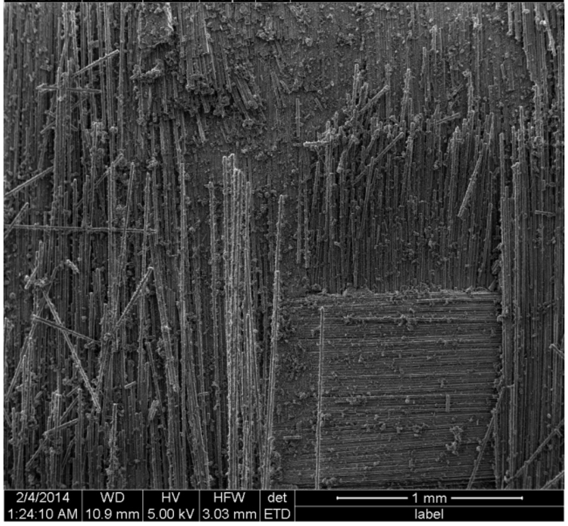
2/4/2014
1:24:10 AM
WD
10.9 mm
HV
5.00 kV
HFW
3.03 mm
det
ETD
1 mm
label

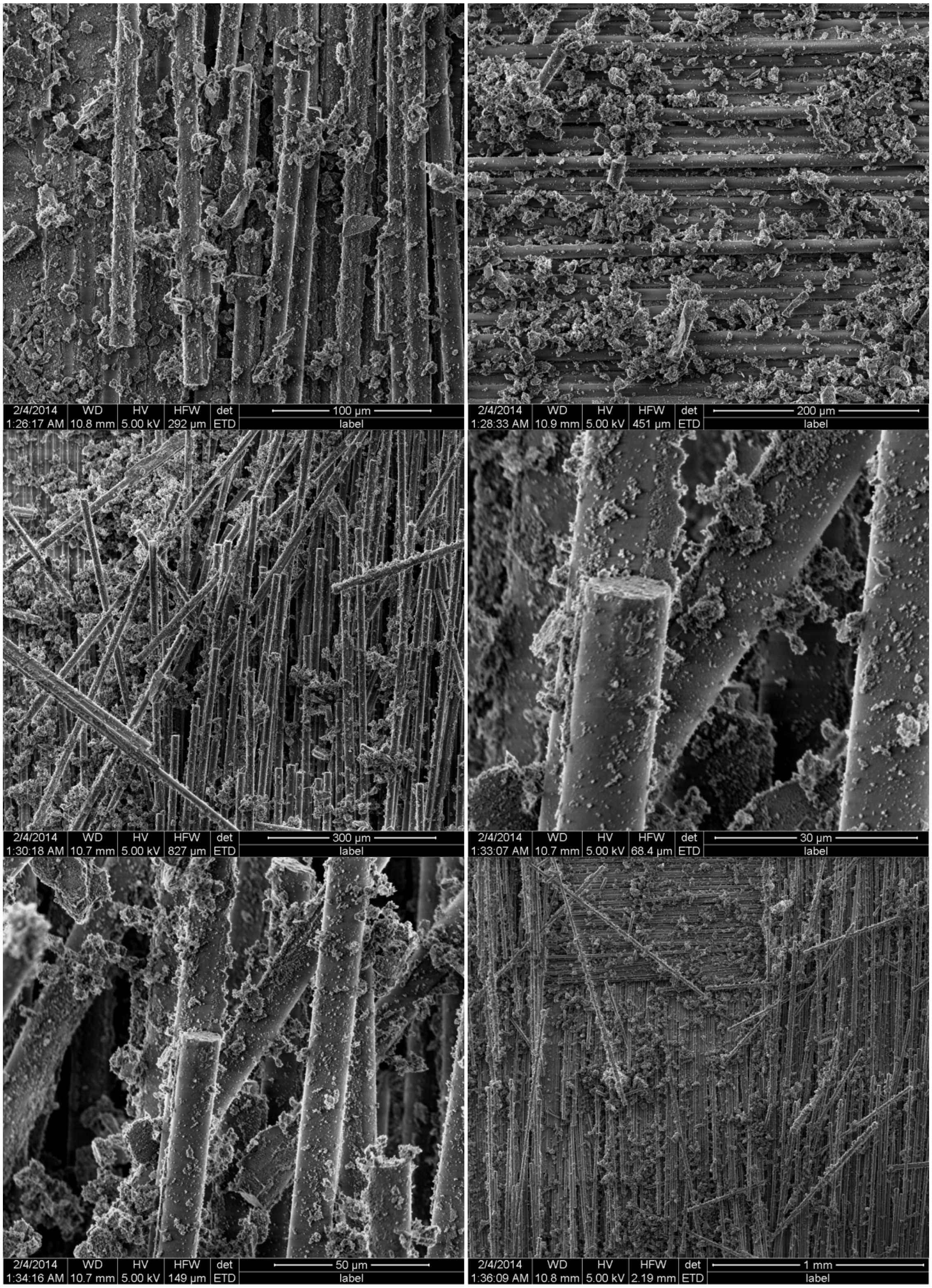
2/4/2014 1:26:17 AM | WD 10.8 mm | HV 5.00 kV | HFW 292 µm | det ETD | 100 µm | label
2/4/2014 1:28:33 AM | WD 10.9 mm | HV 5.00 kV | HFW 451 µm | det ETD | 200 µm | label
2/4/2014 1:30:18 AM | WD 10.7 mm | HV 5.00 kV | HFW 827 µm | det ETD | 300 µm | label
2/4/2014 1:33:07 AM | WD 10.7 mm | HV 5.00 kV | HFW 68.4 µm | det ETD | 30 µm | label
2/4/2014 1:34:16 AM | WD 10.7 mm | HV 5.00 kV | HFW 149 µm | det ETD | 50 µm | label
2/4/2014 1:36:09 AM | WD 10.8 mm | HV 5.00 kV | HFW 2.19 mm | det ETD | 1 mm | label

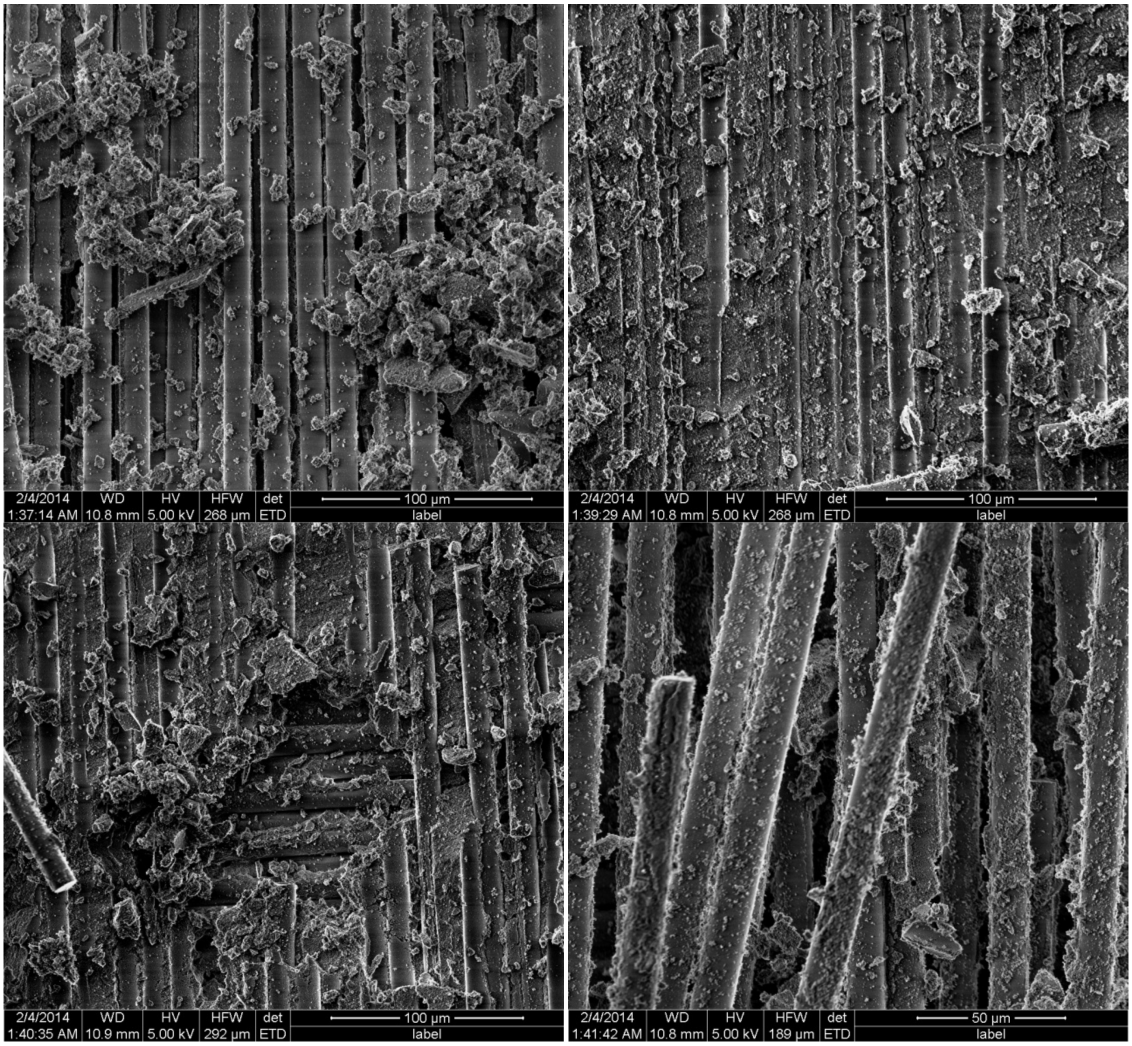
2/4/2014 1:37:14 AM
WD 10.8 mm
HV 5.00 kV
HFW 268 µm
det ETD
100 µm
label
2/4/2014 1:39:29 AM
WD 10.8 mm
HV 5.00 kV
HFW 268 µm
det ETD
100 µm
label
2/4/2014 1:40:35 AM
WD 10.9 mm
HV 5.00 kV
HFW 292 µm
det ETD
100 µm
label
2/4/2014 1:41:42 AM
WD 10.8 mm
HV 5.00 kV
HFW 189 µm
det ETD
50 µm
label

Appendix S: SEM Images of Specimen 9 – DNS Creep at 2 MPa in Air at 1100°C.

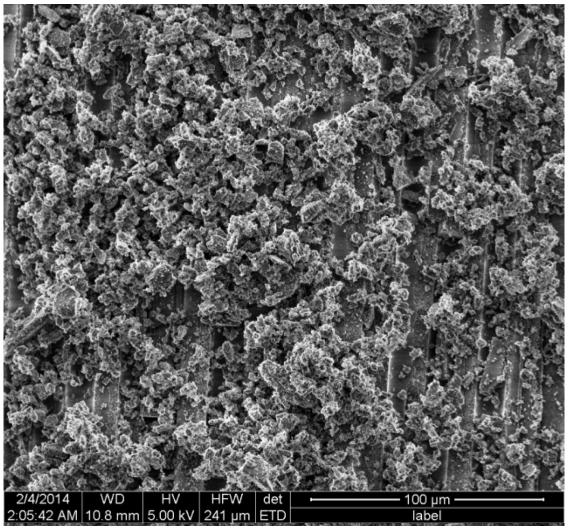
2/4/2014
2:05:42 AM
WD
10.8 mm
HV
5.00 kV
HFW
241 µm
det
ETD
100 µm
label

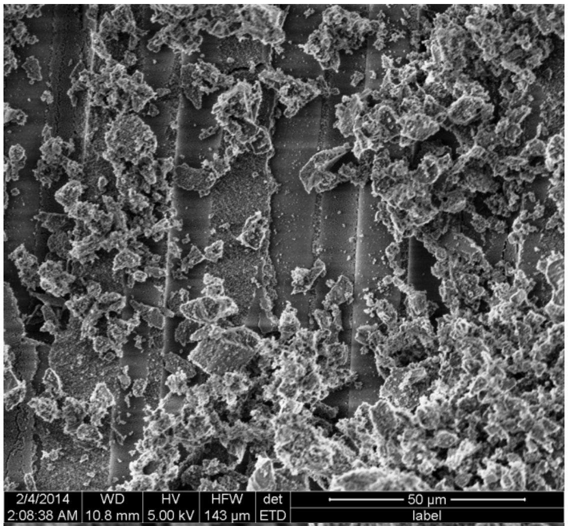
2/4/2014
2:08:38 AM
WD
10.8 mm
HV
5.00 kV
HFW
143 µm
det
ETD
50 µm
label

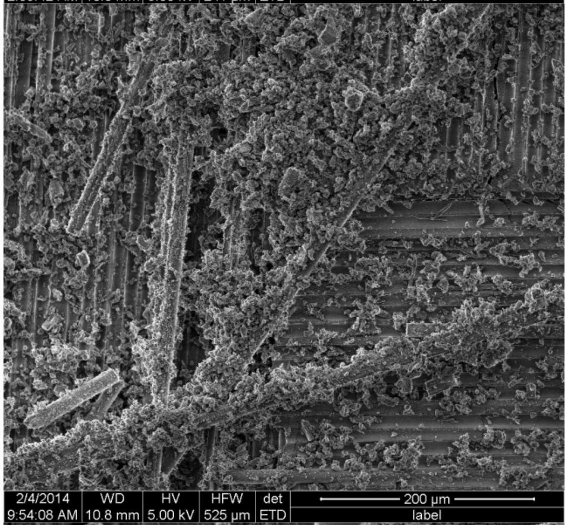
2/4/2014
9:54:08 AM
WD
10.8 mm
HV
5.00 kV
HFW
525 µm
det
ETD
200 µm
label

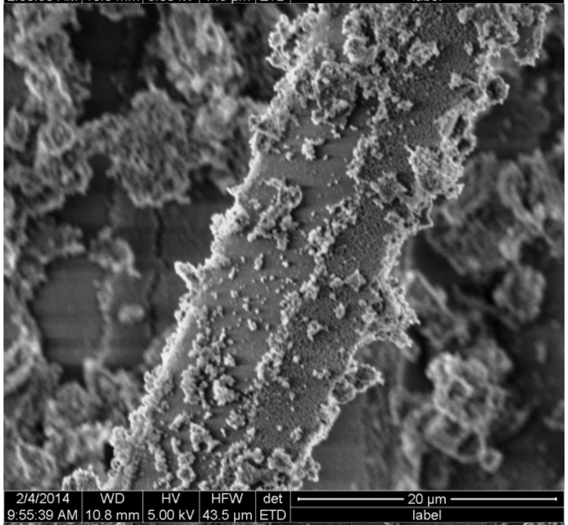
2/4/2014
9:55:39 AM
WD
10.8 mm
HV
5.00 kV
HFW
43.5 µm
det
ETD
20 µm
label

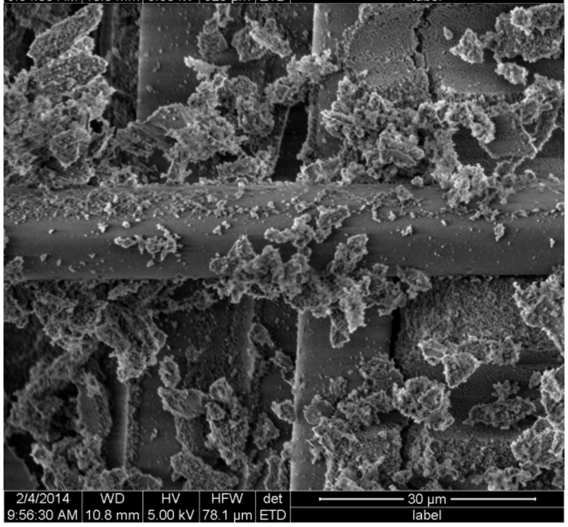
2/4/2014
9:56:30 AM
WD
10.8 mm
HV
5.00 kV
HFW
78.1 µm
det
ETD
30 µm
label

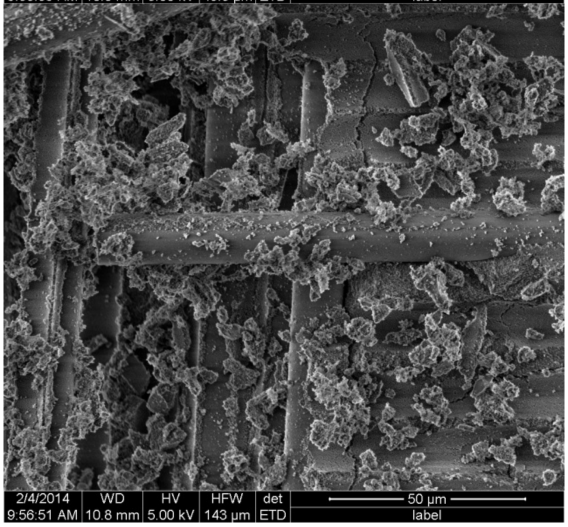
2/4/2014
9:56:51 AM
WD
10.8 mm
HV
5.00 kV
HFW
143 µm
det
ETD
50 µm
label

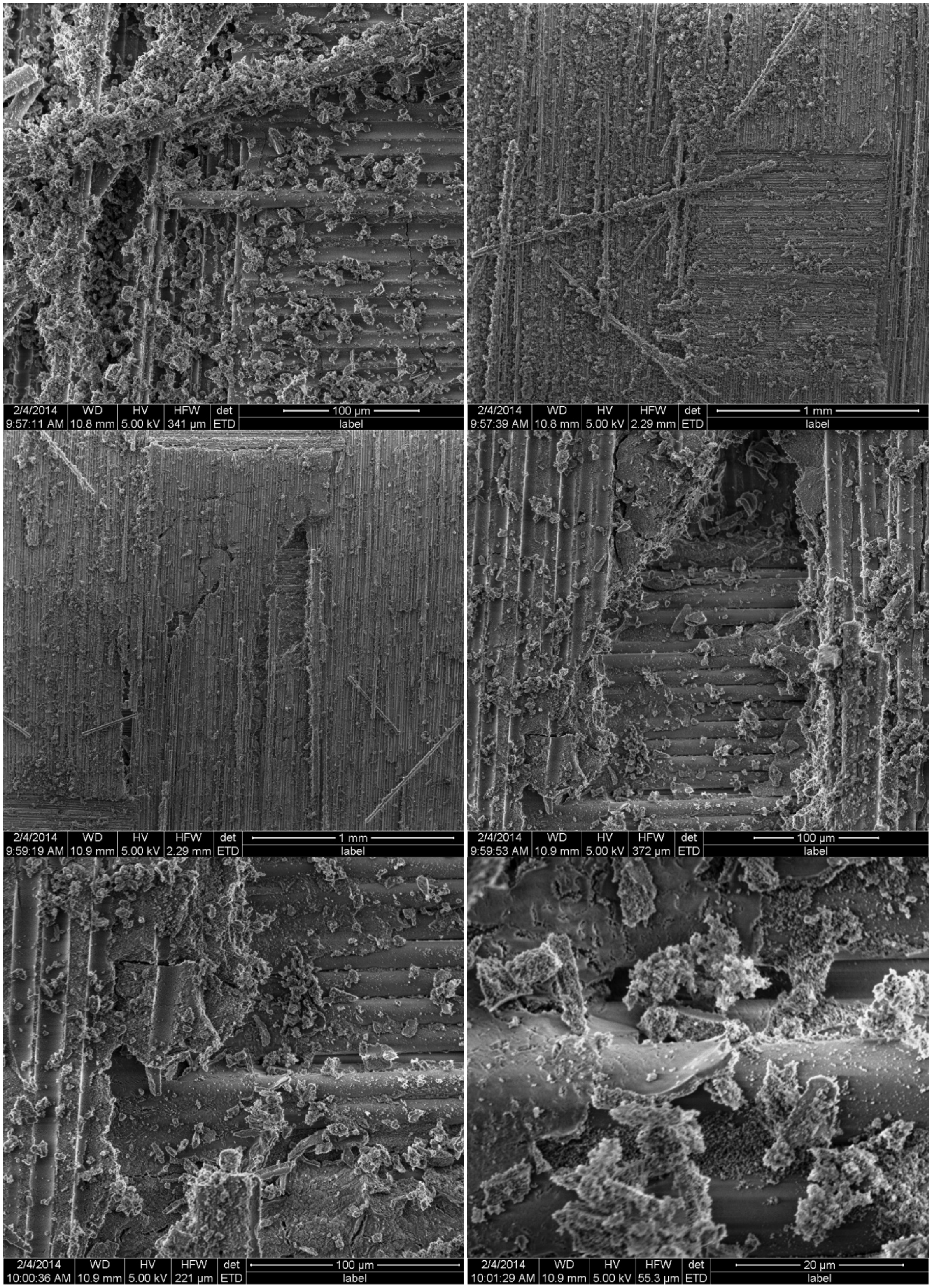
2/4/2014 9:57:11 AM WD 10.8 mm HV 5.00 kV HFW 341 μm det ETD 100 μm label
2/4/2014 9:57:39 AM WD 10.8 mm HV 5.00 kV HFW 2.29 mm det ETD 1 mm label
2/4/2014 9:59:19 AM WD 10.9 mm HV 5.00 kV HFW 2.29 mm det ETD 1 mm label
2/4/2014 9:59:53 AM WD 10.9 mm HV 5.00 kV HFW 372 μm det ETD 100 μm label
2/4/2014 10:00:36 AM WD 10.9 mm HV 5.00 kV HFW 221 μm det ETD 100 μm label
2/4/2014 10:01:29 AM WD 10.9 mm HV 5.00 kV HFW 55.3 μm det ETD 20 μm label

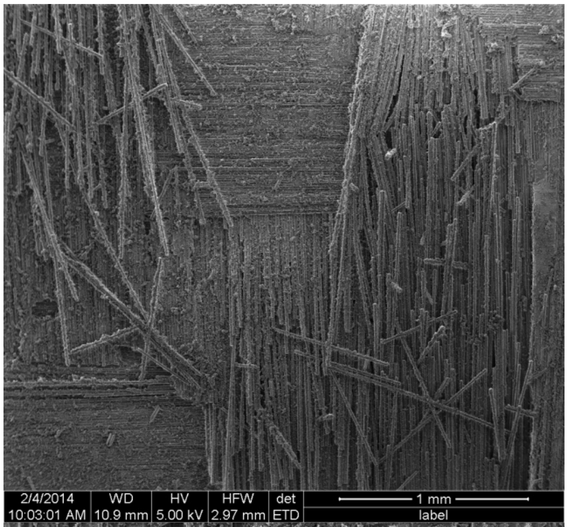
2/4/2014
10:03:01 AM
WD
10.9 mm
HV
5.00 kV
HFW
2.97 mm
det
ETD
1 mm
label

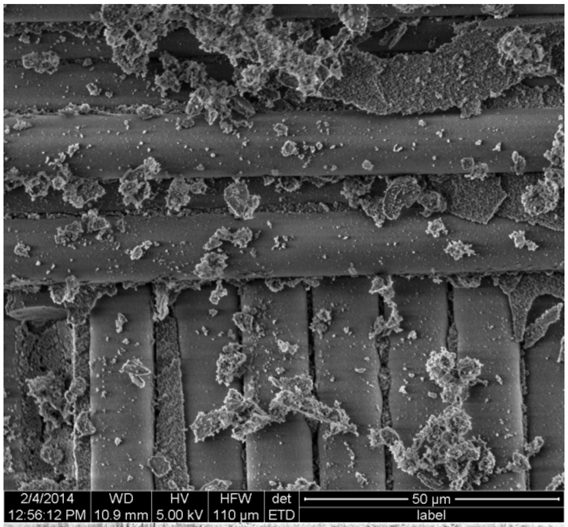
2/4/2014
12:56:12 PM
WD
10.9 mm
HV
5.00 kV
HFW
110 µm
det
ETD
50 µm
label

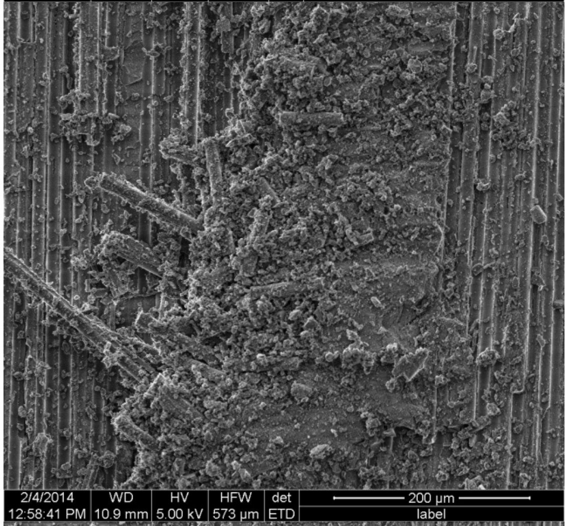
2/4/2014
12:58:41 PM
WD
10.9 mm
HV
5.00 kV
HFW
573 µm
det
ETD
200 µm
label

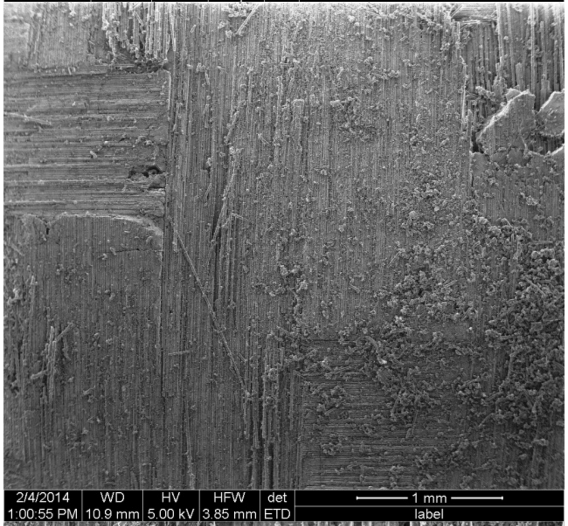
2/4/2014
1:00:55 PM
WD
10.9 mm
HV
5.00 kV
HFW
3.85 mm
det
ETD
1 mm
label

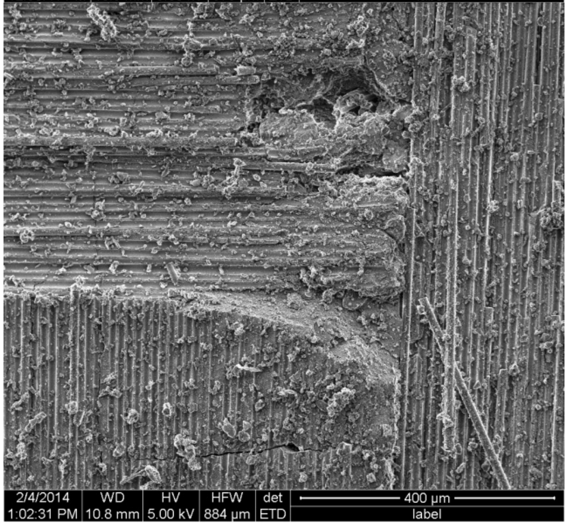
2/4/2014
1:02:31 PM
WD
10.8 mm
HV
5.00 kV
HFW
884 µm
det
ETD
400 µm
label

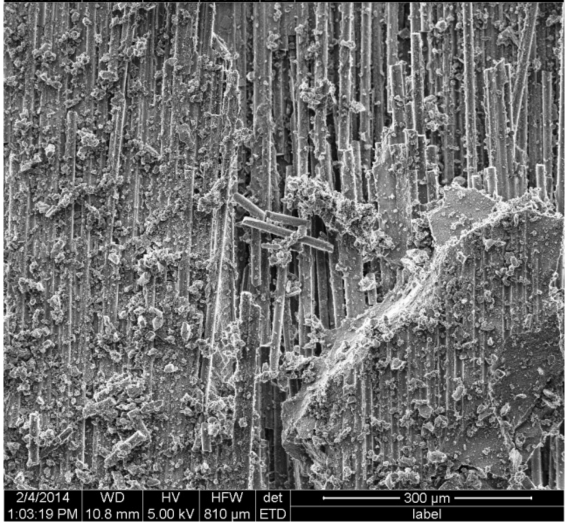
2/4/2014
1:03:19 PM
WD
10.8 mm
HV
5.00 kV
HFW
810 µm
det
ETD
300 µm
label

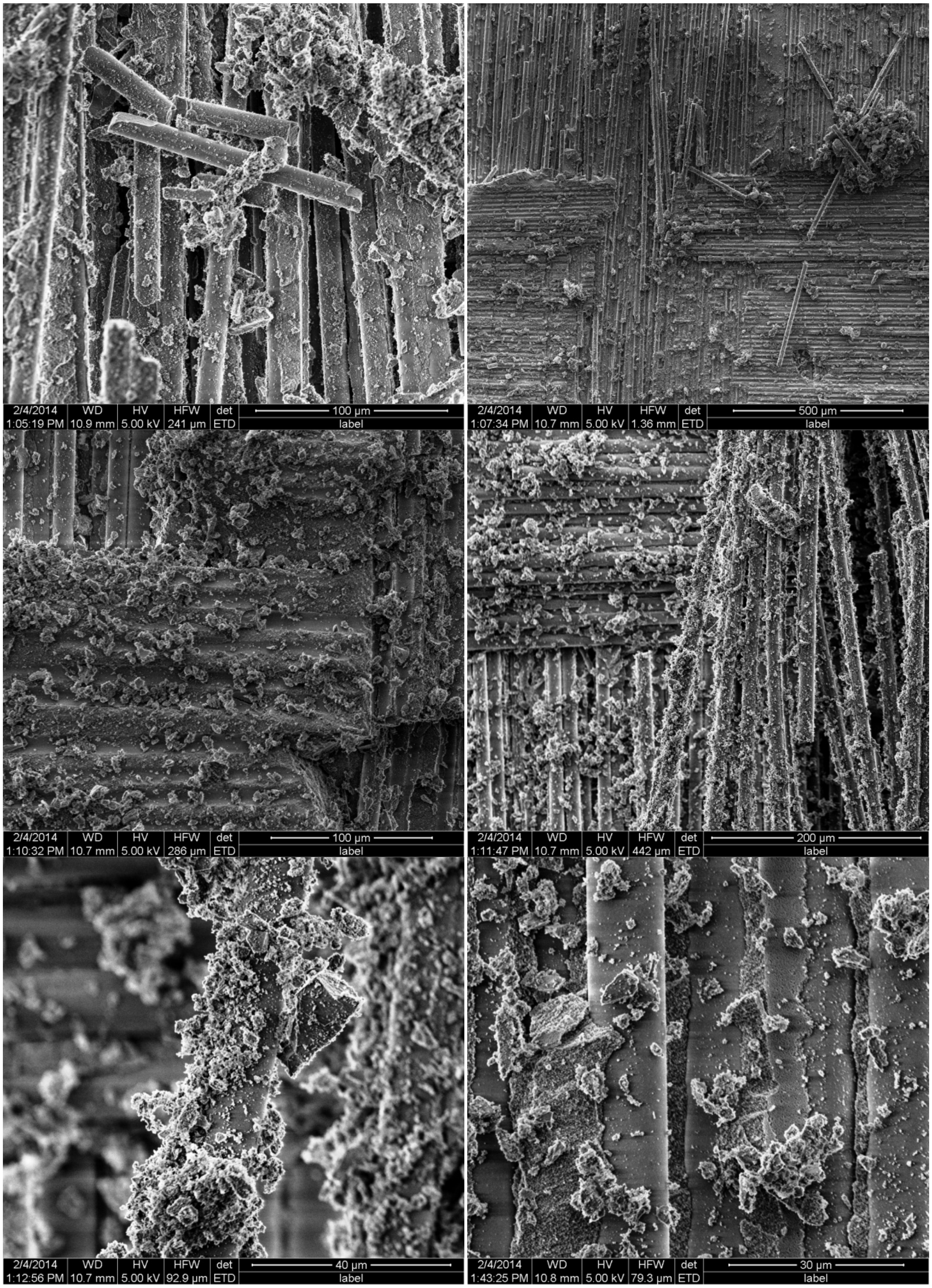
2/4/2014 1:05:19 PM WD 10.9 mm HV 5.00 kV HFW 241 µm det ETD 100 µm label
2/4/2014 1:07:34 PM WD 10.7 mm HV 5.00 kV HFW 1.36 mm det ETD 500 µm label
2/4/2014 1:10:32 PM WD 10.7 mm HV 5.00 kV HFW 286 µm det ETD 100 µm label
2/4/2014 1:11:47 PM WD 10.7 mm HV 5.00 kV HFW 442 µm det ETD 200 µm label
2/4/2014 1:12:56 PM WD 10.7 mm HV 5.00 kV HFW 92.9 µm det ETD 40 µm label
2/4/2014 1:43:25 PM WD 10.8 mm HV 5.00 kV HFW 79.3 µm det ETD 30 µm label

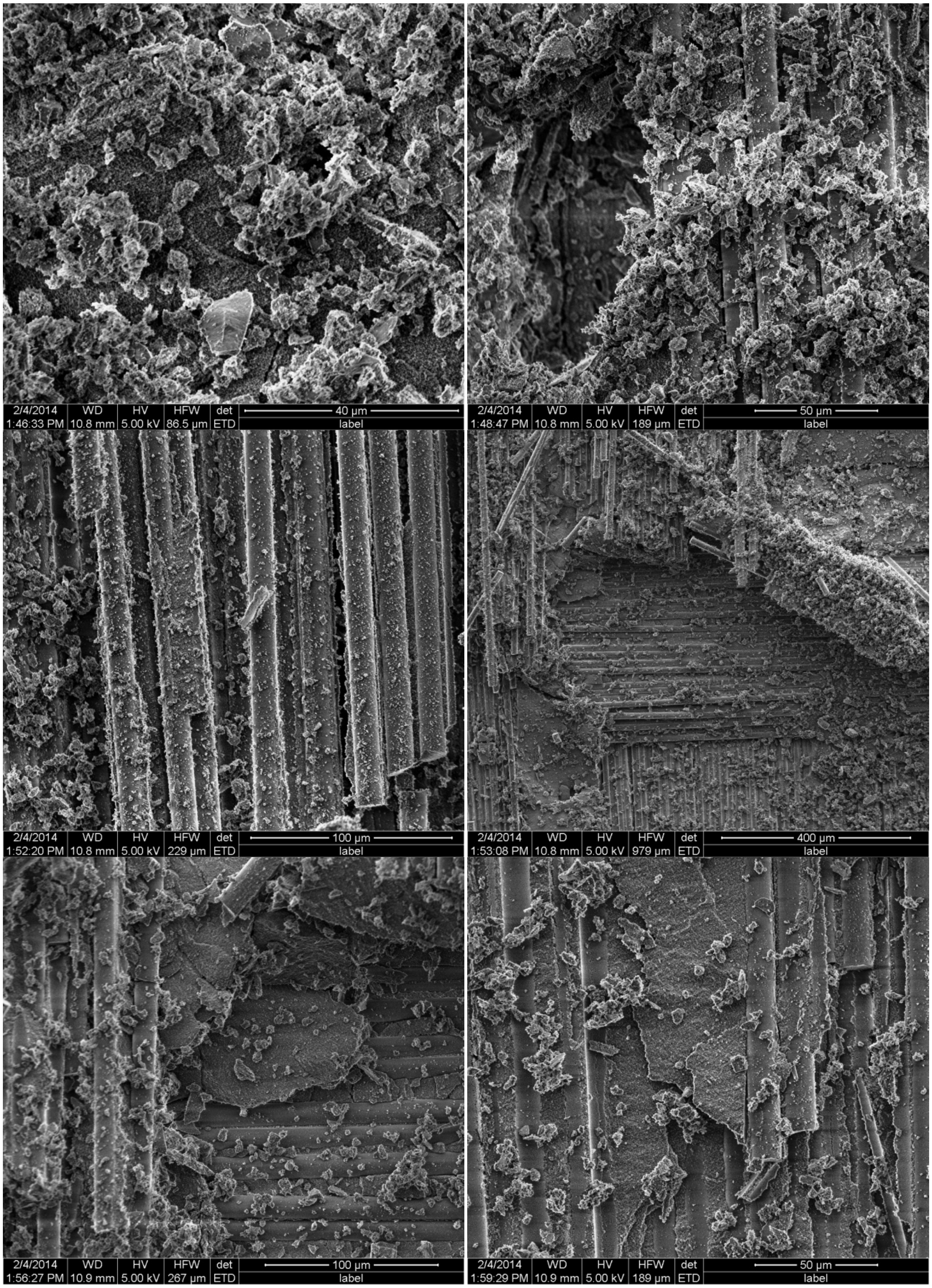
2/4/2014 WD HV HFW det 40 µm
1:46:33 PM 10.8 mm 5.00 kV 86.5 µm ETD label
2/4/2014 WD HV HFW det 50 µm
1:48:47 PM 10.8 mm 5.00 kV 189 µm ETD label
2/4/2014 WD HV HFW det 100 µm
1:52:20 PM 10.8 mm 5.00 kV 229 µm ETD label
2/4/2014 WD HV HFW det 400 µm
1:53:08 PM 10.8 mm 5.00 kV 979 µm ETD label
2/4/2014 WD HV HFW det 100 µm
1:56:27 PM 10.9 mm 5.00 kV 267 µm ETD label
2/4/2014 WD HV HFW det 50 µm
1:59:29 PM 10.9 mm 5.00 kV 189 µm ETD label

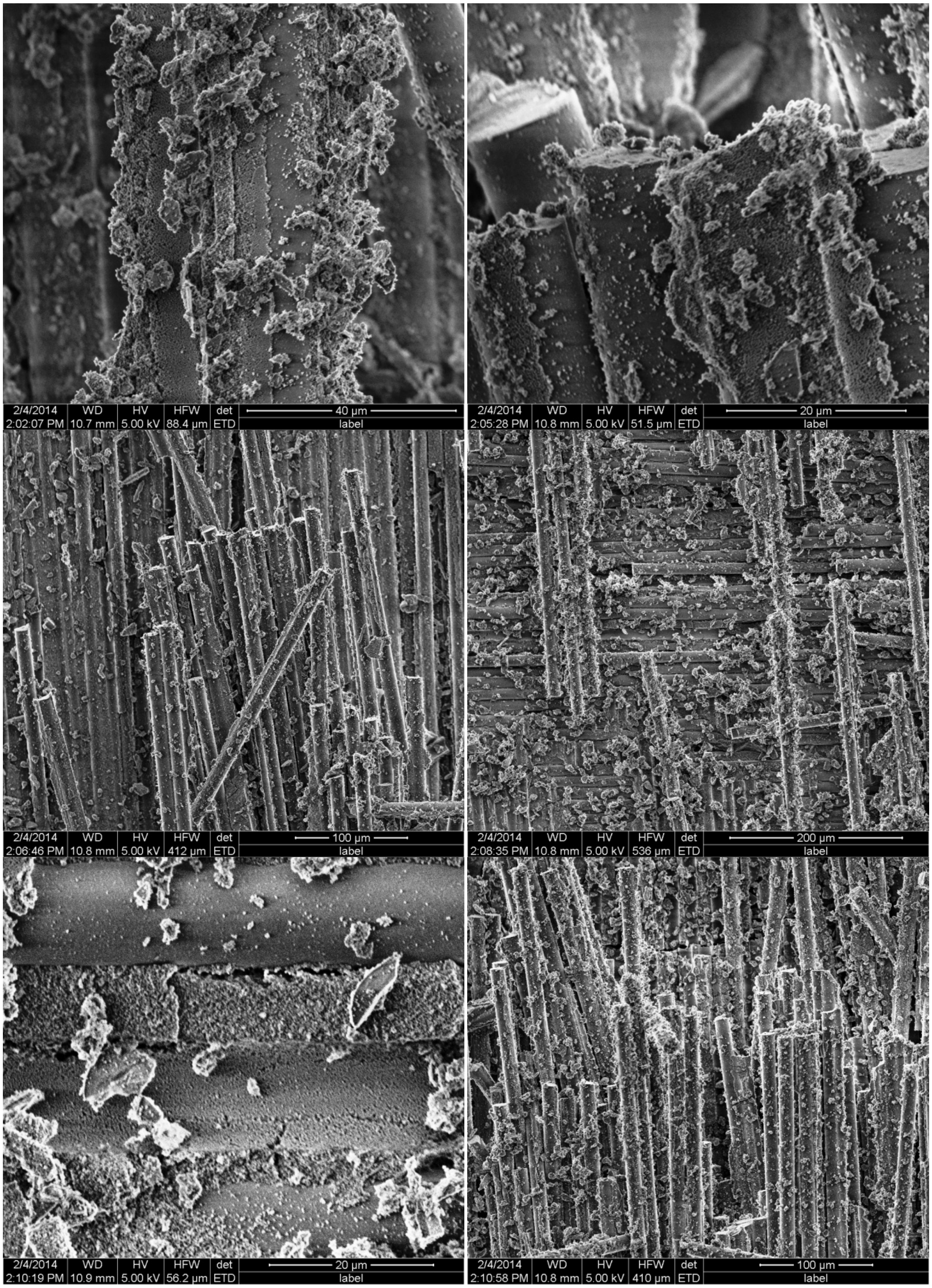
2/4/2014 2:02:07 PM | WD 10.7 mm | HV 5.00 kV | HFW 88.4 µm | det ETD | 40 µm | label
2/4/2014 2:05:28 PM | WD 10.8 mm | HV 5.00 kV | HFW 51.5 µm | det ETD | 20 µm | label
2/4/2014 2:06:46 PM | WD 10.8 mm | HV 5.00 kV | HFW 412 µm | det ETD | 100 µm | label
2/4/2014 2:08:35 PM | WD 10.8 mm | HV 5.00 kV | HFW 536 µm | det ETD | 200 µm | label
2/4/2014 2:10:19 PM | WD 10.9 mm | HV 5.00 kV | HFW 56.2 µm | det ETD | 20 µm | label
2/4/2014 2:10:58 PM | WD 10.8 mm | HV 5.00 kV | HFW 410 µm | det ETD | 100 µm | label

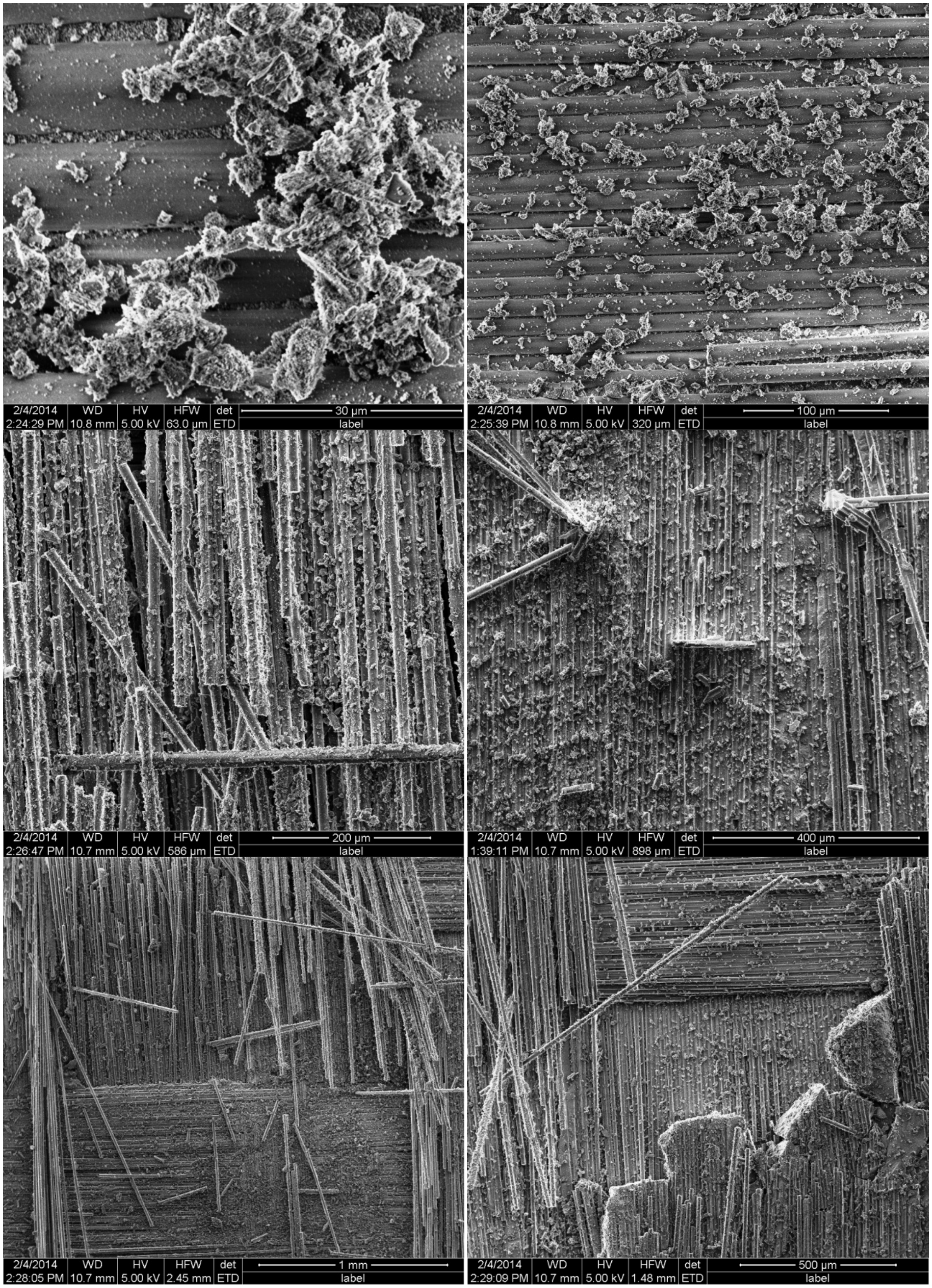
2/4/2014 2:24:29 PM | WD 10.8 mm | HV 5.00 kV | HFW 63.0 µm | det ETD | 30 µm | label
2/4/2014 2:25:39 PM | WD 10.8 mm | HV 5.00 kV | HFW 320 µm | det ETD | 100 µm | label
2/4/2014 2:26:47 PM | WD 10.7 mm | HV 5.00 kV | HFW 586 µm | det ETD | 200 µm | label
2/4/2014 1:39:11 PM | WD 10.7 mm | HV 5.00 kV | HFW 898 µm | det ETD | 400 µm | label
2/4/2014 2:28:05 PM | WD 10.7 mm | HV 5.00 kV | HFW 2.45 mm | det ETD | 1 mm | label
2/4/2014 2:29:09 PM | WD 10.7 mm | HV 5.00 kV | HFW 1.48 mm | det ETD | 500 µm | label

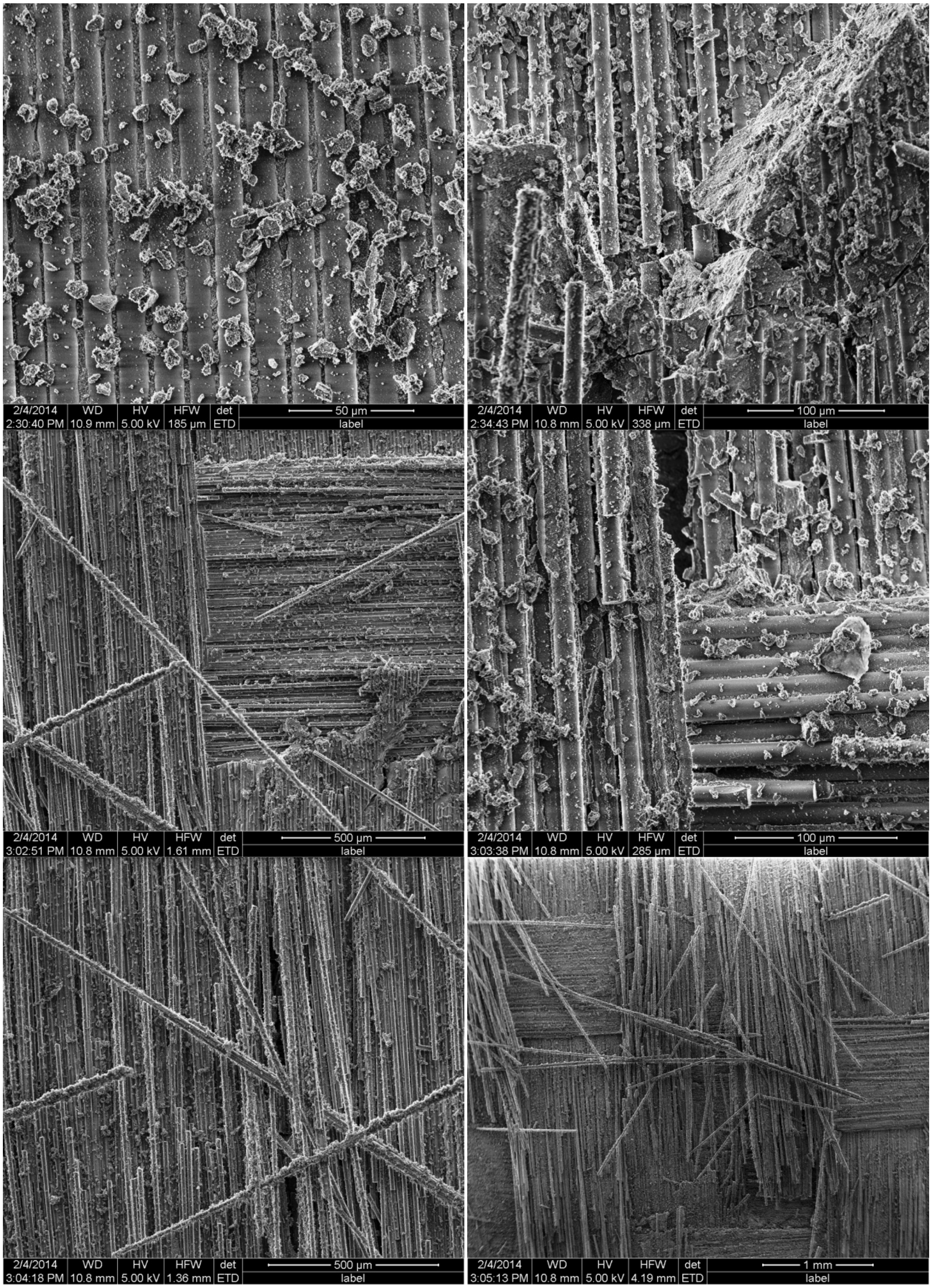
2/4/2014 2:30:40 PM | WD 10.9 mm | HV 5.00 kV | HFW 185 µm | det ETD | 50 µm | label
2/4/2014 2:34:43 PM | WD 10.8 mm | HV 5.00 kV | HFW 338 µm | det ETD | 100 µm | label
2/4/2014 3:02:51 PM | WD 10.8 mm | HV 5.00 kV | HFW 1.61 mm | det ETD | 500 µm | label
2/4/2014 3:03:38 PM | WD 10.8 mm | HV 5.00 kV | HFW 285 µm | det ETD | 100 µm | label
2/4/2014 3:04:18 PM | WD 10.8 mm | HV 5.00 kV | HFW 1.36 mm | det ETD | 500 µm | label
2/4/2014 3:05:13 PM | WD 10.8 mm | HV 5.00 kV | HFW 4.19 mm | det ETD | 1 mm | label

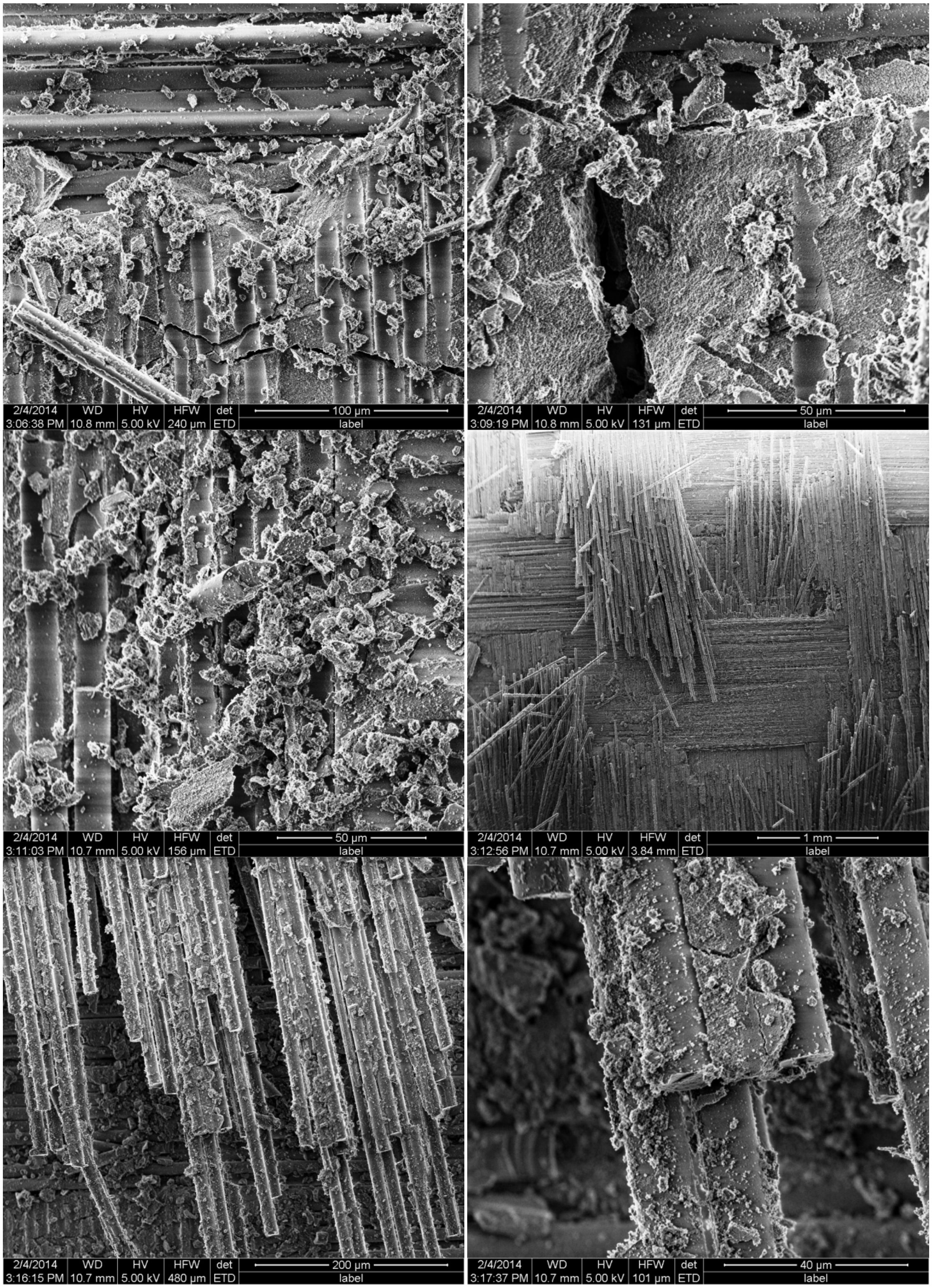
2/4/2014 3:06:38 PM WD 10.8 mm HV 5.00 kV HFW 240 µm det ETD 100 µm label
2/4/2014 3:09:19 PM WD 10.8 mm HV 5.00 kV HFW 131 µm det ETD 50 µm label
2/4/2014 3:11:03 PM WD 10.7 mm HV 5.00 kV HFW 156 µm det ETD 50 µm label
2/4/2014 3:12:56 PM WD 10.7 mm HV 5.00 kV HFW 3.84 mm det ETD 1 mm label
2/4/2014 3:16:15 PM WD 10.7 mm HV 5.00 kV HFW 480 µm det ETD 200 µm label
2/4/2014 3:17:37 PM WD 10.7 mm HV 5.00 kV HFW 101 µm det ETD 40 µm label

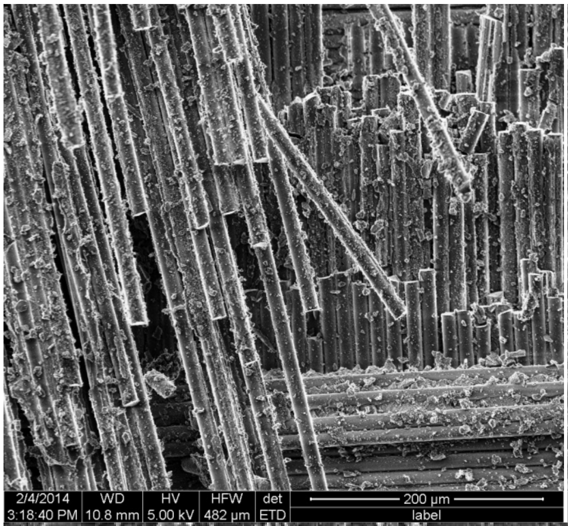
2/4/2014
3:18:40 PM
WD
10.8 mm
HV
5.00 kV
HFW
482 µm
det
ETD
200 µm
label

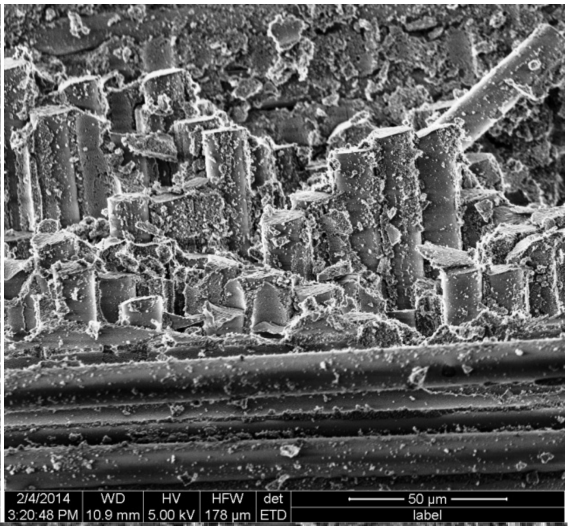
2/4/2014
3:20:48 PM
WD
10.9 mm
HV
5.00 kV
HFW
178 µm
det
ETD
50 µm
label

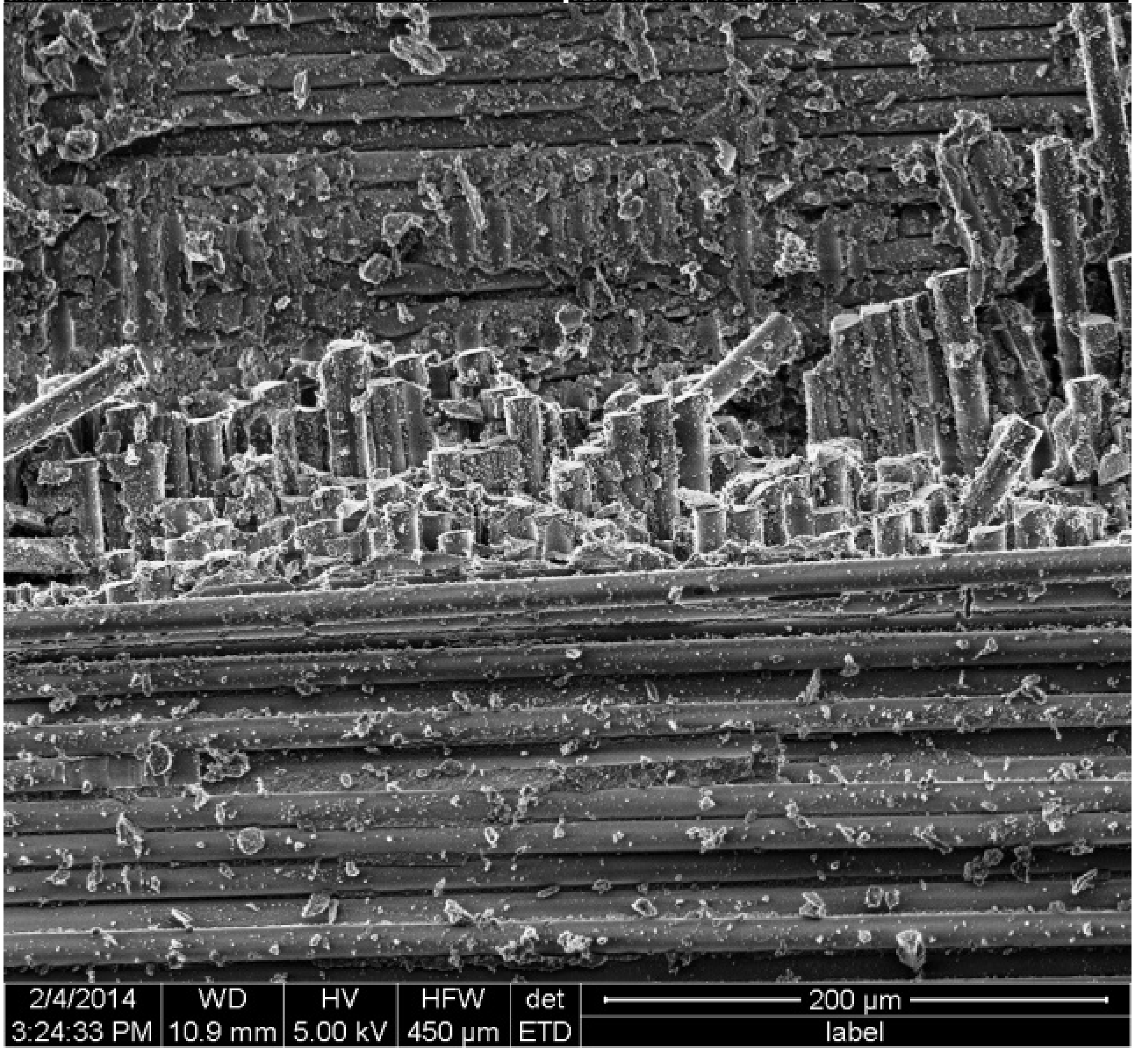
2/4/2014
3:24:33 PM
WD
10.9 mm
HV
5.00 kV
HFW
450 µm
det
ETD
200 µm
label

Appendix T: SEM Images of Specimen 11 – DNS Creep at 6 MPa in Steam at 1100^{o}C.

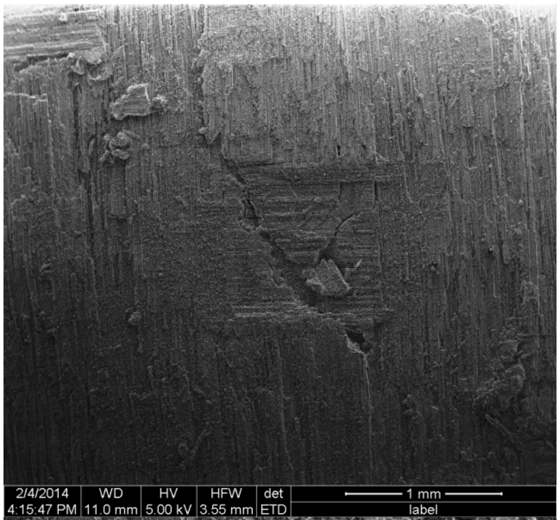
2/4/2014 4:15:47 PM
WD 11.0 mm
HV 5.00 kV
HFW 3.55 mm
det ETD
1 mm
label

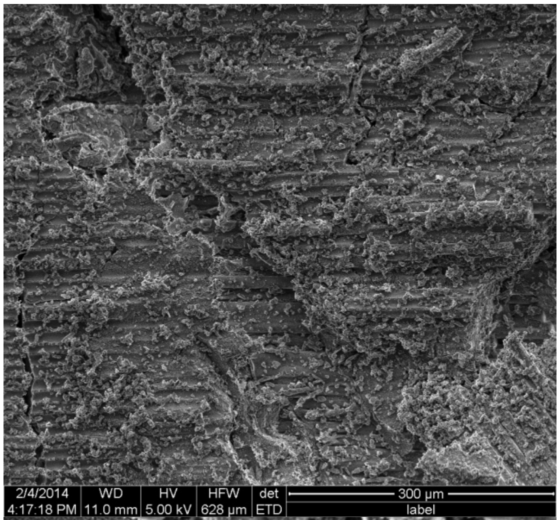
2/4/2014 4:17:18 PM
WD 11.0 mm
HV 5.00 kV
HFW 628 µm
det ETD
300 µm
label

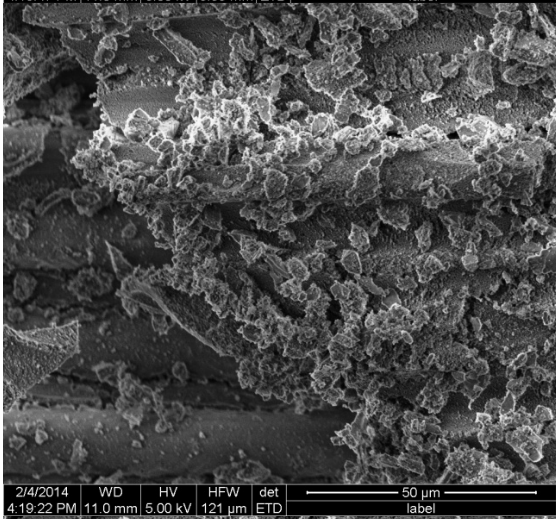
2/4/2014 4:19:22 PM
WD 11.0 mm
HV 5.00 kV
HFW 121 µm
det ETD
50 µm
label

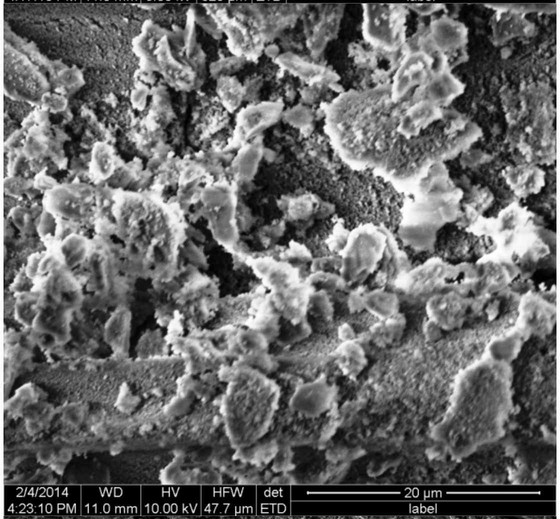
2/4/2014 4:23:10 PM
WD 11.0 mm
HV 10.00 kV
HFW 47.7 µm
det ETD
20 µm
label

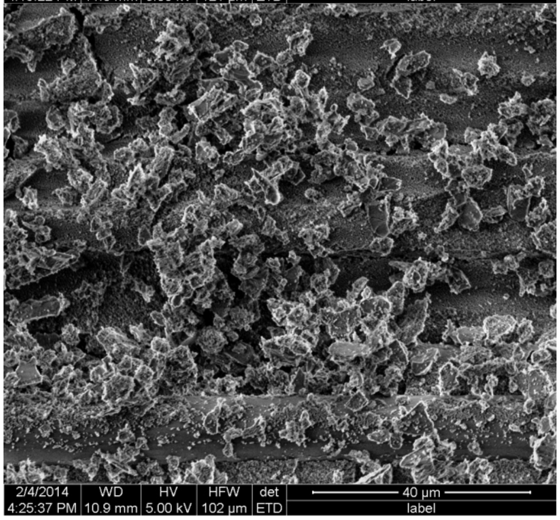
2/4/2014 4:25:37 PM
WD 10.9 mm
HV 5.00 kV
HFW 102 µm
det ETD
40 µm
label

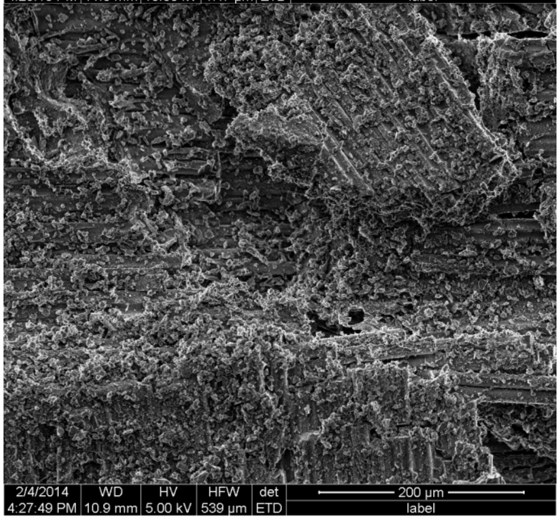
2/4/2014 4:27:49 PM
WD 10.9 mm
HV 5.00 kV
HFW 539 µm
det ETD
200 µm
label

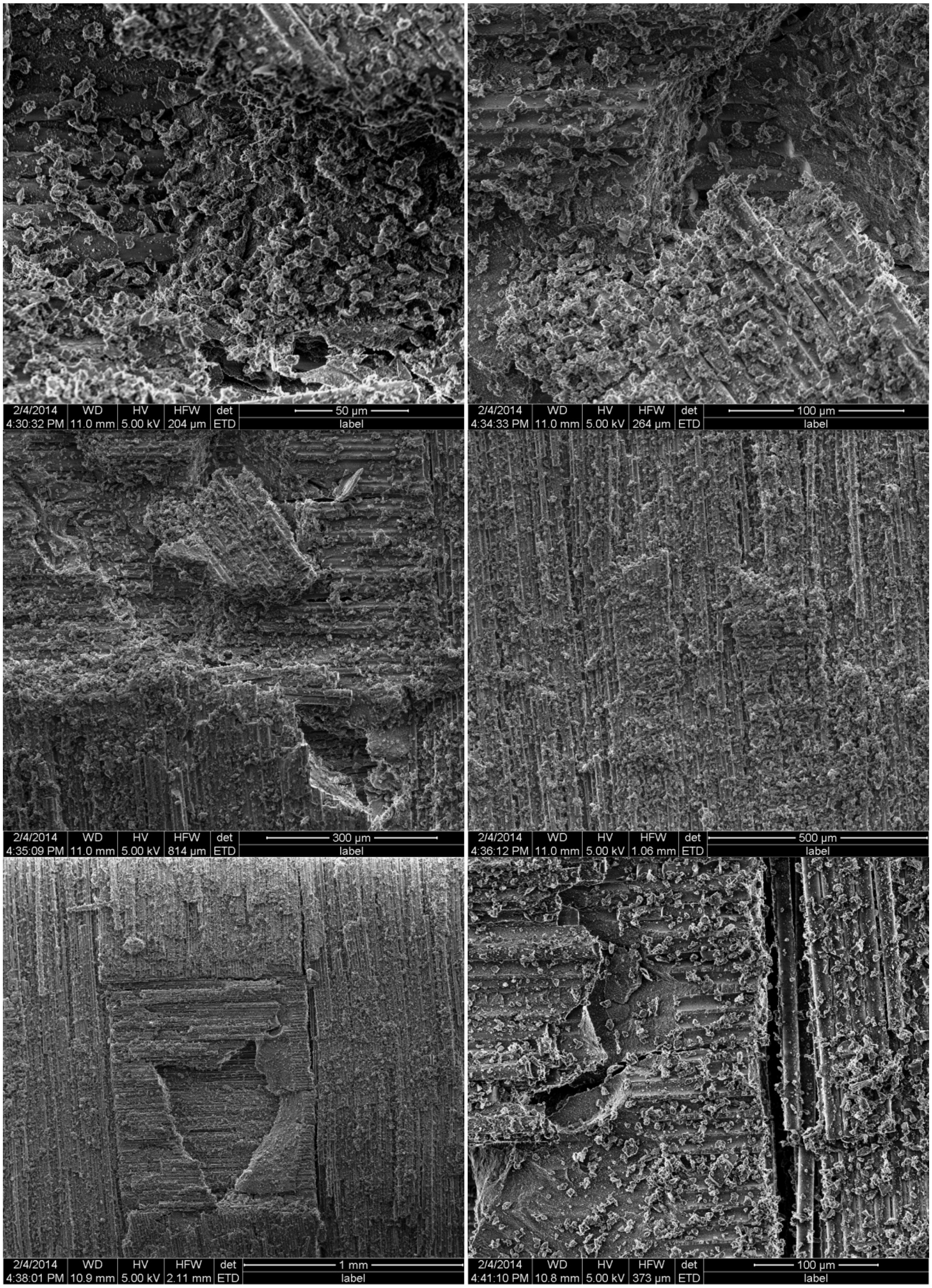
2/4/2014 4:30:32 PM WD 11.0 mm HV 5.00 kV HFW 204 µm det ETD 50 µm label
2/4/2014 4:34:33 PM WD 11.0 mm HV 5.00 kV HFW 264 µm det ETD 100 µm label
2/4/2014 4:35:09 PM WD 11.0 mm HV 5.00 kV HFW 814 µm det ETD 300 µm label
2/4/2014 4:36:12 PM WD 11.0 mm HV 5.00 kV HFW 1.06 mm det ETD 500 µm label
2/4/2014 4:38:01 PM WD 10.9 mm HV 5.00 kV HFW 2.11 mm det ETD 1 mm label
2/4/2014 4:41:10 PM WD 10.8 mm HV 5.00 kV HFW 373 µm det ETD 100 µm label

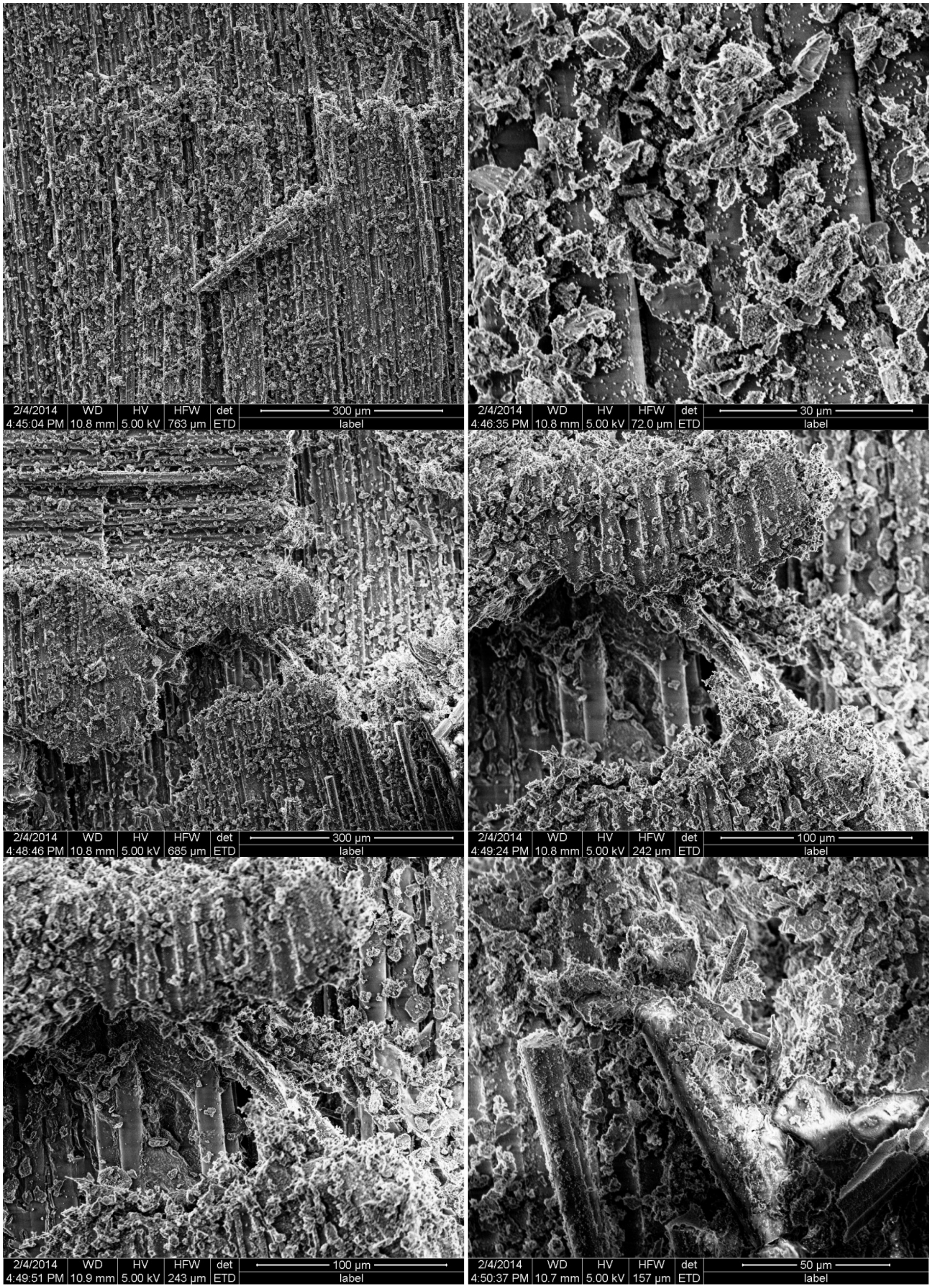
2/4/2014 4:45:04 PM WD 10.8 mm HV 5.00 kV HFW 763 µm det ETD 300 µm label
2/4/2014 4:46:35 PM WD 10.8 mm HV 5.00 kV HFW 72.0 µm det ETD 30 µm label
2/4/2014 4:48:46 PM WD 10.8 mm HV 5.00 kV HFW 685 µm det ETD 300 µm label
2/4/2014 4:49:24 PM WD 10.8 mm HV 5.00 kV HFW 242 µm det ETD 100 µm label
2/4/2014 4:49:51 PM WD 10.9 mm HV 5.00 kV HFW 243 µm det ETD 100 µm label
2/4/2014 4:50:37 PM WD 10.7 mm HV 5.00 kV HFW 157 µm det ETD 50 µm label

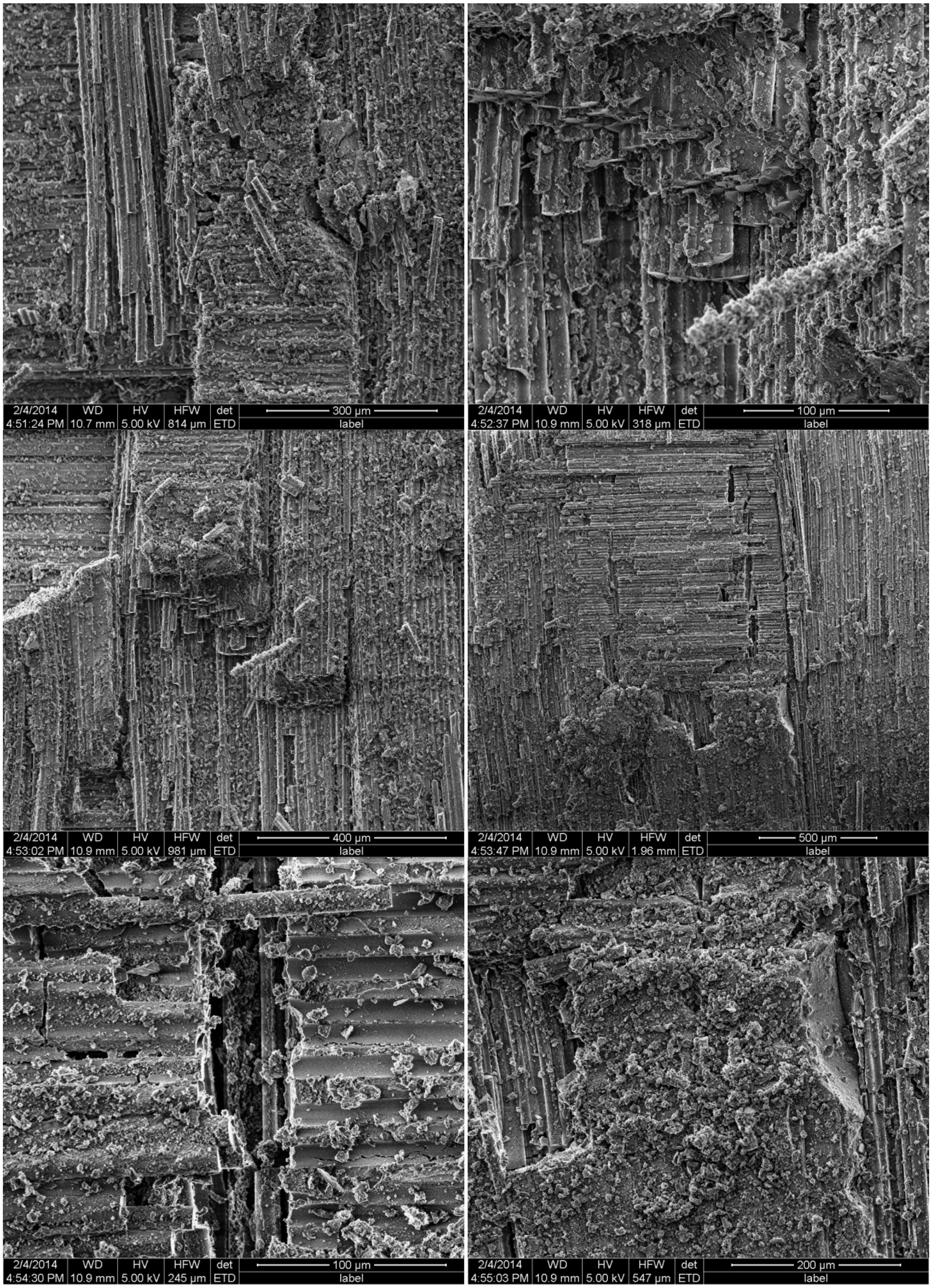
2/4/2014 4:51:24 PM
WD 10.7 mm
HV 5.00 kV
HFW 814 µm
det ETD
300 µm
label
2/4/2014 4:52:37 PM
WD 10.9 mm
HV 5.00 kV
HFW 318 µm
det ETD
100 µm
label
2/4/2014 4:53:02 PM
WD 10.9 mm
HV 5.00 kV
HFW 981 µm
det ETD
400 µm
label
2/4/2014 4:53:47 PM
WD 10.9 mm
HV 5.00 kV
HFW 1.96 mm
det ETD
500 µm
label
2/4/2014 4:54:30 PM
WD 10.9 mm
HV 5.00 kV
HFW 245 µm
det ETD
100 µm
label
2/4/2014 4:55:03 PM
WD 10.9 mm
HV 5.00 kV
HFW 547 µm
det ETD
200 µm
label

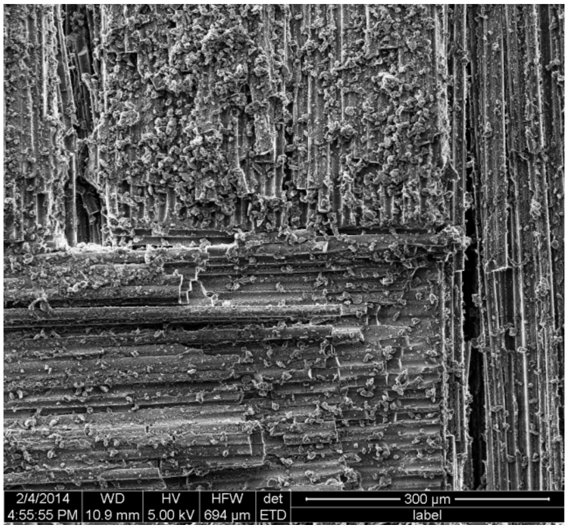
2/4/2014
4:55:55 PM
WD
10.9 mm
HV
5.00 kV
HFW
694 µm
det
ETD
300 µm
label

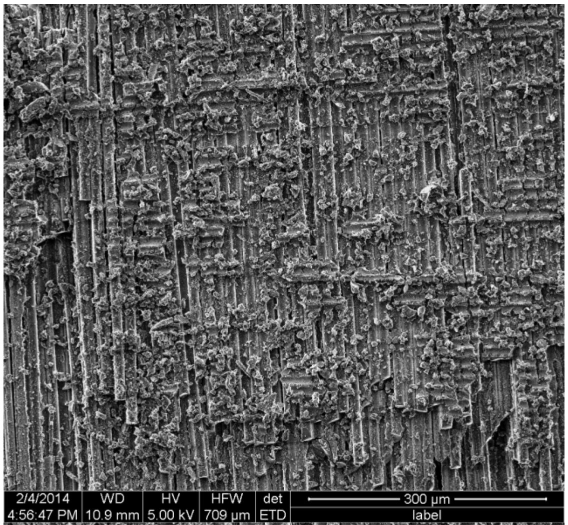
2/4/2014
4:56:47 PM
WD
10.9 mm
HV
5.00 kV
HFW
709 µm
det
ETD
300 µm
label

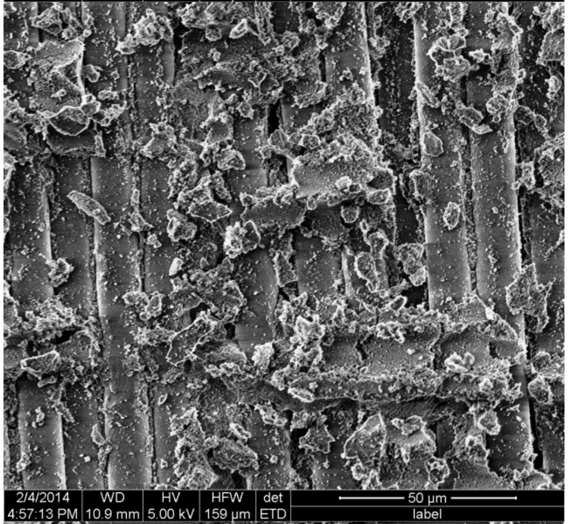
2/4/2014
4:57:13 PM
WD
10.9 mm
HV
5.00 kV
HFW
159 µm
det
ETD
50 µm
label

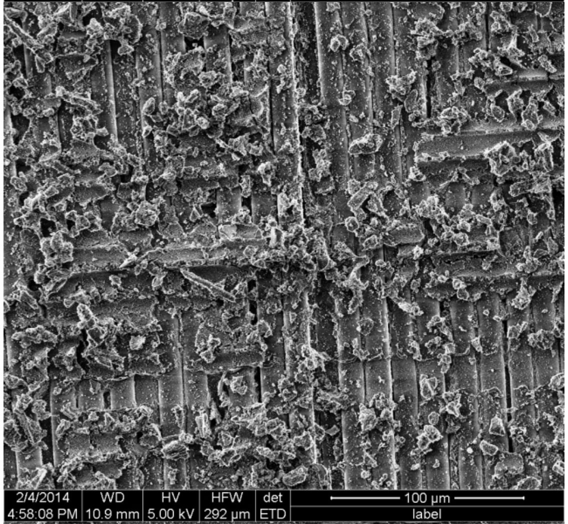
2/4/2014
4:58:08 PM
WD
10.9 mm
HV
5.00 kV
HFW
292 µm
det
ETD
100 µm
label

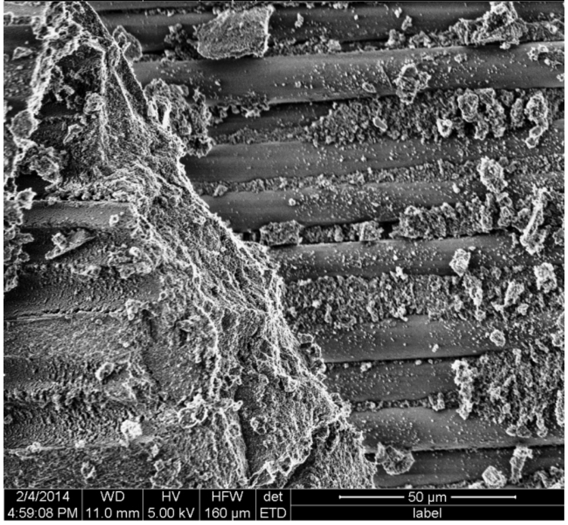
2/4/2014
4:59:08 PM
WD
11.0 mm
HV
5.00 kV
HFW
160 µm
det
ETD
50 µm
label

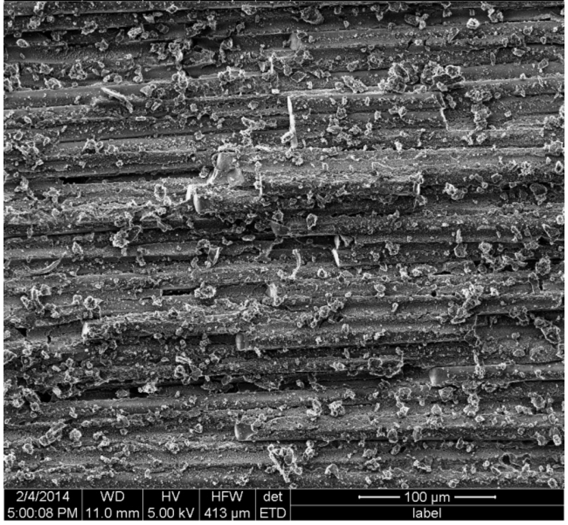
2/4/2014
5:00:08 PM
WD
11.0 mm
HV
5.00 kV
HFW
413 µm
det
ETD
100 µm
label

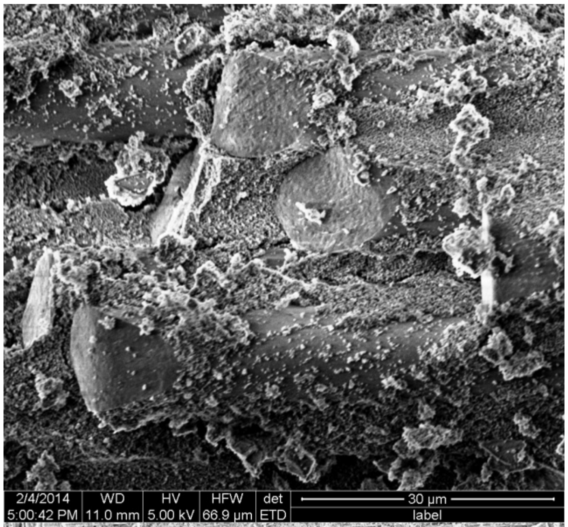
2/4/2014
5:00:42 PM
WD
11.0 mm
HV
5.00 kV
HFW
66.9 µm
det
ETD
30 µm
label

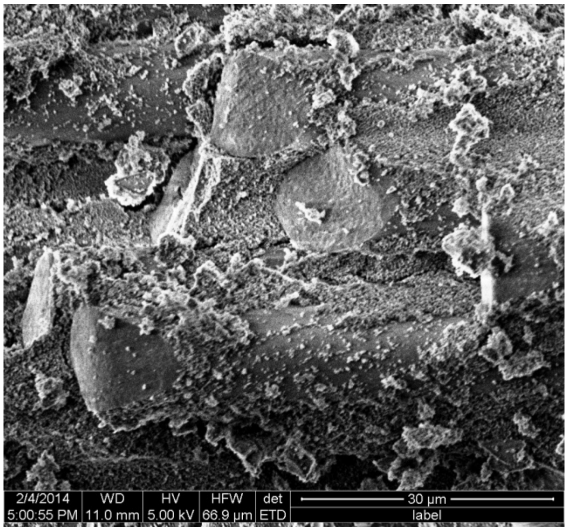
2/4/2014
5:00:55 PM
WD
11.0 mm
HV
5.00 kV
HFW
66.9 µm
det
ETD
30 µm
label

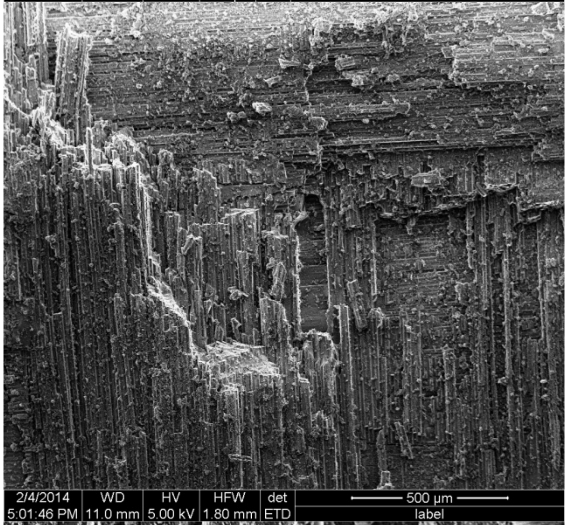
2/4/2014
5:01:46 PM
WD
11.0 mm
HV
5.00 kV
HFW
1.80 mm
det
ETD
500 µm
label

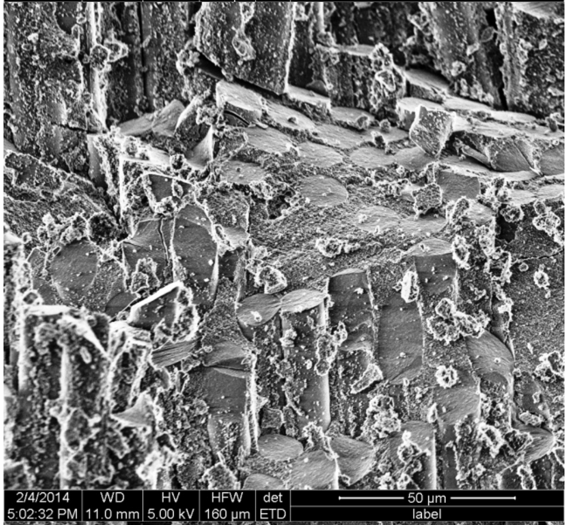
2/4/2014
5:02:32 PM
WD
11.0 mm
HV
5.00 kV
HFW
160 µm
det
ETD
50 µm
label

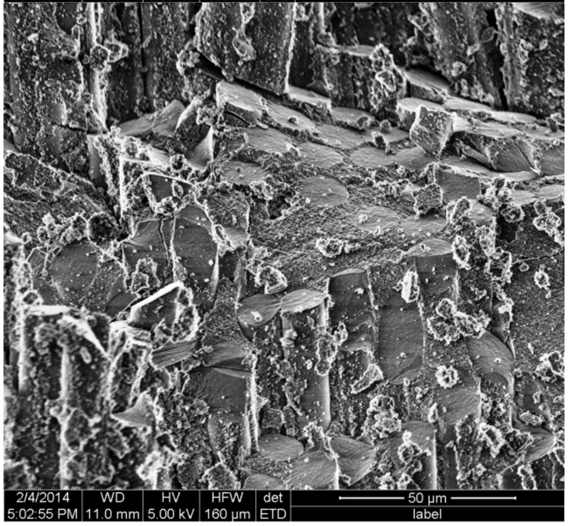
2/4/2014
5:02:55 PM
WD
11.0 mm
HV
5.00 kV
HFW
160 µm
det
ETD
50 µm
label

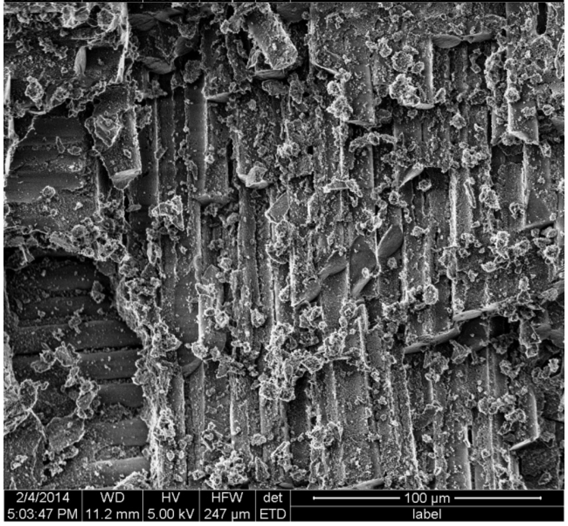
2/4/2014
5:03:47 PM
WD
11.2 mm
HV
5.00 kV
HFW
247 µm
det
ETD
100 µm
label

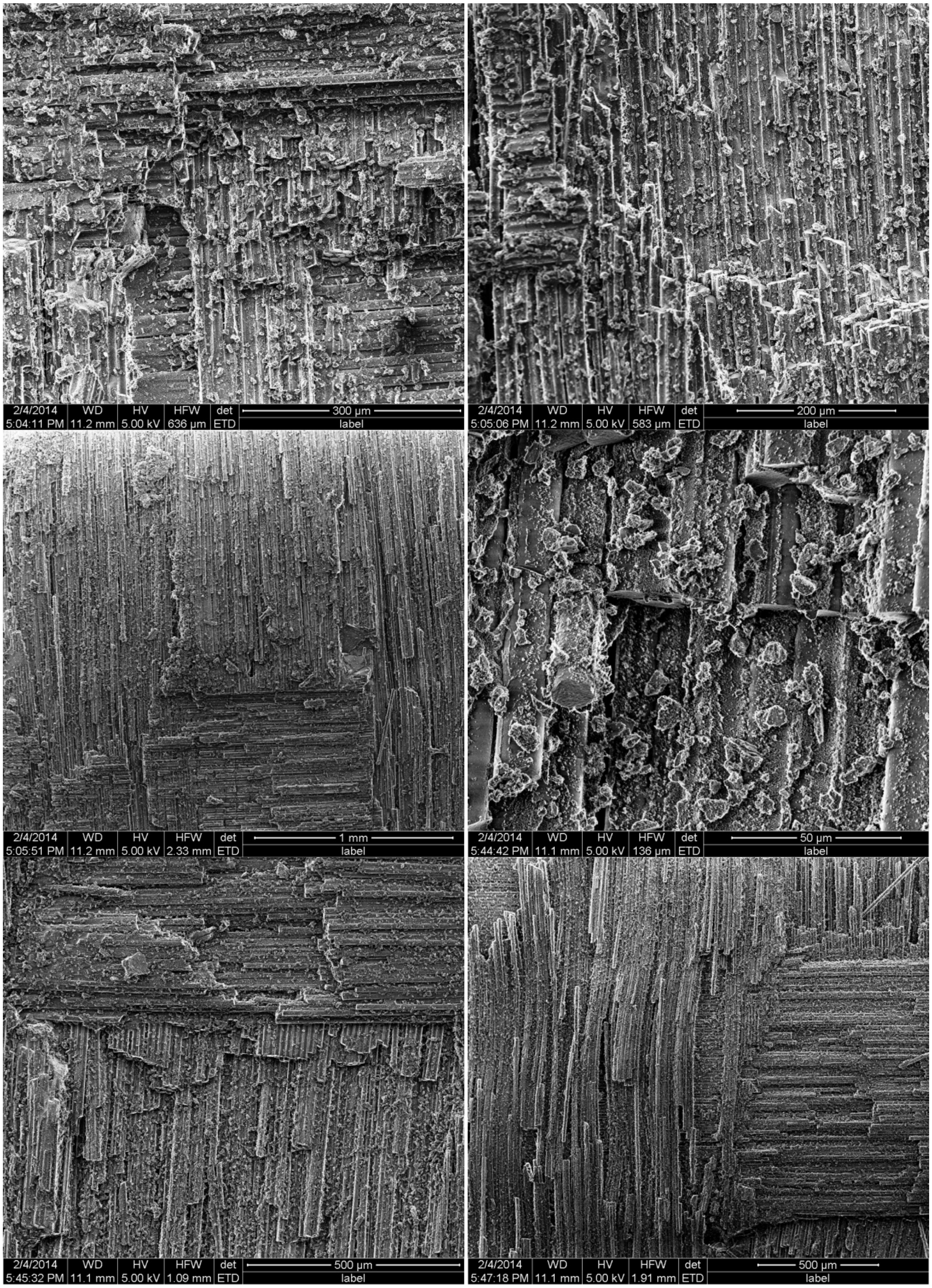
2/4/2014 5:04:11 PM WD 11.2 mm HV 5.00 kV HFW 636 µm det ETD 300 µm label
2/4/2014 5:05:06 PM WD 11.2 mm HV 5.00 kV HFW 583 µm det ETD 200 µm label
2/4/2014 5:05:51 PM WD 11.2 mm HV 5.00 kV HFW 2.33 mm det ETD 1 mm label
2/4/2014 5:44:42 PM WD 11.1 mm HV 5.00 kV HFW 136 µm det ETD 50 µm label
2/4/2014 5:45:32 PM WD 11.1 mm HV 5.00 kV HFW 1.09 mm det ETD 500 µm label
2/4/2014 5:47:18 PM WD 11.1 mm HV 5.00 kV HFW 1.91 mm det ETD 500 µm label

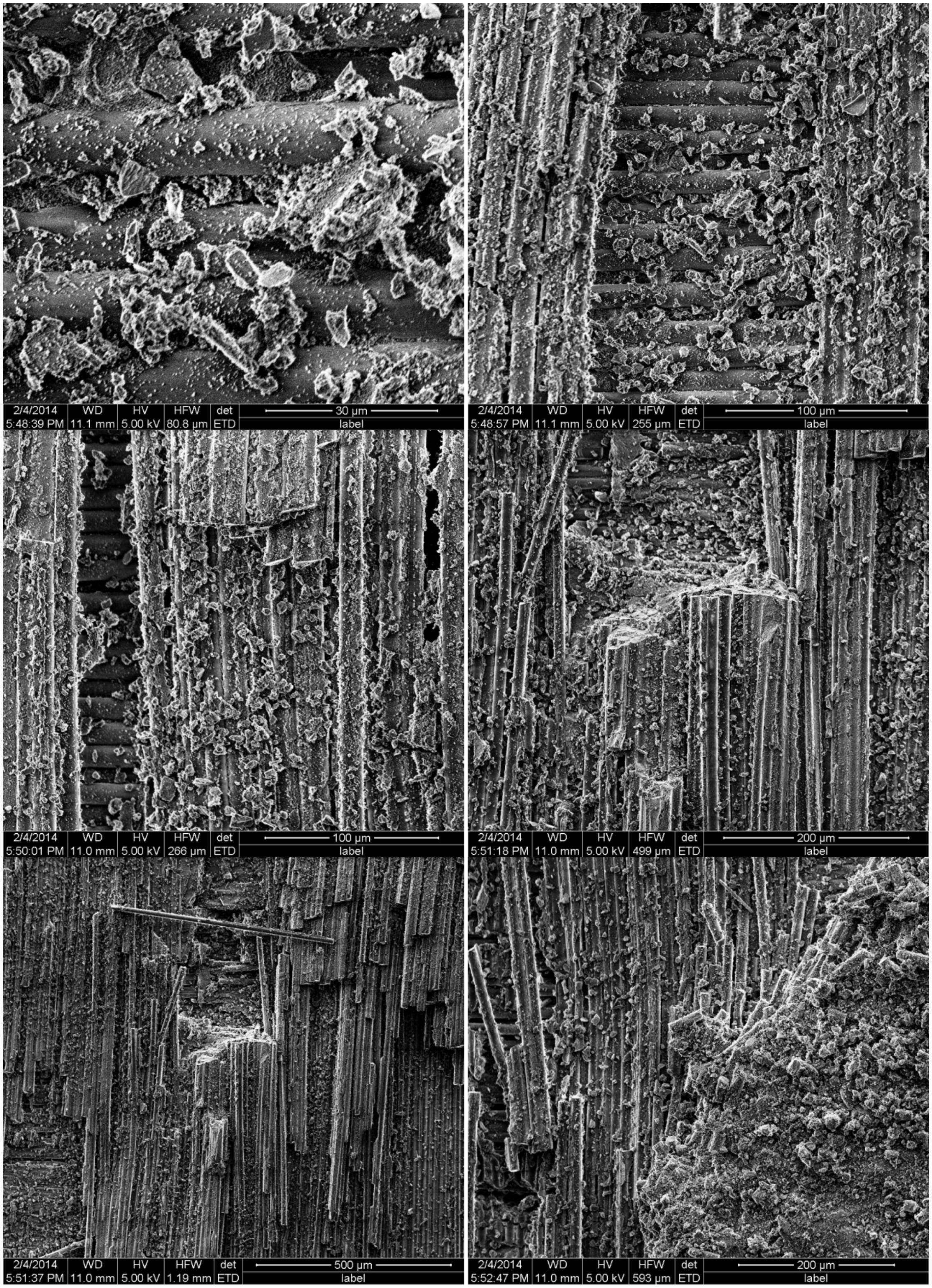
2/4/2014 5:48:39 PM WD 11.1 mm HV 5.00 kV HFW 80.8 µm det ETD 30 µm label
2/4/2014 5:48:57 PM WD 11.1 mm HV 5.00 kV HFW 255 µm det ETD 100 µm label
2/4/2014 5:50:01 PM WD 11.0 mm HV 5.00 kV HFW 266 µm det ETD 100 µm label
2/4/2014 5:51:18 PM WD 11.0 mm HV 5.00 kV HFW 499 µm det ETD 200 µm label
2/4/2014 5:51:37 PM WD 11.0 mm HV 5.00 kV HFW 1.19 mm det ETD 500 µm label
2/4/2014 5:52:47 PM WD 11.0 mm HV 5.00 kV HFW 593 µm det ETD 200 µm label

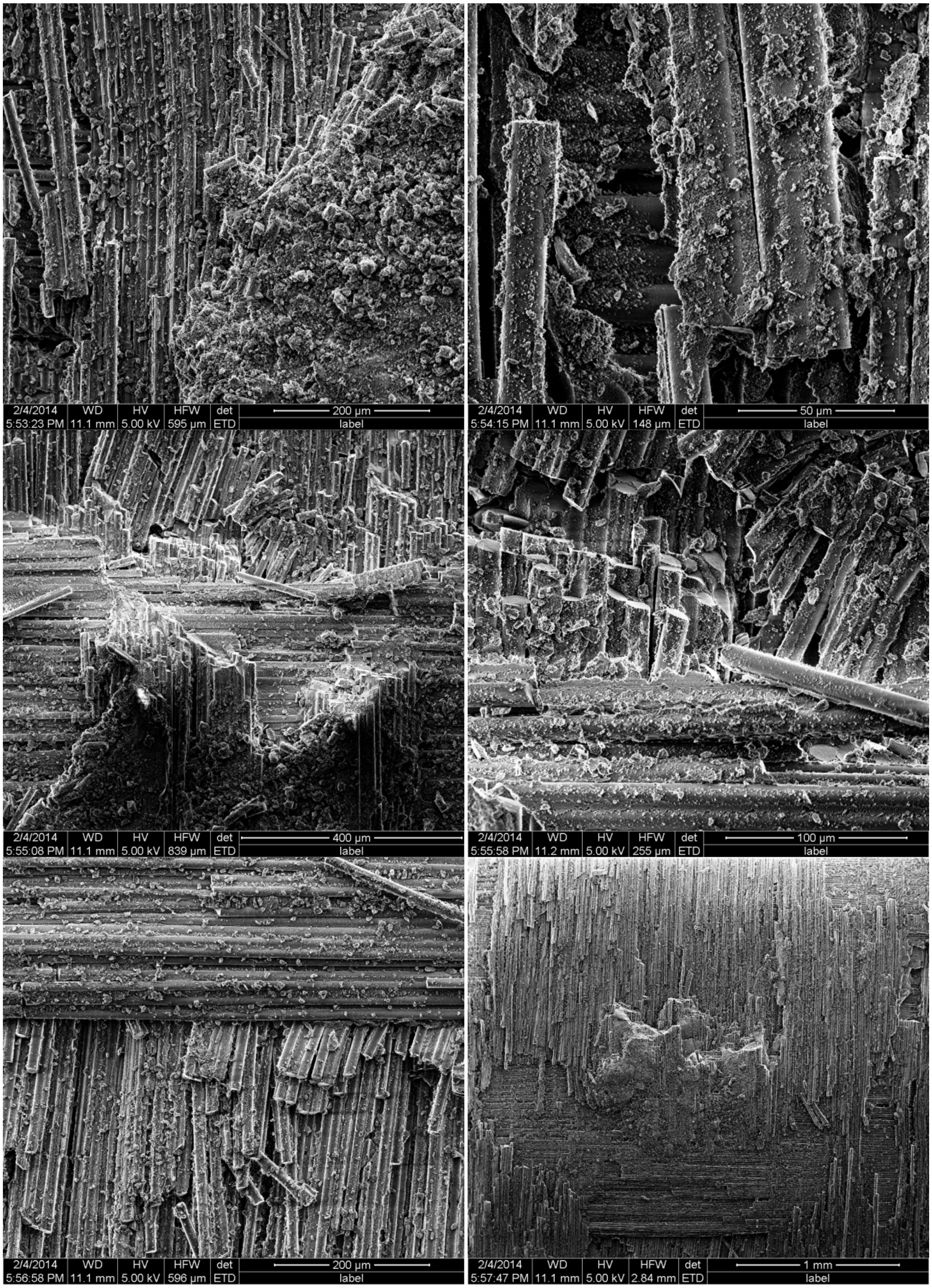
2/4/2014 5:53:23 PM WD 11.1 mm HV 5.00 kV HFW 595 µm det ETD 200 µm label
2/4/2014 5:54:15 PM WD 11.1 mm HV 5.00 kV HFW 148 µm det ETD 50 µm label
2/4/2014 5:55:08 PM WD 11.1 mm HV 5.00 kV HFW 839 µm det ETD 400 µm label
2/4/2014 5:55:58 PM WD 11.2 mm HV 5.00 kV HFW 255 µm det ETD 100 µm label
2/4/2014 5:56:58 PM WD 11.1 mm HV 5.00 kV HFW 596 µm det ETD 200 µm label
2/4/2014 5:57:47 PM WD 11.1 mm HV 5.00 kV HFW 2.84 mm det ETD 1 mm label

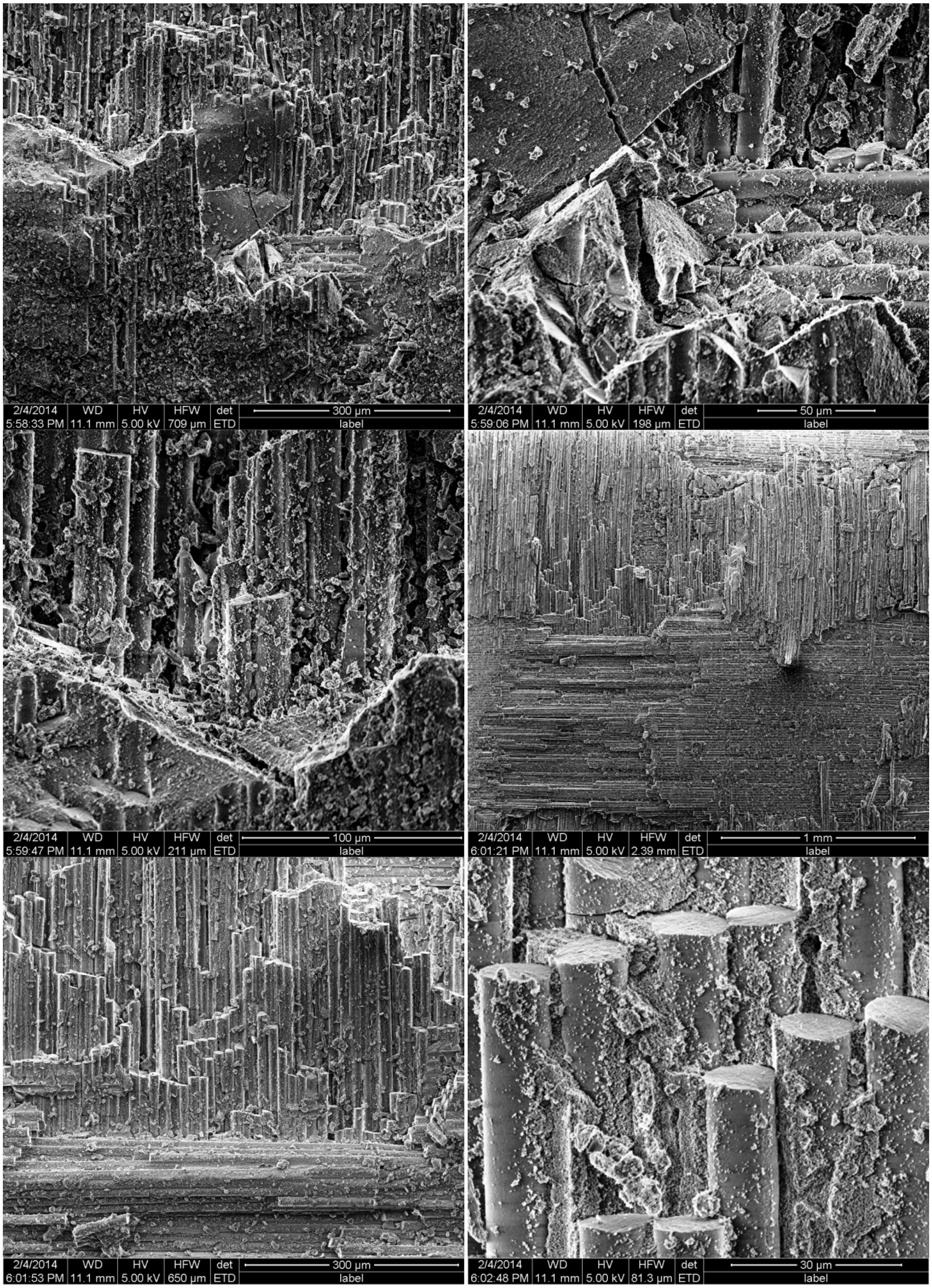
2/4/2014 5:58:33 PM WD 11.1 mm HV 5.00 kV HFW 709 µm det ETD 300 µm label
2/4/2014 5:59:06 PM WD 11.1 mm HV 5.00 kV HFW 198 µm det ETD 50 µm label
2/4/2014 5:59:47 PM WD 11.1 mm HV 5.00 kV HFW 211 µm det ETD 100 µm label
2/4/2014 6:01:21 PM WD 11.1 mm HV 5.00 kV HFW 2.39 mm det ETD 1 mm label
2/4/2014 6:01:53 PM WD 11.1 mm HV 5.00 kV HFW 650 µm det ETD 300 µm label
2/4/2014 6:02:48 PM WD 11.1 mm HV 5.00 kV HFW 81.3 µm det ETD 30 µm label

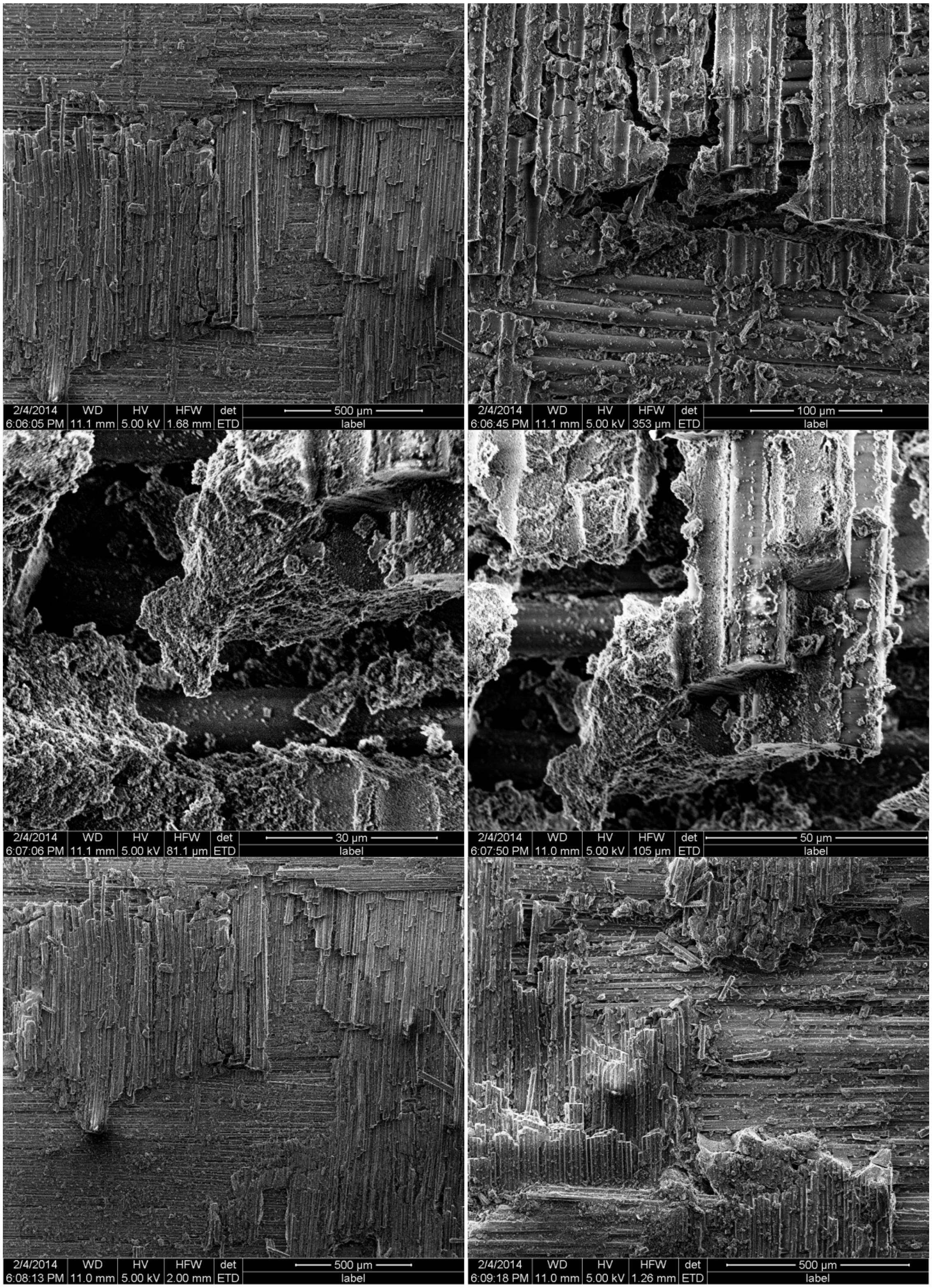
2/4/2014 WD HV HFW det 500 µm
6:06:05 PM 11.1 mm 5.00 kV 1.68 mm ETD label
2/4/2014 WD HV HFW det 100 µm
6:06:45 PM 11.1 mm 5.00 kV 353 µm ETD label
2/4/2014 WD HV HFW det 30 µm
6:07:06 PM 11.1 mm 5.00 kV 81.1 µm ETD label
2/4/2014 WD HV HFW det 50 µm
6:07:50 PM 11.0 mm 5.00 kV 105 µm ETD label
2/4/2014 WD HV HFW det 500 µm
6:08:13 PM 11.0 mm 5.00 kV 2.00 mm ETD label
2/4/2014 WD HV HFW det 500 µm
6:09:18 PM 11.0 mm 5.00 kV 1.26 mm ETD label

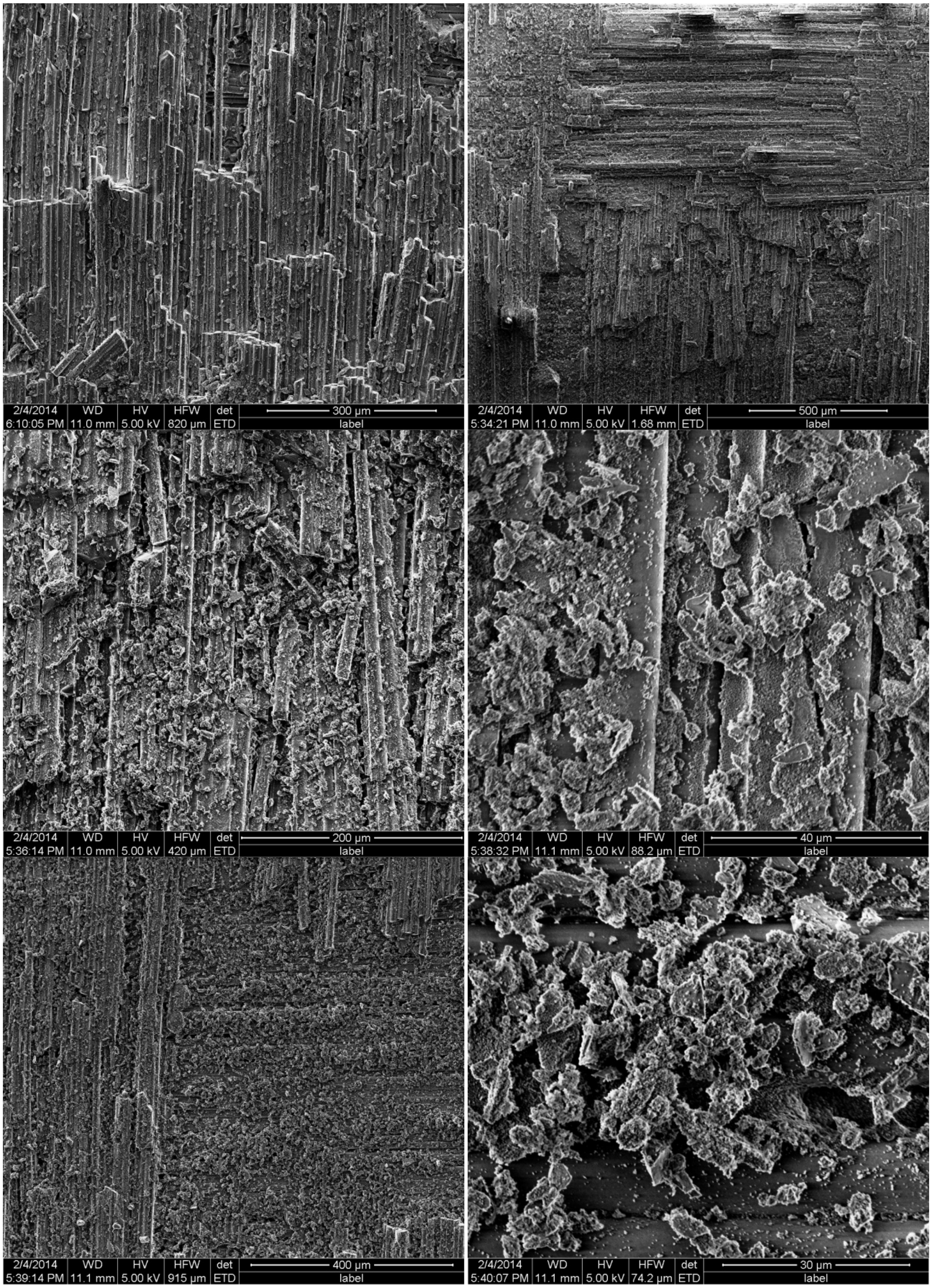
2/4/2014 6:10:05 PM | WD 11.0 mm | HV 5.00 kV | HFW 820 µm | det ETD | 300 µm | label
2/4/2014 5:34:21 PM | WD 11.0 mm | HV 5.00 kV | HFW 1.68 mm | det ETD | 500 µm | label
2/4/2014 5:36:14 PM | WD 11.0 mm | HV 5.00 kV | HFW 420 µm | det ETD | 200 µm | label
2/4/2014 5:38:32 PM | WD 11.1 mm | HV 5.00 kV | HFW 88.2 µm | det ETD | 40 µm | label
2/4/2014 5:39:14 PM | WD 11.1 mm | HV 5.00 kV | HFW 915 µm | det ETD | 400 µm | label
2/4/2014 5:40:07 PM | WD 11.1 mm | HV 5.00 kV | HFW 74.2 µm | det ETD | 30 µm | label

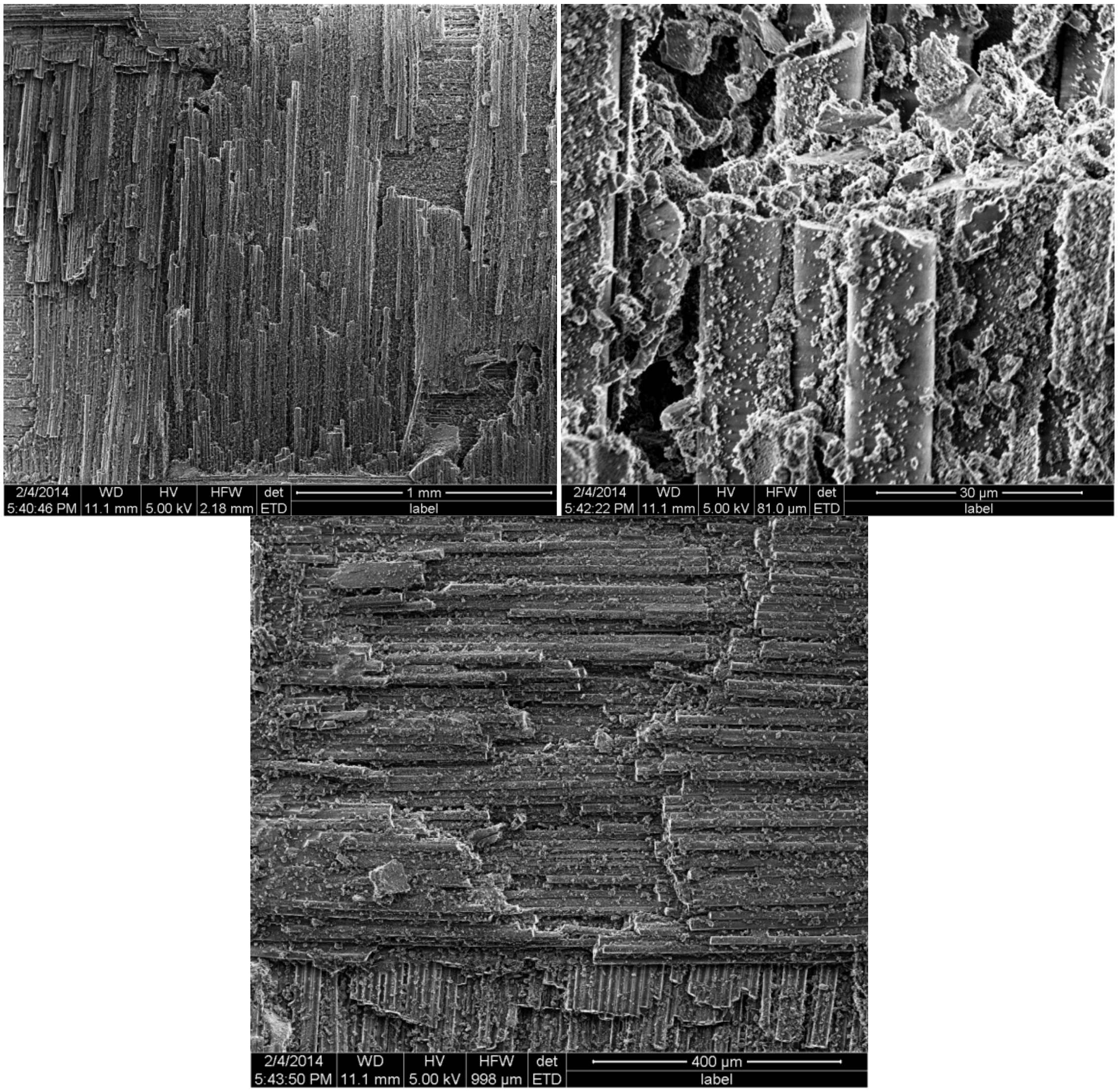
2/4/2014
5:40:46 PM
WD
11.1 mm
HV
5.00 kV
HFW
2.18 mm
det
ETD
1 mm
label
2/4/2014
5:42:22 PM
WD
11.1 mm
HV
5.00 kV
HFW
81.0 µm
det
ETD
30 µm
label
2/4/2014
5:43:50 PM
WD
11.1 mm
HV
5.00 kV
HFW
998 µm
det
ETD
400 µm
label

Appendix U: SEM Images of Specimen 13 – DNS Creep at 2 MPa in Steam at 1100^{o}C.

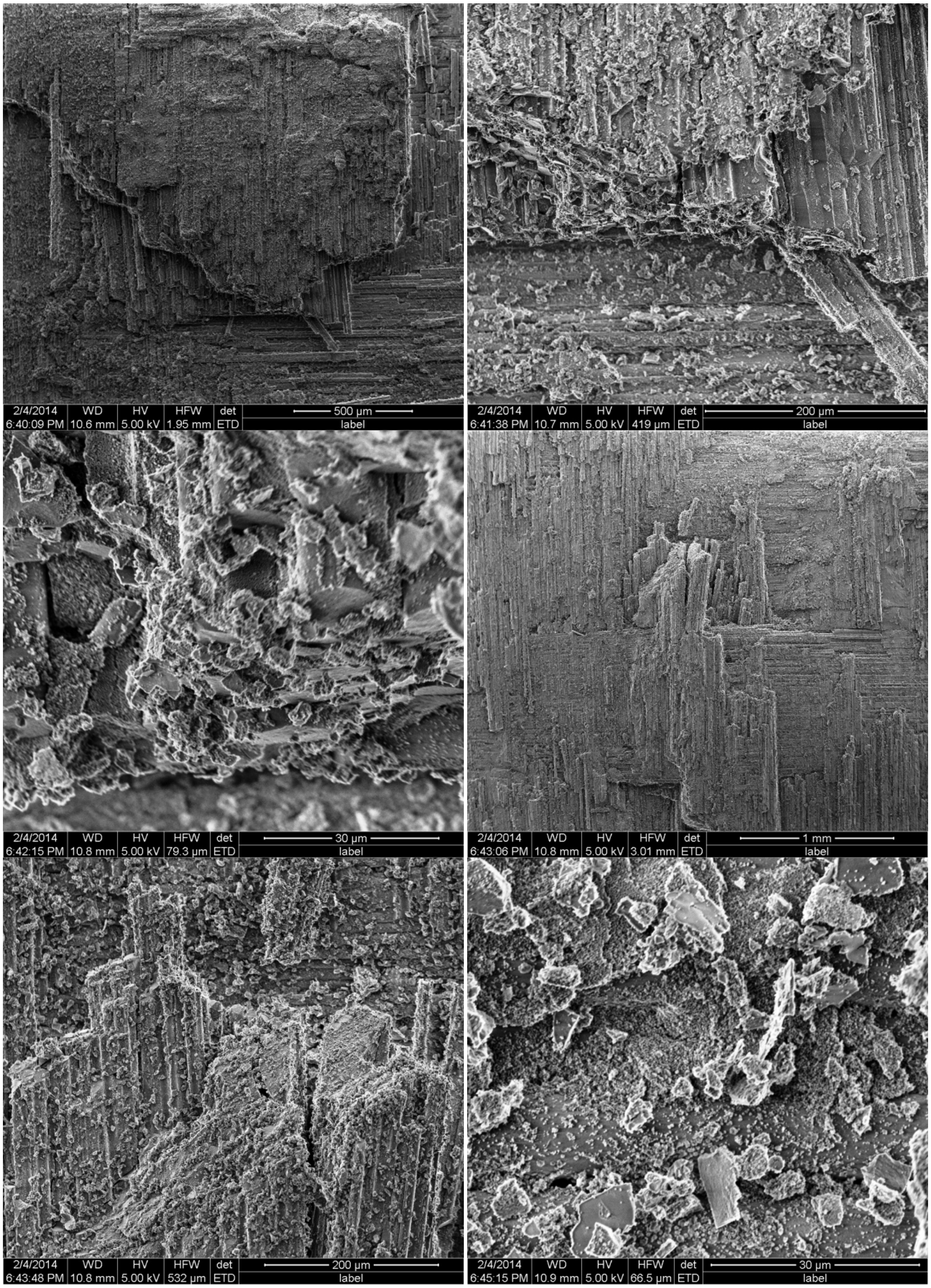
2/4/2014 6:40:09 PM WD 10.6 mm HV 5.00 kV HFW 1.95 mm det ETD 500 µm label
2/4/2014 6:41:38 PM WD 10.7 mm HV 5.00 kV HFW 419 µm det ETD 200 µm label
2/4/2014 6:42:15 PM WD 10.8 mm HV 5.00 kV HFW 79.3 µm det ETD 30 µm label
2/4/2014 6:43:06 PM WD 10.8 mm HV 5.00 kV HFW 3.01 mm det ETD 1 mm label
2/4/2014 6:43:48 PM WD 10.8 mm HV 5.00 kV HFW 532 µm det ETD 200 µm label
2/4/2014 6:45:15 PM WD 10.9 mm HV 5.00 kV HFW 66.5 µm det ETD 30 µm label

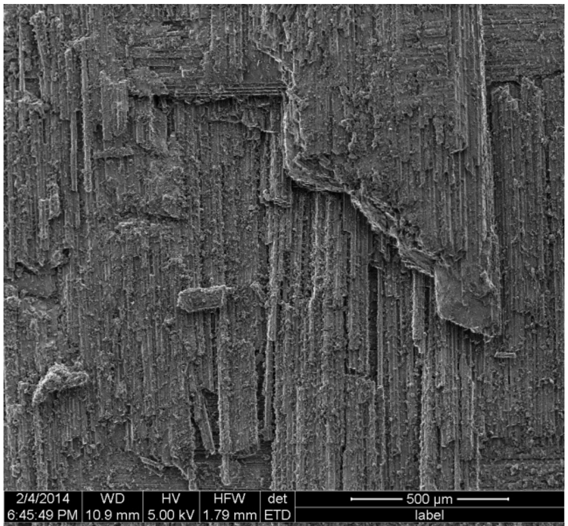
2/4/2014
6:45:49 PM
WD
10.9 mm
HV
5.00 kV
HFW
1.79 mm
det
ETD
500 μm
label

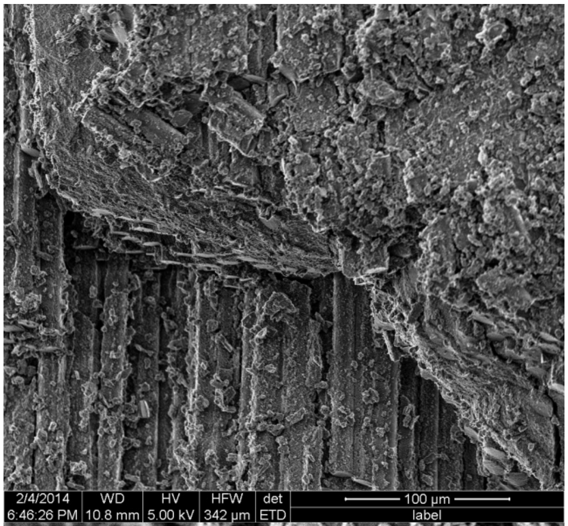
2/4/2014
6:46:26 PM
WD
10.8 mm
HV
5.00 kV
HFW
342 μm
det
ETD
100 μm
label

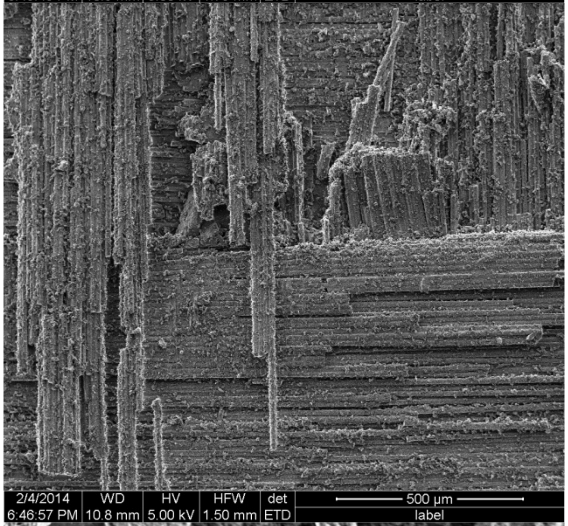
2/4/2014
6:46:57 PM
WD
10.8 mm
HV
5.00 kV
HFW
1.50 mm
det
ETD
500 μm
label

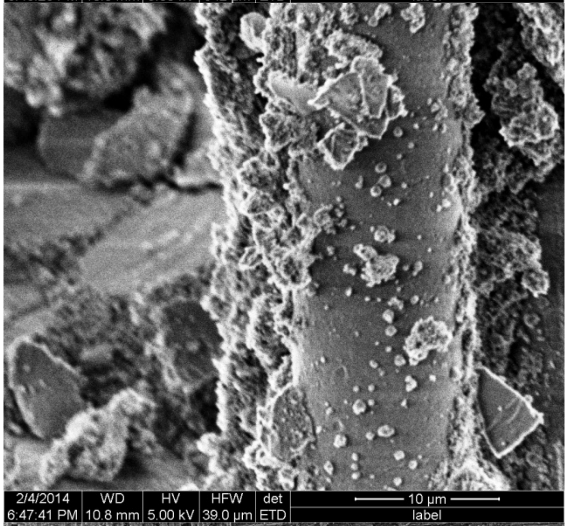
2/4/2014
6:47:41 PM
WD
10.8 mm
HV
5.00 kV
HFW
39.0 μm
det
ETD
10 μm
label

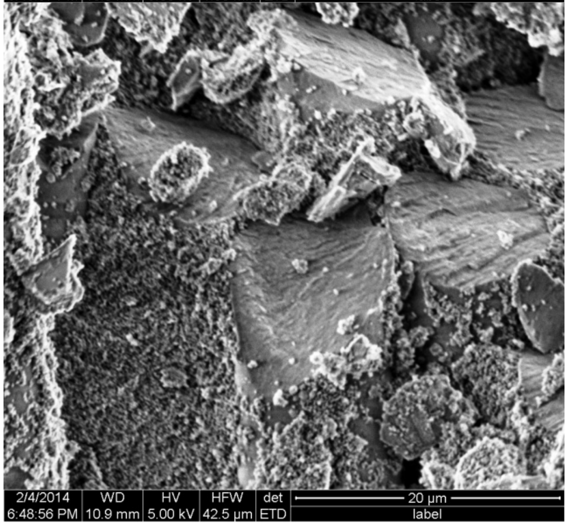
2/4/2014
6:48:56 PM
WD
10.9 mm
HV
5.00 kV
HFW
42.5 μm
det
ETD
20 μm
label

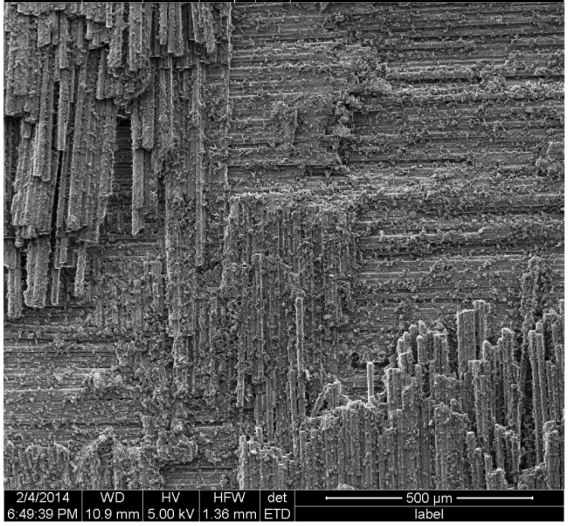
2/4/2014
6:49:39 PM
WD
10.9 mm
HV
5.00 kV
HFW
1.36 mm
det
ETD
500 μm
label

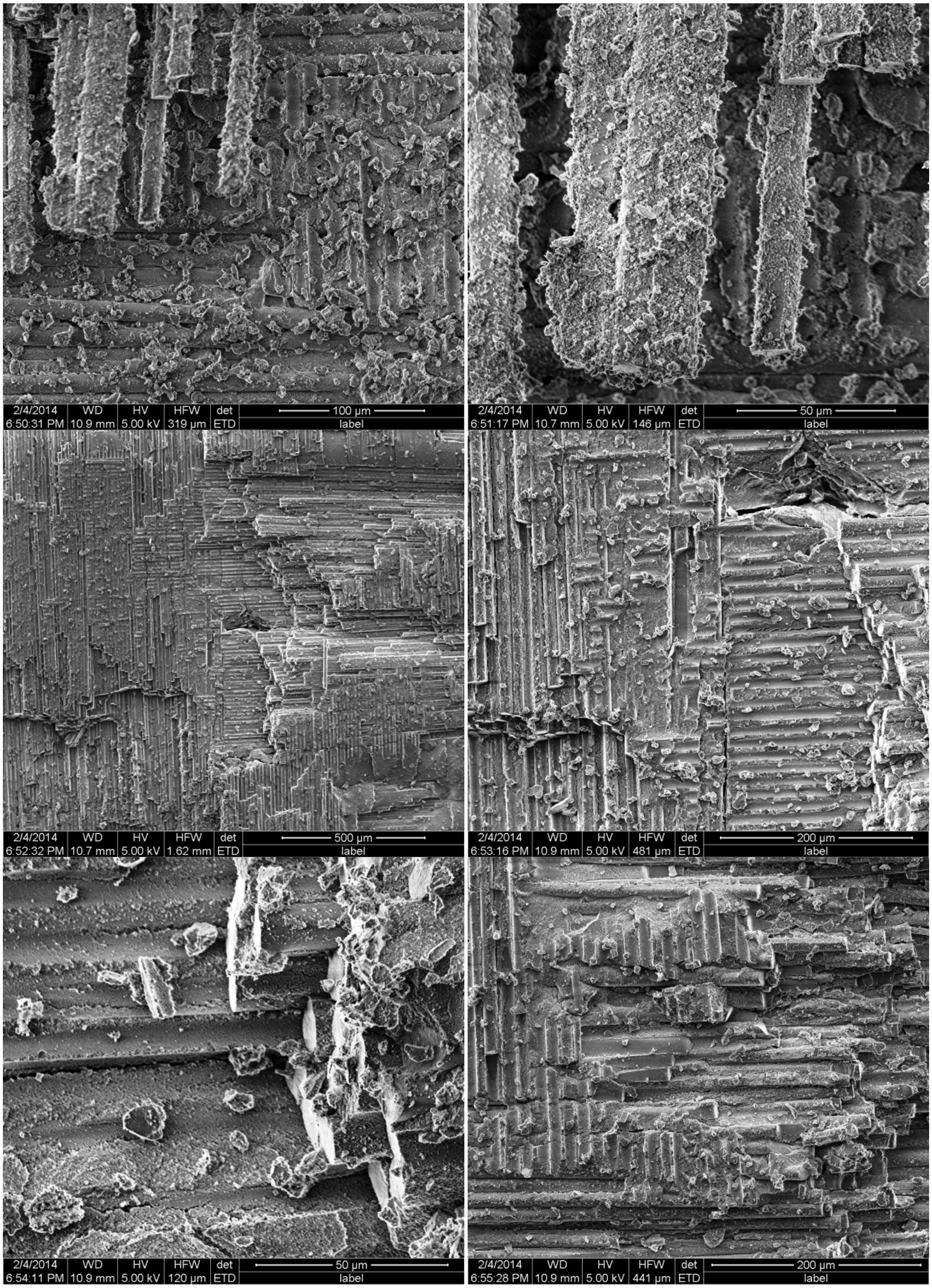
2/4/2014 6:50:31 PM WD 10.9 mm HV 5.00 kV HFW 319 µm det ETD 100 µm label
2/4/2014 6:51:17 PM WD 10.7 mm HV 5.00 kV HFW 146 µm det ETD 50 µm label
2/4/2014 6:52:32 PM WD 10.7 mm HV 5.00 kV HFW 1.62 mm det ETD 500 µm label
2/4/2014 6:53:16 PM WD 10.9 mm HV 5.00 kV HFW 481 µm det ETD 200 µm label
2/4/2014 6:54:11 PM WD 10.9 mm HV 5.00 kV HFW 120 µm det ETD 50 µm label
2/4/2014 6:55:28 PM WD 10.9 mm HV 5.00 kV HFW 441 µm det ETD 200 µm label

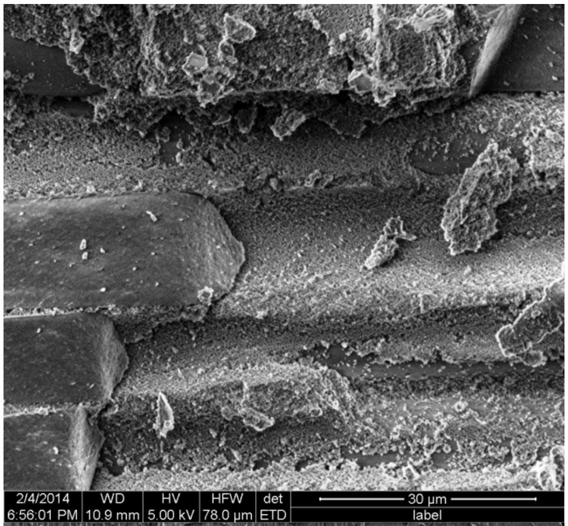
2/4/2014
6:56:01 PM
WD
10.9 mm
HV
5.00 kV
HFW
78.0 µm
det
ETD
30 µm
label

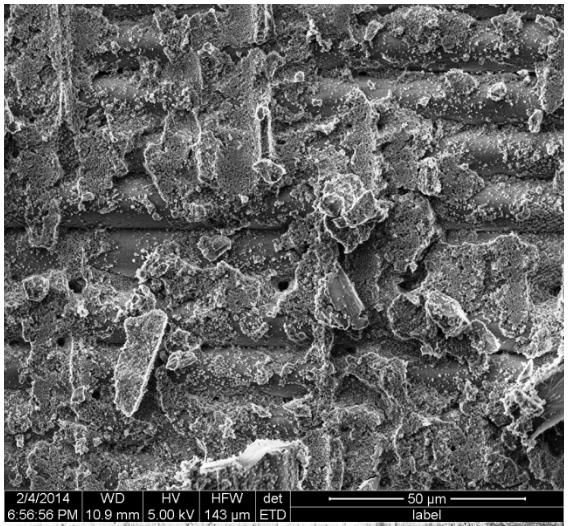
2/4/2014
6:56:56 PM
WD
10.9 mm
HV
5.00 kV
HFW
143 µm
det
ETD
50 µm
label

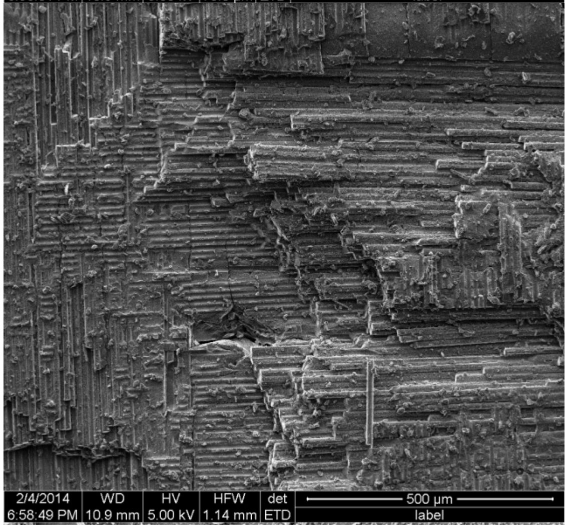
2/4/2014
6:58:49 PM
WD
10.9 mm
HV
5.00 kV
HFW
1.14 mm
det
ETD
500 µm
label

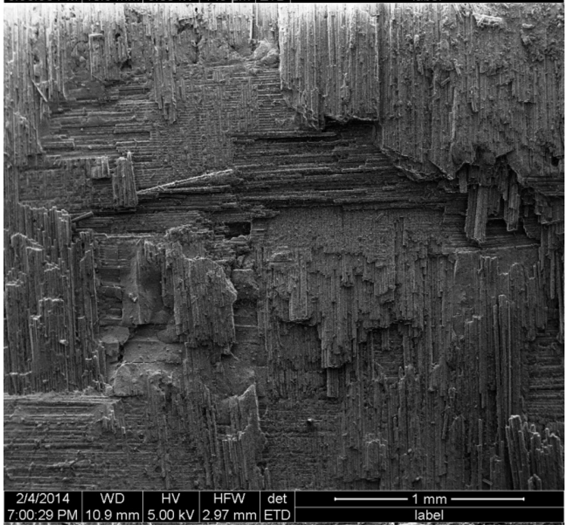
2/4/2014
7:00:29 PM
WD
10.9 mm
HV
5.00 kV
HFW
2.97 mm
det
ETD
1 mm
label

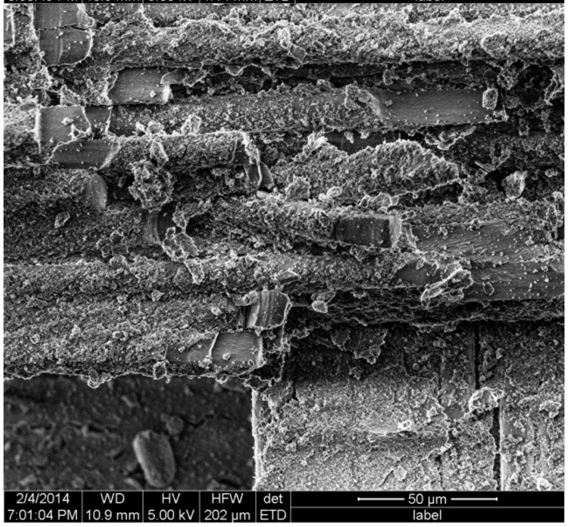
2/4/2014
7:01:04 PM
WD
10.9 mm
HV
5.00 kV
HFW
202 µm
det
ETD
50 µm
label

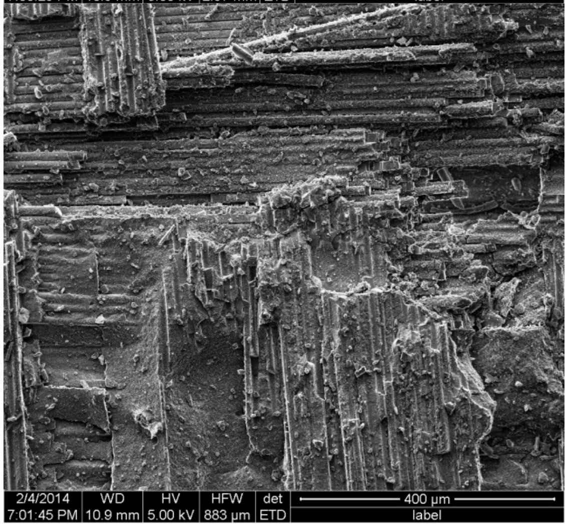
2/4/2014
7:01:45 PM
WD
10.9 mm
HV
5.00 kV
HFW
883 µm
det
ETD
400 µm
label

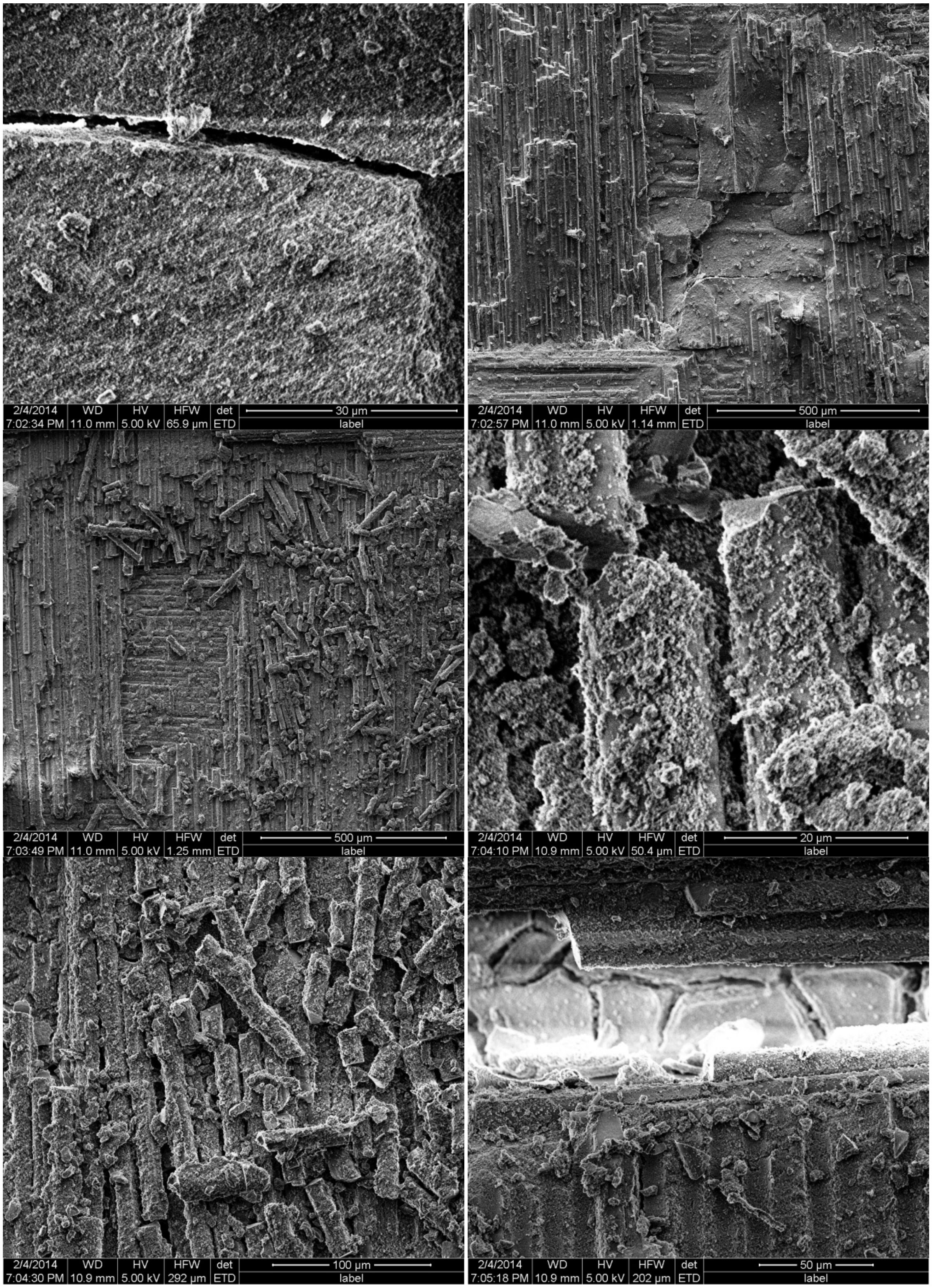
2/4/2014 7:02:34 PM | WD 11.0 mm | HV 5.00 kV | HFW 65.9 µm | det ETD | 30 µm | label
2/4/2014 7:02:57 PM | WD 11.0 mm | HV 5.00 kV | HFW 1.14 mm | det ETD | 500 µm | label
2/4/2014 7:03:49 PM | WD 11.0 mm | HV 5.00 kV | HFW 1.25 mm | det ETD | 500 µm | label
2/4/2014 7:04:10 PM | WD 10.9 mm | HV 5.00 kV | HFW 50.4 µm | det ETD | 20 µm | label
2/4/2014 7:04:30 PM | WD 10.9 mm | HV 5.00 kV | HFW 292 µm | det ETD | 100 µm | label
2/4/2014 7:05:18 PM | WD 10.9 mm | HV 5.00 kV | HFW 202 µm | det ETD | 50 µm | label

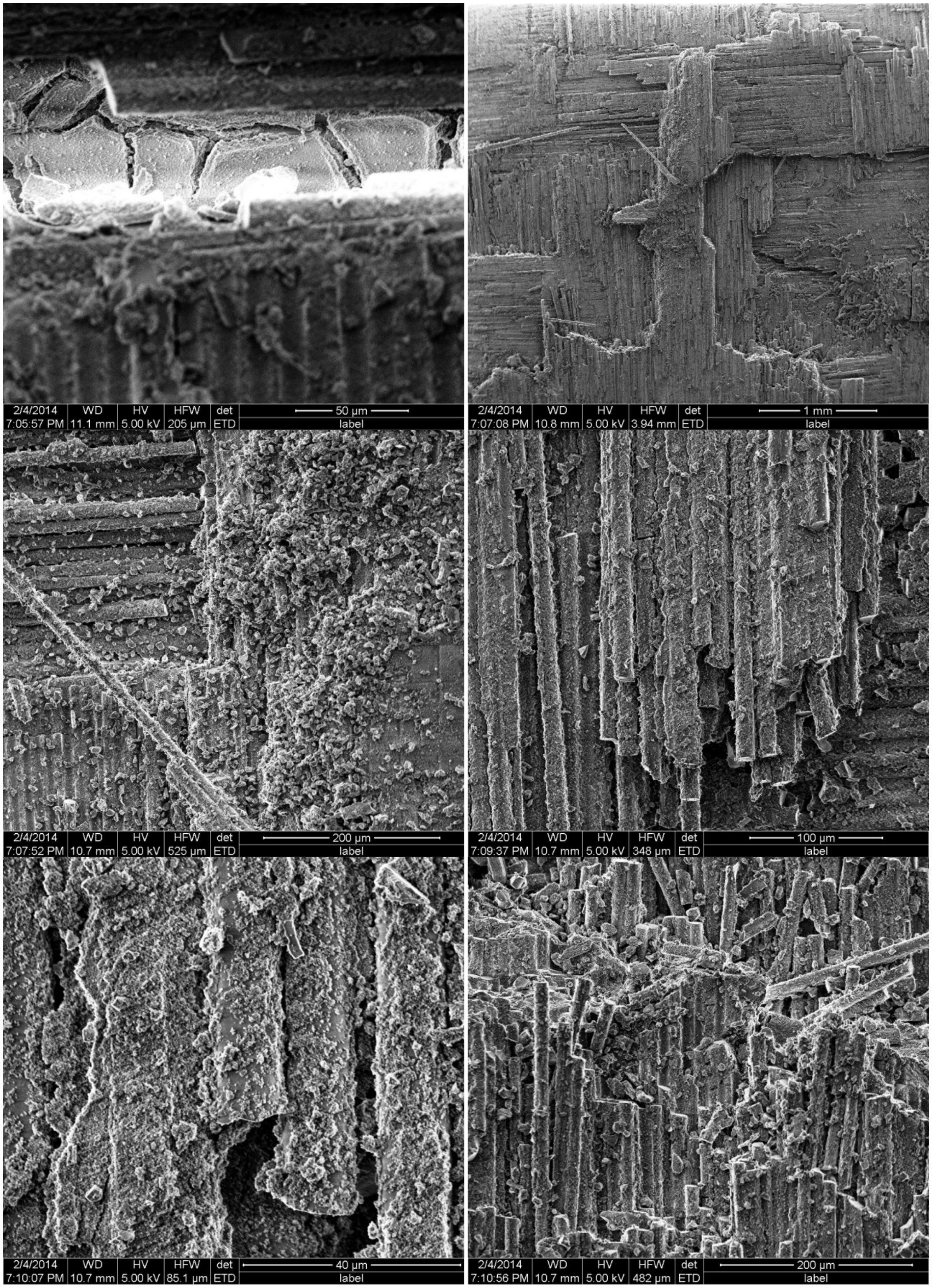
2/4/2014 7:05:57 PM | WD 11.1 mm | HV 5.00 kV | HFW 205 µm | det ETD | 50 µm | label
2/4/2014 7:07:08 PM | WD 10.8 mm | HV 5.00 kV | HFW 3.94 mm | det ETD | 1 mm | label
2/4/2014 7:07:52 PM | WD 10.7 mm | HV 5.00 kV | HFW 525 µm | det ETD | 200 µm | label
2/4/2014 7:09:37 PM | WD 10.7 mm | HV 5.00 kV | HFW 348 µm | det ETD | 100 µm | label
2/4/2014 7:10:07 PM | WD 10.7 mm | HV 5.00 kV | HFW 85.1 µm | det ETD | 40 µm | label
2/4/2014 7:10:56 PM | WD 10.7 mm | HV 5.00 kV | HFW 482 µm | det ETD | 200 µm | label

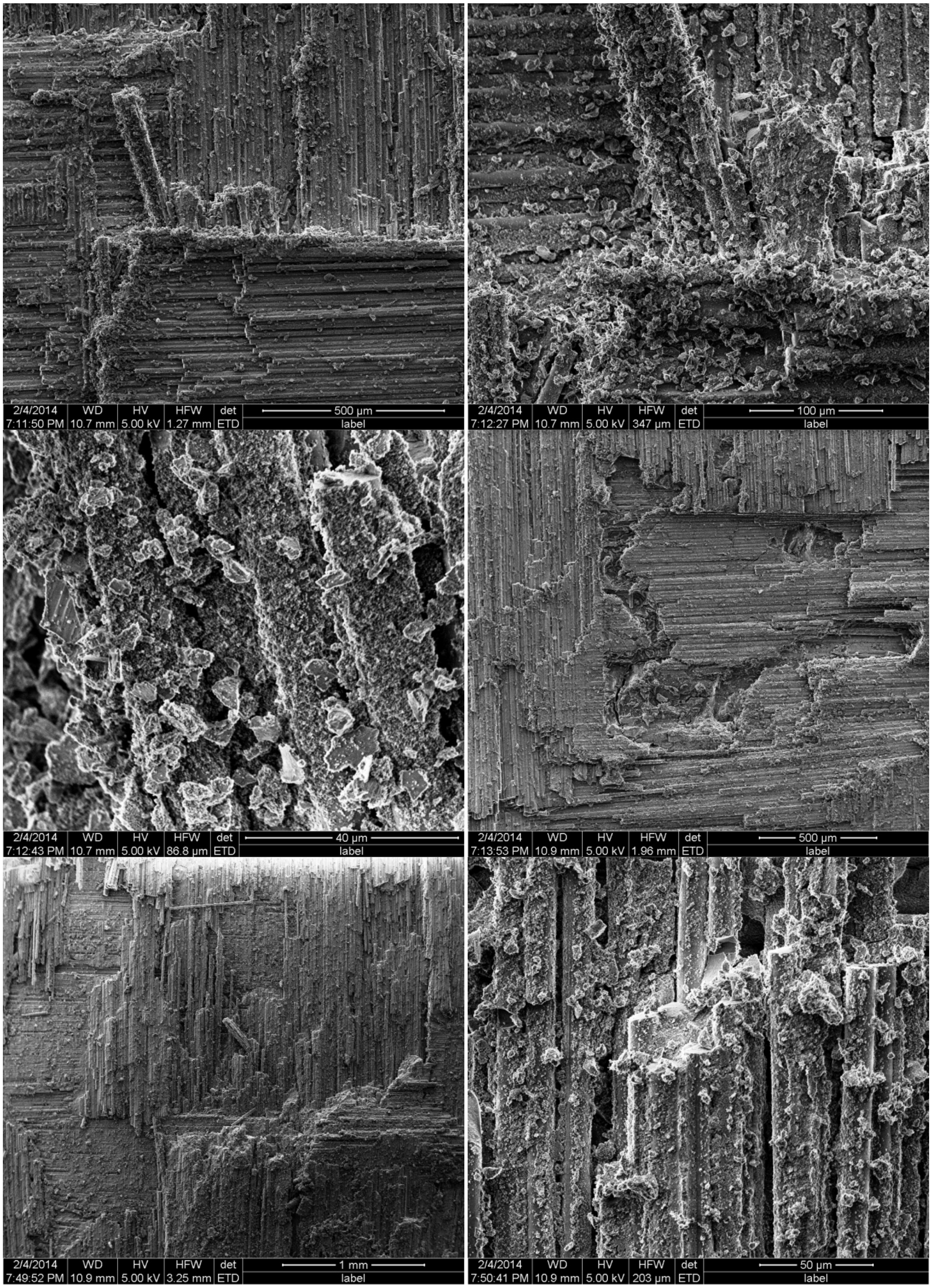
2/4/2014 7:11:50 PM WD 10.7 mm HV 5.00 kV HFW 1.27 mm det ETD 500 µm label
2/4/2014 7:12:27 PM WD 10.7 mm HV 5.00 kV HFW 347 µm det ETD 100 µm label
2/4/2014 7:12:43 PM WD 10.7 mm HV 5.00 kV HFW 86.8 µm det ETD 40 µm label
2/4/2014 7:13:53 PM WD 10.9 mm HV 5.00 kV HFW 1.96 mm det ETD 500 µm label
2/4/2014 7:49:52 PM WD 10.9 mm HV 5.00 kV HFW 3.25 mm det ETD 1 mm label
2/4/2014 7:50:41 PM WD 10.9 mm HV 5.00 kV HFW 203 µm det ETD 50 µm label

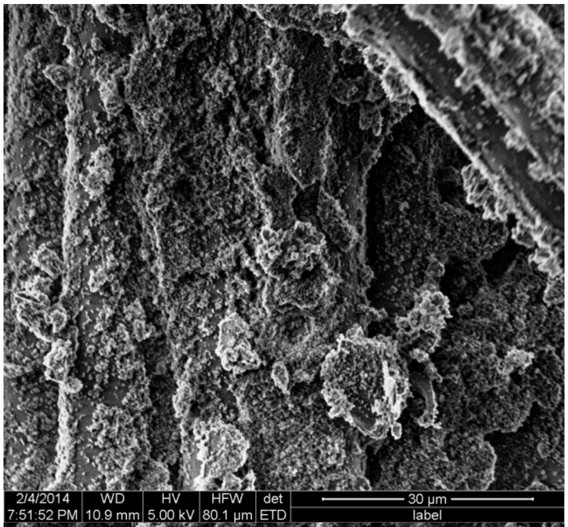
2/4/2014
7:51:52 PM
WD
10.9 mm
HV
5.00 kV
HFW
80.1 µm
det
ETD
30 µm
label

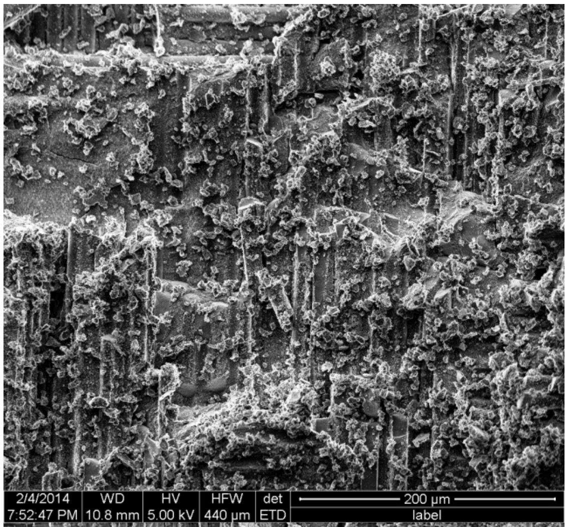
2/4/2014
7:52:47 PM
WD
10.8 mm
HV
5.00 kV
HFW
440 µm
det
ETD
200 µm
label

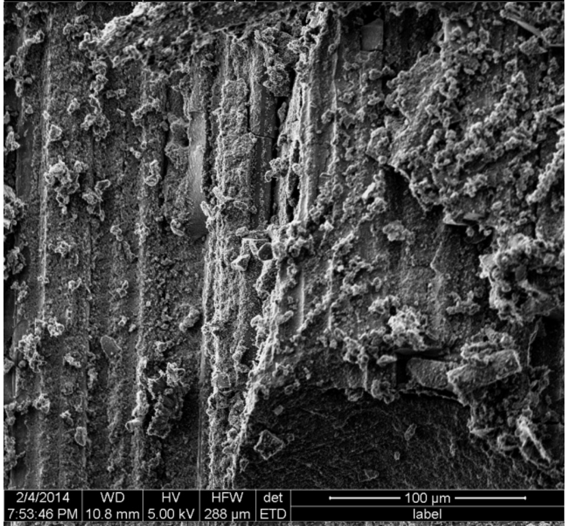
2/4/2014
7:53:46 PM
WD
10.8 mm
HV
5.00 kV
HFW
288 µm
det
ETD
100 µm
label

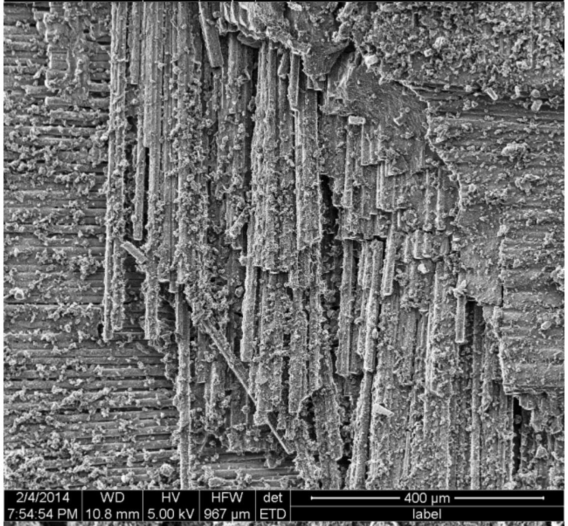
2/4/2014
7:54:54 PM
WD
10.8 mm
HV
5.00 kV
HFW
967 µm
det
ETD
400 µm
label

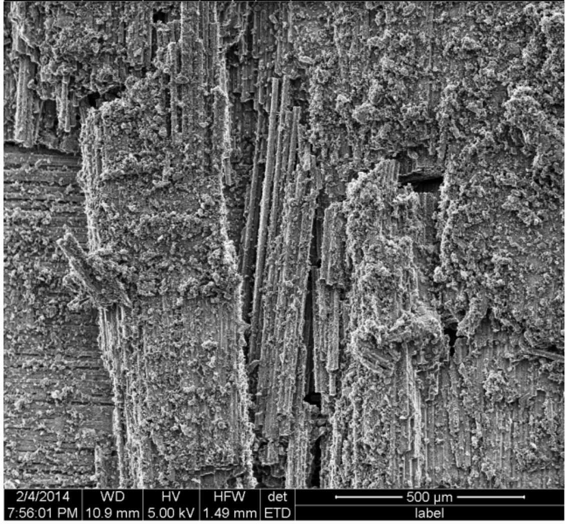
2/4/2014
7:56:01 PM
WD
10.9 mm
HV
5.00 kV
HFW
1.49 mm
det
ETD
500 µm
label

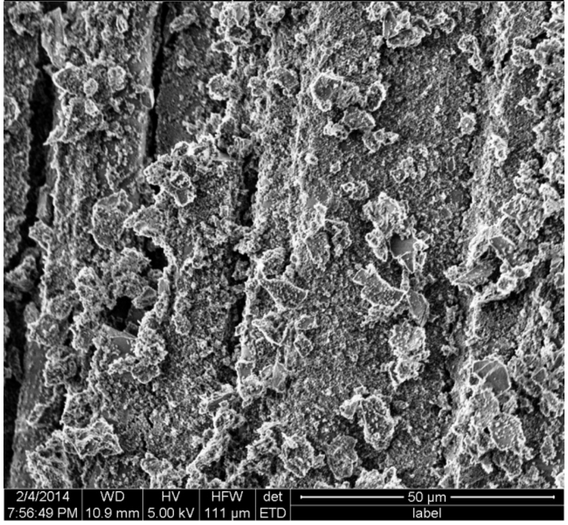
2/4/2014
7:56:49 PM
WD
10.9 mm
HV
5.00 kV
HFW
111 µm
det
ETD
50 µm
label

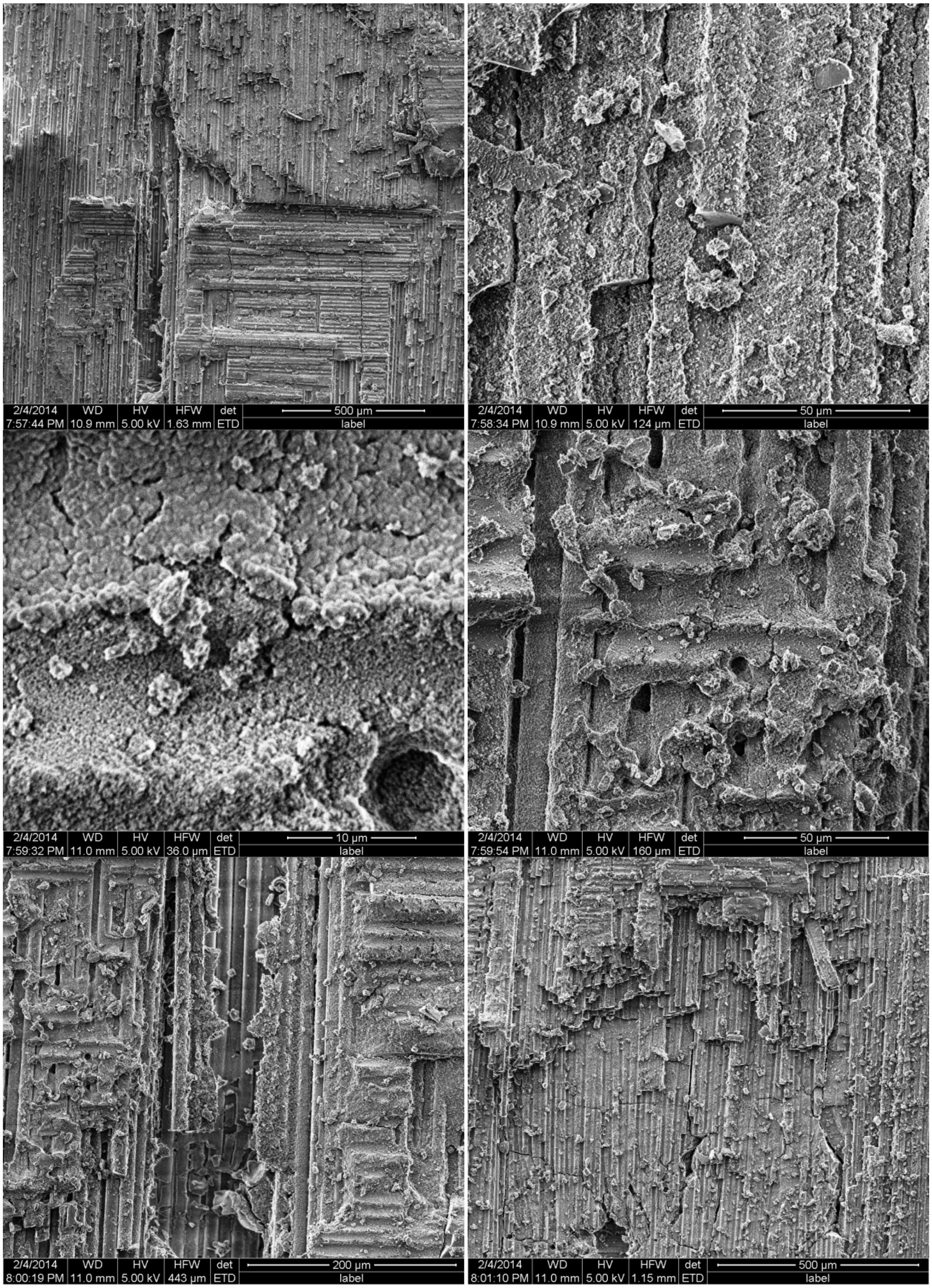
2/4/2014 7:57:44 PM WD 10.9 mm HV 5.00 kV HFW 1.63 mm det ETD 500 µm label
2/4/2014 7:58:34 PM WD 10.9 mm HV 5.00 kV HFW 124 µm det ETD 50 µm label
2/4/2014 7:59:32 PM WD 11.0 mm HV 5.00 kV HFW 36.0 µm det ETD 10 µm label
2/4/2014 7:59:54 PM WD 11.0 mm HV 5.00 kV HFW 160 µm det ETD 50 µm label
2/4/2014 8:00:19 PM WD 11.0 mm HV 5.00 kV HFW 443 µm det ETD 200 µm label
2/4/2014 8:01:10 PM WD 11.0 mm HV 5.00 kV HFW 1.15 mm det ETD 500 µm label

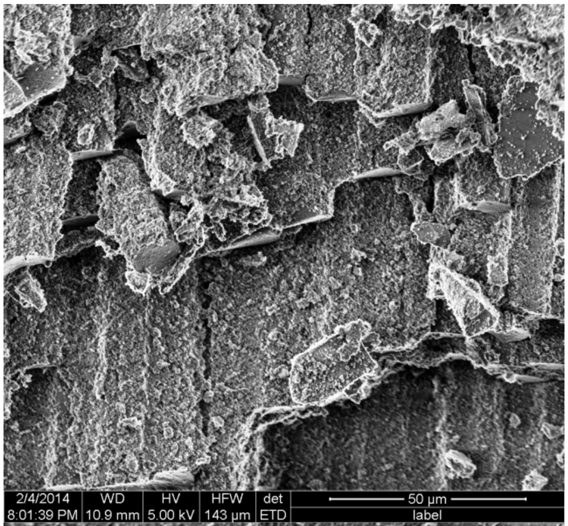
2/4/2014
8:01:39 PM
WD
10.9 mm
HV
5.00 kV
HFW
143 µm
det
ETD
50 µm
label

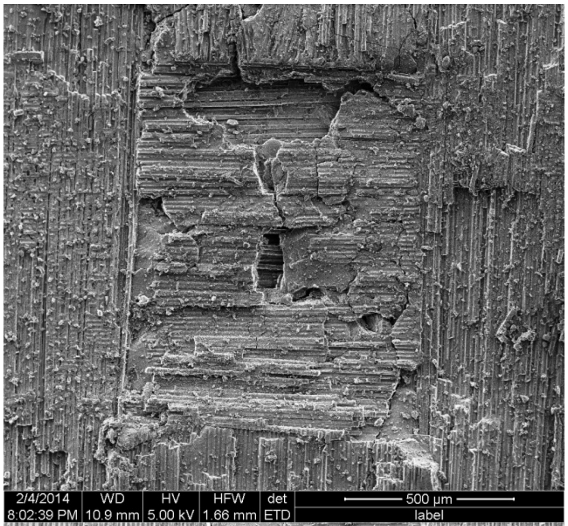
2/4/2014
8:02:39 PM
WD
10.9 mm
HV
5.00 kV
HFW
1.66 mm
det
ETD
500 µm
label

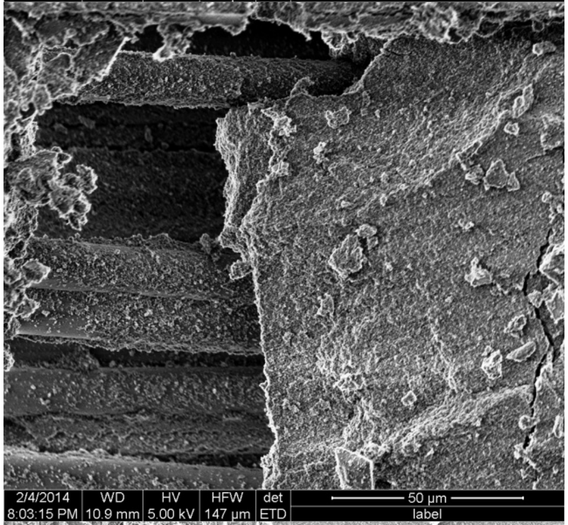
2/4/2014
8:03:15 PM
WD
10.9 mm
HV
5.00 kV
HFW
147 µm
det
ETD
50 µm
label

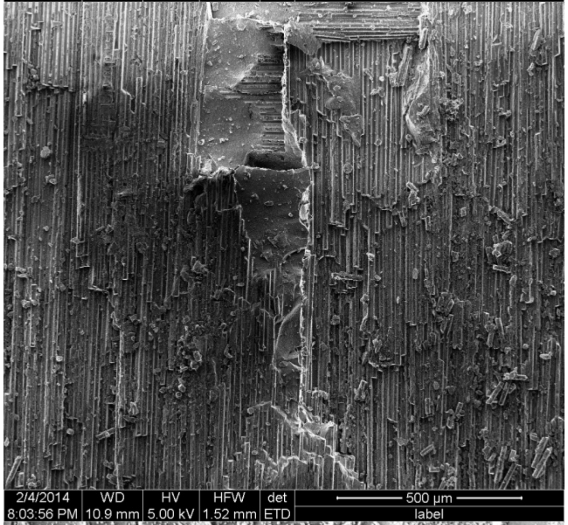
2/4/2014
8:03:56 PM
WD
10.9 mm
HV
5.00 kV
HFW
1.52 mm
det
ETD
500 µm
label

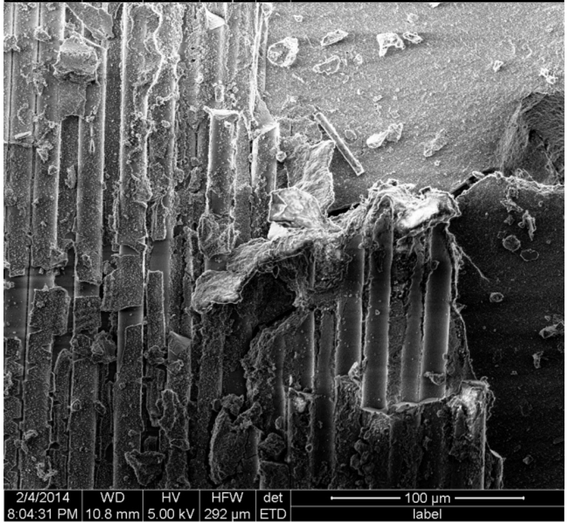
2/4/2014
8:04:31 PM
WD
10.8 mm
HV
5.00 kV
HFW
292 µm
det
ETD
100 µm
label

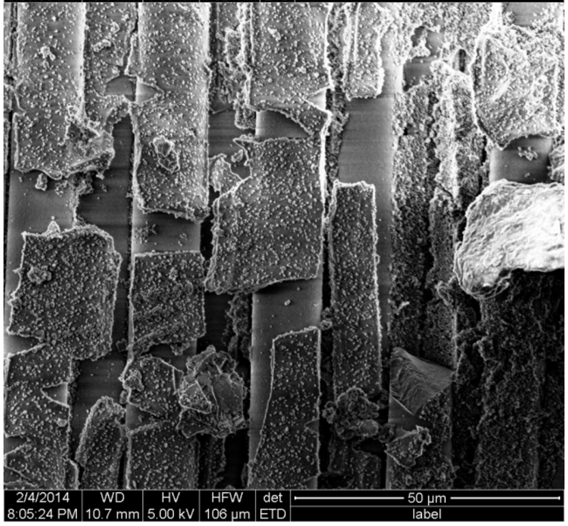
2/4/2014
8:05:24 PM
WD
10.7 mm
HV
5.00 kV
HFW
106 µm
det
ETD
50 µm
label

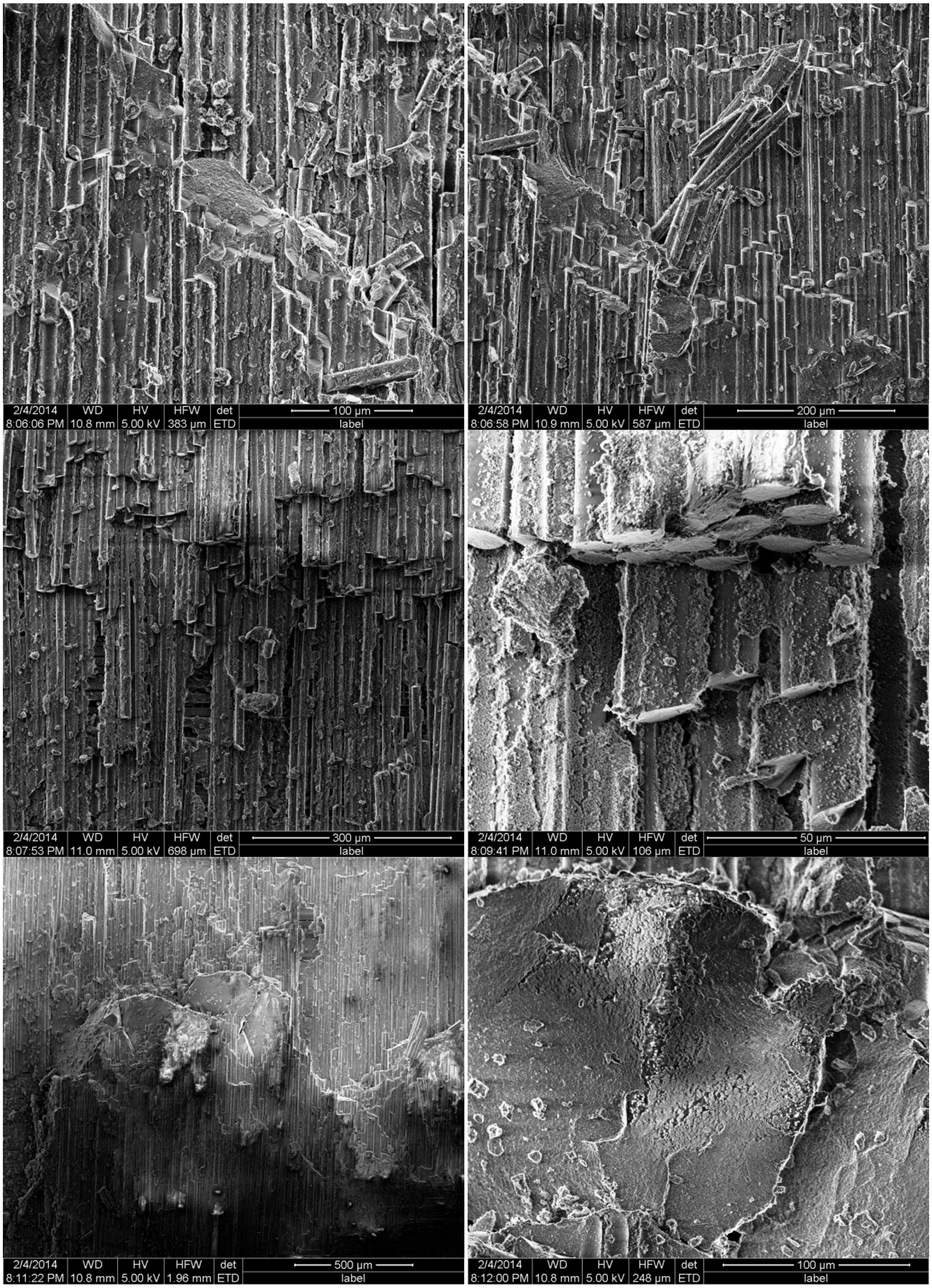
2/4/2014 8:06:06 PM WD 10.8 mm HV 5.00 kV HFW 383 µm det ETD 100 µm label
2/4/2014 8:06:58 PM WD 10.9 mm HV 5.00 kV HFW 587 µm det ETD 200 µm label
2/4/2014 8:07:53 PM WD 11.0 mm HV 5.00 kV HFW 698 µm det ETD 300 µm label
2/4/2014 8:09:41 PM WD 11.0 mm HV 5.00 kV HFW 106 µm det ETD 50 µm label
2/4/2014 8:11:22 PM WD 10.8 mm HV 5.00 kV HFW 1.96 mm det ETD 500 µm label
2/4/2014 8:12:00 PM WD 10.8 mm HV 5.00 kV HFW 248 µm det ETD 100 µm label

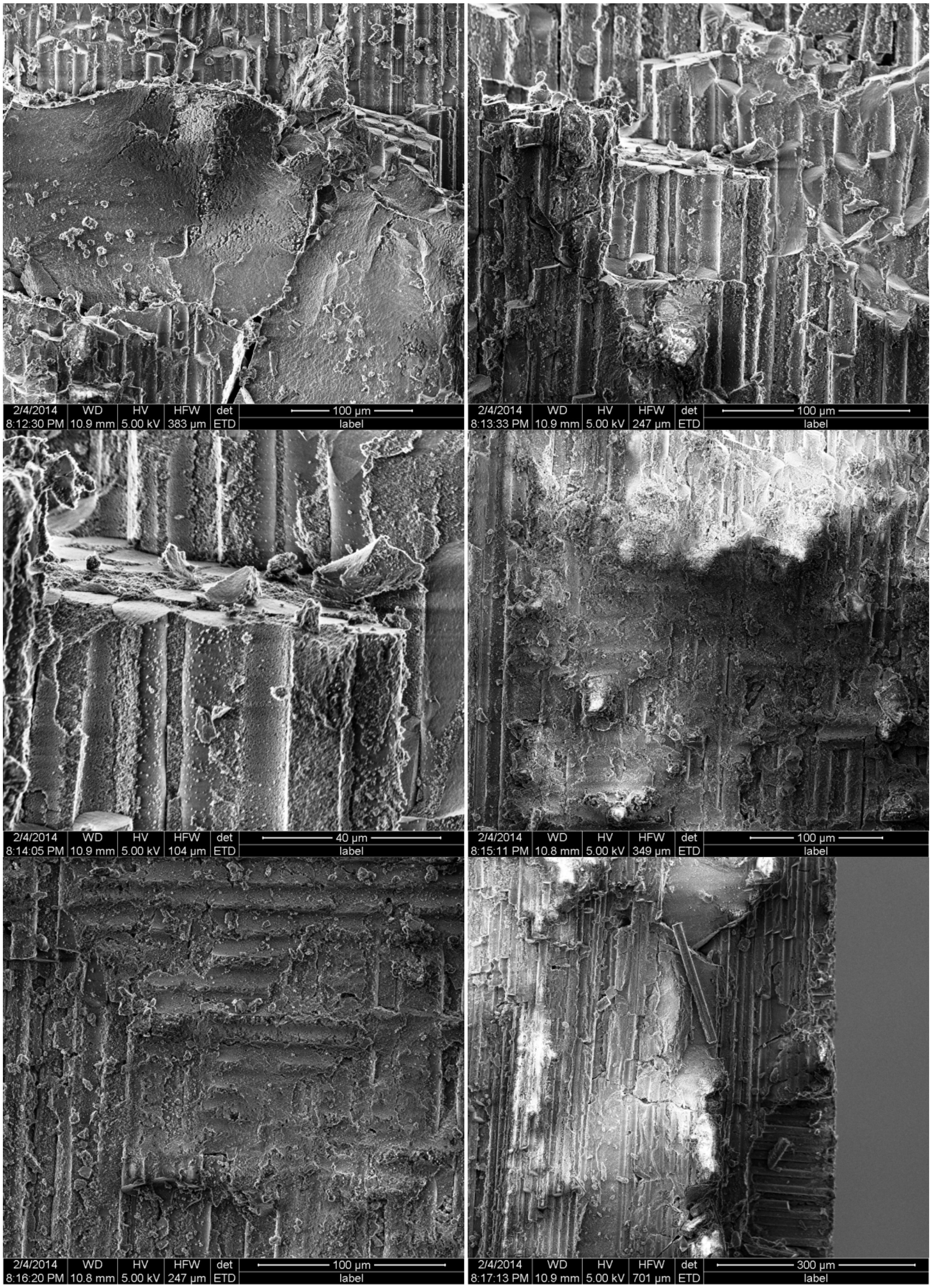
2/4/2014 8:12:30 PM | WD 10.9 mm | HV 5.00 kV | HFW 383 µm | det ETD | 100 µm | label
2/4/2014 8:13:33 PM | WD 10.9 mm | HV 5.00 kV | HFW 247 µm | det ETD | 100 µm | label
2/4/2014 8:14:05 PM | WD 10.9 mm | HV 5.00 kV | HFW 104 µm | det ETD | 40 µm | label
2/4/2014 8:15:11 PM | WD 10.8 mm | HV 5.00 kV | HFW 349 µm | det ETD | 100 µm | label
2/4/2014 8:16:20 PM | WD 10.8 mm | HV 5.00 kV | HFW 247 µm | det ETD | 100 µm | label
2/4/2014 8:17:13 PM | WD 10.9 mm | HV 5.00 kV | HFW 701 µm | det ETD | 300 µm | label

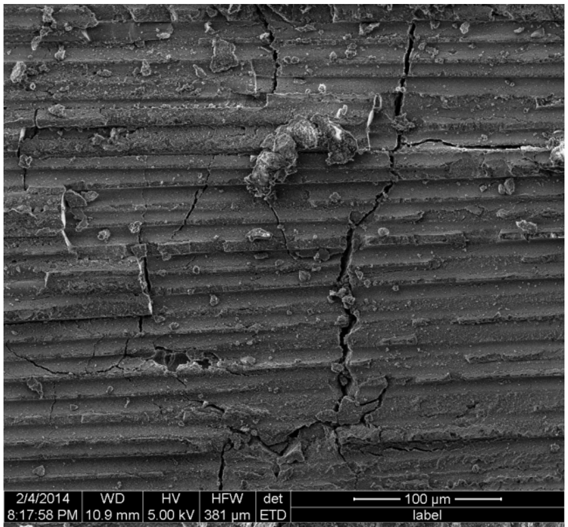
2/4/2014
8:17:58 PM
WD
10.9 mm
HV
5.00 kV
HFW
381 µm
det
ETD
100 µm
label

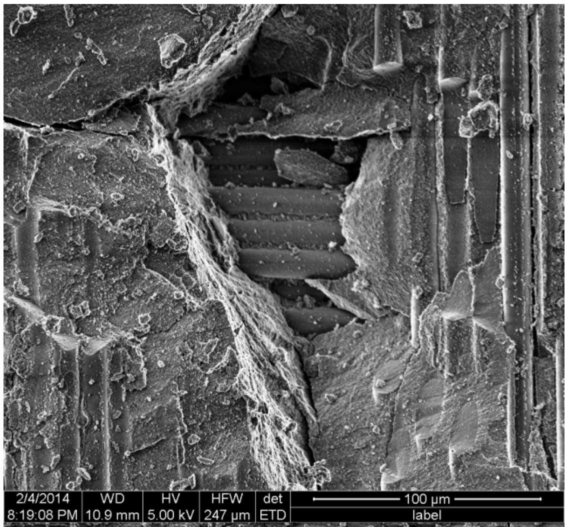
2/4/2014
8:19:08 PM
WD
10.9 mm
HV
5.00 kV
HFW
247 µm
det
ETD
100 µm
label

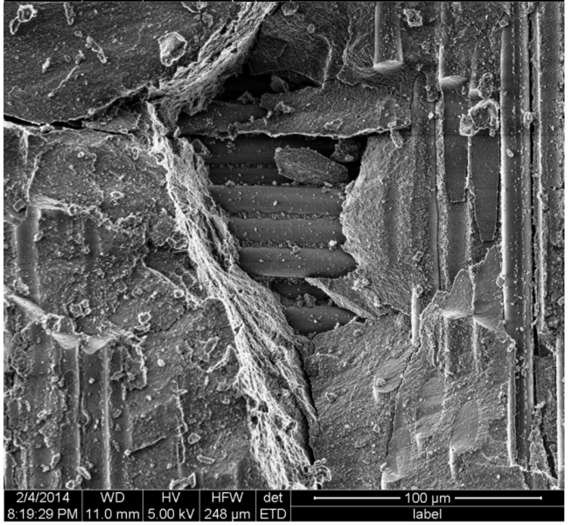
2/4/2014
8:19:29 PM
WD
11.0 mm
HV
5.00 kV
HFW
248 µm
det
ETD
100 µm
label

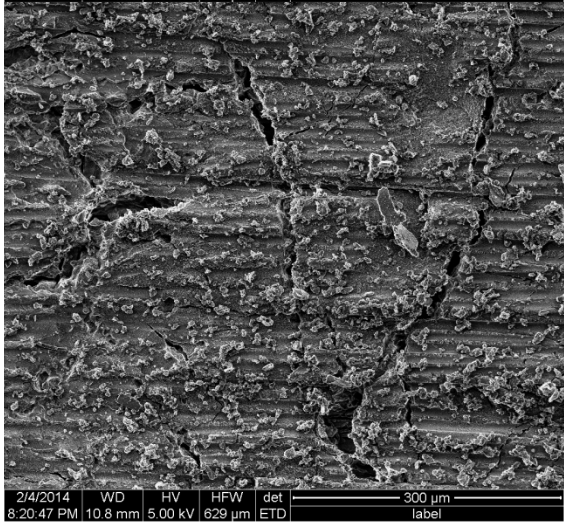
2/4/2014
8:20:47 PM
WD
10.8 mm
HV
5.00 kV
HFW
629 µm
det
ETD
300 µm
label

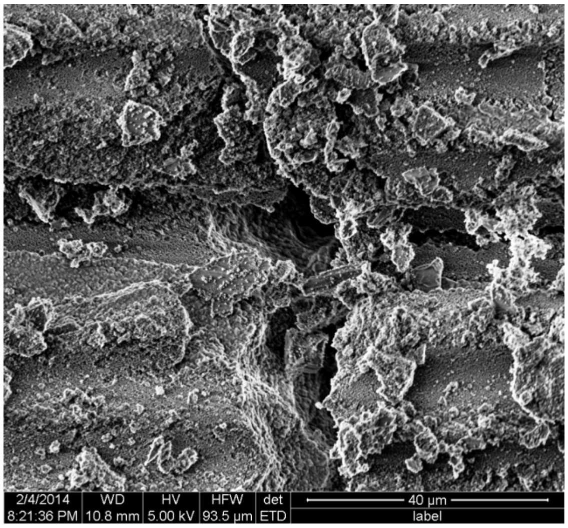
2/4/2014
8:21:36 PM
WD
10.8 mm
HV
5.00 kV
HFW
93.5 µm
det
ETD
40 µm
label

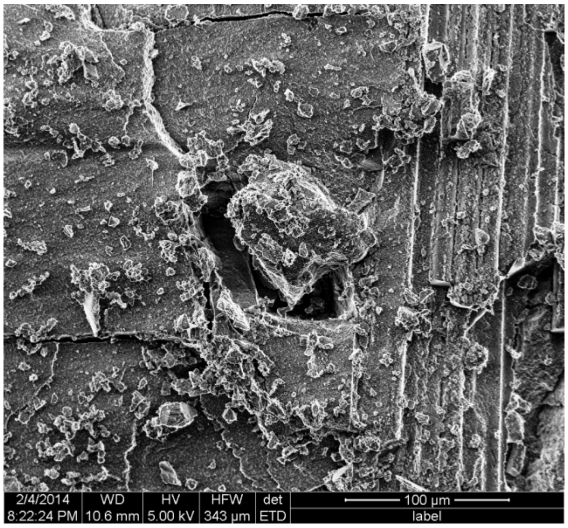
2/4/2014
8:22:24 PM
WD
10.6 mm
HV
5.00 kV
HFW
343 µm
det
ETD
100 µm
label

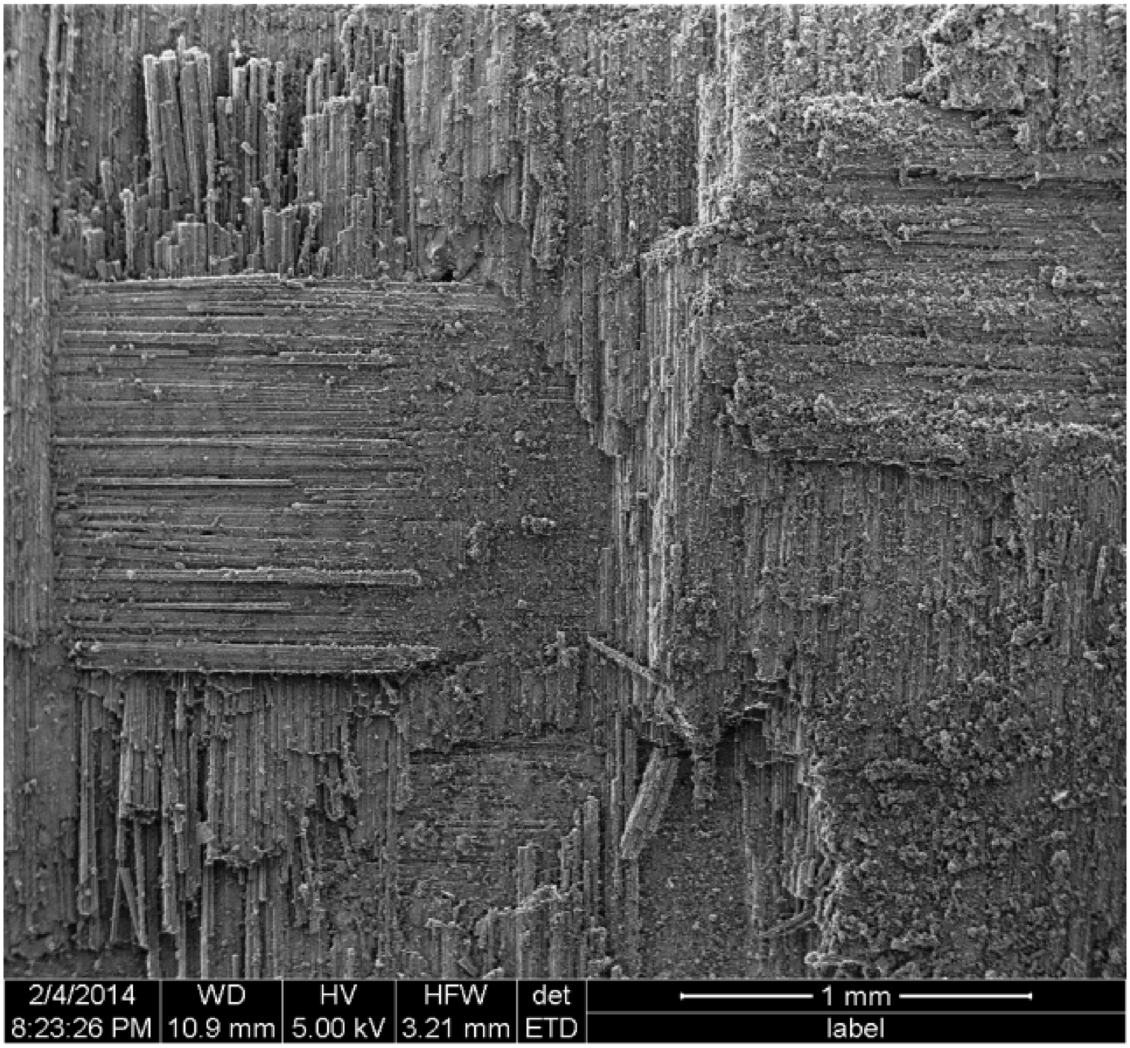
2/4/2014
8:23:26 PM
WD
10.9 mm
HV
5.00 kV
HFW
3.21 mm
det
ETD
1 mm
label

References

[1] Wong, V., "Chapter 4.3.1 Composite Materials," Vol. 2013, 2006, pp. 3.

[2] Daniel, Isaac M.,Ishai, Ori., "Engineering Mechanics of Composite Materials," Oxford University Press, New York, 2006.

[3] Ellyard, D., "Putting it together – science and technology of composite materials," Vol. 2013, 2000.

[4] Smith, F., "The Use of composites in areospace: Past, present and future challenges," 2013.

[5] Cookson, I., "Sector outperforms: 2008 M&A activity matches prior-year record," *Aerospace Components,* No. February, 2009, pp. 1-5.

[6] Messick, D., "Luna Innovations; ODiSI sensing platform provides greater insight into condition of composites," Vol. 2013, 2013, pp. 1.

[7] Anonymous "Composite Materials for Aircraft Industry," *Total Materia,* 2010, pp. 2013.

[8] Cahn, R. W., Evans, A. G.,McLean, M., "High-Temperature Structural Materials," Chapman & Hall for the Royal Society, London; New York, 1996.

[9] Chawla, K.K., "Ceramic matrix composites," Chapman & Hall, London; New York, 1993.

[10] Bansal, N.P., "Handbook of Ceramic Composites," Kluwer Academic Publishers, Boston, 2005.

[11] Baxter, D., "Not Your Mother's China: New Ceramic Composites Are Set to Revolutionize Aviation, Starting with teh LEAP Engine," *GE Reports,* Vol. July, 2012.

[12] Gehm, R., "Future is hot for ceramic matrix composites in engines," *SAE International,* Vol. March, 2009.

[13] Meltzer, P., "Ceramic Matrix Composite seals proving reliable for jet engine nozzles," *Wright-Patterson Air Force Base News,* No. July, 2008.

[14] Evans, A.G., and Zok, F.W., "The physics and mechanics of fibre-reinforced brittle matrix composites," *Journal of Materials Science,* Vol. 29, No. 15, 1994, pp. 3857-3896.

[15] Kerans, R.J., and Parthasarathy, T.A., "Crack deflection in ceramic composites and fiber coating design criteria," *Composites Part A: Applied Science and Manufacturing,* Vol. 30, No. 4, 1999, pp. 521-524.

[16] Kerans, R., Hay, R., Parthasarathy, T., "Interface design for oxidation-resistant ceramic composites," *J Am Ceram Soc,* Vol. 85, No. 11, 2002, pp. 2599-632.

[17] Anonymous "Ceramic Matrix Composite (CMC) Technologies," National Aeronautics and Space Administration, PS–00921–1112–B103, NASA Glenn Research Center, 2012.

[18] DiCarlo, J.A., Yun, H.-., Morscher, G.N., "SiC/SiC Composites for 1200 C and Above," NASA John H. Glenn Research Center at Lewis Field, NASA/TM-2004-213048, Cleveland, Ohio, 2004.

[19] McNulty, J.C., He, M.Y., and Zok, F.W., "Notch sensitivity of fatigue life in a Sylramic™/SiC composite at elevated temperature," *Composites Science and Technology,* No. 61, 2001, pp. 1331-38.

[20] Prewo, K.M., and Batt, J.A., "The oxidative stability of carbon fibre reinforced glass-matrix composites," *Journal of Materials Science,* No. 23, 1988, pp. 523-27.

[21] Mah, T., Hecht, N.L., McCullum, D.E., "Thermal stability of SiC fibres (Nicalon)," *Journal of Materials Science,* No. 19, 1984, pp. 1191-1201.

[22] Heredia, F.E., McNulty, J.C., Zok, F.W., "An oxidation embrittlement probe for ceramic matrix composites," *Journal of the American Ceramic Society,* No. 78, 1995, pp. 2097-100.

[23] More, K.L., Tortorelli, P.F., Ferber, M.K., "Observations of accelerated silicon carbide recession by oxidation at high water-vapor pressures," *Journal of the American Ceramic Society,* Vol. 1, No. 83, 2000, pp. 211-13.

[24] Hermes, E.E., and Kerans, R.J., "Degradation of Non-Oxide Reinforcement and Oxide Matrix Composites," *Mat Res Soc,* Vol. 125, 1988, pp. 73-8.

[25] Szweda, A., Millard, M., and Harrison, M., "Fiber-Reinforced Ceramic-Matrix Composite Member and Method for Making," *1997,* No. 5 601 674.

[26] Sim, S., and Kerans, R., "Slurry Infiltration and 3-D Woven Composites," *Ceram Eng Sci Proc,* Vol. 13, No. 9-10, 1992, pp. 632-41.

[27] Moore, E.H., Mah, T., and Keller, K.A., "3D Composite Fabrication through Matrix Slurry Pressure Infiltration," *Ceram Eng Sci Proc,* Vol. 15, No. 4, 1994, pp. 113-20.

[28] Lewis, M.H., Cain, M., Doleman, P., "*Development of Interfaces in Oxide and Silicate Matrix Composites*," *High-Temperature Ceramic–Matrix CompositesII: Manufacturing and Materials Development*, edited by A.G. Evans and R.G. Naslain, American Ceramic Society, 1995, pp. 41-52.

[29] Lange, F.F., W., W.C., and Evans, A.G., "Processing of Damage-Tolerant, Oxidation-Resistant Ceramic Matrix Composites by a Precursor Infiltration and Pyrolysis Method," *Mater Sci Eng,* Vol. A, No. 195, 1995, pp. 145-50.

[30] Lunderberg, R., and Eckerbom, L., "Design and Processing of All-Oxide Composites," *High-Temperature Ceramic–Matrix Composites II: Manufacturing and Materials Development,* edited by A.G. Evans and R.G. Naslain, American Ceramic Society, 1995, pp. 95-104.

[31] Mouchon, E., and Colomban, P., "Oxide Ceramic Matrix/Oxide Fiber Woven Fabric Composites Exhibiting Dissipative Fracture Behavior," *Composites,* No. 26, 1995, pp. 175-82.

[32] Morgan, P.E.D., and Marshall, D.B., "Ceramic Composites of Monazite and Alumina," *Journal of the American Ceramic Society,* Vol. 78, No. 6, 1995, pp. 1553-1563.

[33] Tu, W., Lange, F.F., and Evans, A.G., "Concept for a damage-tolerant ceramic composite with `strong' interfaces," *Journal of the American Ceramic Society,* Vol. 79, No. 2, 1996, pp. 417-424.

[34] Kerans, R.J., Hay, R.S., Pagano, N.J., "Role of the fiber-matrix interface in ceramic composites," *American Ceramic Society Bulletin,* Vol. 68, No. 2, 1989, pp. 429-442.

[35] Davis, J.B., Loefvander, J.P.A., Evans, A.G., "Fiber coating concepts for brittle-matrix composites," *American Ceramic Society, Journal,* Vol. 76, No. 5, 1993, pp. 1249.

[36] Mackin, T.J., Yang, J.Y., Levi, C.G., "Environmentally compatible double coating concepts for sapphire fiber-reinforced gamma-TiAl," *Materials Science and Engineering A,* Vol. A161, No. 2, 1993, pp. 285-293.

[37] Levi, C.G., Yang, J.Y., Dalgleish, B.J., "Processing and performance of an all-oxide ceramic composite," *Journal of the American Ceramic Society,* Vol. 81, No. 8, 1998, pp. 2077-2086.

[38] Hegedus, A.G., "Ceramic Bodies of Controlled Porosity and Process for Making Same," No. 5 0177 522, 1991,

[39] Dunyak, T.J., Chang, D.R., and Millard, M.L., "Thermal Aging Effects on Oxide/Oxide Ceramic-Matrix Composites," *17th Conference on Metal Matrix, Carbon,*

and Ceramic Matrix Composites, Vol. NASA Conference Publication 3235, Part 2, 1993, pp. 675-90.

[40] Zawada, L.P., and Lee, S.S., "Mechanical Behavior of CMCs for Flaps and Seals," *DARPA Ceramic Technology Insertion Program* , Defence Advanced Projects Agency Conference Publication, Annapolis, MD, 1994, pp. 267-322.

[41] Zawada, L.P., and Lee, S.S., "Evaluation of the Fatigue Performance of Five CMCs for Aerospace Applications," *Sixth International Fatigue Congress,* 1996, pp. 1669-74.

[42] Tian, J.L., "Crack branching in all-oxide ceramic composites," *Journal of the American Ceramic Society,* Vol. 79, No. 1, 1996, pp. 266-274.

[43] Zok, F.W., and Levi, C.G., "Mechanical properties of porous-matrix ceramic composites," *Advanced Engineering Materials,* Vol. 3, No. 1-2, 2001, pp. 15-23.

[44] Zok, F.W., "Developments in oxide fiber composites," *Journal of the American Ceramic Society,* Vol. 89, No. 11, 2006, pp. 3309-3324.

[45] Chermant, J.L., Boitier, G., Darzens, S., "The creep mechanism of ceramic matrix composites at low temperature and stress, by a material science approach," *Journal of the European Ceramic Society,* Vol. 22, No. 14-15, 2002, pp. 2443-2460.

[46] Zhu, S., Mizuno, M., Kagawa, Y., "Monotonic tension, fatigue and creep behavior of SiC-fiber-reinforced SiC-matrix composites: a review," *Composites Science and Technology,* Vol. 59, No. 6, 1999, pp. 833-51.

[47] Zhu, S., Mizuno, M., Cao, J., "Creep and fatigue behavior in Hi-Nicalon-fiber-reinforced silicon carbide composites at high temperatures," *American Ceramic Society, Journal,* Vol. 82, No. 1, 1999, pp. 117-128.

[48] Ruggles-Wrenn, M., Christensen, D.T., Chamberlain, A.L., "Effect of frequency and environment on fatigue behavior of a CVI SiC/SiC ceramic matrix composite at 1200C," *Composites Science and Technology,* Vol. 71, No. 2, 2011, pp. 190-196.

[49] Carrere, P., and Lamon, J., "Fatigue Behavior at High Temperature in Air of a 2D Woven SiC/SiBC with a Self Healing Matrix," *Key Engineering Materials*, Vol. 164-165, 1999, pp. 321-324.

[50] Reynaud, P., Rouby, D., and Fantozzi, G., "Cyclic fatigue behaviour at high temperature of a self-healing ceramic matrix composite," *Annales De Chimie (Science Des Materiaux),* Vol. 30, No. 6, 2005, pp. 649-58.

[51] Darzens, S., Chermant, J.L., Vicens, J., "Understanding of the creep behavior of SiC_f–SiBC composites," *Scripta Materialia,* No. 47, 2002, pp. 433-439.

[52] Carrere, P., and Lamon, J., "Creep behaviour of a SiC/Si-B-C composite with a self-healing multilayered matrix," *Journal of the European Ceramic Society,* Vol. 23, No. 7, 2003, pp. 1105-14.

[53] Ruggles-Wrenn, M., Delapasse, J., Chamberlain, A.L., "Fatigue behavior of a Hi-Nicalon (TM)/SiC-B4C composite at 1200 degrees C in air and in steam," *Materials Science and Engineering A - Structural Materials Properties Microstructure and Processing,* Vol. 534, 2012, pp. 119-128.

[54] Ruggles-Wrenn, M.B., and Jones, T.P., "Tension–compression fatigue of a SiC/SiC ceramic matrix composite at 1200 °C in air and in steam," *International Journal of Fatigue,* Vol. 47, No. 0, 2013, pp. 154-160.

[55] Ruggles-Wrenn, M., and Kurtz, G., "Notch Sensitivity of Fatigue Behavior of a Hi-Nicalon (TM)/SiC-B4C Composite at 1,200 degrees C in Air and in Steam," *Applied Composite Materials,* Vol. 20, No. 5, 2013, pp. 891-905.

[56] Ruggles-Wrenn, M., Mehrman, J.M., and Baek, S.S., "Influence of hold times on the elevated-temperature fatigue behavior of an oxide-oxide ceramic composite in air and in steam environment," *Composites Science and Technology,* Vol. 67, No. 7-8, 2007, pp. 1425-38.

[57] Ruggles-Wrenn, M., and Braun, J.C., "Effects of steam environment on creep behavior of Nextel™720/alumina ceramic composite at elevated temperature," *Materials Science & Engineering: A,* Vol. 497, No. 1, 2008, pp. 101.

[58] Ruggles-Wrenn, M., and Genelin, C.L., "Creep of Nextel™720/alumina–mullite ceramic composite at 1200°C in air, argon, and steam," *Composites Science & Technology,* Vol. 69, No. 5, 2009, pp. 663.

[59] Ruggles-Wrenn, M., Koutsoukos, P., and Baek, S., "Effects of environment on creep behavior of two oxide/oxide ceramic–matrix composites at 1200 °C," *Journal of Materials Science,* Vol. 43, No. 20, 2008, pp. 6734.

[60] Ruggles-Wrenn, M., and Kutsal, T., "Effects of steam environment on creep behavior of Nextel (TM) 720/alumina-mullite ceramic composite at elevated temperature," *Composites: Part A, Applied Science & Manufacturing,* Vol. 41, No. 12, 2010, pp. 1807.

[61] Ruggles-Wrenn, M., and Ozer, M., "Creep behavior of Nextel™720/alumina–mullite ceramic composite with ±45° fiber orientation at 1200°C," *Materials Science & Engineering: A,* Vol. 527, No. 20, 2010, pp. 5326.

[62] Ruggles-Wrenn, M.B., and Laffey, P.D., "Creep behavior in interlaminar shear of Nextel™720/alumina ceramic composite at elevated temperature in air and in steam," *Composites Science and Technology,* Vol. 68, No. 10–11, 2008, pp. 2260-2266.

[63] Ruggles-Wrenn, M., Siegert, G.T., and Baek, S.S., "Creep behavior of Nextel™720/alumina ceramic composite with ±45° fiber orientation at 1200°C," *Composites Science & Technology,* Vol. 68, No. 6, 2008, pp. 1588.

[64] Ruggles-Wrenn, M., and Szymczak, N.R., "Effects of steam environment on compressive creep behavior of Nextel (TM) 720/Alumina ceramic composite at 1200 deg C," *Composites: Part A, Applied Science & Manufacturing,* Vol. 39, No. 12, 2008, pp. 1829.

[65] Ruggles-Wrenn, M., Yeleser, T., Fair, G., "Effects of Steam Environment on Creep Behavior of Nextelâ„¢610/Monazite/Alumina Composite at 1,100Â°C," *Applied Composite Materials,* Vol. 16, No. 6, 2009, pp. 379-392.

[66] Choi, S.R., Kowalik, R.W., Alexander, D.J., "Assessments of life limiting behavior in interlaminar shear for Hi-Nic SiC/SiC ceramic matrix composite at elevated temperature," *Ceramic Engineering and Science Proceedings,* Vol. 28, No. 2, 2008, pp. 179-189.

[67] Choi, S.R., and Bansal, N.P., "Interlaminar tension/shear properties and stress rupture in shear of various continuous fiber-reinforced ceramic matrix composites," *Ceramic Transactions,* Vol. 175, 2006, pp. 119-134.

[68] Choi, S.R., and Bansal, N.P., "Shear strength as a function of test rate for SiCf/BSAS ceramic matrix composite at elevated temperature," *Journal of the American Ceramic Society,* 2004.

[69] Choi, S.R., Bansal, N.P., Calomino, A.M., "Shear strength behaviors of ceramic matrix composites at elevated temperatures," *Ceramic Transactions,* Vol. 165, 2005, pp. 131-145.

[70] Choi, S.R., Kowalik, R.W., Alexander, D.J., "Elevated-temperature stress rupture in interlaminar shear of a Hi-Nic SiC/SiC ceramic matrix composite," *Composites Science and Technology,* Vol. 69, No. 7, 2009, pp. 890-897.

[71] Chamis, C.C., "Failure criteria for filamentary composites," *Testing and Design,* Vol. ASTM STP 460, 1969, pp. 336-460.

[72] Sandhu, R.S., "A Survey of Failure Theories of Isotropic and Anisotropic Materials," *AFFDL-TR-72-71,* No. AD756889, 1972.

[73] Owen, M.J., and Rice, D.I., "Biaxial strength behavior of glass-reinforced polyester resins," *Composite Materials: Testing and Design, 6th Conf.* Vol. ASTM STP 787, ed. I., 1982, pp. 124-44.

[74] Soni, S.R., "A comparative study of failure envelopes in composite laminates," *Journal of Reinforced Plastics and Composites,* 1983.

[75] Tsai, S.W., "A survey of macroscopic failure criteria for composite materials," *Journal of Reinforced Plastics and Composites,* 1984.

[76] Tsai,Stephen W.,, "Composites design," Think Composites, Dayton, Ohio, 1988,

[77] Rowlands, R.E., "Strength (failure) theories and their experimental correlation," *Handbook of Composites,* edited by G.C. Sih and A.M. Skudra, Vol. 3, Failure Mechanics of Composites, Elsevier Science, 1985, pp. 71-125.

[78] Nahas, M.N., "Survey of failure and post-failure theories of laminated fiber-reinforced composites," *Journal of Composites Technology and Research,* Vol. 8, No. 4, 1986, pp. 138-53.

[79] Chen, A.S., and Matthews, F.L., "A review of multiaxial/biaxial loading tests for composite materials," *Composites,* Vol. 24, No. 5, 1993, pp. 395-406.

[80] Anonymous "Special Issue," *Composites Science and Technology,* Vol. 58, 1998.

[81] Anonymous "Special Issue," *Composites Science and Technology,* Vol. 62, 2002.

[82] Anonymous "Special Issue," *Composites Science and Technology,* Vol. 64, 2004.

[83] Hinton, M.J., and Soden, P.D., "Predicting failure in composite laminates: the background to the exercise," *Composites Science and Technology,* Vol. 58, No. 7, 1998, pp. 1001-1010.

[84] Soden, P.D., Hinton, M.J., and Kaddour, A.S., "Lamina properties, lay-up configurations and loading conditions for a range of fibre-reinforced composite laminates," *Composites Science and Technology,* Vol. 58, No. 7, 1998, pp. 1011-1022.

[85] Petrovic, J.J., and Stout, M.G., "Fracture of Al_2O_3 in Combined Tension-Torsion: 1. Experiments," *Journal of the American Ceramic Society,* Vol. 64, No. 11, 1981, pp. 656-660.

[86] Stout, M.G., and Petrovic, J.J., "Multiaxial Loading Fracture of Al2O3 Tubes: 1. Experiments," *Journal of the American Ceramic Society,* Vol. 67, No. 1, 1984, pp. 14-18.

[87] Nohut, S., Usbeck, A., Ozcoban, H., "Determination of the multiaxial failure criteria for alumina ceramics under tension-torsion test," *Journal of the European Ceramic Society,* Vol. 30, No. 16, 2010, pp. 3339-49.

[88] Kawai, N., Kotani, T., Kakimoto, Y., "Fracture behavior of silicon nitride ceramics under combined compression–torsion stresses analyzed by multiaxial fracture statistics," *Journal of the European Ceramic Society,* Vol. 31, No. 9, 2011, pp. 1827-1833.

[89] Liao, K., George, E.R., and Reifsnider, K.L., "Characterization of ceramic matrix composite tubes under uniaxial/biaxial monotonic and cyclic loading," *Multiaxial fatigue and deformation testing techniques,* edited by Kalluri and P.J. Bonacuse, Vol. ASTM STP 1280, American Society for Testing and Materials, 1997, pp. 224-40.

[90] DeRienzo, J.M., "Biaxial (tension-torsion) testing of an oxide/oxide ceramic matrix composite," *AFIT-ENY-13-M-10,* No. DTIC ADA579147, 2013.

[91] Jurf, R.A., and Butner, S.C., "Advances in Oxide-Oxide CMC," *Journal of Engineering for Gas Turbines & Power,* Vol. 122, No. 2, 2000, pp. 202.

[92] ASTM Standard C1425-13, "Standard Test Method for Interlaminar Shear Strength of 1–D and 2–D Continuous Fiber-Reinforced Advanced Ceramics at Elevated Temperatures," 2011.

[93] Laffey, P.D., "The Effects of Environment on the Interlaminar Shear Performance of an Oxide/Oxide Ceramic Matrix Composite at Elevated Temperature," *AFIT-GAE-ENY-07-J11,* No. DTIC ADA470171, 2007.

[94] Pope, M.T., "Creep Behavior in Interlaminar Shear of a CVI SiC/SiC Composite at Elevated Temperatures in Air and Steam," *AFIT-GMS-ENY-12-M02,* No. DTIC ADA558751, 2012.

[95] ASTM Standard C1358-13, "Standard Test Method for Monotonic Compressive Strength Testing of Continuous Fiber-Reinforced Advanced Ceramics with Solid Rectangular Cross-Section Test Specimens at Ambient Temperatures," 2011.

[96] ASTM Standard E2207-08(2013)e1, "Standard Practice for Strain-Controlled Axial-Torsional Fatigue Testing with Thin-Walled Tubular Specimens," 2013.

[97] Anonymous "793 Tuning and Calibration," *MTS Systems Corporation,* No. 100-147-134 C, 2008.

[98] Buchanan, D.J., John, R., and Zawada, L.P., "Off-axis creep behavior of oxide/oxide NeXtel (TM) 720/AS-0," *Composites Science and Technology,* Vol. 68, No. 6, 2008, pp. 1313-1320.

[99] Scherer, G.W., "Coarsening in a viscous matrix," *Journal of the American Ceramic Society,* Vol. 81, No. 1, 1998, pp. 49-54.

[100] Bordia, R.K., and Jagota, A., "Crack growth and damage in constrained sintering films," *Journal of the American Ceramic Society,* Vol. 76, No. 10, 1993, pp. 2475-85.

[101] Scherer, G.W., "Viscous Sintering with a Pore-Size Distribution and Rigid Inclusions," *Journal of the American Ceramic Society,* Vol. 71, No. 10, 1988, pp. C447-C448.

[102] Scherer, G.W., "Viscous sintering of a bimodal pore-size distribution," *Journal of the American Ceramic Society,* Vol. 67, No. 11, 1984, pp. 709-15.

[103] Zawada, L.P., Hay, R.S., Lee, S.S., "Characterization and High-Temperature Mechanical Behavior of an Oxide/Oxide Composite," *Journal of the American Ceramic Society,* Vol. 86, No. 6, 2003, pp. 981-990.

[104] Parikh, N.M., "Effect of Atmosphere on Surface Tension of Glass," *Journal of the American Ceramic Society,* Vol. 41, No. 1, 1958, pp. 18-22.

[105] Antti, M.-., Lara-Curzio, E., and Warren, R., "Thermal degradation of an oxide fibre (Nextel 720)/aluminosilicate composite," *Journal of the European Ceramic Society,* Vol. 24, No. 3, 2004, pp. 565-78.

[106] Ruggles-Wrenn, M., Radzicki, A.T., Baek, S.S., "Effect of loading rate on the monotonic tensile behavior and tensile strength of an oxide-oxide ceramic composite at 1200degC," *Materials Science & Engineering: A (Structural Materials: Properties, Microstructure and Processing),* Vol. 492, No. 1-2, 2008, pp. 88-94.

[107] Amijima, S., Fujii, T., and Hamaguchi, M., "Static and fatigue tests of a woven glass fabric composite under biaxial tension-torsion loading," *Composites,* Vol. 22, No. 4, 1991, pp. 281-289.

[108] Kuo-Shih Liu, and Tsai, S.W., "A progressive quadratic failure criterion for a laminate," *Composites Science and Technology,* Vol. 58, No. 7, 1998, pp. 1023-32.

REPORT DOCUMENTATION PAGE	*Form Approved* *OMB No. 0704-0188*

The public reporting burden for this collection of information is estimated to average 1 hour per response, including the time for reviewing instructions, searching existing data sources, gathering and maintaining the data needed, and completing and reviewing the collection of information. Send comments regarding this burden estimate or any other aspect of this collection of information, including suggestions for reducing the burden, to Department of Defense, Washington Headquarters Services, Directorate for Information Operations and Reports (0704-0188), 1215 Jefferson Davis Highway, Suite 1204, Arlington, VA 22202-4302. Respondents should be aware that notwithstanding any other provision of law, no person shall be subject to any penalty for failing to comply with a collection of information if it does not display a currently valid OMB control number.

PLEASE DO NOT RETURN YOUR FORM TO THE ABOVE ADDRESS.

1. REPORT DATE *(DD-MM-YYYY)* 27-03-2013	**2. REPORT TYPE** Master's Thesis	**3. DATES COVERED** *(From - To)* April 2012 - March 2014

4. TITLE AND SUBTITLE

Experimental Investigation of Mechanical Behavior of an Oxide/Oxide Ceramic Composite in Interlaminar Shear and under Combined Tension-Torsion Loading

5a. CONTRACT NUMBER

5b. GRANT NUMBER

5c. PROGRAM ELEMENT NUMBER

6. AUTHOR(S)

Hilburn Skyler R, Capt, USAF

5d. PROJECT NUMBER

5e. TASK NUMBER

5f. WORK UNIT NUMBER

7. PERFORMING ORGANIZATION NAME(S) AND ADDRESS(ES)

Air Force Institute of Technology
Graduate School of Engineering and Management (AFIT/EN)
2950 Hobson Way
Wright-Patterson AFB OH 45433-7765

8. PERFORMING ORGANIZATION REPORT NUMBER

AFIT-ENY-14-M-26

9. SPONSORING/MONITORING AGENCY NAME(S) AND ADDRESS(ES)

Air Force Research Laboratory
Larry Zawada
2230 10th Street
Wright-Patterson AFB, OH 45433
larry.zawada@us.af.mil

10. SPONSOR/MONITOR'S ACRONYM(S)

AFRL/RXCC

11. SPONSOR/MONITOR'S REPORT NUMBER(S)

12. DISTRIBUTION/AVAILABILITY STATEMENT

Distribution Statement A.
Approved for Public Release; Distribution Unlimited

13. SUPPLEMENTARY NOTES

This work is declared a work of the U.S. Government and is not subject to copyright protection in the United States.

14. ABSTRACT

Creep behavior in interlaminar shear of an oxide-oxide ceramic composite, Nextel™720/aluminosilicate (N720/AS), was investigated at 1100°C in laboratory air and in steam. The interlaminar shear strength (ILSS) was determined as 7.65 MPa. The creep behavior was examined for interlaminar shear stresses in the 2-6 MPa range. Primary and secondary creep regimes were observed in all tests conducted in air and in steam. Tertiary creep was noted in the tests performed at 6 MPa. Larger creep strains and higher creep strain rates were produced in steam. Surprisingly, the presence of steam had a beneficial effect on creep lifetimes. It appears that matrix strengthening occurred in steam, which resulted in longer creep lifetimes in interlaminar shear. Additionally, exploratory tension-torsion tests of thin-walled tubular specimens of N720/AS were performed at room temperature in air. The failure stress levels determined in tension-torsion tests and in compression tests were used together with data from literature to construct a biaxial failure envelope. The efficacy of Tsai-Wu and Tsai-Hill multiaxial failure theories was also explored.

15. SUBJECT TERMS

Ceramic Matrix Composites, Composite Materials, Ceramic Fibers, Ceramic Materials, Fiber Reinforced Composites, Alumina, Aluminosilicate, Mullite, Creep, Oxides, Nextel™ 720 Fiber, Tube, Biaxial, Involute, Tension-Torsion, Interlaminar Shear

16. SECURITY CLASSIFICATION OF:			**17. LIMITATION OF ABSTRACT**	**18. NUMBER OF PAGES**	**19a. NAME OF RESPONSIBLE PERSON**
a. REPORT	**b. ABSTRACT**	**c. THIS PAGE**			Dr. Marina B. Ruggles-Wrenn, AFIT/ENY
U	U	U	UU	187	**19b. TELEPHONE NUMBER** *(Include area code)* 9372553636x4641 marina.ruggles-wrenn@afit.edu

Reset